Structural characterization and across-fault seal assessment of the Aurora CO_2 storage site, northern North Sea

Nora Holden

Master Thesis in Geosciences
Structural Geology and Tectonics
60 credits

Department of Geosciences
Faculty of Mathematics and Natural Sciences

UNIVERSITY OF OSLO

June 2021

Structural characterization and across-fault seal assessment of the Aurora CO_2 storage site, northern North Sea

Supervisors: Elin Skurtveit, Anja Sundal, Mark J. Mulrooney, Johnathon L. Osmond, and Alvar Braathen

This work is published digitally through DUO – Digitale Utgivelser ved UiO
http://www.duo.uio.no/

Printed: Reprosentralen, Universitetet i Oslo

Acknowledgements

First, I want to express my gratitude and sincere appreciation to my main supervisor Elin Skurtveit for your encouragement and guidance at every stage of this process. I am also grateful to my co-supervisors Anja Sundal, Mark J. Mulrooney, Johnathon L. Osmond, and Alvar Braathen for your productive discussions, critical assessments of various drafts, and for challenging me to present at the NGF Winter conference. A special thank you goes out to my co-supervisor Johnathon L. Osmond for your patience in teaching me how to use Petrel and Move.

Secondly, I want to thank my fellow students and friends at the Geoscience M.Sc. program at UiO who have made working on this thesis enjoyable and provided support and guidance. I would also like to extend a thank you to the student administration and IT department at the Department of Geoscience. Your patience and guidance have been crucial when working on my master thesis.

Finally, a personal thank you goes to my partner, Povilas Nefas, and my family for taking such an interest in my studies and encouraging and supporting me throughout this process.

Nora Holden

Oslo, Norway. June 15th, 2021

Preface

This master's thesis (ECTS 60) is submitted to the Department of Geosciences, University of Oslo (UiO), in the candidacy of the Master of Science in Geosciences (ECTS 120) following the Structural Geology and Tectonics program. The main supervisor of the thesis is Associate professor Elin Skurtveit (UiO, NGI) together with co-supervisors at the University of Oslo Associate professor Anja Sundal, Postdoctoral fellow Mark J. Mulrooney, Ph.D. fellow Johnathon L. Osmond, and Professor Alvar Braathen.

This thesis serves as a contribution to the University of Oslo and the Norwegian CCS Research Center (NCCS) project under Task 9 – Structural de-risking. Task 9 aim to reduce the risk related to CO_2 injection and storage by improving knowledge on faults and their influence on CO_2 migration and containment. Seismic data is courtesy of Gassnova SF, well data is courtesy of the NPD Diskos repository and the Northern Lights project (Equinor ASA, Total E&P Norge AS, and A/S Norske Shell). Software is courtesy of Schlumberger (Petrel E&P Software Platform) and Petroleum Experts (Move suite).

Abstract

The proposed Aurora CO_2 storage site is located in the Horda Platform, northern North Sea. Within the storage site, two storage aquifers and an overlying seal, which form part of the Lower Jurassic Dunlin Group, represent a CO_2 storage complex. The storage site is bordered by the thick-skinned (first-order) Tusse and Svartalv fault zones. In addition, numerous thin-skinned (second-order) faults displace the storage complex within the projected up-dip CO_2 migration path.

Faults play an essential role within a CO_2 storage site as they can serve as barriers or conduits to fluid flow, thus affecting the migration of injected CO_2. To determine their possible role and improve the geological understanding of the storage site, assessment of fault geometries (strike, dip, and throw) is performed applying a detailed structural geomodel created using the GN10M1 3D seismic survey, regional 2D seismic lines, and well data. Thereafter, the geomodel is used to assess across-fault juxtaposition and membrane seals, using the shale gouge ratio (SGR) method, assess the spatial and temporal evolution of faults, and discuss plausible CO_2 migration paths and gross rock volumes (GRV) of small-scale structural closures.

Results herein show that first-order faults are predominately N–S striking, W-dipping, and formed during Permian to Triassic rifting (Rift Phase 1). In contrast, second-order faults show predominately N–S to NW–SE strikes, varying dip directions, and formed during the Early to Middle Jurassic or the Middle Jurassic to Early Cretaceous (Rift Phase 2). The storage complex is laterally extensive and dips (2°) to the south, and, therefore, injected CO_2 is expected to migrate northwards and encounter the Svartalv Fault Zone from the footwall side. The fault zone offsets the seal unit (throw >80 m) thus juxtaposing the storage units against shallower successions and potentially allow across-fault migration. However, SGR values exceeding 30% are present across the fault zone potentially preventing this. Second-order faults exhibit throws less than the thickness of the primary seal (<80 m). Results from across-fault seal assessment of the second-order faults show that E and NE dipping faults are more likely to baffle fluid flow, compared to W and SW dipping faults. Three triangular two-way closures, are present north of the injection well and possess a combined GRV of 68×10^6 m^3 in the primary and 93.6×10^6 m^3 in the secondary storage unit, potentially increasing the storage capacity of the Aurora storage site. Results herein show that faults within the Aurora storage site may have an overall positive impact on CO_2 storage by creating small baffles and likely preventing migration out of the storage units. However, higher uncertainties are related to the sealing potential of the Svartalv Fault Zone, which offsets the primary seal, due to challenges in assessing membrane seals using present-day methods.

Table of contents

1 Introduction

This study provides an assessment of the structural architecture and evolution of faults within the Aurora storage site, the presence of across-fault seals, and discuss plausible CO_2 migration pathways and gross rock volumes of structural closures in the Aurora storage site. This chapter introduces the motivation, the Aurora Exploitation License, previous research on structural characterization and across-fault seal assessment within, or in the proximity of, the Aurora storage site, and the main research objectives.

1.1 Motivation

Carbon capture and storage (CCS) is considered one of the key technologies needed to meet the 1.5°C target set by the Paris Agreement and, moreover, to achieve net zero emission from the energy sector by 2050 (IPCC, 2018; IEA, 2021). Norway, as a frontrunner on this technology, has been employing CCS for 25 years in the Sleipner field (since 1996) located in the North Sea (Torp and Gale, 2004; Arts et al., 2008) and in the Snøhvit field (since 2008) in the Barents Sea (Eiken et al., 2011).

Drawing on this uniquely long experience in CCS, Norway is planning a full-scale CCS operation by 2024. The Norwegian Government has named the project Longship, which will contribute to the development of carbon capture, transport, and storage technologies. Furthermore, the project will stimulate technological development from an international perspective (Norwegian Ministry of Petroleum and Energy, 2019). In the first stages of the Longship project, CO_2 will be captured at Norcem AS and potentially Fortum Oslo Varme. The CO_2 will then be transported by ship to a new receiving terminal (Naturgassparken) in the municipality of Øygarden (Figure 1.1). From here, CO_2 will be pumped into pipelines and injected into saline sandstone aquifers located approximately 2.6 km below the seabed (Equinor, 2019). The transport and storage aspects of Longship will be operated by the Northern Lights project, which is an industry-driven collaboration between Equinor ASA, A/S Norske Shell, and Total E&P Norge AS. As a contribution to research on CCS in Norway, the Research Council of Norway launched a Center for Environment-friendly Energy Research, called the Norwegian CCS research center (NCCS). NCCS will operate from 2016–2024, and aim to work alongside the Northern Lights project to fast-track CCS deployment (NCCS, 2019).

In the first phase of the Northern Lights project, 1.5 Mt CO_2 per year will be injected into the proposed storage site for 25 years. In March 2021, the Northern Lights partners launched a joint venture that aims to expand the capacity by an additional 3.5 Mt CO_2 per year. Two candidates have been evaluated for offshore sub-surface CO_2 storage by the Northern Lights project, Smeaheia, and Aurora (Figure 1.1).

The Smeaheia storage site is located 20–40 km west of Western Norway and consists of three closures, Alpha, Beta, and Gamma (Figure 1.1). However, risk of pressure depletion within the Alpha prospect and uncertainty in the sealing potential of the crystalline basement across the Øygarden Fault Complex in the Beta structure have been observed (Mulrooney et al., 2020; Wu et al., 2021). Therefore, the Northern Lights project decided to change the focus to the Aurora storage site in June 2017 (Equinor, 2019).

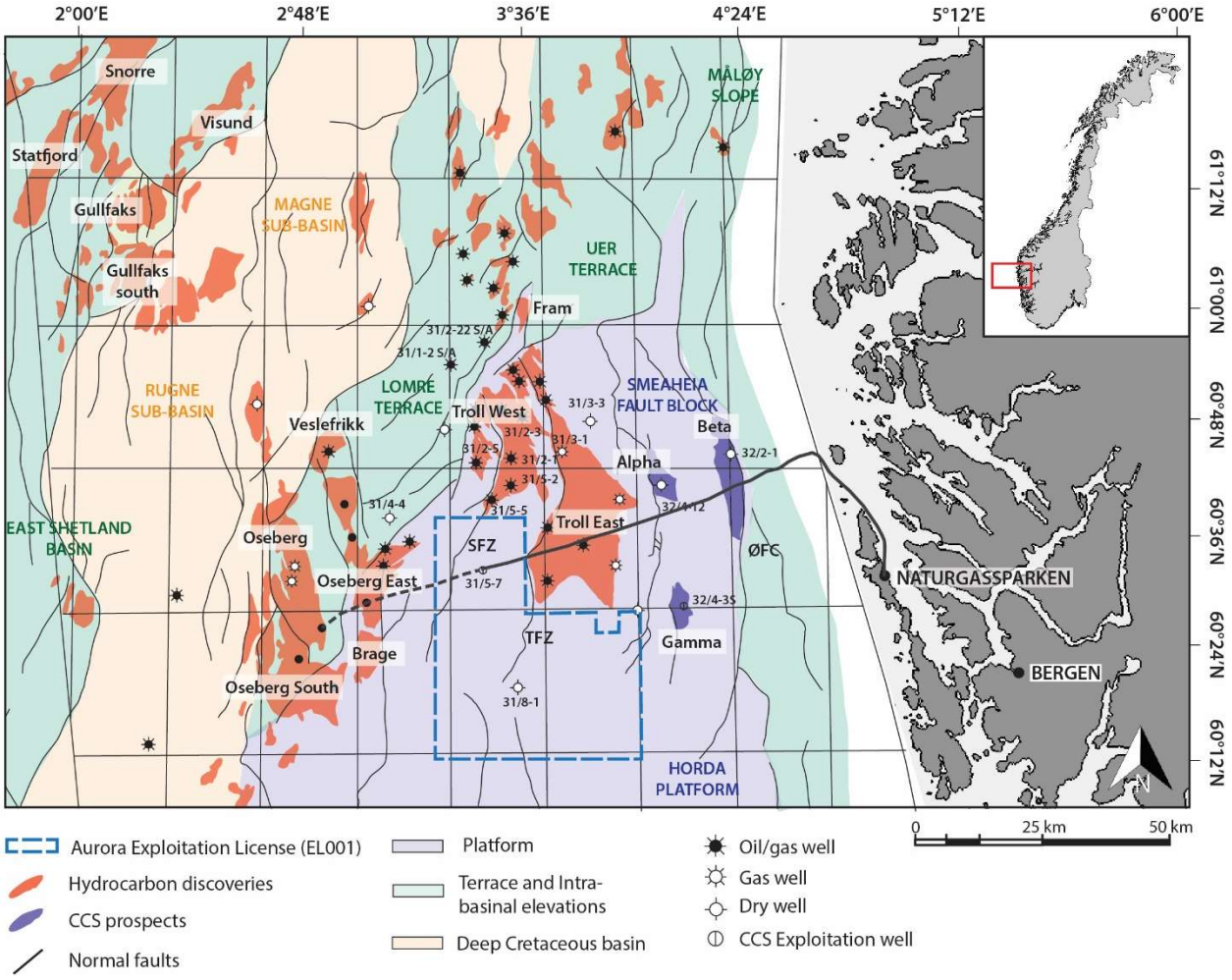

Figure 1.1 Map showing the location of the Aurora Exploitation License (EL001), hydrocarbon discoveries, and CCS prospects. Outline of hydrocarbon discoveries, structural elements, and CCS prospects are compiled from NPD Factmaps, NPD Factpages, and Wu et al. (2021), respectively. Note that not all wells have been included in the map. Abbreviations: ØFC = Øygarden Fault Complex, TZF = Troll Fault Zone, SFZ = Svartalv Fault Zone.

1.2 The Aurora Exploitation License (EL001)

In January 2019, Norwegian authorities granted the Aurora Exploitation License (EL001) to the Northern Lights project. The license is in the Horda Platform, which is an established oil and gas producing area approximately 60 km west of Naturgassparken in Øygarden, western Norway. More precisely, the license is located just south of the producing Troll West and East oil and gas fields,

approximately 15 km east of the Oseberg East, Brage, and Veslefrikk hydrocarbon fields, and approximately 30 km west of the Smeaheia CCS prospects (Figure 1.1).

Within the Aurora storage site, the Lower Jurassic Dunlin Group has been suggested as a storage complex (i.e., storage and seal units) by the Norwegian authorities (NPD CO2 Atlas, 2011). The storage units consist of the Johansen and Cook formations, which are saline aquifer sandstones. The clay-rich Drake Formation, which directly overlies the Cook Formation, is considered a regional seal for the storage units (e.g., Gassnova, 2012). The storage complex is further introduced in sub-section 2.2.3.

The storage complex dips gently towards the south, therefore, the Northern Lights project has estimated that injected CO_2 will migrate northwards and into the Troll license (Equinor, 2019). However, the proposed CO_2 storage units within the Aurora Exploitation License are located approximately 500 meters below the producing formations in the Troll fields, and no pressure communication is observed between the two, further supporting the sealing qualities of the Drake Formation (Equinor, 2019).

The Aurora Exploitation License is located in an eastward tilted fault block bordered by two basement-involved (i.e., first-order) fault zones, the Tusse Fault Zone to the east and the Svartalv Fault Zone to the west (Figure 1.1). In addition, numerous smaller-scale faults without basement involvement (i.e., second-order) intersect the storage complex (e.g., Gassnova, 2012; Furre et al., 2020). The structural framework of the storage site is further introduced in section 2.1.

To confirm the presence of suitable storage and seal units within the Aurora Exploitation License, the 31/5-7 confirmation well (Eos) was drilled by the Northern Lights project from 2nd of December 2019 to 7th of March 2020. The well is located approximately 10 km south of the border between the Aurora Exploitation License and the Troll License (Figure 1.1). This well will later be re-entered, side-tracked, and used as a CO_2 injector (hereafter referred to as the injection well; Equinor, 2019; Furre et al., 2020). It is expected that the final closure for injected CO_2 is located more than 20 km north of well 31/5-7 and approximately 400 m below the Troll West field (Furre et al., 2020). In October 2020, the Northern Lights project disclosed the dataset from the well to be used in research.

Herein, the study area (i.e., the area that is modelled and analyzed) is delimited to the structural features around well 31/5-7 (Figure 1.2). Considering that CO_2 is likely to migrate northwards into the Troll West Field license, the study area covers approximately 420 km^2, partly within the Aurora Exploitation License and partly within the Troll West field (Figure 1.2). The eastern and western extent of the study area is limited by the availability of 3D seismic survey data (the seismic survey is presented in sub-section 3.2.1). The southern border of the study area was selected to include the entire lateral extent of faults. The northern border of the study area was set approximately 4 km north of the Aurora Exploitation License to overlap parts of the Troll West field that have been mapped and analyzed by previous studies (Bretan et al., 2011; Whipp et al., 2014; Duffy et al., 2015) and enable comparison.

1.3 Research background

To develop relevant research objectives, this section highlights a selection of recent research on structural characterization and across-fault seal assessment within, or in the proximity of, the Aurora storage site (i.e., the northern Horda Platform). A broader review of the geological setting, theoretical concepts, and methods are presented in chapter 2 and section 3.1.

The storage complex and the northern North Sea are intersected and displaced by numerous faults formed during multiple rift phases. Therefore a number of structural characterization and evolution studies have been conducted in this area (e.g., Ziegler, 1975a; Færseth, 1996). Examples of recent studies in the proximity of the Aurora storage site are; assessments of the Oseberg field by Deng et al. (2017), the Troll East and West fields by Whipp et al. (2014) and Duffy et al. (2015), and the Smeaheia fault block by Mulrooney et al. (2020) and Wu et al. (2021) (see Figure 1.2). These studies mainly focused on describing fault geometries, evolution, lateral propagation, and interaction styles, which are described in chapter 2 and section 3.1. However, there are no published studies focusing on the structural characterization and evolution of the Aurora storage site.

In a CO_2 storage site, faults may act as both barriers and conduits to fluids (e.g., Bjørlykke, 1993). Assessment of seal potential of faults intersecting the storage complex is therefore essential to ensure safe and effective CO_2 injection and storage (Gassnova, 2012). Previous studies assessing fault leakage risks have been conducted (Bretan et al., 2011; Gassnova, 2012; Equinor, 2019). While these studies agree that the risk of up-fault migration of CO_2 to shallower successions is low, there is no consensus as to whether migration across the Svartalv Fault Zone and into hydrocarbon-bearing units will occur. Migration out of the storage complex and into producing hydrocarbon reservoirs is undesirable as it could potentially conflict with production in the Troll West field if it occurs prior to the end of the field life (Gassnova, 2012).

Bretan et al. (2011) evaluated potential across-fault seals and their influence on migration of CO_2 in the Troll West field (see outline of study in Figure 1.2). They applied two analyses to predict fault seals, that is, fault juxtaposition and membrane seal analysis (methods further introduced in sub-sections 3.1.2 and 3.1.2.2). They observed that the Svartalv Fault Zone (location of faults shown in Figure 1.2), has a higher risk of across-fault migration. This risk was associated with the observation that the storage unit (i.e., the Johansen Formation) is juxtaposed against the Brent and Viking Group, which are sand-rich hydrocarbon-bearing units within the Troll West field. However, they found that there was a high likelihood that a membrane seal is present along the fault, and therefore concluded that the Svartalv Fault Zone is likely to be sealing.

A comprehensive report by Gassnova (2012) analyzed the CO_2 storage potential of the Johansen and Cook formation from 2008 to 2012. Similar to Bretan et al. (2011), they assessed the presence of across-

fault seals and their influence on CO_2 migration but covered a larger area (Figure 1.2). Gassnova (2012) found similar results to Bretan et al. (2011) and suggested that there is a risk of across-fault migration due to the juxtaposition of storage units against the Brent and Viking Group. However, in contrast to Bretan et al. (2011), Gassnova (2012) concluded that a potential membrane seal is too thin to prevent CO_2 from migrating across the fault. The study performed by Gassnova provided a basis for further evaluation by the Northern Lights project (Equinor, 2019), which was performed using a recently acquired 3D seismic survey (CGG17M01). Similar to Bretan et al. (2011), Equinor (2019) suggest that the fault is likely to be sealing despite the juxtaposition of storage units against the Brent and Viking groups. However, these three studies were conducted prior to the drilling of the injection well (31/5-7), and therefore, there is a need for a renewed assessment of fault seals across the Svartalv Fault Zone.

Furthermore, there has not been published a detailed overview of the influence of second-order faults on migration of CO_2. In the Aurora storage site, the second-order faults have throw values less than the thickness of the seal (Gassnova, 2012; Furre et al., 2020). Gassnova (2012) and Furre et al. (2020) suggest that due to the relatively low throws these faults will not lead to migration of CO_2 out of the storage units, but rather provide baffles to flow. However, these studies have not published a detailed overview of the structural architecture of the second-order faults within the storage site, their sealing or non-sealing capacity, or discussed their influence on CO_2 migration pathways and gross rock volumes of structural closures within the Aurora storage site.

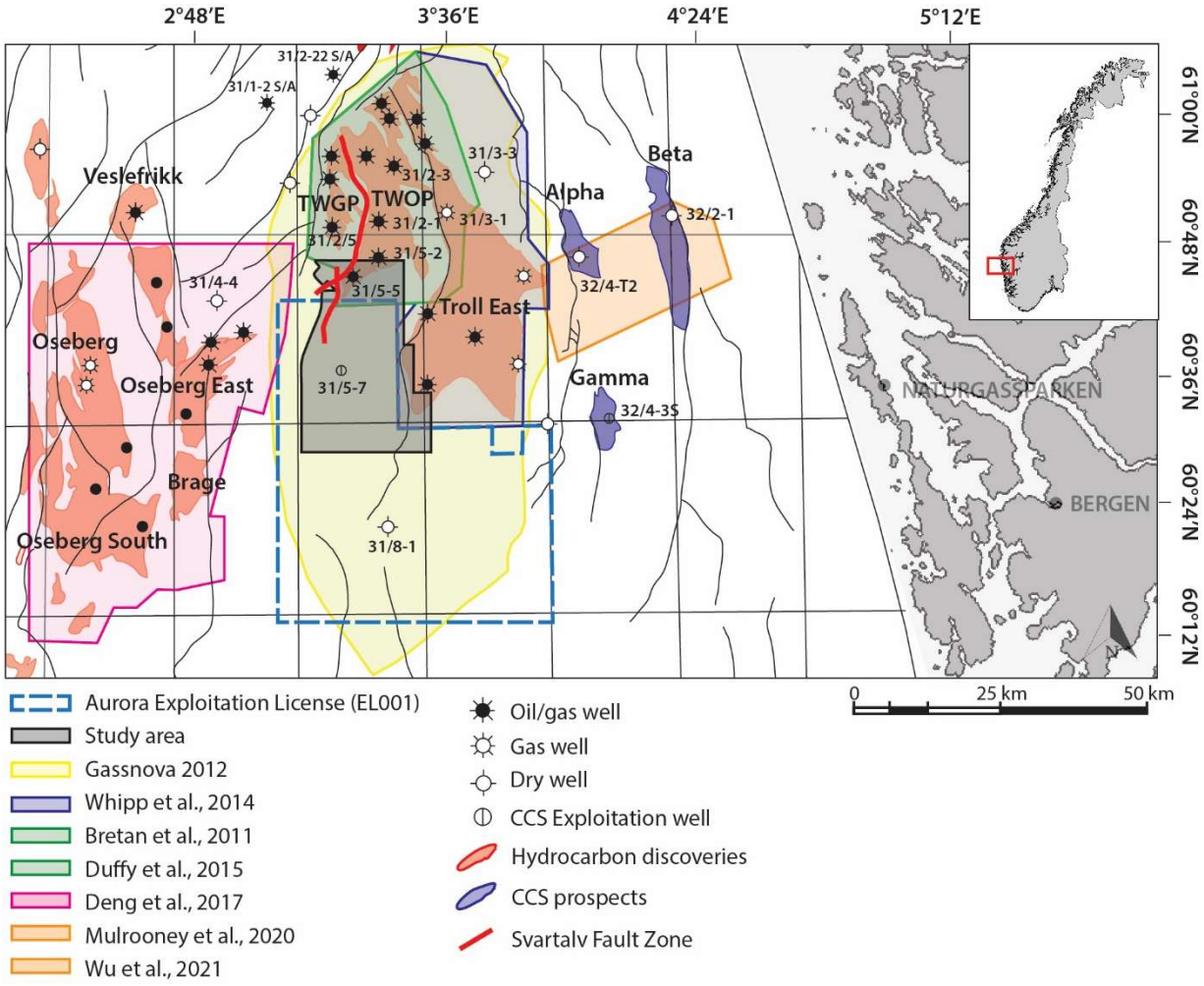

Figure 1.2 Map showing the outline of the study area in this study and the outline of seven recent studies in the vicinity of the Aurora Exploitation License (Bretan et al., 2011; Gassnova, 2012; Whipp et al., 2014; Duffy et al., 2015; Deng et al., 2017; Mulrooney et al., 2020; Wu et al., 2021). Abbreviations: TWGP = Troll West Gas Province, TWOP = Troll West Oil Province.

1.4 Research objectives

Meeting the need for knowledge presented in the previous section, the main objectives of this study are to i) establish a structural geomodel of the Aurora storage site, ii) assess the spatial and temporal evolution of faults, iii) assess the presence of across-fault seals, and iv) discuss plausible CO_2 migration paths and gross rock volumes of relevant structural closures given injection into well 31/5-7.

These objectives are achieved by creating a detailed 3D geomodel of the Lower Jurassic storage complex and intersecting faults, assessing lateral and vertical variations in fault throw and interaction styles, creating Allan diagrams (Allan, 1989) and 1D triangle diagrams (Knipe, 1997) of juxtaposition seal and membrane seal scenarios using the SGR method (Yielding et al., 1997; Freeman et al., 1998), and applying these scenarios to discuss plausible CO_2 migration pathways and gross rock volumes of structural closures. A broader review of theoretical concepts and methods used in this study is outlined

in chapter 3. By performing these tasks, this study contributes to an improved understanding of the evolution and architecture of the faults and their influence on CO_2 migration, thus reducing uncertainties associated with CO_2 storage within the Aurora storage site.

1.5 Study outline

The remainder of the study is outlined as follows. The second chapter provides background information about the structural and stratigraphic framework of the northern North Sea in general and the Horda Platform in particular, as well as the evolution that led to their formation. The third chapter presents theoretical concepts, data, and methods, including i) the main theoretical concepts related to fault geometry, fault juxtaposition, and membrane seal analysis, ii) the data applied, and limitations related to the data, and iii) the methods used to create a 3D geomodel and fault analysis. The fourth chapter presents the results of this study, including i) the results related to structural and stratigraphic characterization, and ii) results related to the across-fault seal analysis. These results are discussed in the fifth chapter. This discussion includes i) the structural evolution of faults within the study area, ii) how the faults in the study area will affect the migration of CO_2 in a juxtaposition or membrane seal scenario, and iii) potential structural traps and closure volumes. The main findings in this study are discussed and compared with previous studies on fault evolution and across-fault seal assessment. Moreover, limitations related to the interpreted geomodel, fault throw analysis, and across-fault seal assessment are discussed, and suggestions for further work are provided. The sixth chapter concludes the study by summarizing the main findings. In addition, a reference list and appendix are included at the end of the study.

2 Geological setting

The following chapter places the study area and storage complex into a geological context. As previously mentioned, the study area is located within the Horda Platform in the northern North Sea, and the target formations for CO_2 injection, the Johansen and Cook formations, are within the Lower Jurassic Dunlin Group. As such, this chapter focuses on describing the structural and stratigraphical framework and geological evolution of the northern North Sea in general and the Horda Platform in particular.

2.1 Structural framework

The Norwegian Continental Shelf (NCS) is located offshore western Norway. It consists of three main provinces: the Western Barents Sea, the Norwegian-Greenland Sea, and the North Sea (see insert in Figure 2.1A). The North Sea borders the Norwegian Sea to the north (62°N) and the Norwegian-Danish Basin to the south and southeast (56°N; Figure 2.1A). A dominant structural feature within the North Sea is the trilete rift system (Davies et al., 2001) comprising three rift arms: the Viking Graben, the Central Graben, and the Moray Firth Basin (Figure 2.1A).

The northern North Sea is defined as the area within the North Sea located between approximately 58°N and 62°N and is an approximately 200 km-wide, predominately N–S trending intracratonic basin (i.e., basin located above continental crust; Faleide et al., 2010). The northern North Sea is characterized by numerous normal faults with predominately N–S, NE–SW, and NW–SE strike. Main structural features within the northern North Sea include the Viking Graben, Sogn Graben, Horda Platform, Tampen Spur, and the East Shetland Basin (Figure 2.1B). The Viking Graben is flanked by the Horda Platform to the east, and the Tampen Spur and the East Shetland Basin to the west (Figure 2.1B and Figure 2.2A).

The Horda Platform lies just offshore Bergen and represents an N–S trending, 300 km long and 50 km wide structural high within the northern North Sea. The Horda Platform is bound by the Øygarden Fault Complex to the east, Måløy Slope to the north, Åsta Graben to the south, and Oseberg Fault Block and Utsira High to the west (Figure 2.1B).

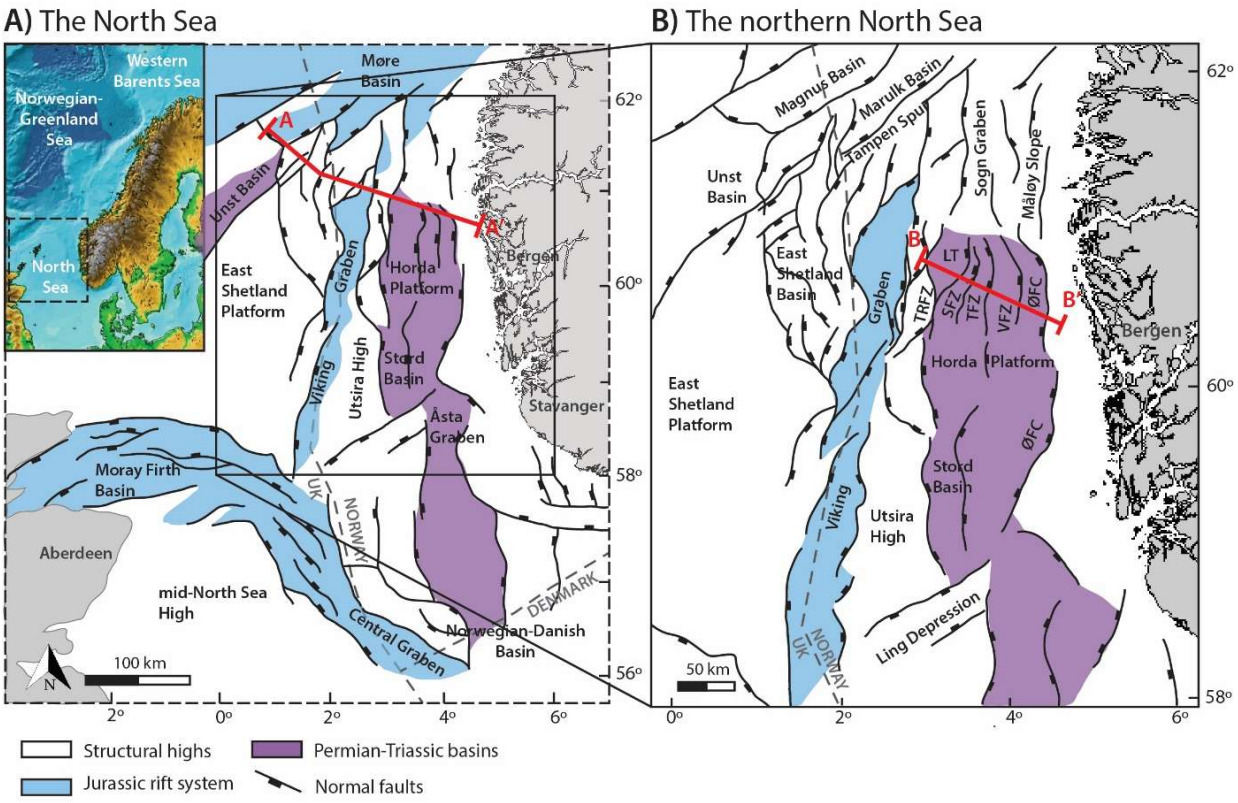

Figure 2.1 Structural element maps of (A) the North Sea, and (B) the northern North Sea. Insert in (A) shows the location of the North Sea on the NCS. Insert is modified from Faleide et al. (2010) and structural element maps are compiled from Færseth (1996) and Whipp et al. (2014). Crosslines A-A' and B-B' are displayed in Figure 2.2. Abbreviations: LT = Lomre Terrace, TRFZ = Troll Fault Zone, SFZ = Svartalv Fault Zone, TFZ = Tusse Fault Zone, VFZ = Vette Fault Zone, ØFC = Øygarden Fault Complex.

In section view, the northern North Sea basin is characterized by large, rotated fault blocks with associated sedimentary basins that fill asymmetric half-grabens (Figure 2.2A; Christiansson et al., 2000). The Viking Graben displays the thinnest crystalline basement and the thickest sequence of overlying successions. The Øygarden Fault Complex is located on the eastern margin of the basin and represents a significant change in crustal thickness at the transition from onshore to offshore Norway (Christiansson et al., 2000). A high-velocity lower crustal body is present beneath the crystalline basement in the Horda Platform (Figure 2.2A; e.g., Fossen, 1992; Færseth et al., 1995; Færseth, 1996; Christiansson et al., 2000).

In section view, the Horda Platform comprises five major N–S striking fault zones; the Øygarden Fault Complex and the Vette, Tusse, Svartalv, and Troll fault zones (Figure 2.2B; Færseth, 1996). These major fault zones bound four 6–15 km wide rotated fault blocks (the Vette-, Tusse-, Svartalv-, and Troll fault blocks), have vertical displacement (i.e., throw) exceeding 1.5 km, are up to 60 km long, and displaces the crystalline basement (i.e., thick-skinned faults; Whipp et al., 2014). Due to the basement involvement of these fault zones, they are herein termed first-order faults inspired by Gabrielsen (1984). In the Horda Platform, a population of smaller predominately N–S to NW–SE trending faults intersects the Upper Triassic to Cretaceous successions (Whipp et al., 2014). They are more closely spaced, have

lower throw values (30–100 m), and are shorter (2–10 km) compared to the first-order faults (Whipp et al., 2014). These smaller-scale scale faults generally have no basement involvement and are herein termed second-order faults (i.e., third-class faults in Gabrielsen (1984)). A population of low displacement, non-tectonic polygonal faults, intersect and are stratabound to the sedimentary overburden (i.e., Cretaceous and Cenozoic successions; Mulrooney et al., 2020).

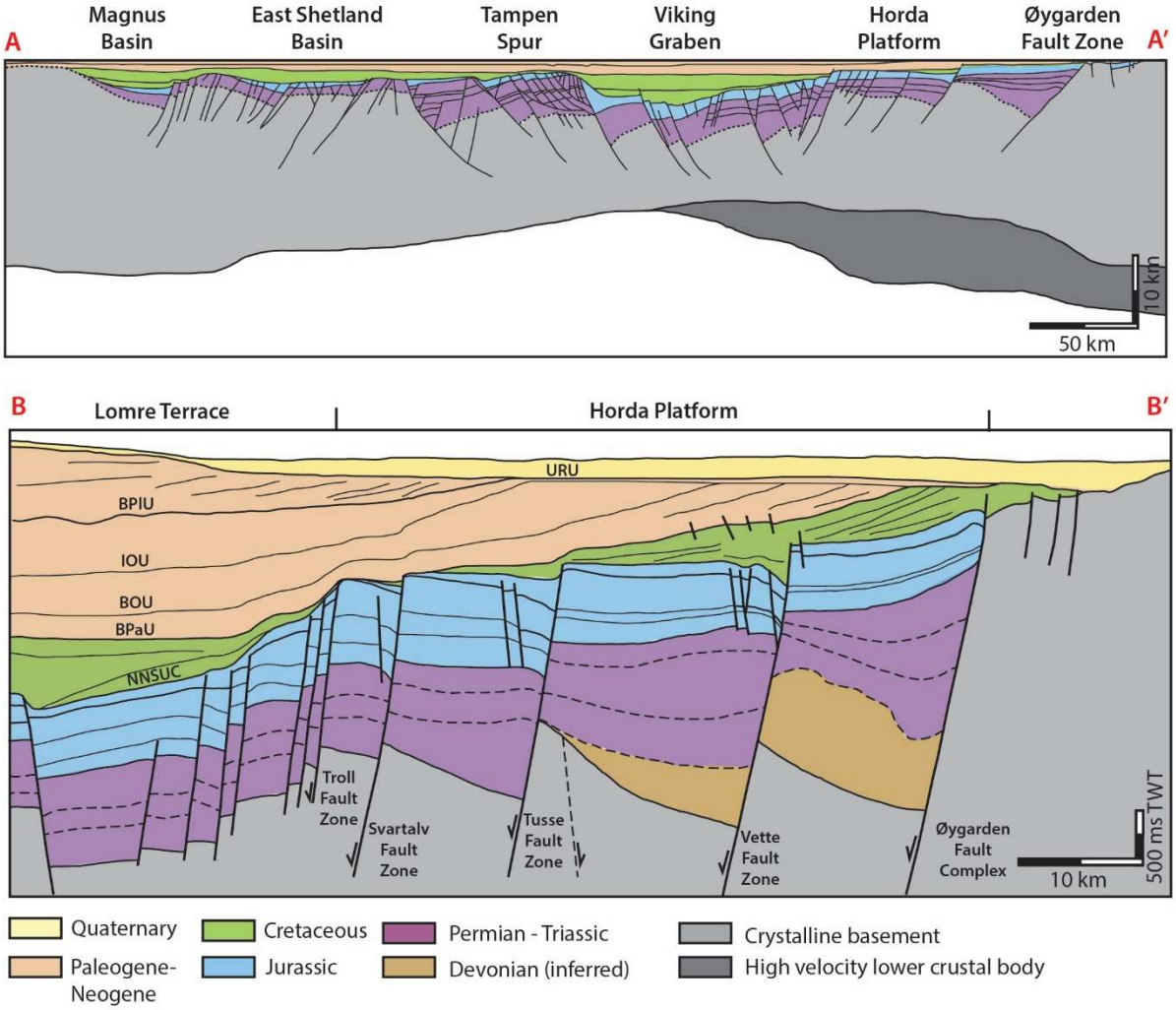

Figure 2.2 Interpreted crosslines shown in Figure 2.1 of the northern North Sea (A-A') and the Horda Platform (B-B'). Crossline A-A' is compiled from Faleide et al. (2010) and Christiansson et al. (2000), and crossline B-B' is modified from Whipp et al. (2014). Note the difference in vertical scale. Abbreviations: NNSUC = Northern North Sea Unconformity Complex, BPaU = Base Paleogene Unconformity, BOU = Base-Oligocene Unconformity, IOU = Intra-Oligocene Unconformity, BPlU = Base Pleistocene Unconformity, URU = Upper Regional Unconformity.

2.2 Geological evolution

In this section, the main events that led to the development of structural features and deposition of sediments in the northern North Sea in general, and the Horda Platform in particular, are described. For the purpose of this study, rift events that led to the development of faults within the Aurora storage site

and the deposition of the Lower Jurassic Dunlin Group (i.e., the storage complex) are described in more detail. An overview of successions deposited within the Horda Platform is provided in (Figure 2.3).

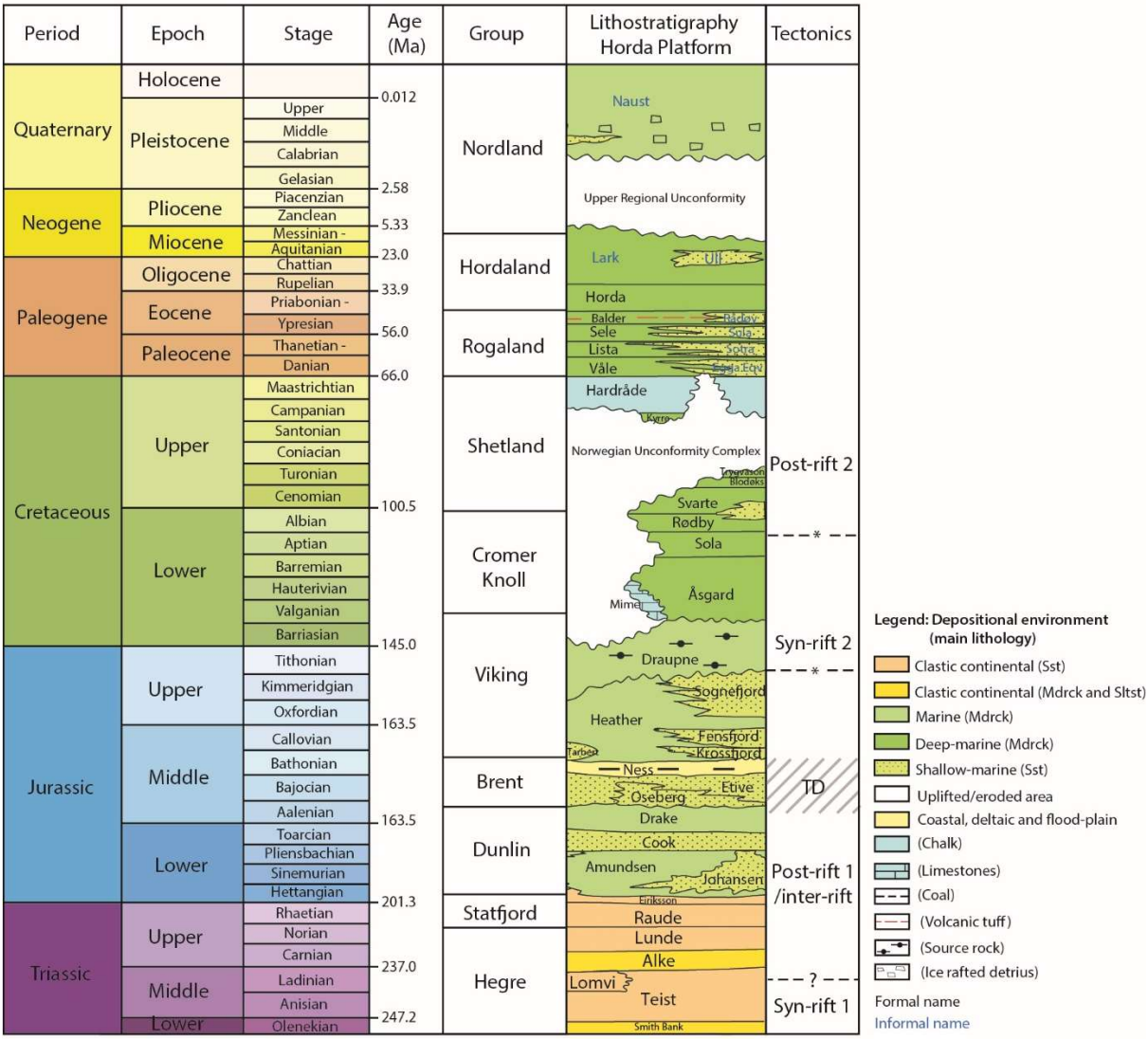

Figure 2.3 Stratigraphic chart of Triassic to Quaternary deposits in the Horda Platform. Modified from NPD (2014). Tectonic events are based on Tusse Fault Zone activity described by Whipp et al. (2014). Abbreviations: TD = growth and collapse of the Central North Sea Dome, Sst = Sandstone, Mdst = Mudstone, Sltst = Siltstone. * Note the timing of the onset and cessation of Syn-rift 2 is interpreted to be diachronous across the Horda Platform (Bell et al., 2014).

2.2.1 Pre-Permian

Contractional tectonics during the Ordovician to Devonian led to the formation of the Caledonian orogeny (e.g., Ziegler, 1975a; Coward, 1990; Gee et al., 2008). During the final phase of the Caledonian orogeny (425–405 Ma), the Scandian Phase, the western margin of Baltica was subducted beneath the Laurentian lithospheric plate and led to the closure of the Iapetus Ocean (e.g., Roberts and Gee, 1985; Gee et al., 2008). Allochthonous nappes from Baltica, Laurentia, and the Iapetus Ocean were

transported ESE on a weak decollement and emplaced onto the western margin of Baltica (Gee and Sturt, 1985; Hossack and Cooper, 1986; Milnes et al., 1997; Fossen and Dunlap, 1998; Lundmark et al., 2013). The contractional tectonics during the Caledonian orogeny led to the formation of a highly heterogeneous basement, with NW–SE, and ENE–WSW oriented shear zones (Andersen and Jamtveit, 1990; Ziegler, 1990). The high-velocity lower crustal body present beneath the heterogeneous basement in the Horda Platform (Figure 2.1A) formed during the Caledonian orogeny and is interpreted to consist of partially eclogitized rocks (Christiansson et al., 2000).

During the Early Devonian, gravitational collapse of the Caledonian orogeny led to E–W to NW–SE oriented extensional tectonics that affected a wide area from the western coast of Norway to Greenland (Norton et al., 1986; Andersen and Jamtveit, 1990; Fossen, 1992; Braathen et al., 2000; Braathen et al., 2002). This phase of extension was facilitated by the reactivation of low-angle Caledonian thrust zones, such as the Nordfjord-Sogn Detachment Zone and the Møre-Trøndelag Fault Complex (Norton, 1987). Multiple Devonian continental basins were formed in the hanging wall of these shear zones onshore western Norway (Steel et al., 1977; Osmundsen and Andersen, 2001). Devonian basins consisting of low-grade clastic metamorphic rocks are also present in the deeper parts of the eastern Horda Platform, Utsira High, and East Shetland Platform and are visible as packages of intrabasement reflectivity (Figure 2.2A; Lervik et al., 1989; Færseth, 1996; Marshall and Hewett, 2003; Khani et al., 2017).

2.2.2 Permian to Early Triassic

The first major rift phase that led to the formation of the northern North Sea Rift, occurred during the Late Permian to Early Triassic (i.e., Rift Phase 1; e.g., Ziegler, 1990; Færseth, 1996). Rift phase 1 was initiated due to E–W extensional tectonics likely related to the break-up of the Pangean supercontinent (e.g., Ziegler, 1982). Initiation and rift orientation during Rift Phase 1 has been determined by dating sedimentary rocks and fault rocks, and the observation of N–S oriented Permian dykes onshore western Norway (e.g., Færseth et al., 1976; Ziegler, 1982; Torsvik et al., 1997).

During Rift Phase 1, fault activity was distributed over a 170–180 km wide area from the East Shetland Basin to the northern Horda Platform, with the rift axis located beneath the present-day Horda Platform (Figure 2.4A; Færseth, 1996). The location of the rift axis was likely influenced by favorably oriented underlying Devonian shear zones (e.g., Ziegler, 1990; Bartholomew et al., 1993; Phillips et al., 2019). In the Horda Platform, Rift Phase 1 exhibited slip rates of 0.1–1.5 mm/y (Bell et al., 2014) with a mean thinning factor (β) of 1.33 (Odinsen et al., 2000a; Odinsen et al., 2000b). The E–W extension led to the development of large-scale (4–5 km throw) predominately N–S striking faults that dipped towards the Horda Platform (e.g., Øygarden Fault Complex, Vette Fault Zone, Tusse Fault Zone, and Svartalv Fault Zone; Færseth, 1996). Locally these faults deviate from the N–S trend and align with NW–SE or NE–SW oriented Caledonian and Devonian structural grains (Færseth et al., 1995; Whipp et al., 2014).

Extension led to the rotation of fault blocks, creating accommodation in the hanging walls and erosion of the uplifted footwalls. The eroded material from the footwalls was deposited in the hanging walls of the large-scale N–S trending faults creating N–S oriented basins such as the Stord and East Shetland Basins (Ziegler, 1990; Bartholomew et al., 1993; Færseth, 1996; Phillips et al., 2019). In the Horda Platform, it is estimated that the hanging walls are filled with up to 3 km of wedge-shaped, syn-rift sediments (Færseth, 1996; Duffy et al., 2015; Phillips et al., 2019). These wedge-shaped sediments are dominated by the Triassic Hegre Group comprised of the Smith Banken, Teist, Lomvi, Alke, and Lunde formations, which were deposited in large fluvial systems (Figure 2.3; Deegan and Scull, 1977; Vollset and Doré, 1984; Lervik et al., 1989). In the Horda Platform, the Teist, Lomvi, and Lunde formations are predominately sand-rich units, separated by the more mud-rich units of the Smith Banken and Alke formations (Steel, 1993). The Hegre Group has a maximum thickness located in the eastern part of the northern North Sea and thins towards the west (Steel, 1993).

2.2.3 Middle Triassic to Early Jurassic

Rift Phase 1 was followed by an inter-rift period (Middle Triassic to Early Jurassic) dominated by relative tectonic quiescence and thermal subsidence (e.g., Roberts et al., 1993; Steel, 1993; Færseth, 1996). While the inter-rift period was dominated by tectonic quiescence in the northern North Sea, some authors suggest that NW–SE striking second-order faults nucleated and some first-order Permian to Triassic faults reactivated during the late inter-rift period in the western parts of the Horda Platform (Deng et al., 2017).

During the inter-rift period, a broad basin developed in the North Sea which subsided due to thermal cooling and sedimentary loading (Ziegler, 1990; Bartholomew et al., 1993). This period was characterized by the deposition of major clastic wedges, sourced from the Norwegian and Scottish highlands such as the continental and fluvio-deltaic to shallow marine sediments of the Statfjord, Dunlin, and Brent groups (Deegan and Scull, 1977; Helland-Hansen et al., 1992; Steel, 1993). In the Horda Platform, the Late Triassic to Early Jurassic Statfjord Group overlies the Triassic Hegre Group conformably and consists of the clastic continental to shallow marine sandstones of the Raude and Eiriksson formations (Figure 2.3; Deegan and Scull, 1977). The Statfjord Group is relatively thin in the Horda Platform but thickens westwards towards the Viking graben (NPD CO2 Atlas, 2011).

The Lower Jurassic Dunlin Group overlies the Statfjord Group conformably in the Horda Platform and comprises the Amundsen, Johansen, Cook, and Drake formations (Figure 2.3; Deegan and Scull, 1977). The Amundsen Formation consists mainly of siltstones and mudstones (Vollset and Doré, 1984) and was deposited in an outer shelf environment (Marjanac and Steel, 1997). In the Horda Platform, the Amundsen Formation interfingers with the Johansen Formation and it is, therefore, subdivided into a lower and upper unit (Marjanac and Steel, 1997).

The overlying Johansen Formation downlaps onto a thin lower Amundsen unit west and northwest in the Horda Platform (Marjanac and Steel, 1997). The Johansen Formation predominately consists of sandstones deposited in a shallow marine environment (Vollset and Doré, 1984). The formation is typically divided into three units: a lowermost unit consisting of fine-grained sandstones which coarsen upwards, a middle unit consisting of massive medium- to coarse-grained sandstones, and an uppermost unit consisting of sandstones that fine upwards (Vollset and Doré, 1984). The internal geometry of the Johansen Formation is characterized by large-scale basin-dipping clinoforms (Marjanac and Steel, 1997) and was deposited in a high-energy shallow marine shelf sourced from the east (Vollset and Doré, 1984). More precisely, the deposition history comprised an early progradational phase with northwestward delta progradation, an aggradational stage where thick spit bar deposits developed, and finally a rapid transgressional stage (Sundal et al., 2016). The Johansen Formation is restricted to the Horda Platform where it has a maximum thickness of approximately 160 m and pinches out in the Veslefrikk and Brage areas (Marjanac and Steel, 1997).

The Cook Formation either conformably overlies the upper Amundsen Formation or unconformably the Johansen Formation (Figure 2.3; Sundal et al., 2016). In the Horda Platform, the Cook Formation is sand-rich and consists of thick units (several tens of meters) of clean sandstones with subordinate thin heterolithic intervals (Marjanac and Steel, 1997). The internal geometry of the Cook Formation is defined by basinward-dipping and basinward-tapering sedimentary bodies consistent with prograding shelfal sands (Vollset and Doré, 1984). The formation is thickening eastwards, with a maximum thickness located in the Gullfaks Field areas (Marjanac and Steel, 1997). The uppermost formation within the Dunlin group, the Drake Formation, is either interbedded within the Cook Formation or overlies it conformably and was deposited in a lower shoreface setting (Figure 2.3; Marjanac and Steel, 1997). In the Horda Platform, the lower part of the Drake Formation is predominantly clay-rich while the upper parts are more coarser-grained due to an increase in siltstone and sandstone interbeds (Marjanac and Steel, 1997).

The Brent Group overlies the Dunlin Group conformably and was deposited during the Middle Jurassic (Figure 2.3). In the Horda Platform, the Brent Group consists of the Oseberg, Rannoch, Etive, Ness, and Tarbert formations (Deegan and Scull, 1977). The group is interpreted as a large delta that prograded northwards from the northern tip of the Horda Platform into the Sogn Graben (e.g., Deegan and Scull, 1977; Helland-Hansen et al., 1992). The lowermost formation in the Brent Group, the Oseberg Formation, consists of medium to coarse-grained sandstones that were deposited in a predominately shallow marine environment (Helland-Hansen et al., 1992). The Oseberg Formation is overlain by the Rannoch, and Etive formations which represent the main progradational successions in the Brent delta (Helland-Hansen et al., 1992). These formations are comprised of sandstones deposited in a middle- to upper-shoreface environment (e.g., Vollset and Doré, 1984; Graue et al., 1987). The Ness Formation represents a thick unit consisting of mixed sandstones, mudstones, and coal layers,

which reflect deposition in a delta-plain or coastal plain setting (e.g., Vollset and Doré, 1984; Graue et al., 1987). The uppermost Tarbert Formation represents the main retrogradational succession in the Brent delta, and consists of fine- to medium- grained sandstones (Vollset and Doré, 1984; Helland-Hansen et al., 1992). The deposition of the upper part of Ness and Tarbert formations occurred, in some places, simultaneously with the onset of Middle Jurassic to Early Cretaceous rifting (i.e., Rift Phase 2; e.g., Helland-Hansen et al., 1992).

2.2.4 Middle Jurassic to Early Cretaceous

Renewed rifting took place during Middle Jurassic to Early Cretaceous (Badley et al., 1988; Underhill and Partington, 1993; Cowie et al., 2005; Bell et al., 2014; Duffy et al., 2015; Phillips et al., 2019). The initiation of Rift Phase 2 was likely driven by the collapse of the Central North Sea Dome during the Middle to Late Jurassic and far-field stresses related to rifting in the North Atlantic (Doré et al., 1997; Ravnås and Steel, 1997; Davies et al., 2001; Torsvik et al., 2002; Whipp et al., 2014). This rifting resulted in the formation of the North Sea trilete rift system comprising the Viking Graben, Moray Firth Basin, and the Central Graben (Figure 2.1A; Davies et al., 2001). The initiation and cessation of Rift Phase 2 are interpreted to have been diachronous throughout the northern North Sea (Færseth, 1996; Bell et al., 2014).

Extension during Rift Phase 2 exhibited slower slip rates (0.01 mm/y), compared to Rift Phase 1, (Bell et al., 2014) with a mean thinning factor (β) of 1.08 (Odinsen et al., 2000a; Odinsen et al., 2000b). Although the magnitude of the rift phases was similar, extension during Rift Phase 2 was more localized, and the rift axis was centered beneath the 25–40 km wide Viking Graben (Figure 2.4B; Ziegler, 1990; Bartholomew et al., 1993; Færseth, 1996; Bell et al., 2014). Within the Horda Platform, Rift Phase 2 was characterized by reactivation of faults formed during Rift Phase 1, and the formation of a new fault population of smaller, N–S and NW–SE striking faults that abuts or cross-cut the larger faults (e.g., Færseth et al., 1995; Færseth, 1996; Bell et al., 2014; Whipp et al., 2014; Duffy et al., 2015; Deng et al., 2017). The Permian to Triassic Øygarden Fault Complex, and the Vette- and Tusse fault zones are interpreted to have become reactivated later in the rift phase compared to faults located closer to the rift axis in the Viking Graben. This eastwards migration of fault activity is estimated to have occurred over a 30 Myr period (Bell et al., 2014) and is based on the observation of relatively little syn-rift wedging in the Jurassic successions, but clear syn-rift wedging in the Cretaceous successions across the easternmost Permian to Triassic faults (Bell et al., 2014; Phillips et al., 2019; Mulrooney et al., 2020).

While there is consensus on the E–W extension orientation during Rift Phase 1, there is no clear consensus among authors on the extension orientation in Rift Phase 2. Some authors suggest that the rift orientation remained E–W oriented during both rift phases and that the observed change in fault

strikes is due to stress perturbations surrounding pre-existing structures (e.g., Badley et al., 1988; Bartholomew et al., 1993; Brun and Tron, 1993; Bell et al., 2014). Others suggest that the strike deviation is a result of rotation of the rift orientations. For example, an anticlockwise rotation of extension from E–W during Rift Phase 1, to NE–SW, during the inter-rift phase, and back to E–W during Rift Phase 2 (Deng et al., 2017).

The Middle Jurassic to Early Cretaceous syn-rift sediments is represented by the fully marine Viking Group. The group conformably overlies the Brent Group and comprises the Heather, Krossfjord, Fensfjord, Sognefjord, and Draupne formations in the Horda Platform (Figure 2.3; Vollset and Doré, 1984). The Krossfjord, Fensfjord, and Sognefjord formations consist of shallow marine, coarse-grained clastic wedges sourced from the Norwegian mainland and are mainly restricted to the Horda Platform (Vollset and Doré, 1984; Steel, 1993). The clastic wedges interfinger basinward with the shelfal deposits of the Heather Formation (Steel, 1993). Late Jurassic to Early Cretaceous marine flooding resulted in the deposition of the deep marine, organic-rich mudstones of the Draupne Formation, which represents the uppermost formation of the Viking Group (Vollset and Doré, 1984).

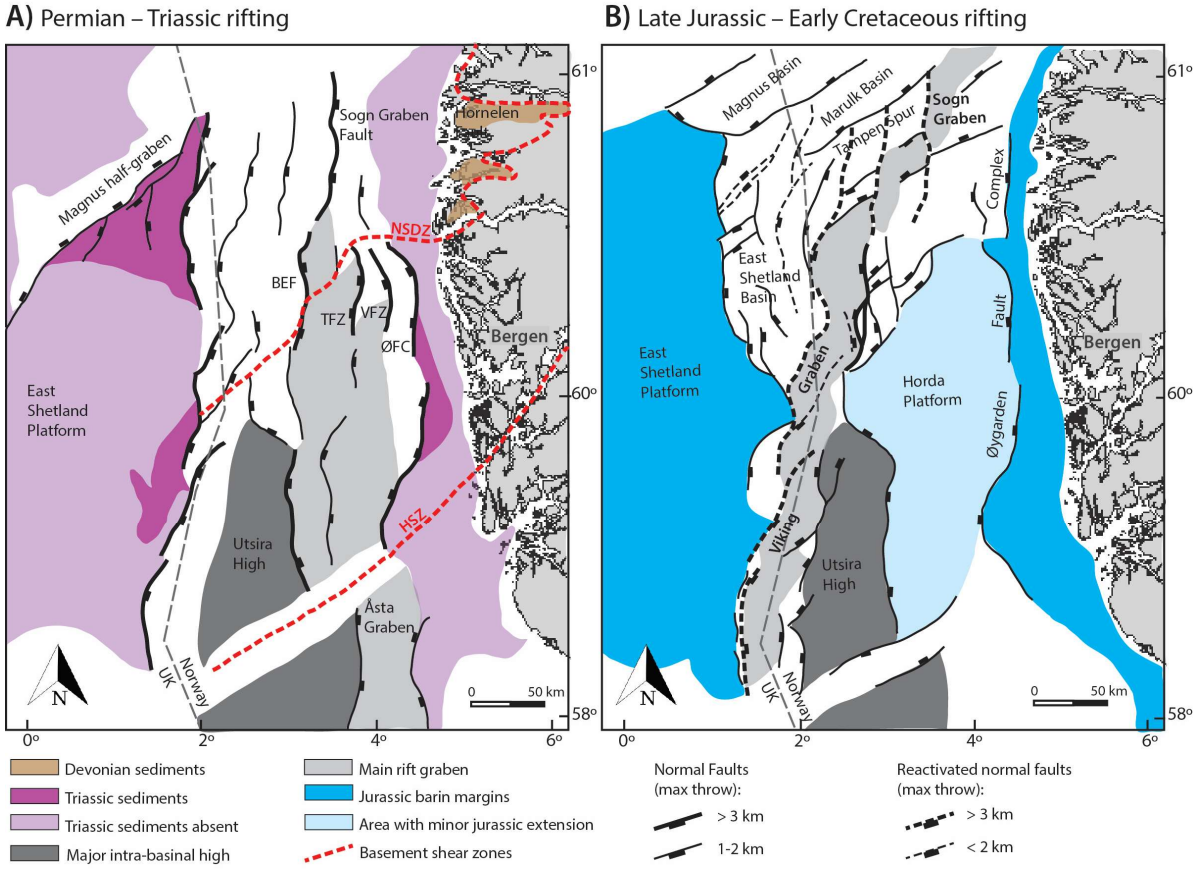

Figure 2.4 Main Structural elements of the northern North Sea resulting from (A) Permian-Triassic rifting (Rift Phase 1) and, (B) Late Jurassic-Early Cretaceous rifting (Rift Phase 2). Modified from Færseth (1996). Abbreviations: NSDZ = Nordfjord-Sogn Detachment Zone, HSZ = Hardanger Shear Zone, ØFC = Øygarden Fault Complex, VFZ = Vette Fault Zone, TFZ = Tusse Fault Zone, BEF= Brage East Fault.

2.2.5 Cretaceous and Cenozoic

During the Early Cretaceous, major rifting ceased and subsidence within the North Sea became controlled by thermal subsidence and sediment loading (i.e., post-rift: e.g., Gabrielsen et al., 2001). In the North Sea, a widespread unconformity formed, representing the transition from active stretching during Rift Phase 1 and the post-rift period (e.g., Badley et al., 1988; Gabrielsen et al., 1990; Nottvedt et al., 1995; Kyrkjebø et al., 2004). This unconformity is called the 'Base Cretaceous Unconformity', 'Late Cimmerian Unconformity' (e.g., Ziegler, 1975b), or the 'northern North Sea Unconformity Complex' (Gabrielsen et al., 2001; Kyrkjebø et al., 2004). Subsidence and sea-level rise during the Cretaceous led to the accumulation of deep-water mudstones and marls, and shallow marine deposits on the surrounding platforms (Brekke et al., 2001) such as the Cromer Knoll and Shetland groups. The Cromer Knoll Group consists of predominately calcareous claystones, siltstones, and marls (e.g., Isaksen and Tonstad, 1989; Gabrielsen et al., 2001), while the Shetland Group consists of chalky limestones, marls, and mudstones (Isaksen and Tonstad, 1989). In the Horda Platform, the Shetland Group either overlies the Cromer Knoll Group conformably or the Jurassic successions unconformably.

Thermal subsidence ceased during the latest Cretaceous and a wide epicontinental basin centered at the Viking Graben developed during the Cenozoic (Gabrielsen et al., 2001; Faleide et al., 2002). Two major phases of uplift occurred during the Cenozoic. The first phase was related to rifting, magmatism, and the break-up of the North Atlantic Ocean during Late Paleocene to Early Eocene, while the second phase was related to isostatic response due to glacial erosion at the transition from Pliocene to Pleistocene (Faleide et al., 2002). The Cenozoic basin in the northern North Sea is filled with approximately 2.5–3 km of sediments sourced from the East Shetland Platform and the Norwegian mainland (Cameron et al., 1993; Jordt et al., 1995; Faleide et al., 2002). Cenozoic successions in the Horda Platform include the Rogaland, Hordaland, and Nordland groups (Figure 2.3). The Rogaland and Hordaland groups mainly consist of marine to deep marine claystones, siltstones, and minor sandstones with ash-rich layers related to extensive volcanism during the break-up of the North Atlantic Ocean (Knox and Harland, 1979; Isaksen and Tonstad, 1989). The Nordland Group, representing the shallowest succession in the North Sea, was deposited in a predominately marine setting becoming increasingly glacially influenced up-section (e.g., Cameron et al., 1987). The Nordland Group forms thick successions of westward prograding wedges underlying thin sheet-like glacially derived successions (Eidvin et al., 1999; Eidvin et al., 2014). The angular unconformity separating the westward-dipping and sheet-like successions in the Horda Platform is called the Upper Regional Unconformity (URU) and was formed during multiple episodes of glacial erosion between 1.1 and 0.8 Ma, linked to the Norwegian Channel Ice Stream and the formation of the Norwegian Channel (Sejrup et al., 1996; Ottesen et al., 2014).

3 Theory, data, and methods

The following chapter focuses on presenting relevant theoretical concepts (section 3.1), the data used (section 3.2), and the methods applied (section 3.3) in this study.

3.1 Theory

Before addressing structural characterization, fault evolution, and the influence of faults on migration of CO_2 within the Aurora storage site, it is necessary to first provide a theoretical background on fault geometry (e.g., strike, dip, throw, and interaction styles; sub-section 3.1.1) and across-fault seal assessment (sub-section 3.1.2).

3.1.1 Fault geometry

The 3D fault geometry, lateral and vertical distribution of displacement (or throw), and interaction with nearby faults inform the spatial and temporal evolution of faults and control the position of juxtaposed successions, thus influence the sealing or non-sealing potential of faults (e.g., Lohr et al., 2008).

3.1.1.1 Fault strike and dip

When buoyant CO_2 is injected into a storage site at the location of an injection well, it will likely migrate up-dip within the storage units. Therefore, the strike of faults, relative to the dip of the storage formation and the location of the injection well, is important to consider.

Faults oriented obliquely to the migration direction could potentially redirect and/or slow down the CO_2 migration while faults oriented parallel to the migration direction can channel migrating CO_2 and increase the max plume front advancement (e.g., Andersen and Sundal, 2021). Furthermore, the strike of faults can provide information on the spatial and temporal evolution. Assuming that faults are close to dip-slip and develop perpendicular to the rift orientations (Anderson, 1951), the strike of faults can be used to assess rift orientations. Recent studies have also found that along-strike variations in newly formed faults can occur as a result of stress perturbations near pre-existing structures (Maerten et al., 2002; Henza et al., 2010). Furthermore, along-strike variations have been interpreted to represent paleo-linkage points and can, therefore, be used to assess the lateral fault growth history (Schlische, 1995).

The dip direction of the faults will play an important role in assessing across-fault migration of CO_2. Depending on the dip of the fault relative to the location of the CO_2 plume, it can act as a barrier or conduit to across-fault migration. Figure 3.1 illustrates two scenarios where a normal fault with opposite dip intersects the storage complex (i.e., storage and seal units). In a juxtaposition-seal scenario (further presented in sub-section 3.1.3; Allan, 1989), the fault in Figure 3.1A will likely trap CO_2 in the footwall until it reaches a spill point, at which it will migrate across the fault and into the hanging wall, while the fault in Figure 3.1B is less likely to trap CO_2 and rather allow fluids to migrate into the footwall.

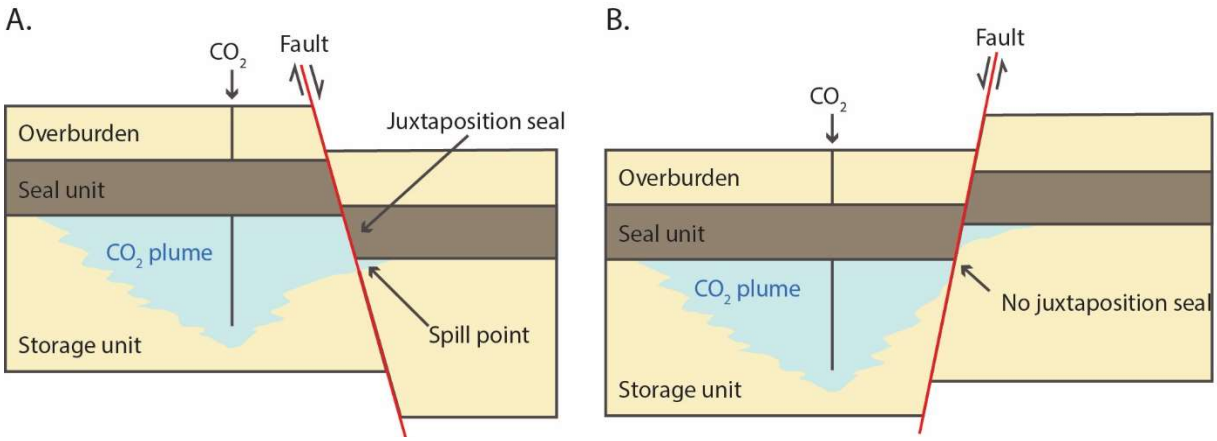

Figure 3.1 Illustrations showing the effect of normal fault dip direction on the migration of CO_2 for a juxtaposition scenario. Figures inspired by Miocic et al. (2019).

3.1.1.2 Fault throw and growth models

Assessment of lateral and vertical variations in displacement (throw) can be used to estimate fault growth trends, timing, and interaction styles (e.g., Peacock and Sanderson, 1991). Furthermore, assessment of displacement is particularly useful in CO_2 storage sites as it controls the position of juxtaposed successions and the presence of a membrane seal, thus influencing the sealing or non-sealing potential of faults (sub-section 3.1.2).

The displacement of a fault is defined by Leith (1923) as the relative separation between two originally adjacent points on the fault surface. For a normal fault, the displacement can be subdivided into 'dip separation' and 'real displacement' (Figure 3.2A; Peacock et al., 2000; Lohr et al., 2008). Dip separation, also referred to as slip, describes separation parallel to fault dip, with 'throw' representing the vertical component and 'heave' representing the horizontal component. Real separation describes separation parallel to movement direction with 'vertical displacement' and 'horizontal displacement' describing the vertical and horizontal components, respectively.

In seismic, a fault can be identified as an intersection line (i.e., fault trace) between a fault surface and an arbitrary surface (Figure 3.2B). For a normal fault, with isolated fault tips that does not penetrate the surface (i.e., blind faults), the displacement is typically greatest at the center of the fault and decreases

to zero towards the fault tips (Figure 3.2C; e.g., Walsh and Watterson, 1987). While a fault is often observed as a single discrete surface in seismic, it is a heterogeneous 3D volume or zone of deformed host-rock (e.g., Caine et al., 1996). A fault zone consists of the 'fault core' (or slip surface) where the majority of the displacement occurs, a 'damage zone' and a 'process zone' (Figure 3.2D; McGrath and Davison, 1995; Cowie and Shipton, 1998). The damage zone and process zone are often highly fractured and can contain deformation bands (e.g., Fossen et al., 2007). Due to limitations in seismic resolution, it can be challenging to resolve the structural complexities of the fault zone, however, they are important to bear in mind as they may influence across-fault fluid migration (sub-section 3.1.2.2).

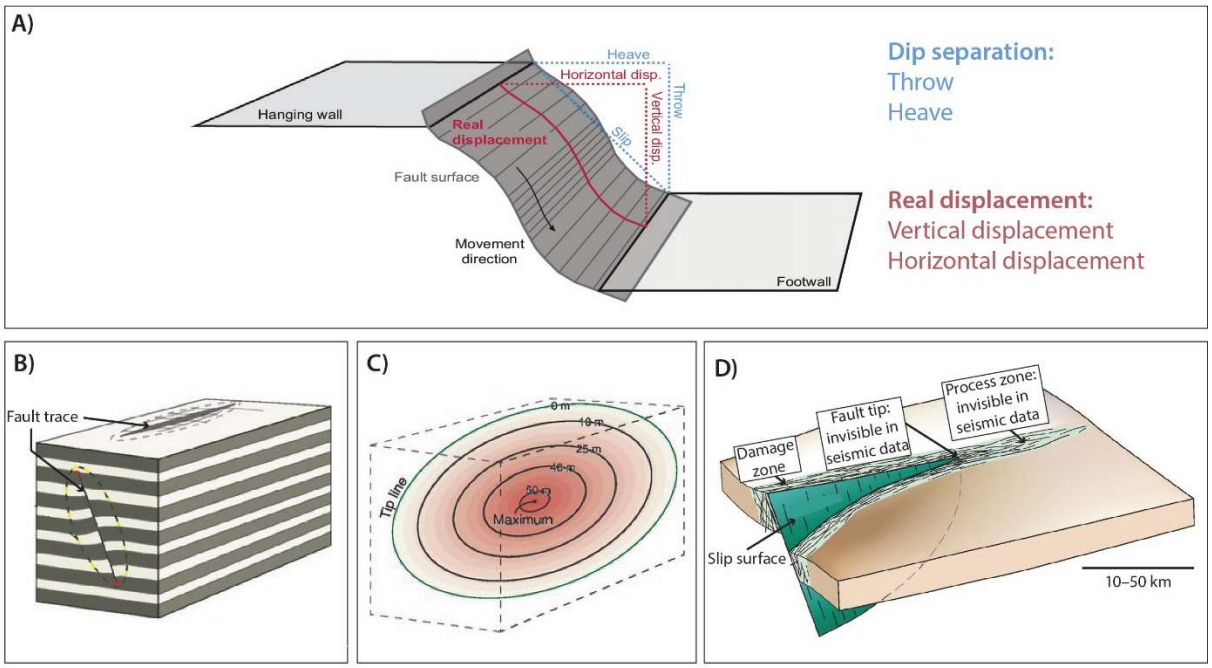

Figure 3.2 Conceptual figures showing A) the relationship between dip separation (parallel to fault dip) and real displacement (parallel to movement direction), B) the intersection between the fault surface and an arbitrary surface (i.e., fault trace), C) displacement contours for an isolated fault, and D) the damage zone and process zone surrounding the slip surface. Figure A is modified from Lohr et al. (2008) using terminology from Peacock et al. (2000), figures B and C are modified from Fossen (2016). and figure D is modified from Fossen et al. (2007).

Displacement vs. length profiles (e.g., Walsh and Watterson, 1987), displacement vs. depth profiles in combination with the expansion index (E.I.) by Thorsen (1963), and maximum displacement vs. length plots (e.g., Walsh and Watterson, 1988; Cowie and Scholz, 1992) are often used to inform lateral and vertical variations in throw. In 3D seismic fault modelling, the throw is often used as a proxy for displacement due to the challenge in resolving kinematic indicators (e.g., slickenlines; e.g., Walsh and Watterson, 1988; Peacock and Sanderson, 1991; Whipp et al., 2014), thus creating throw vs. length, throw vs. depth and maximum throw vs. length plots.

Throw vs. length profiles can be used to investigate the lateral evolution of a fault (i.e., the fault segmentation and linkage history) by plotting the along-strike fault throw against its resolvable trace length for each interpreted horizon (e.g., Bell et al., 2014; Whipp et al., 2014). An isolated fault will

typically have a near symmetrical throw vs. length profile with maximum throw at the center of the fault, decreasing to zero at the fault tips (stage 1 in Figure 3.3A; e.g., Walsh and Watterson, 1988). Steep displacement (or throw) gradients near the fault tips typically indicate that the fault interacts with a nearby fault, creating a relay zone (stage 2 in Figure 3.3A; e.g., Peacock and Sanderson, 1991). These zones are particularly interesting in fault-controlled CO_2 storage sites because they can act as conduits for fluid flow (e.g., Trudgill and Cartwright, 1994; Rotevatn et al., 2007). As the faults propagate, the relay zone can become breached and form a through-going fault. In a throw vs. length profile, these paleo-linkage points can be identified by throw minimas (stage 3 in Figure 3.3A; e.g., Peacock and Sanderson, 1991).

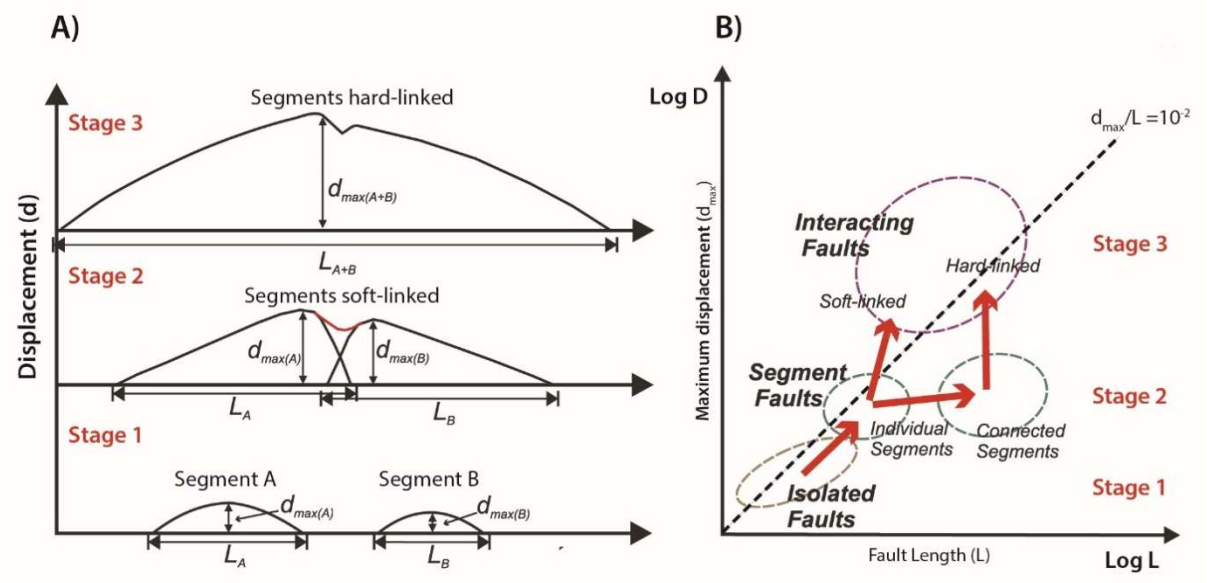

Figure 3.3 Fault segmentation and linkage illustrated using an A) throw vs. length profile and B) maximum throw vs. length plots. Modified from Kim and Sanderson (2005).

Maximum throw vs. length plots are often used to describe fault growth trends by plotting the maximum throw of a fault against its maximum resolvable trace length (e.g., Walsh and Watterson, 1988; Cowie and Scholz, 1992). Figure 3.3B shows an example of a maximum throw (displacement) vs. length plot for two faults through three stages. The first stage represents isolated faults, the second stage represents segmented faults, and the third stage represents interacting faults. Note that the two fault segments grow rapidly in fault length as they become connected (stage 2), and then mainly by grow by throw (displacement) accumulation (stage 3).

At present, there are two end-member models that explain fault growth, referred to as the 'propagating' and 'constant length' fault growth models (Rotevatn et al., 2019). The propagation model assumes that a fault will grow at a synchronous increase in fault length and displacement (Figure 3.4A; Walsh and Watterson, 1988; Trudgill and Cartwright, 1994; Cartwright et al., 1995). The relationship between

maximum fault throw (T_{max}) and trace length (L) is suggested to follow equation 3.1.1 (Watterson, 1986).

$$T_{max} = CL^n \tag{3.1.1}$$

Where C is a constant related to the material properties, and n is somewhere between 0.5 and 2 (e.g., Walsh and Watterson, 1988; Cowie and Scholz, 1992). The propagation model suggests that there is a systematic power-law relationship between maximum fault throw and trace length (i.e., n = 1) through the fault life and that measurements of maximum throw and length adhere to a straight trend line (Figure 3.4A). In contrast, the constant length fault growth model assumes that a fault first grows rapidly in length, then has a near-constant length while mainly growing by displacement accumulation (Figure3.4B; Walsh et al., 2002; Walsh et al., 2003). The theories behind this model, therefore, expect the ratio of maximum throw and trace length (T_{max}/L) to change throughout the fault life (i.e., $n \neq 1$) with younger faults having lower ratios compare to older and more mature faults. A hybrid model has also been proposed, where the fault life is divided into two stages. Stage 1 is best described by the propagation model, and stage 2, is best described by the constant length fault growth model (Figure 3.4C; Rotevatn et al., 2019).

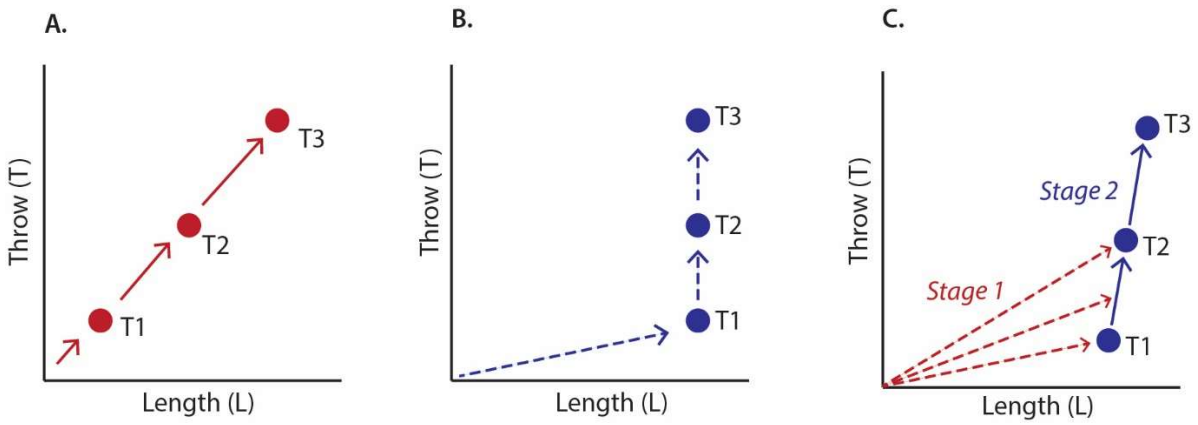

Figure 3.4 Illustration of the maximum displacement-length plots for the A) propagation model, B) constant length model, and C) a hybrid model. T1-T3 represents fault growth at three different times. Figure A) and B) are modified from (Nicol et al., 2017), and figure C) is modified from (Rotevatn et al., 2019).

Throw vs. depth profiles can be used to investigate the temporal evolution of faults assuming that increasing depth in the seismic section positively correlates to age (e.g., Bell et al., 2014; Serck and Braathen, 2019; Mulrooney et al., 2020). These profiles are created by measuring the throw at interpreted horizons near the fault and plotting it against its corresponding depth. For a blind fault (i.e., a fault not breaching the surface), the point of maximum throw usually represents the depth of fault nucleation (e.g., Cartwringt and Mansfield, 1998; Hongxing and Anderson, 2007). Multiple maximum throws can indicate multiple phases of rifting (i.e., reactivation), or vertical linkage of fault segments (Cartwright et al., 1998). In a throw vs. depth profile, intervals with no gradient represent periods of

fault inactivity, while intervals with positive gradients are interpreted as periods of active fault growth (Cartwright et al., 1998).

Throw vs. depth profiles is often plotted together with the expansion index by Thorsen (1963). Faults that intersect the free surface and have slip rates less than the sedimentation rates, will allow sediments to accumulate in the hanging wall and are referred to as a growth fault (Ocamb, 1961). This across-fault growth records initiation, cessation, and duration of faulting (Thorsen, 1963). The fault timing and magnitude can therefore be constrained by dividing the hanging-wall thickness of a succession by its corresponding footwall thickness, referred to as the expansion index (E.I.; Thorsen, 1963). An E.I. of 1 suggests no across-fault thickening, and no syn-sedimentary fault activity, while a value over 1 suggests across-fault thickening and syn-sedimentary fault activity. Values less than 1 suggest that the hanging-wall thickness is less than the footwall thickness, which is relatively unusual and is therefore considered erroneous (Thorsen, 1963).

Figure 3.5 shows three examples of throw vs. depth profiles and expansion indices for faults within the Smeaheia CO_2 storage site in the Horda Platform (Mulrooney et al., 2020). The throw vs. depth profile in Figure 3.5A presents a fault with throw increasing down-section into the basement-cover contact, indicating basement-involvement. A second throw maximum is located in the Upper Jurassic successions and E.I. values exceeding 1 is observed in the Upper Jurassic to Early Cretaceous indicating reactivation during these periods. Figure 3.5B and C represents faults nucleated in the Late Jurassic to Cretaceous successions. Furthermore, the relatively flat upper tip-line in Figure 3.5C indicates that the fault breached the surface or was eroded.

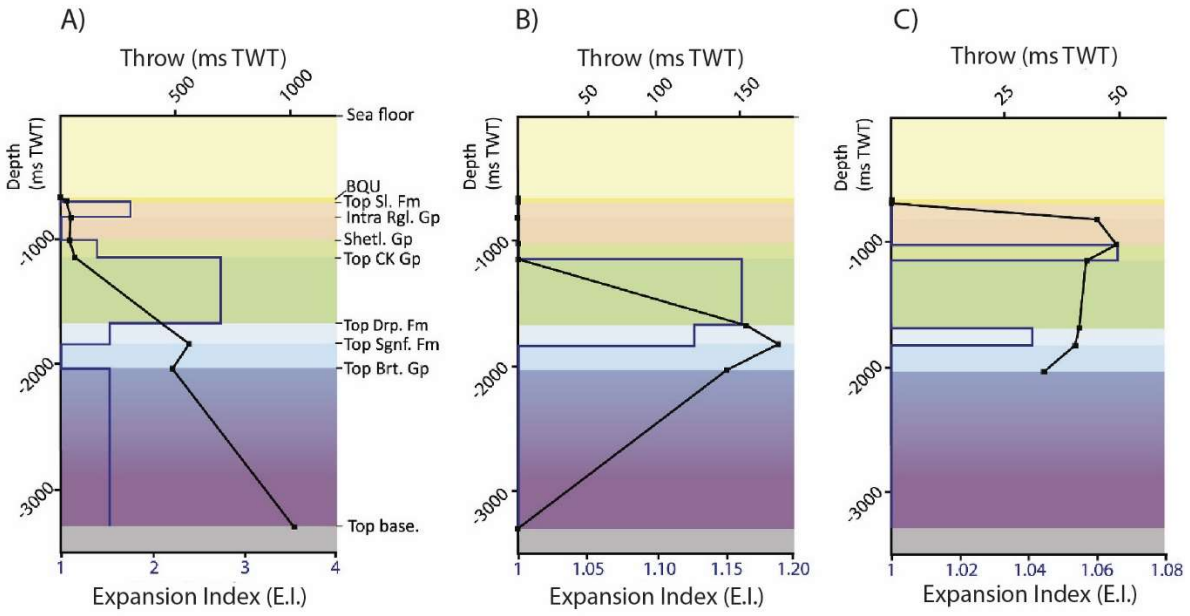

Figure 3.5 Example of throw vs. depth profiles with corresponding expansion indices (E.I.) for three faults in the Horda Platform, northern North Sea. Modified from Mulrooney et al. (2020).

3.1.1.3 Fault interaction styles

How faults within a fault network interact is important to consider in a CO_2 storage site as it can determine whether faults allow CO_2 to migrate across overlap zones (i.e., in relay zones) or become trapped where two or more faults are hard-linked creating a fault-bound trap (e.g., Biddle and Wielchowsky, 1994). Duffy et al. (2015) presented conceptual models showing how different fault interaction styles influence the throw vs. length profile and the throw strike-projection of two fault populations (i.e., first-order and second-order faults; Figure 3.6). They highlighted four types of mechanical fault tip interactions; isolated, retarded, abutting, and cross-cutting. Retarded fault tips can be related to soft-linked fault and relay zones, while abutting or cross-cutting fault tips are related to hard-linked faults.

Figure 3.6A shows a second-order fault with isolated fault tips that do not interact with the first-order fault. Here, the throw vs. length profile is symmetrical and the throw strike-projection has elliptical throw contours. Figure 3.6B shows a second-order fault that is retarded by the first-order fault. This results in the second-order fault having a slightly skewed profile towards the location of the first-order fault. Furthermore, the throw strike-projection is distorted in both the first-order and second-order fault. Figure 3.6C shows a scenario where the second-order fault are abutted against the first-order fault. The location where the second-order fault abuts against the first-order fault can be seen as an abrupt change in throw in the throw vs. length profile for the first-order fault. Moreover, the throw of the second-order fault is not zero where the two faults interact indicating hard-linkage. Figure 3.6D shows a simple cross-cutting scenario where the first-order fault is not reactivated. This results in a symmetrical profile for both faults, and the intersection can be easily distinguished in the throw-strike projection for the second-order fault. If the faults are surface breaching, the throw strike-projections will have a flat upper tip-line (see the complete conceptual model in Duffy et al. (2015)).

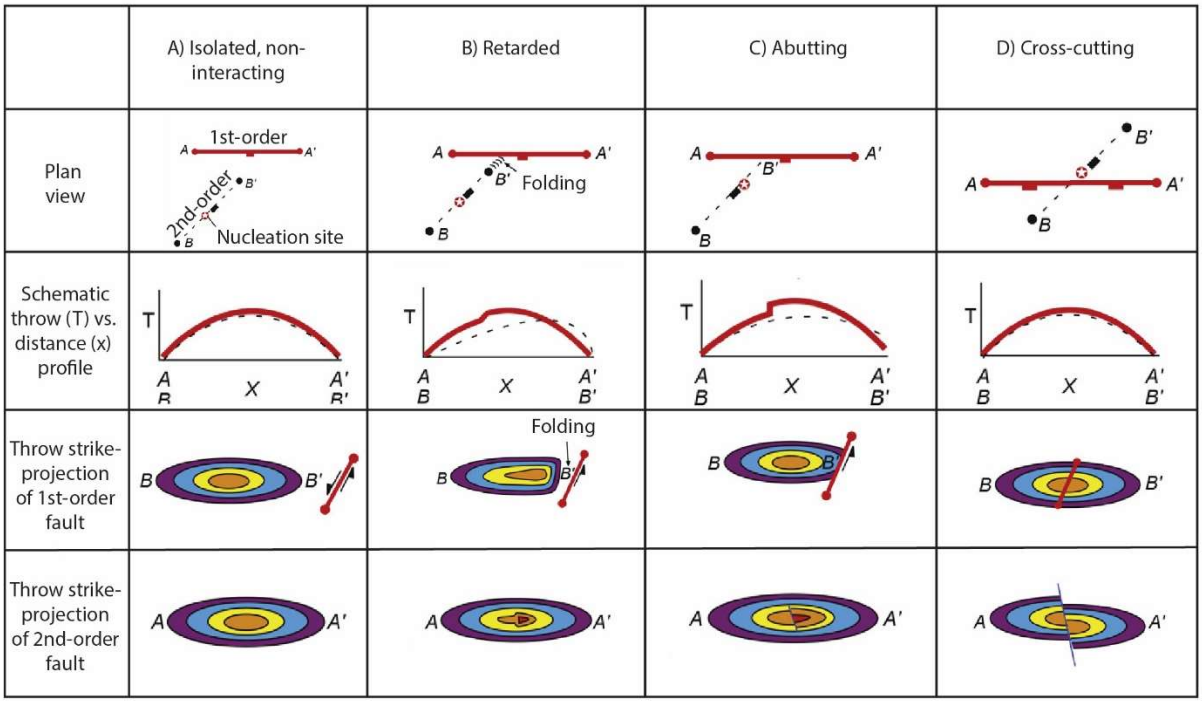

Figure 3.6 Conceptual models showing how four different interaction styles influence the throw vs. length profile and the throw strike-projection. Throw strike-projections are displayed for blind fault. Modified from Duffy et al. (2015).

3.1.2 Across-fault seals

In a fault-controlled hydrocarbon reservoir or CO_2 storage site, faults can act as across-fault barriers (seals) or conduits for fluid flow (e.g., Bjørlykke, 1993). In hydrocarbon reservoirs, across-fault seals have been observed to retain significant hydrocarbon columns (e.g., Fristad et al., 1997; Yielding et al., 1997; Lyon et al., 2005; Færseth et al., 2007) and it is assumed that faults will have a similar effect on migration of injected CO_2 in a fault-controlled CO_2 storage site (e.g., Bretan et al., 2011; Mulrooney et al., 2020; Wu et al., 2021). It is, therefore, essential to understand the processes that contribute to the development of across-fault seals within the Aurora storage site. Across-fault seals can be categorized into juxtaposition seals and membrane seals (or fault rock seals; Pei et al., 2015). The basic concepts of these across-fault seals are illustrated in Figure 3.7.

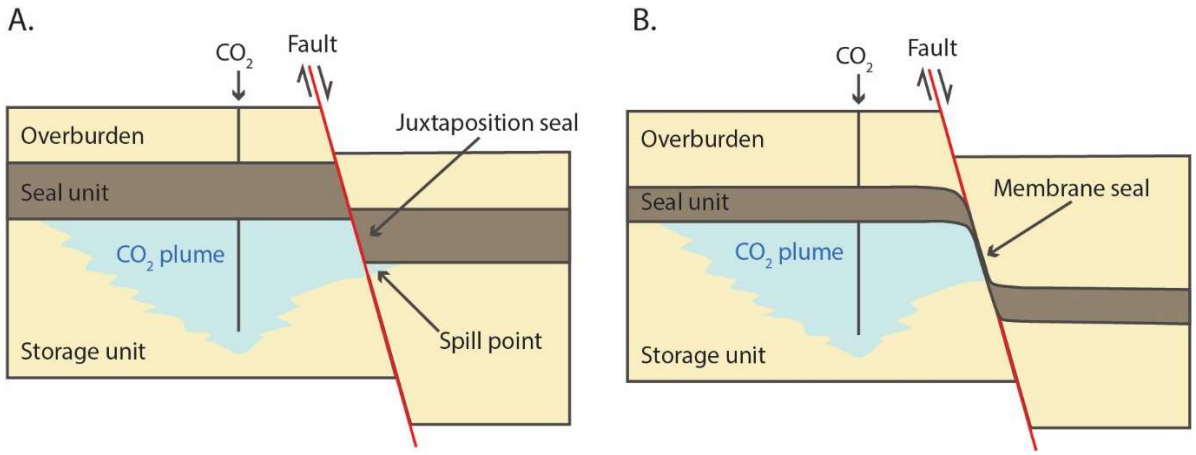

Figure 3.7 Illustrations showing two types of across-fault seals in a fill-to-spill scenario, A) a juxtaposition seal and B) a form of membrane seal (clay smear). Figure A is modified from and figure B is inspired by Miocic et al. (2019).

3.1.2.1 Juxtaposition seals

When a sequence of units are cut due to normal faulting, the hanging wall side moves down relative to the footwall side (e.g., Dennis, 1967). This movement can lead to units with different lithologies and petrophysical properties, for example, different porosities, permeabilities, and capillary entry pressures (further introduced in sub-section 3.1.2.2), becoming juxtaposed. In a juxtaposition-seal scenario, mudstones are considered to represent lower permeability units and sandstones to represent higher permeability units, relative to the mudstones. If a lower permeability unit becomes juxtaposed against a higher permeability storage unit, it is likely to create a juxtaposition seal (Figure 3.7A; Allan, 1989; Knipe, 1997). In contrast, if the higher permeability storage unit is juxtaposed against itself (i.e., self-juxtaposition) or another higher permeability unit, it is less likely to seal. In an attempt to quantify the risk related to across-fault seals, Færseth et al. (2007) suggested that across-fault juxtaposition seals, containing a single fault plane, have the highest probability of sealing (70–100%), compared to self-juxtaposed storage units (0–30%) and membrane seals (50–70%) (sub-section 3.1.2.2).

Two types of diagrams are commonly used when assessing the presence of juxtaposition seals in seismic; the Allan diagram by Allan (1989), and the 1D triangle diagram by Knipe (1997). Allan (1989) introduced a model that displays the juxtapositions of footwall and hanging-wall units onto the fault plane, thus providing an overview of the fault juxtaposition, the stratigraphic units, and the fault throw. A case example from Allan (1989) is illustrated in Figure 3.8. In this case, fluids migrating within the structure encounter three sandstone layers (layers with blocked ends in Figure 3.8A). Fluids become trapped at the highest points of these sandstone layers, two in the footwall (yellow and blue in Figure 3.8A) and one in the hanging wall (purple in Figure 3.8A) fault block. The fluids accumulate within the trap until they are juxtaposed against a sandstone in the adjacent fault block. At these ‘spill points’, the fluids will spill from the base of the structure and migrate up-dip within the adjacent fault block.

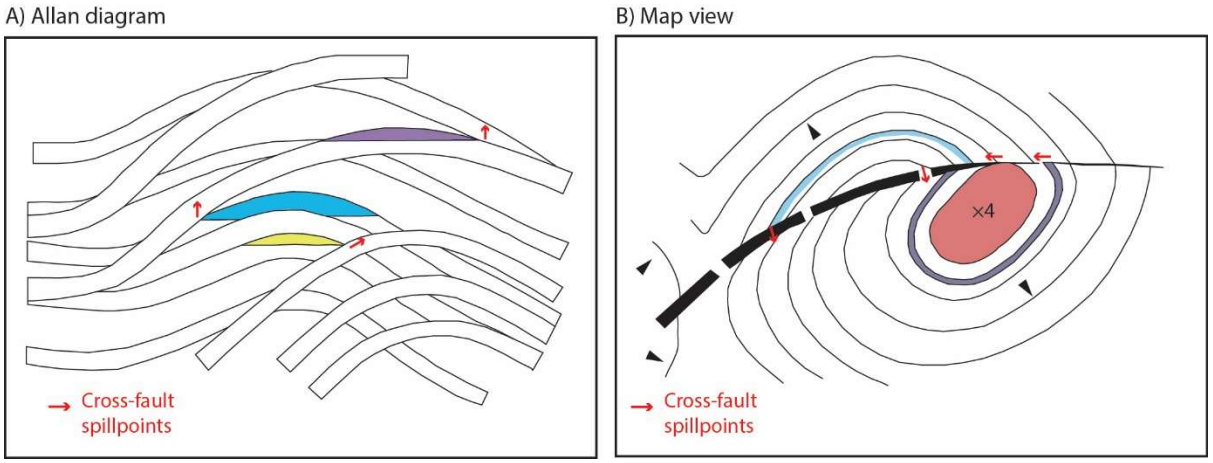

Figure 3.8 Example of a cross-fault migration scenario illustrated in an A) Allan diagram and B) map view. In this Allan diagram, the hanging wall is in front of the footwall. Higher permeability beds are indicated by blocked ends and low permeability beds are open spaces. ×4 = four sandstones filled to limits of simple closure. Redrawn from Allan (1989).

The model by Allan (1989) is based on two assumptions. First, that a fault itself has no sealing or non-sealing properties, and second, that the potential for a fault to trap fluids solely depends on the petrophysical properties of the juxtaposed stratigraphy. Allan diagrams have been applied in multiple studies assessing across-fault seals in hydrocarbon fields and more recently in proposed CO_2 storage sites (e.g., Bretan et al., 2011; Mulrooney et al., 2020).

Knipe (1997) introduced a model that provides a 1D representation of fault juxtapositions, called the triangle diagram. Figure 3.9 illustrates the basic concepts of creating a 1D triangle diagram. In this simplified scenario, three units consisting of mudstone and sandstone are displaced due to normal faulting (Figure 3.9A). In the 1D triangle diagram, the mudstone and sandstone units in the footwall are kept constant, while the hanging-wall side is moved down with increasing throw from left to right (Figure 3.9B). Three juxtaposition scenarios are illustrated in Figure 3.9B; unit B sandstone in the footwall is juxtaposed on unit A mudstone in the hanging wall (i.e., juxtaposition seal), unit B sandstone is self-juxtaposed (i.e., no juxtaposition seal), and unit B sandstone in the hanging wall is juxtaposed against unit C mudstone (i.e., juxtaposition seal). An advantage of using 1D triangle diagrams, compared to Allan diagrams, is that it allows for fault seal analysis without having to perform detailed 3D mapping of stratigraphic horizons and fault planes first. The 1D triangle diagram can also be used to model other important parameters such as permeability, sealing capacity (e.g. SGR values), and transmissibility (Knipe, 1997).

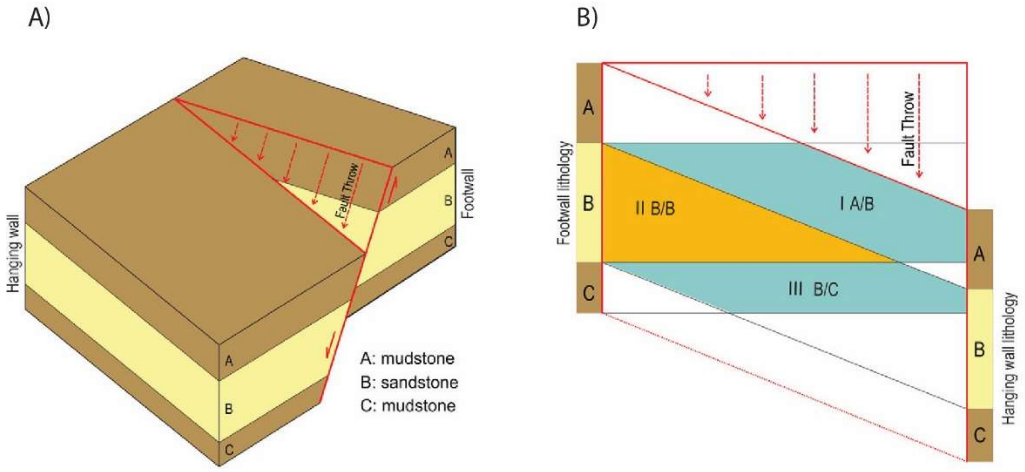

Figure 3.9 Illustrations showing the basic concepts of a 1D triangle juxtaposition diagram. Modified from Pei et al. (2015), which is modified after Knipe (1997).

The most important aspect of juxtaposition assessment in a CO_2 storage site is to identify areas with juxtaposition seals, likely preventing across-fault migration, and areas without juxtaposition seals, likely allowing across-fault migration out of the storage unit. Areas along a fault plane where across-fault migration is more likely to occur should then be assessed for membrane seals, which is the topic of the following sub-section.

3.1.2.2 Membrane seals

Although membrane seals are considered to have a lower probability of sealing, compared to juxtaposition seals (Færseth et al., 2007), areas where storage units are self-juxtaposed or juxtaposed against other high permeability units have been observed to be sealing (e.g., Schowalter, 1979; Watts, 1987; Fristad et al., 1997; Yielding et al., 1997; Lyon et al., 2005; Færseth et al., 2007).

The presence of membrane seals within hydrocarbon reservoirs or CO_2 storage sites depends on the buoyancy pressure exerted by the hydrocarbons or injected CO_2 and the composition of the fault rock (e.g., Schowalter, 1979; Watts, 1987; Allan, 1989; Knipe, 1992). More precisely, the buoyant fluids (e.g., hydrocarbons or injected CO_2) create a pressure difference (ΔP) at the interface of the fault and the buoyant fluid, which is proportional to the column height (h) of the buoyant fluids, the gravitational constant (g), and the difference in density between the formation brine (ρ_w) and the buoyant fluids (ρ_f). The pressure difference can be expressed by equation 3.1.2 (Schowalter, 1979).

$$\Delta P = (\rho_w - \rho_f) g h \tag{3.1.2}$$

The ability of membrane seals to trap buoyant fluids is controlled by the capillary pressure (P_c). The capillary pressure is expressed as proportional to the interfacial tension (*IFT*) between buoyant fluids and formation brine, and the wettability of the fault rock surface with respect to the buoyant fluids (i.e.,

contact angle; θ), and inversely proportional to the pore-throat radius (r) (Purcell, 1949) or the pressure difference between the buoyant fluids (P_f) and formation brine (P_{brine}) (equation 3.1.3; Purcell, 1949; Schowalter, 1979).

$$P_c = P_{hc} - P_f = \frac{2IFT\cos(\theta)}{r} \tag{3.1.3}$$

Leakage across a fault occurs if the buoyancy forces exerted by the buoyant fluids (ΔP) is larger than the pressure required for the buoyant fluids to enter the largest interconnected pore throat of the fault, which is referred to as the capillary threshold pressure (Watts, 1987). Thus, the maximum column height that can be supported by a membrane seal is expressed using equations 3.1.2 and 3.1.3 as

$$h = \frac{2IFTcos(\theta)}{r} \times \frac{1}{(\rho_w - \rho_f)g} \tag{3.1.4}$$

As seen in equation 3.1.4, the maximum column height a membrane seal can hold is, therefore, not necessarily limited to a structural trap but depends on the composition of fault rock, which control the pore-throat size (r) and the wettability parameters (IFT, θ). It is important to note that there are still uncertainties related to the wettability parameters for CO_2, compared to hydrocarbons, which will influence the column height of CO_2 that can be trapped by a fault (further discussed in sub-section 5.3.3; e.g., Miocic et al., 2019; Karolytė et al., 2020).

The following mechanisms have been recognized where the fault itself can be sealing due to reduced pore throat sizes; disaggregation, cataclasis, cementation, and clay smearing (e.g., Knipe, 1992; Fisher and Knipe, 1998; Fossen et al., 2007). Cataclastic and disaggregation deformation zones (or bands) are the principal type of fault rock in clay-poor successions (i.e., clean sandstones with less than 15% clay; Fisher and Knipe, 1998; Sperrevik et al., 2002). Disaggregation zones (or bands) form due to faulting at relatively low confining pressures and burial depths (<1 km), as a result of grain reorganization without fracturing (e.g., Mandl et al., 1977). For example, in areas where the storage units are self-juxtaposed due to faulting at shallow depths. The permeability of a disaggregation zone is often assumed to be similar to that of the host rock, however, they have been observed in outcrop studies to form both increased and decreased permeability (Fossen et al., 2007; Braathen et al., 2018). It is, therefore, not obvious how the presence of such zones will influence CO_2 migration without having access to well cores from the storage site.

Cataclastic deformation zones (or bands) form at higher confining pressures, typically at 1.5–2.5 km burial depth (e.g., Fisher and Knipe, 2001; Lothe et al., 2002). Cataclasis involve grain fracturing and thus reduces the porosity and permeability (e.g., Aydin, 1978; Fisher and Knipe, 1998). Cataclastic bands have been found in Permian sandstones of the southern North Sea (Fisher and Knipe, 2001) and porous sandstones in southeastern Norway (Lothe et al., 2002). While such zones often led to higher

permeability reduction, compared to disaggregation zones, additional factors such as continuity and thickness will affect their influence on across-fault migration (Fossen et al., 2007). Furthermore, cementation can form within cataclastic and disaggregation zones if they are subjected to temperatures exceeding >90°C and >3 km burial depth leading to an increased reduction in permeability of the fault rock (Walderhaug, 1996; Fisher et al., 2000).

Clay smear can form within the fault rock due to the presence of clay-rich successions (>40% phyllosilicate; Weber et al., 1978). Fisher and Knipe (2001) and Yielding (2002) suggest that within the Brent Province, clay smear is the dominant mechanism that leads to higher capillary threshold pressures within the fault rock and that disaggregation and cataclastic deformation zones have a negligible effect on fluid migration, in comparison. Therefore, the presence of clay smears within fault rocks where sandstone on sandstone juxtapositions are present, has been considered to have a sealing potential within proposed CO_2 storage sites (e.g., Bretan et al., 2011; Gassnova, 2012).

As presented above, the ability of the fault rock to prevent across-fault migration depends on the size of the pore-throats in the fault rock (equation 3.1.3). However, the pore-throat radius cannot be determined directly, and it is therefore approximated by applying algorithms predicting the clay content within the fault rocks. Such algorithms include the clay smear potential algorithm (CSP; Bouvier et al., 1989; Fulljames et al., 1996), the shale smear factor algorithm (SSF; Lindsay et al., 1993), and the shale gouge ratio algorithm (SGR; Yielding et al., 1997; Freeman et al., 1998). The equations and concepts of these algorithms are illustrated in Figure 3.10A-C.

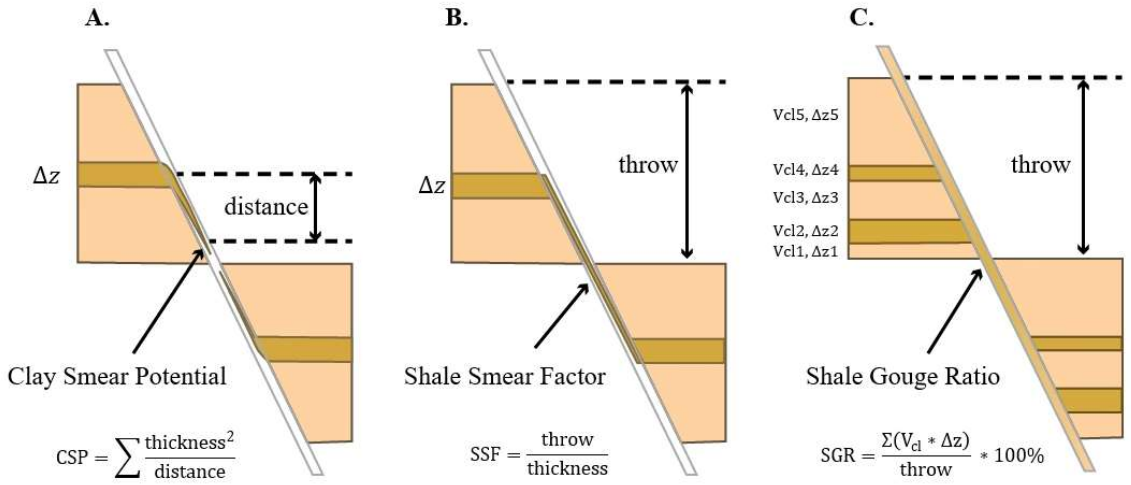

Figure 3.10 Conceptual figures of the main established fault-seal algorithms, A) clay smear potential, B) Shale smear factor, and C) shale gouge ratio. After Yielding et al. (1997), redrawn from Yielding et al. (2010).

The CSP algorithm calculates the total amount of clay that has been smeared from every shale unit along the fault (Figure 3.10A; Bouvier et al., 1989; Fulljames et al., 1996). As such, the value of CSP increases with increasing thickness and number of shale beds and decreases with increasing fault throw.

It is important to note that the CSP algorithm does not predict the thickness of the clay smear, but rather gives an estimate of the relative likelihood that a clay smear is present in the fault zone.

The SSF algorithm simply calculates the ratio of throw to the thickness of a single shale unit (Figure 3.10B). The SSF is therefore a single value that does not change vertically along the fault plane but varies laterally because of variations in fault throw. More precisely, a low value of SSF corresponds to a higher likelihood of intact smear (Lindsay et al., 1993).

The SGR algorithm assumes that the host rock is uniformly mixed into the fault rock (Yielding et al., 1997; Freeman et al., 1998). More precisely, the composition of the fault rock at a certain point in the fault will be the same as the composition of the host rocks that have slipped past that part of the fault. Therefore, the SGR algorithm provides an estimate of the proportion of clay content of beds in the host rock that has slipped past a point on the fault surface and use this as a proxy for fault rock composition (Figure 3.10C; Yielding et al., 1997; Freeman et al., 1998).

The amount of clay in the host rock, referred to as the volumetric clay fraction (V_{cl}; Figure 3.10C), can be derived from well log data (e.g., gamma-ray and neutron-density logs) usually located at opposing sides of the target fault (e.g., Bretan et al., 2003; Bretan and Yielding, 2005). In a frequently used approach (e.g., Lyon et al., 2005; Bretan et al., 2011), the V_{cl} is calculated in two steps (Asquith et al., 2004). First, the gamma-ray index (i_{GR}) is computed by equation 3.1.5.

$$i_{GR} = \frac{GR - GR_{min}}{GR_{max} - GR_{min}} \tag{3.1.5}$$

Where GR represents the gamma-ray value at a given depth, GR_{min} is the gamma-ray value assigned to 0% clay (i.e., the sand-line), and GR_{max} is the gamma-ray value assigned to 100% shale (i.e., the shale-line). The V_{cl} can then be approximated by using equation (3.1.6).

$$V_{cl} = i_{GR} \tag{3.1.6}$$

Finally, the V_{cl} values can be used to assess the presence of clay smear, in combination with throw measurements and thickness of shale beds, by using equation 3.1.7 from Yielding et al. (1997) and Freeman et al. (1998).

$$SGR = \frac{\sum V_{cl} \times \Delta z}{throw} \tag{3.1.7}$$

Allan diagrams (Allan, 1989) and 1D triangle diagrams (Knipe, 1997) can, similar to juxtaposition seals, be used to display the presence of membrane seals for targeted faults. Figure 3.11 shows an example of a subsurface fault-seal model from the West Cameron area in the Gulf of Mexico in Yielding et al. (2010). The sandstone and mudstone successions and throw are projected onto the fault plane using interpreted horizons in Figure 3.11A and Figure 3.11B, respectively. This information is then used, in

combination with V_{cl}, to calculate and project the distribution of SGR onto the fault surface using an Allan diagram (Figure 3.11C).

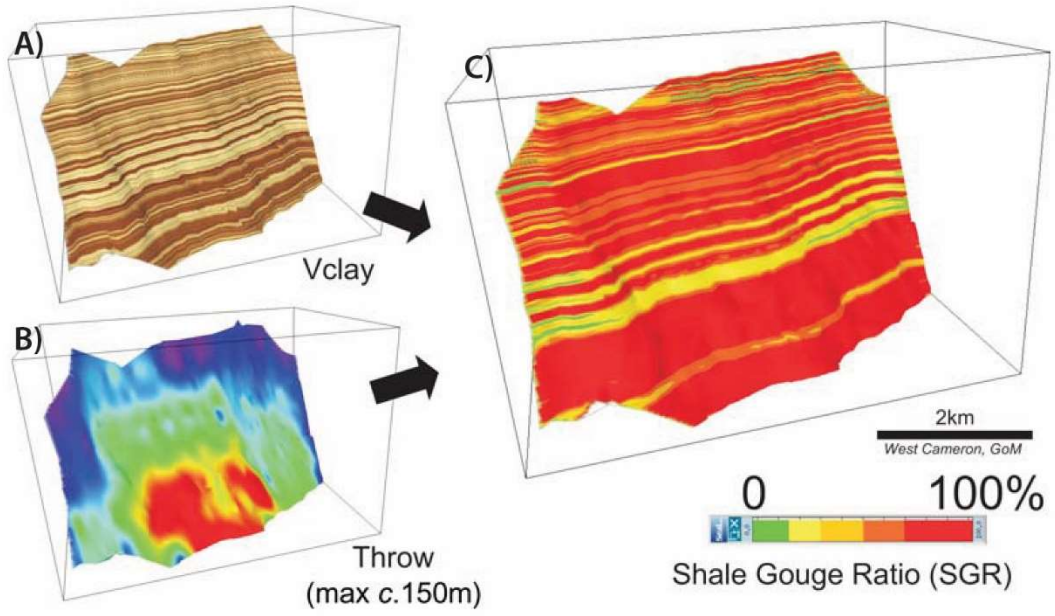

Figure 3.11 Example of a subsurface fault-seal model from the West Cameron area, Gulf of Mexico. The A) sandstone-mudstone sequences, B) throw, and C) SGR values are projected onto the mapped fault surface. From Yielding et al. (2010).

An important aspect of assessing the presence of clay smear using the established fault-seal algorithms (CSP, SSF, and SGR) is that the calculated values need to be calibrated to provide meaningful estimates on the presence of a membrane seal (e.g., Bretan et al., 2003). Calibration by Jev et al. (1993) suggests that CSP values over 30 represent a sealing fault and Yielding et al. (2010) suggest that SSF values less than 4–5 represent a high chance that a continuous smear is present across the fault.

Two approaches are currently available to relate calculated SGR values to 'sealing' and 'leaking' faults, that is, the 'deterministic' and the 'empirical' approach (e.g., Yielding et al., 2010). The deterministic approach is based on laboratory experiments measuring the capillary threshold pressure and clay content of fault rock samples from areas nearby cored wells and extrapolating it onto the targeted fault (Sperrevik et al., 2002). However, fault rock samples are often not available, and as such, an 'empirical' approach is often applied. The empirical approach uses faults that are known to be sealing, mainly from the North Sea, to constrain relationships between SGR and sealing or non-sealing potential (Figure 3.12; Bretan et al., 2003; Yielding et al., 2010). Both approaches show that increasing SGR values correspond to increasing clay content in the fault zone, higher capillary entry pressure, and lower permeability (Yielding et al., 1997; Freeman et al., 1998).

The compilation of 'leaking' and 'sealing' faults from the North Sea in Yielding (2002) shows that SGR values less than 15% are related to leaking faults, SGR values between 15–20% represents a threshold pressure between leaking and sealing faults, and SGR values exceeding 20% are related to sealing faults

(Figure 3.12). Furthermore, calibration by Bretan et al. (2003) show that, while buoyant fluids exhibit a correlation between increasing SGR and increasing buoyancy pressure being retained by the fault for SGR values between 20–40%, there is no increase in strength of the fault for SGR values above 40%.

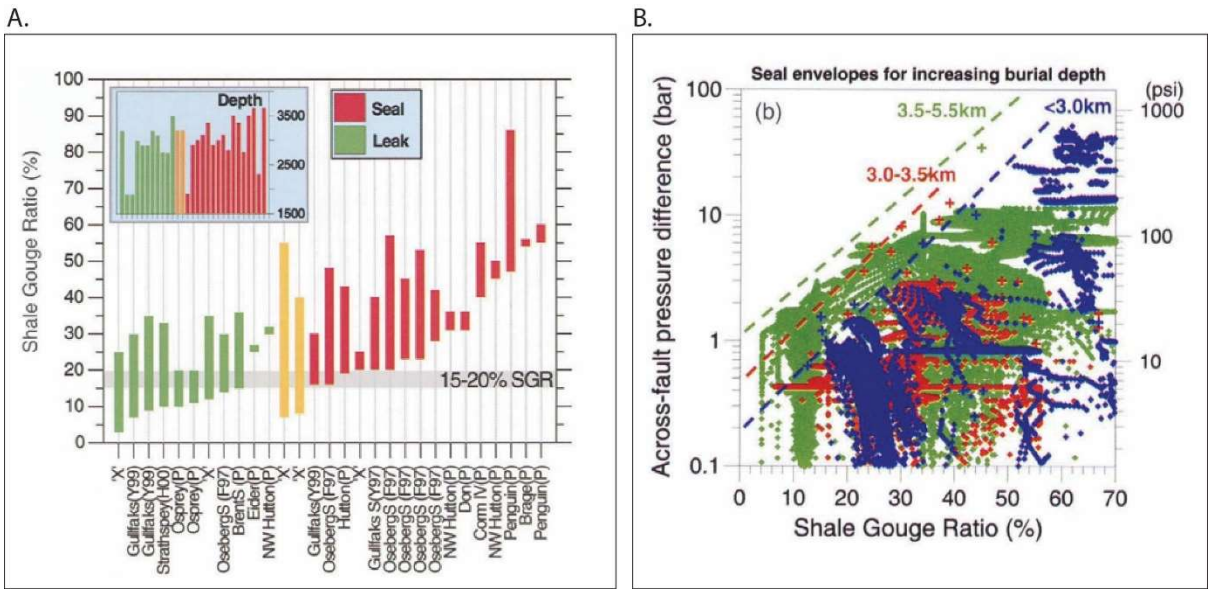

Figure 3.12 A) Compilation of leaking and sealing faults in the Brent Province, northern North Sea. Faults are characterized as sealing (red), leaking (green) or support an oil-water contact less than 15m, at 3200 m burial depth (yellow). Inset shows burial depth for the same sequence of faults. Abbreviated references: F97 = Fristad et al. (1997), Y97 = Yielding et al. (1997), Y99 = Yielding et al. (P = Phelps,pers.commun, H00 = Harris et al. (2000). B) Comparison of SGR and *in situ* across-fault pressure differences and corresponding seal-failure envelopes. Figures from Yielding (2002).

Further estimation of hydrocarbon column heights, using the SGR method, can be assessed by applying the seal-failure envelopes of compiled SGR ratios and across-fault pressure differences (AFPD(bar)) calibrated by Yielding (2002) (Figure 3.12B) and the equation 3.1.2 assuming that ΔP = AFPD(bar). It has been suggested that these calibrations can be directly applied to estimate the sealing and non-sealing potential of faults and calculate CO_2 column heights (Bretan et al., 2011), while others suggest that this will not be successful (e.g., Miocic et al., 2019; Karolytė et al., 2020). How the theoretical concepts introduced in this section have been applied in this study is presented in section 3.3 and the main limitations and uncertainties related to applying these concepts in a CO_2 storage site are discussed in section 5.3.3.

3.2 Data

This section describes the data supporting this study. The data include 3D seismic data (sub-section 3.2.1), 2D seismic data (sub-section 3.2.2), and well data (sub-section 3.2.3). An in-house velocity model was used to depth convert data (sub-section 3.2.4). These data have been used to create a detailed

3D geomodel of the study area and perform fault modelling and fault analysis. Limitations of the data applied are discussed in sub-section 3.2.5.

3.2.1 3D seismic data

Seismic reflection data provides an image of the subsurface by measuring the time (ms) it takes for a seismic wave to propagate down to an interface and reflect up to the receiver (i.e., two-way-time; TWT). The strength of the reflected seismic wave depends on the variations in acoustic impedance (AI) at an interface, which is the product of the bulk rock density (ρ) and the compressional wave velocity (v). Because velocity and rock density vary as a function of depth and petrophysical properties, the acoustic impedance can be related to variations in lithology of the subsurface (e.g., Brown, 2011). Seismic reflection data have been widely applied in hydrocarbon exploration and can be acquired along a single line (2D seismic, see sub-section 3.2.2) or systematically over an area (3D seismic). Therefore, 3D seismic data provide a volume in which cross-sections can be derived along any orientation within the survey area, including horizontal sections.

Data from the 3D seismic survey GN10M1 was utilized in this study. The survey was acquired from Gassnova in 2010 and the quality is considered to be good to very good at the depth of the Lower Jurassic storage complex (Gassnova, 2012). The GN10M1 survey covers ca. 1370 km^2 in the Norwegian quadrants 31/2, 31/5, and the northernmost part of 31/8 within the Horda Platform (Figure 3.13). The Troll West field is located in the northern half of the survey while the northern part of the Aurora exploitation license EL001 is located in the southern half. The GN10M1 survey is a pre-stack merge of three 3D surveys: GN1001, NPD-TW-08-4D-TROLLCO2, and NH0301 (Table 3.1) with inline traces trending E–W and crosslines trending N–S (Gassnova, 2012). The inline and crossline spacing (bin size) is 25 m and 12.5 m, respectively. GN10M1 is displayed in ms TWT with a record down to 4000 ms TWT. As previously mentioned in section 1.2, the area used for analysis and modelling in this study (referred to as the study area) covers approximately 420 km^2 of the GN10M1 survey. (Figure 3.13).

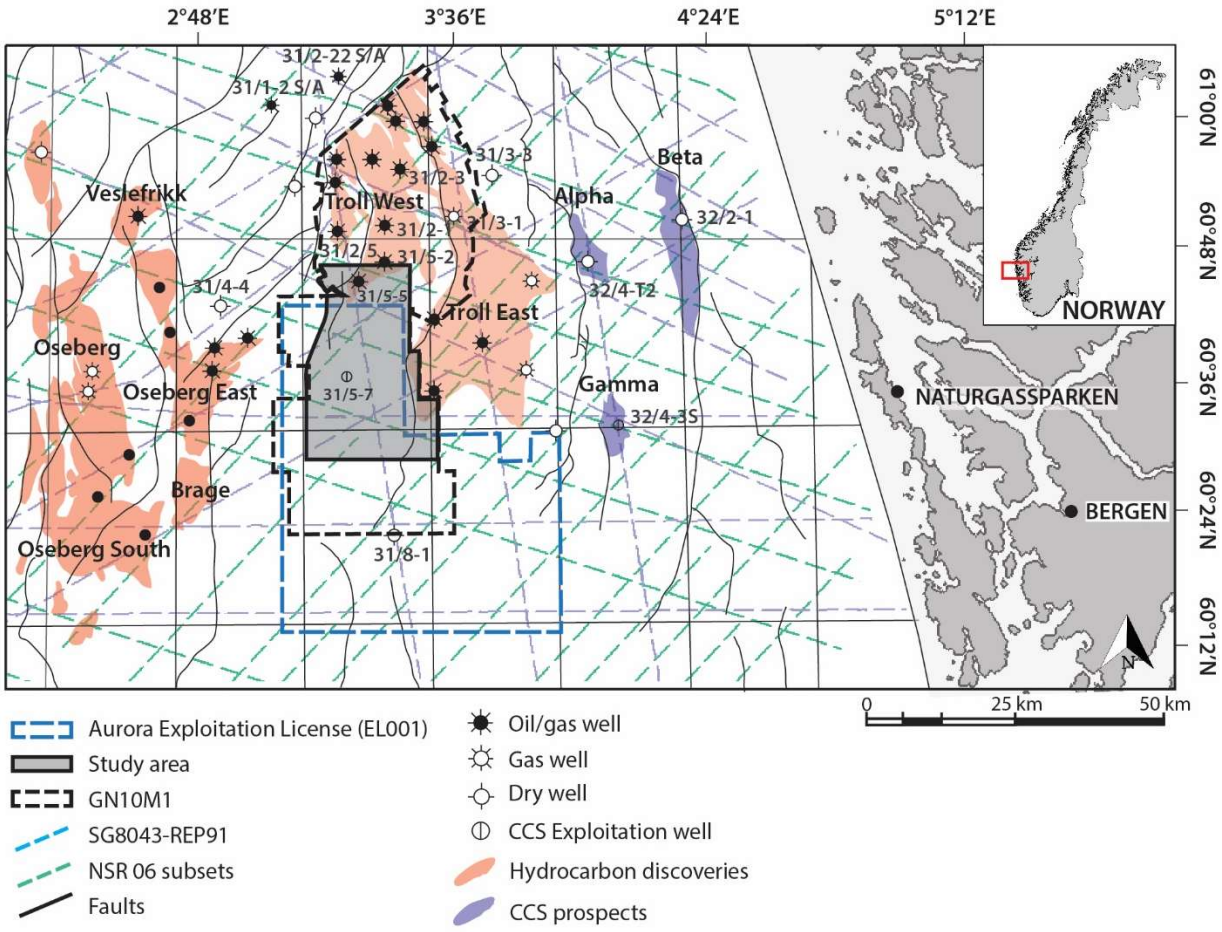

Figure 3.13 Map displaying the outline of GN10M1 3D seismic survey, 2D seismic lines, outline of the Aurora exploitation license (EL001), and the study area. Note that not all wells have been included in the map.

To achieve a thorough understanding of a 3D seismic dataset it is important to determine its polarity and phase (Herron, 2011). The Society of Exploration Geophysicists (SEG) has defined two polarity conventions, that is, normal and reverse. In normal polarity conventions a downward increase in acoustic impedance is represented as a peak and a downward decrease in acoustic impedance is represented as a trough. The opposite is true for reverse polarity. The polarity of the survey can be determined by analyzing a reflection event where the acoustic impedance is known, or predictable (e.g., Brown, 2011). For example, the seabed that represents an increase in impedance due to the transition from water to sediments. Or, at a hydrocarbon-water contact that represents an increase in impedance due to the transition from a hydrocarbon saturated unit to a brine saturated unit.

The Troll West Field, located within the GN01M1 survey, has a direct hydrocarbon indicator in form of a flatspot (Bolle, 1992). Analyzing the seabed reflection and the Troll flatspot events identified within the GN10M1 data, a peak represents a downward increase in acoustic impedance. Therefore, the survey is consistent with the normal polarity convention. In figures and tables throughout this study, an increase

in acoustic impedance (peak) is displayed using red or black while a decrease (trough) is displayed using blue or white.

The phase of a seismic survey is typically determined by analyzing a high amplitude reflection that is known to represent a single interface or sharp contact, for example, a flatspot (e.g., Brown, 2011; Herron, 2011). Analyzing the Troll flatspot, it is represented by a single high-amplitude reflection event where the side lobes are low and symmetrical. This signature is typical for zero-phase wavelets, therefore, the GN10M1 seismic cube is interpreted as a zero-phase survey. The 3D seismic survey is cropped at 4000 ms TWT, with imaging down into the Lower Triassic and in some areas the crystalline basement.

Table 3.1 Summary of 3D seismic surveys used herein. Information about the surveys is from the NPD Diskos repository and seismic quality from Gassnova (2012). Abbreviations: ILN = inline and XLN = crossline.

3D survey	**Area (km^2)**	**Quality**	**Year**	**Company**	**Inline direction (shot direction)**
GN1001	503	Excellent	2010	Gassnova SF	E–W
NPD-TW-08-4D-TROLLCO2	293	Good	2008	Norwegian Petroleum Directorate	E–W
NH0301	718	Good/very good	2003	Norsk Hydro Produksjon AS	NE–SW
GN10M1	1370	Good/very good	2010	Gassnova SF	E–W

3.2.2 2D seismic data

2D seismic data provides an image of the sub-surface along a single line. A suite of 2D seismic data was used in this study and extends laterally outside of the 3D seismic survey and deeper into the subsurface, compared to the 3D seismic data. Therefore, this data was used to provide a regional context for the observable structural and stratigraphical trends outside of the GN10M1 volume. Furthermore, two 2D lines, in particular, were used to determine whether faults within the study area extended down into the basement (i.e., thick-skinned faults) displacing the basement-cover contact and the shape of these thick-skinned faults in cross-section (Figure 3.14).

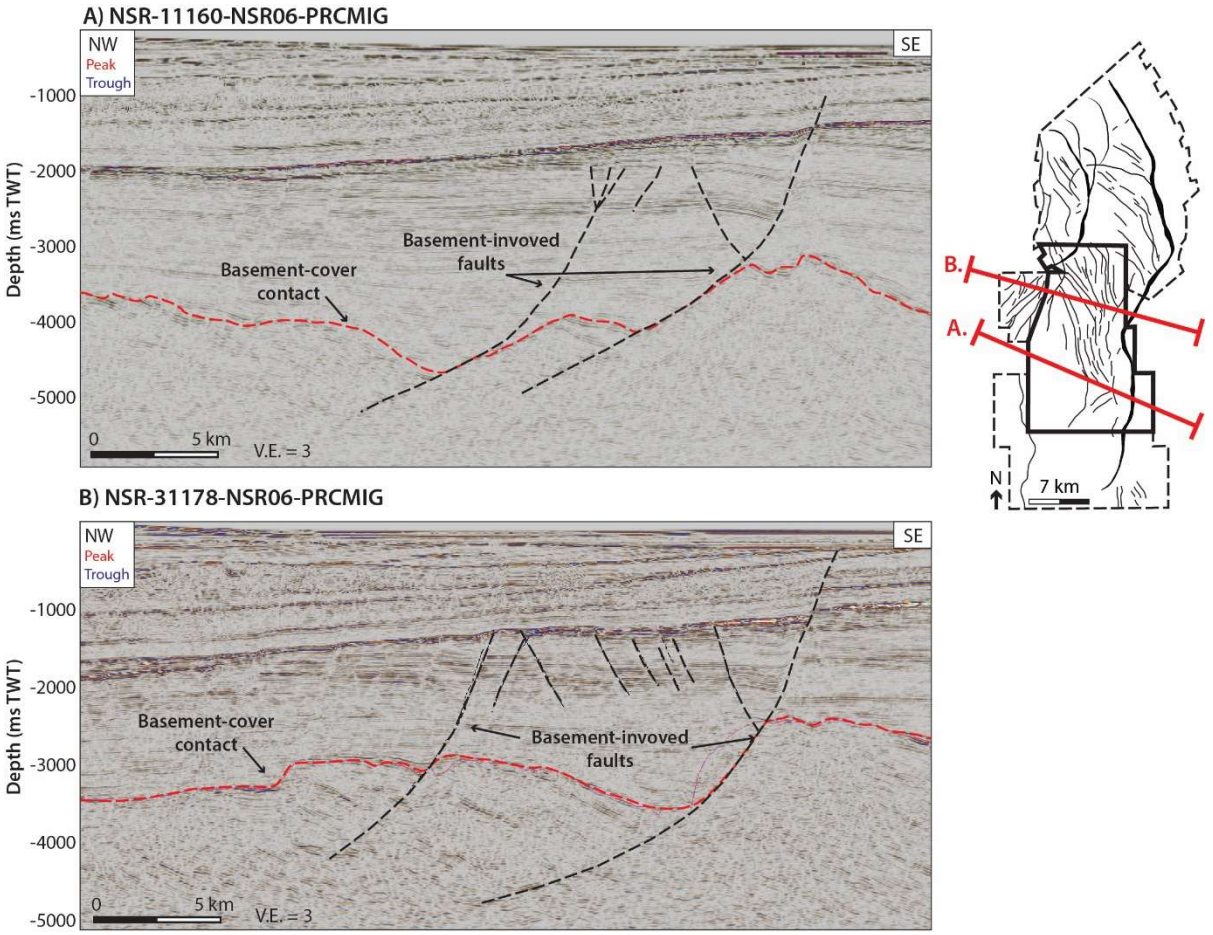

Figure 3.14 Two 2D seismic lines from the NSR 06 subset crossing through the study area showing the basement-involvement of faults.

Three 2D seismic datasets are applied in this study; NSR Subset, NSR-06 Subset, and SG8043-REP91 with a spacing of 4-10 km. The 2D seismic data was acquired from the NPD Diskos repository. Again, the Troll flatspot and/or the seabed reflectors are examined to determine the polarity of the 2D seismic surveys and the quality of the seismic is determined by their ability to display the storage and seal units (Table 3.2).

Table 3.2 Summary of 2D seismic surveys used in this study. The quality of the 2D seismic datasets is based on the data quality assessment according to Herron (2011).

2D survey	**Polarity**	**Imaging depth (ms TWT)**	**Quality**	**Year of survey and company**	**Line orientation**	**Number of lines**
NSR/ NSR-06 Subset	Normal	9300/9200	Good/very good	(2006) TGS	NW–SE and NE–SW	22/24
SG8043-REP91	Normal	7000	Good	(1991) Saga Petroleum ASA	N–S, NW–SE, and E–W	65

3.2.3 Well data

In this study, 99 wells were available for analysis, located in the Norwegian quadrants 25, 26, 30, 31, 32, 35, and 36. Wellbore information was acquired from the NPD Diskos repository. Most of the wells used in this study are located in the Troll West and East fields to the north and northeast of the study area, and in the Oseberg, Brage, and Veslefrikk fields to the west of the study area (Figure 3.13).

Only two wells are present within the study area, 31/5-7, and 31/5-5 (Figure 3.13). As previously mentioned, well 31/5-7 was drilled by the Northern Lights Project and will later be used as an injector within the Aurora storage site. The well confirmed 116-meter-thick Johansen Formation, 57-meter-thick Cook Formation, and 128-meter-thick Drake Formation at approximately 2.6 km TVD RKB. The oil and gas well 31/5-5 is located within the northernmost part of the study area, however, this well does not penetrate the storage complex and was suspended in 1995 (NPD Factpages, 2020). Therefore, except for well 31/5-7, there are no other wells that penetrate the storage complex within the delineated study area in Figure 3.13. However, numerous wells penetrate the storage complex in the Troll West Field and have been used to correlate well and seismic data within the study area. This includes wells 31/5-2, 31/2-5, 31/2-3, 31/2-4, 31/2-8, 30/6-14, 31/4-3, 31/6-1, 31/2-1, and 31/6-2 (Table 3.3).

In Figure 3.15 eight of these wells are displayed together with the gamma-ray log to show variations in the main interpreted horizons used in this study (further introduced in 3.3.2). Log curve signatures from gamma-ray, neutron-density, and sonic logs have been used to create well-ties (sub-section 3.3.1). Furthermore, gamma-ray logs have also been applied for converting the volumetric clay fraction (V_{clay}) to be used for shale gouge ratio analysis (sub-section 3.3.5).

Table 3.3 Table showing the depth of well tops and depths for wells penetrating the storage complex in the vicinity of the study area. *Depth to Top Lower Drake Formation in well 31/5-7 are acquired from Equinor ASA, while in 31/5-2, 31/2-5, and 31/2-1 it is inferred for this study. The location of the wells is illustrated in Figure 3.15.

Well name / Well top and depth (m MD RKB)	**31/5-7**	**31/5-2**	**31/2-5**	**31/2-1**	**31/2-3**	**31/2-4**	**31/2-8**	**30/6-14**	**31/4-3**	**31/6-1**	**31/6-2**
Top Brent Group	2424	1956	1957	1880	1811	1784	2516	2559	2326	1804	1930
Top Upper Drake Fm.	2510	2035	2070	1984	1901	1901	2719	2588	2410	1834	1974
Top Lower Drake Fm.	2585	2114*	2136*	2045*	–	–	–	–	–	–	–
Top Cook Fm.	2638	2175	2200	2092	2010	2007	2824	2648	2447	1964	–
Top Upper Amundsen Fm.	2695	2192	2277	2133	2054	2106	2895	2733	2470	–	–
Top Johansen Fm.	2702	2225	2307	2175	2096	2125	2985	–	2542	1980	2054
Top Lower Amundsen Fm.	2818	2323	2380	2272	2175	2240	3033	–	–	2082	3137
Top Statfjord Gp.	2832	2335	2403	2292	2235	2256	3047	2783	2701	2110	2163

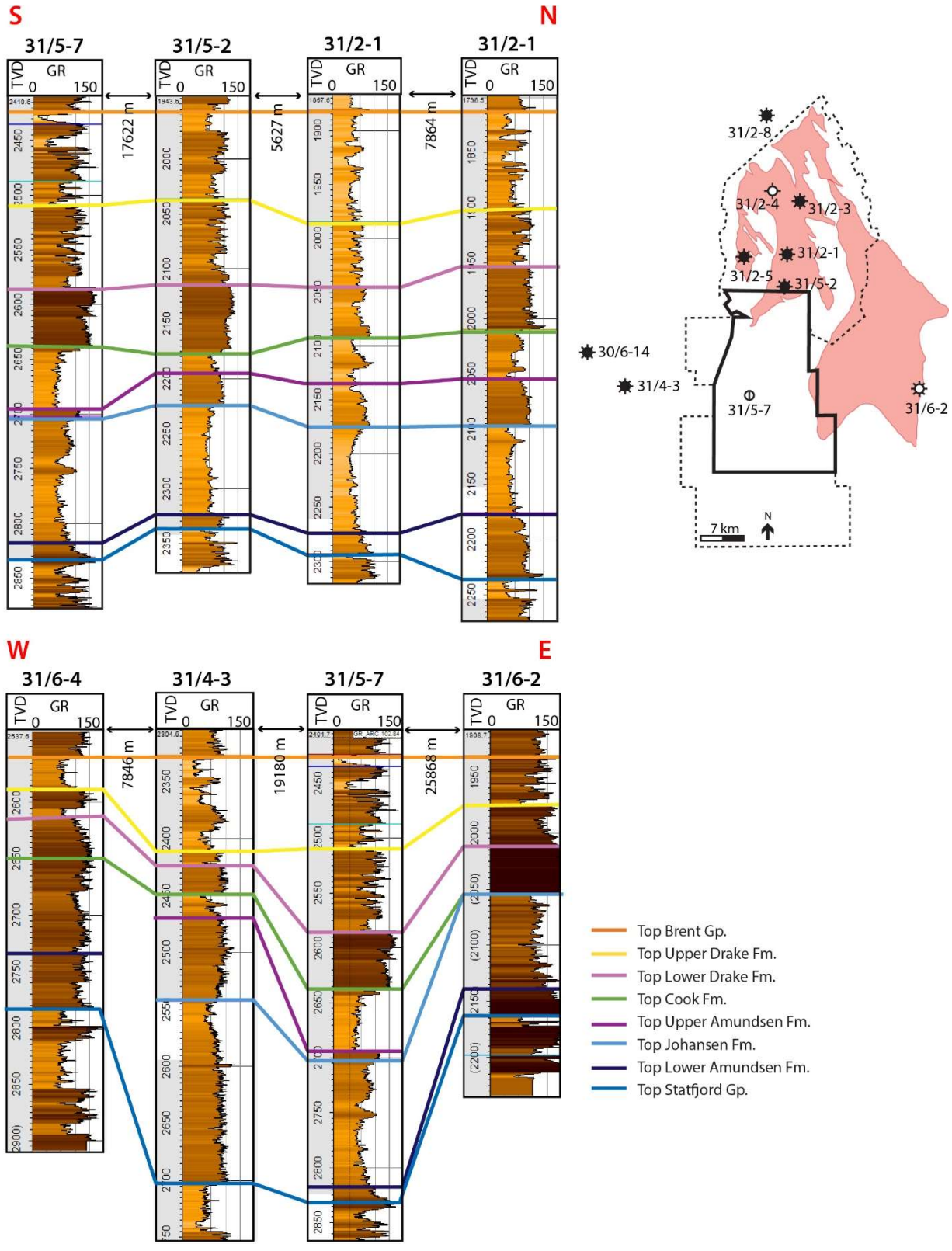

Figure 3.15 N–S trending and E–W trending well correlations flattened on Top Brent Gp illustrating thickness variations in Dunlin Group formations, gamma-ray logs, and formation tops from NPD. Formation tops in 31/5-7 are by Equinor ASA. I have inferred the position of Top Lower Drake in all wells except for well 31/5-7.

3.2.4 Velocity model

A velocity model covering the Horda Platform was created by the NCCS team at UiO during spring 2021 (NCCS v.2.0). This in-house model was applied in this study to convert data from the time domain (ms TWT) to the depth domain (m). The velocity model was created using time-depth curves from 24 wells in the vicinity of the study area: 31/2-1, 31/2-2R, 31/2-4R, 31/2-5, 31/2-8, 31/3-1, 31/3-3, 31/5-2, 31/6-1, 31/6-2R, 31/6-3, 31/6-6, 32/2-1, 32/4-1 T2, 32/4-3 S, 30/6-5, 31/1-1, 31/4-3, 31/5-6, 31/5-7, 31/8-1, 31/2-8, 35/11-10, 35/12-3S and interval velocity from one well: 31/2-9S. The time-depth curves were quality controlled by examining the location of the well picks against adjacent seismic data. Most of the time-depth curves showed excellent correlation, while other wells had no velocity data. Depth converted data was assessed to ensure an excellent correlation between horizon, well picks, and seismic.

Figure 3.16 shows the interpreted horizons and faults before and after depth conversion overlying velocities from the NCCS v.2.0 model. The vertical scale is in time and is therefore not representative of the depth converted interpretations. However, comparison shows that depth conversion of the interpretations results in more steeply dipping horizons in the deeper parts of the study area and more steeply dipping and planar faults in section view. Depth conversion was performed to more accurately image structural features in the subsurface, which improves the assessment of fault geometries (e.g., throw) and across-fault seal interpretations (sub-section 3.3.3; e.g., Lyon et al., 2004; Lyon et al., 2005). Furthermore, depth conversion was necessary to calculate SGR values and to discuss gross rock volumes of structural closures (sub-section 3.3.5).

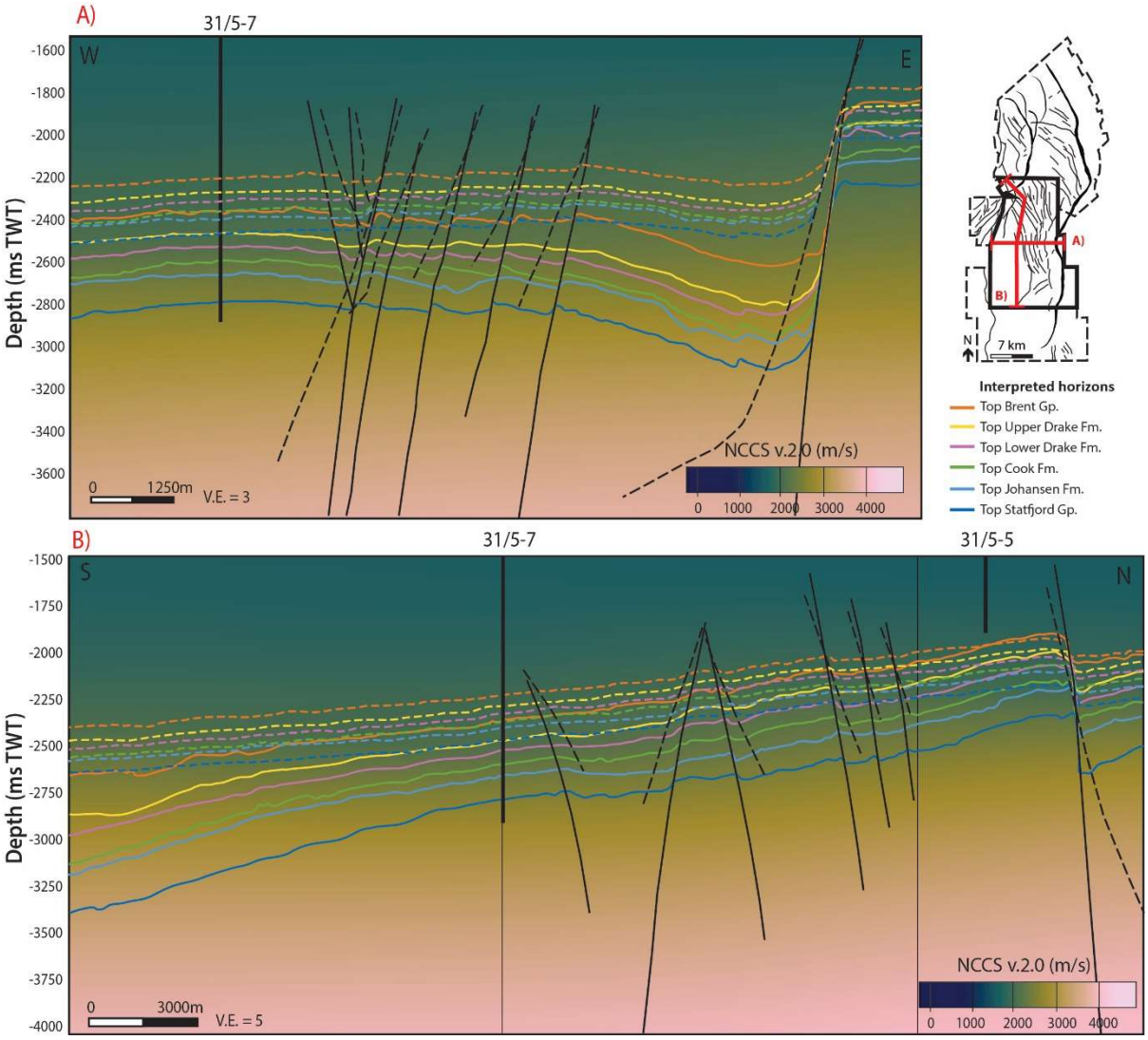

Figure 3.16 Cross-sections showing the interpreted horizons and faults before (dashed lines) and after (solid lines) depth conversion. Background colors show the variations in velocities of the NCCS v.2.0 velocity model applied herein. Note that the vertical scale is in ms TWT, and as such is not representative of the depth converted interpretations. Inset map shows the location of the two cross lines.

3.2.5 Data limitations

When interpreting seismic data, it is important to be aware of the limitations/uncertainties associated with the data used, and how they can affect the results. Some limitations of seismic data are related to factors resulting from either the data acquisition stage (e.g., detector spacing and seismic resolution) and the data processing stage (e.g., signal-to-noise ratio; Sheriff, 1977).

When creating a structural geomodel and performing across-fault seal assessment, the resolution of the seismic data is important and is, therefore, the focus of this sub-chapter. Sheriff (1977) expresses the resolution of seismic data as the minimum distance, either vertically or horizontally, between two features that can be individually distinguished and are controlled by the wavelength (λ) of the seismic

signal. The wavelength can be found by measuring the distance between two peaks, or by dividing the seismic velocity (v) by the dominant frequency (f_d) of the seismic (Sheriff, 1977). With depth, the seismic velocity increases due to compaction, and the dominant frequency decreases due to attenuation of higher frequencies (Sheriff, 1977). Consequently, the wavelength increases with depth making the resolution poorer.

Vertical resolution typically ranges between one-quarter and one-eighth of the dominant wavelength (λ_d) of the pulse (Sheriff, 1977). A simple way to estimate the dominant frequency from seismic is to measure the time difference over, say, ten peaks at the depth of interest. In the GN10M1 survey, ten cycles take 0.258 seconds, which gives a dominant frequency of 39 Hz. Assuming an average velocity of 2.5 kms^{-1} at 2.5 km depth, the dominant wavelength can be calculated using equation 3.2.1.

$$\lambda_d = \frac{v}{f_d} = \frac{2.5\ kms^{-1}}{39\ Hz} \approx 0.06\ km = 60\ m \tag{3.2.1}$$

The dominant wavelength is therefore 60 meters, and the vertical resolution of the GN10M1 is in the range of 7.5–15 m (λ /8–λ /4), respectively.

The horizontal resolution of a seismic dataset can be explained in the terms of Fresnel Zones. The Fresnel Zone is defined as the part of a reflector, which the seismic energy is reflected from so that it arrives back at the receiver within half a wavelength, and interferes constructively to increase the reflected signal (Denham and Sheriff, 1981). Migration of seismic data is the main process that improves the horizontal resolution by focusing the energy spread over a Fresnel Zone and collapses diffraction patterns (Loewenthal et al., 1976). In 2D migration the Fresnel Zone can only be collapsed in the in-line direction (Berkhout, 1982), while 3D migration allows accurate positioning of reflections in all directions thus increasing the horizontal resolution (e.g., Cartwright and Huuse, 2005). The horizontal resolution of 3D seismic is, therefore, more or less equal to the bin spacing (here 12.5 × 25 m; Denham and Sheriff, 1981).

3.3 Methods

This section describes the workflow and methods applied in this study to achieve the main objectives; i) establish a detailed structural geomodel of the Aurora storage site, ii) assess the spatial and temporal evolution of faults, iii) assess the presence of across-fault seals, and iv) discuss plausible CO_2 migration pathways and gross rock volumes of relevant structural closures. The workflow is presented in Figure 3.17 and comprises three main stages; (stage 1) literature study, software training and examination of data, (stage 2) detailed seismic horizon- and fault interpretation, and (stage 3) fault modelling and fault

analysis. Petrel E&P Software Platform (v. 2020.1) was used to perform the seismic interpretation and Petroleum Experts (PETEX) Move suite (v. 2020.1) to perform fault modelling and fault analysis. All figures showing structure and thickness maps, as well as fault throw diagrams are presented using the uniform color maps (e.g., 'batlow', 'hawaii' or 'oslo') created by Crameri et al. (2020) to reduce distortion effects and visual errors.

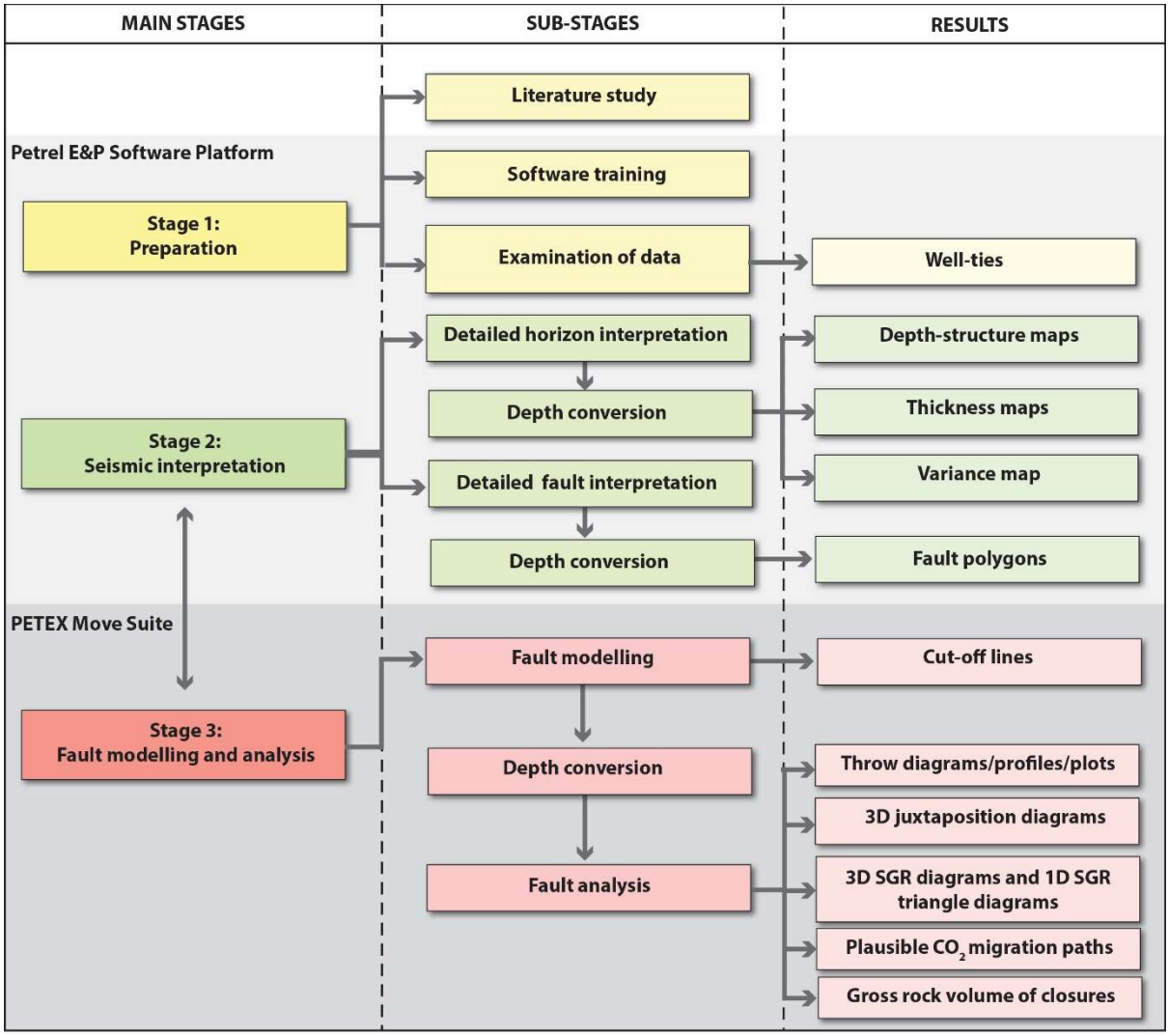

Figure 3.17 Flowchart illustrating the workflow applied in this study, consisting of three main stages divided into multiple sub-stages. Results are illustrated in the column to the right.

Below, the methods used to create well-ties, horizon interpretation, fault interpretation, fault modelling, and fault analysis are described.

3.3.1 Well-ties

Before performing horizon and fault interpretations, it is important to examine the data made available for analysis (Figure 3.17). In this study, 2D and 3D seismic data, and wellbore data (presented in section

3.2) are used to create a detailed structural geomodel of the Aurora storage site. Wellbore penetrations provide data with higher vertical resolution compared to seismic data, but with little to no lateral information. Therefore, areas, where the wellbores can be tied to the seismic data, represent points of higher certainty.

Well-ties can be used to establish a time-depth relationship between the wellbore data, presented in depth-domain, and seismic data, presented in time-domain (sub-section 3.2.4). This time-depth relationship can be established by using vertical seismic profiles (VSP) surveys or checkshot surveys, where the seismic receivers are placed in the borehole (e.g., Kearey et al., 2002). Furthermore, well-ties can be used to pick formation tops more accurately in the subsurface by creating a synthetic seismogram (Sheriff, 1977). A synthetic seismogram is created in the following three steps. First, the velocity and density logs are multiplied to create an acoustic impedance log. Second, a reflection coefficient log is generated from the acoustic impedance log. And third, the reflection coefficient log is convolved with a seismic wavelet to produce the synthetic seismogram (Sheriff, 1977). The synthetic seismograms derived from the well data together with the formation top picks are then compared with the original seismic data in section view.

Herein, well-ties were performed in Petrel using four wells (31/5-7, 31/2-5, 31/2-1, and 31/5-2) in, or in the vicinity of, the study area. The synthetic seismograms were correlated for depths representative for the storage complex (i.e., between Top Brent Group and Top Statfjord Group) and applying a minor bulk shift (max ± 8 ms). A statistical wavelet was extracted from the seismic and no stretching or squeezing of the synthetic was applied. As well 31/5-7 is the only well penetrating the storage complex within the study area, higher confidence was placed on the correlation of well tops from 31/5-7 with the seismic. The well-tie for well 31/5-7 have a maximum correlation, comparing the generated synthetic seismogram and the GN10M1 seismic, of 64% with -5 ms TWT bulk shift applied (Figure 3.18).

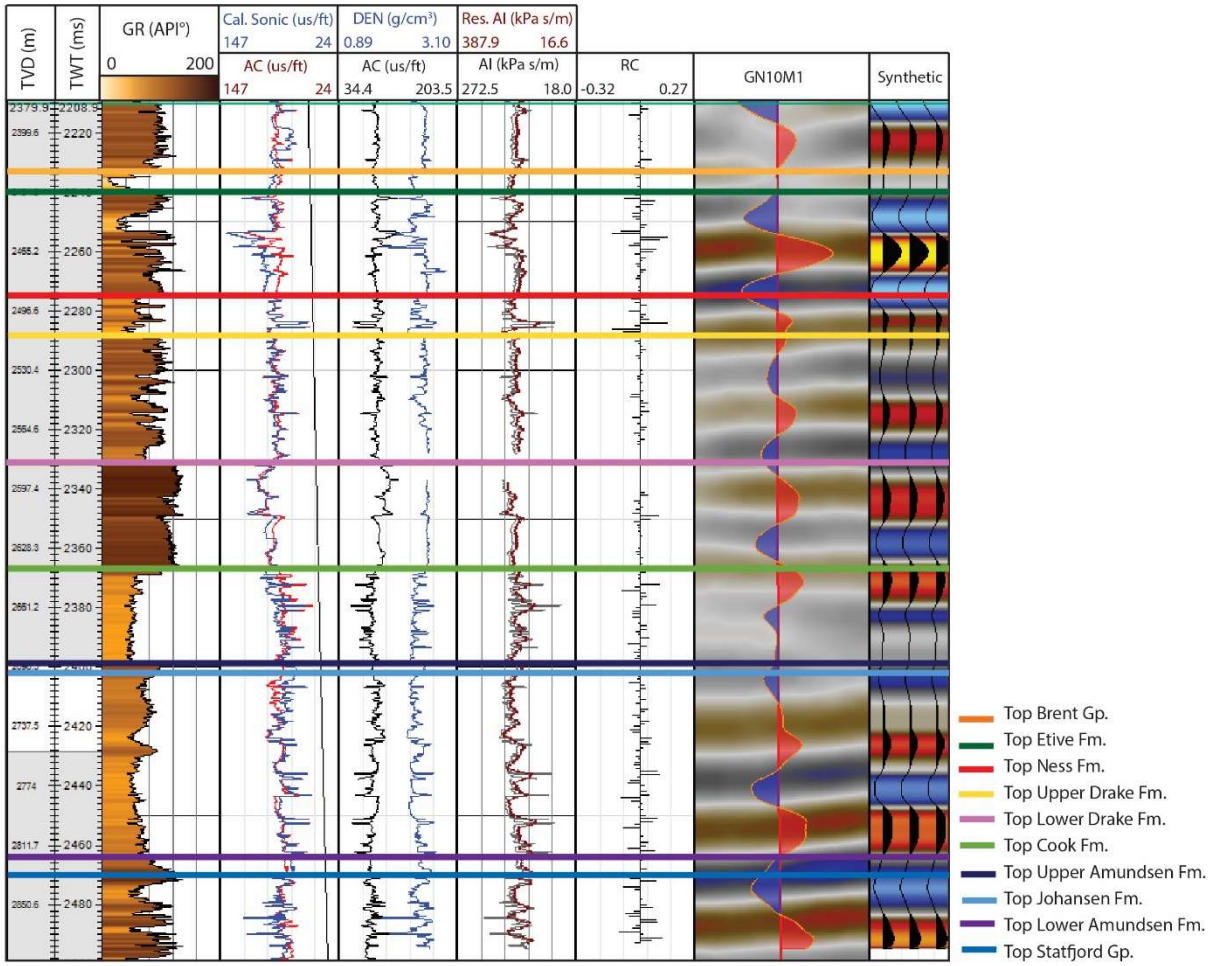

Figure 3.18 Well-tie for injection well 31/5-7 showing the formation tops picked in this study, well log data, and the synthetic seismogram. Abbreviations: Cal. Sonic = calibrated sonic log, Res. AI = Resampled AI.

3.3.2 Horizon interpretation

A detailed interpretation of the storage complex is the next step of the workflow (Figure 3.17) and is essential to create a detailed structural geomodel and perform across-fault seal assessment. As previously mentioned, the target group for CO_2 storage (i.e., the storage complex) in the Aurora storage site is the Lower Jurassic Dunlin Group, which includes the Amundsen, Cook, Johansen, and Drake formations (described in sub-section 2.2.3). The Drake Formation, which represents the seal unit, consists of a lower unit that is more clay-rich and is, therefore, assumed to have better sealing properties (lower permeability and higher capillary entry pressure) compared to the upper unit (Gassnova, 2012). Therefore, similar to Gassnova (2012), the Drake Formation has been interpreted herein on two reflectors, called the Top Lower Drake Formation and the Top Upper Drake Formation (Figure 3.18).

The Amundsen Formation is sub-divided into two units; the Lower Amundsen Formation, which overlies the Statfjord Group, and the Upper Amundsen Formation, which overlies the Johansen Formation (Figure 3.18). These units have, however, not been interpreted because the Upper Amundsen

Formation is considered too thin (7 m in 31/5-7) and lacks lateral continuity, to provide as the primary seal (Gassnova, 2012; Sundal et al., 2015). Vertical movement due to faulting could led to stratigraphy above or below the storage complex to have become juxtaposed against it. Therefore, the Top Statfjord Group, which underlies the Dunlin Group, and the Brent Group, which overlies the Dunlin Group, have also been interpreted

In light of these considerations, the following six horizons have been interpreted herein: Top Statfjord Group, Top Cook Formation, Top Johansen Formation, Top Lower Drake Formation, Top Upper Drake Formation, and Top Brent Group (Figure 3.18). These six interpreted horizons bound five successions, herein named the 'primary storage unit' (consisting of the Lower Amundsen and Johansen formations), the 'secondary storage unit' (consisting of the Cook and Upper Amundsen formations), the 'primary seal unit' (consisting of the Lower Drake Formation), the Upper Drake Formation, and the Brent Group. The reflector picks were selected based on well tops in the four wells that were tied to the seismic (Figure 3.19).

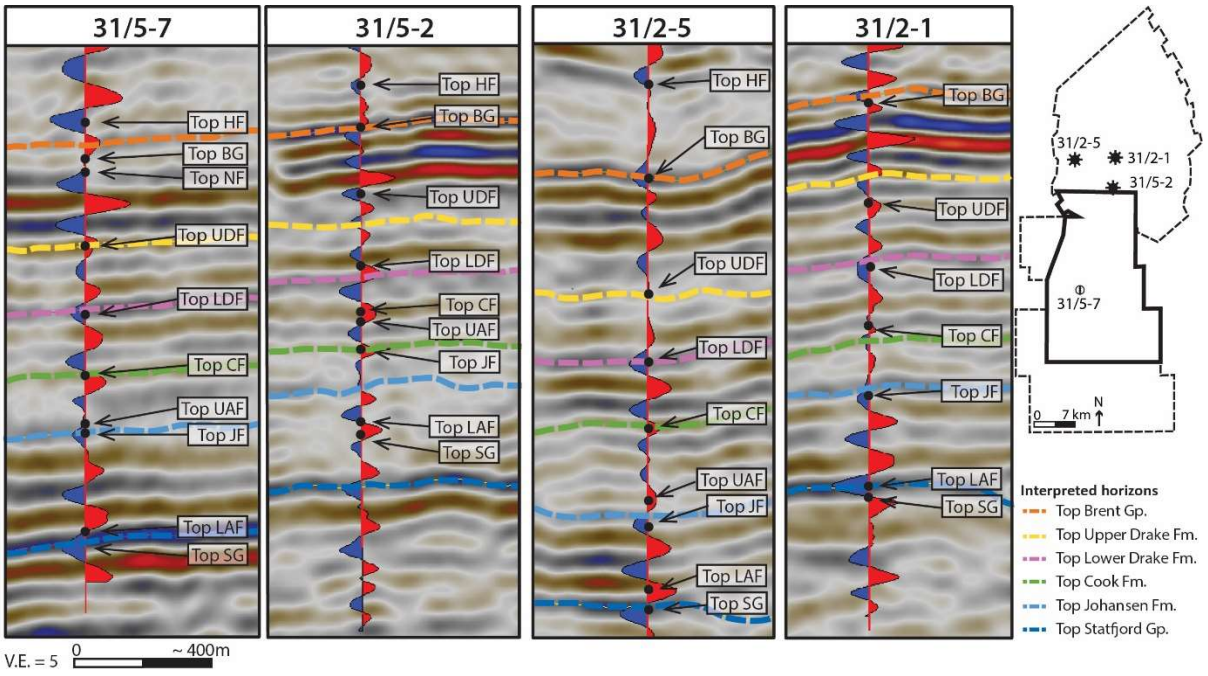

Figure 3.19 Seismic sections, generated synthetic wiggle trace, well tops, and interpreted horizon (stippled lines) tops are presented for four wells. Inset map shows the location of the wells. Abbreviations: HF = Heather Formation, BG = Brent Group, NF = Ness Formation, UDF = Upper Drake Formation, LDF = Lower Drake Formation, CF = Cook Formation, UAF = Upper Amundsen Formation, JF = Johansen Formation, LAF = Lower Amundsen Formation, and SG = Sognefjord Group.

Deviation from the interpreted horizons and the well tops in the four wells are observed and listed in Table 3.4. The largest deviation is observed in wells 31/5-2 and 31/2-1, while 31/5-7 and 31/5-2 show a better correlation with the interpreted horizons. As previously mentioned, higher confidence is placed in the well tops of the 31/5-7 well that targeted the Dunlin Group. Some deviation (-8 m) is present in well 31/5-7 for the Top Brent Group. This was due to selecting the trough overlying the Top Brent

Group well top (peak) in 31/5-7 as it correlates better with the Top Brent Group well tops within the Troll West field (wells 31/5-2 and 31/2-5) and because it represents a more continuous and higher amplitude reflector throughout the study area. Any uncertainties related to the interpreted horizons and their influence on the results are discussed in sub-section 5.3.1.

Table 3.4 List of the deviation from the synthetic wiggle traces and well tops with the interpreted horizons in this study for four wells shown in Figure 3.19. A negative number indicates a deviation down-section from the interpreted horizon to the well top, while the opposite is true for a positive number.

Interpreted horizons	**31/5-7 (m)**	**31/5-2 (m)**	**31/2-5 (m)**	**31/2-1 (m)**
Top Brent Group	+8	0	0	-7
Top Upper Drake Formation	0	+13	0	-25
Top Lower Drake Formation	0	+11	0	-8
Top Cook Formation	0	+25	0	+9
Top Johansen Formation	0	+25	-7	+7
Top Statfjord Group	0	+37	0	-7

In Table 3.5, the interpreted reflectors are compared with the reflector picks in Gassnova (2012), Sundal et al. (2016), and Whipp et al. (2014), which interpreted the Dunlin Group within or in the proximity of the study area. The GN10M1 3D seismic survey, which is applied in this study, was also applied in Gassnova (2012) and Sundal et al. (2016), while the NH0301 covering the Troll West field was used in Whipp et al. (2014). It is important to note, however, that these studies were conducted prior to the drilling of well 31/5-7, and as such the reflector picks were tied to wells within the Troll West and East fields (e.g., 31/2-1 and 31/2-5). Gassnova (2012) noted a mismatch (i.e., ± 10 ms TWT) between the reflectors picked and the well tops within the Dunlin Group. This mismatch was partly due to picking Z-crossing instead of a peak or a trough, and partly because the wells were originally matched to the 2D seismic available when they were drilled (Gassnova, 2012). The latter could also lead to the mismatch observed in wells 31/5-2 and 31/2-1 observed herein (Table 3.4).

Table 3.5 List of horizons interpreted within the GN10M1 3D seismic volume in this study. Comments on boundary character based on the log response are obtained from NPD Fact pages and well-log information from the injection well (31/5-7) (well log data courtesy of Equinor ASA, Total, and Shell). Reflectors picked in Gassnova (2012), Sundal et al. (2016), and Whipp et al. (2014) are listed.

Seismic horizon	**Reflector pick**	**Reflection Quality**	**Reflector pick in Gassnova (2012)**	**Reflector pick in Sundal et al. (2016)**	**Reflector pick in Whipp et al. (2014)**	**Comments on upper boundary character**
Top Brent Group	Trough	Strong, continuous	S-crossing	S-crossing	Trough	Decrease in acoustic impedance at the transition from the Lower Heather Formation claystones to sandstones of the Tarbert Formation.
Top Upper Drake Formation	Peak	Strong, disrupted	S-Crossing	Trough	Trough*	Gradual decrease in gamma-ray and sonic-log from the Etive Formation sandstones to more clay-rich Upper Drake Formation.
Top Lower Drake Formation	Trough	Very strong, continuous	Trough	-	-	Sharp decrease in acoustic impedance in the transition into the more clay-rich primary seal (i.e., the Lower Drake Formation).
Top Cook Formation	Peak	Strong, continuous	Z-crossing	S-crossing	-	Increase in acoustic impedance from the clay-rich primary seal to the sand-rich Cook Formation.
Top Johansen Formation	Trough	Weak, disrupted	S-crossing	S-crossing	-	Decreasing gamma-ray values at the transition from Upper Amundsen Formation to the Johansen Formation.
Top Statfjord Group	Trough	Strong, continuous	Z-crossing	S-crossing	Trough	Sharp decrease in gamma-ray at the transition from fully marine mudstones of the Lower Amundsen Formation to Statfjord Group sandstones

*A ‘near Top Dunlin (Drake) Formation’ is interpreted in Whipp et al. (2014).

Horizon interpretation, surface modelling, and analysis have been divided into seven stages in this study (Figure 3.20A–G). First, the target horizons were interpreted from survey inlines and crosslines (Figure 3.20A). The horizons were interpreted at least every 10th inline and cross line, creating a raw geomodel with 120×250 m grid resolution. In areas with higher structural complexity or around faults of particular interest, a denser spacing interval of (2–5) was applied. In areas where the interpreted reflector becomes too thin to be identified (below the vertical resolution), the reflector below or above has been selected for simplicity. For example, for the Top Upper Drake Formation in the hanging wall of the Tusse Fault Zone and the Top Johansen Formation in a small area 2 km east of injection well 31/5-7. A helpful technique when interpreting complex areas is to flatten the seismic on the interpretations. This vertically shifts the seismic image to a horizontal datum representing the basin geometry at the time of deposition and was applied in areas with higher structural complexity. Furthermore, the footwall of the Tusse Fault Zone represents an area with poor seismic at the eastern extent of the GN10M1 survey. To select accurate reflectors, 2D lines and correlation with nearby wells (31/6-1 and 31/6-2) were applied.

The grid created from the interpreted inlines and crosslines, creates a framework of the interpreted surfaces (Figure 3.20B). This framework was then autotracked to fill in the un-interpreted areas and create a continuous surface (Figure 3.20C). In this study, autotracking was performed with a confidence of no less than 60%. If the autotracked interpretations showed signs of interpretation errors, the gridded interpretations were revised or the line spacing was decreased to provide a more geologically valid interpretation. When the autotracked horizon interpretations were of satisfactory quality and geological validity, they were converted to gridded surfaces and displayed as time-structure maps (Figure 3.20D). All surfaces were made with a 10 x 10 grid increment spacing oriented to the projection system (UTM 31N), and areas within the study area with missing data (i.e., gaps in the autotracking, Figure 3.20C) were interpreted across.

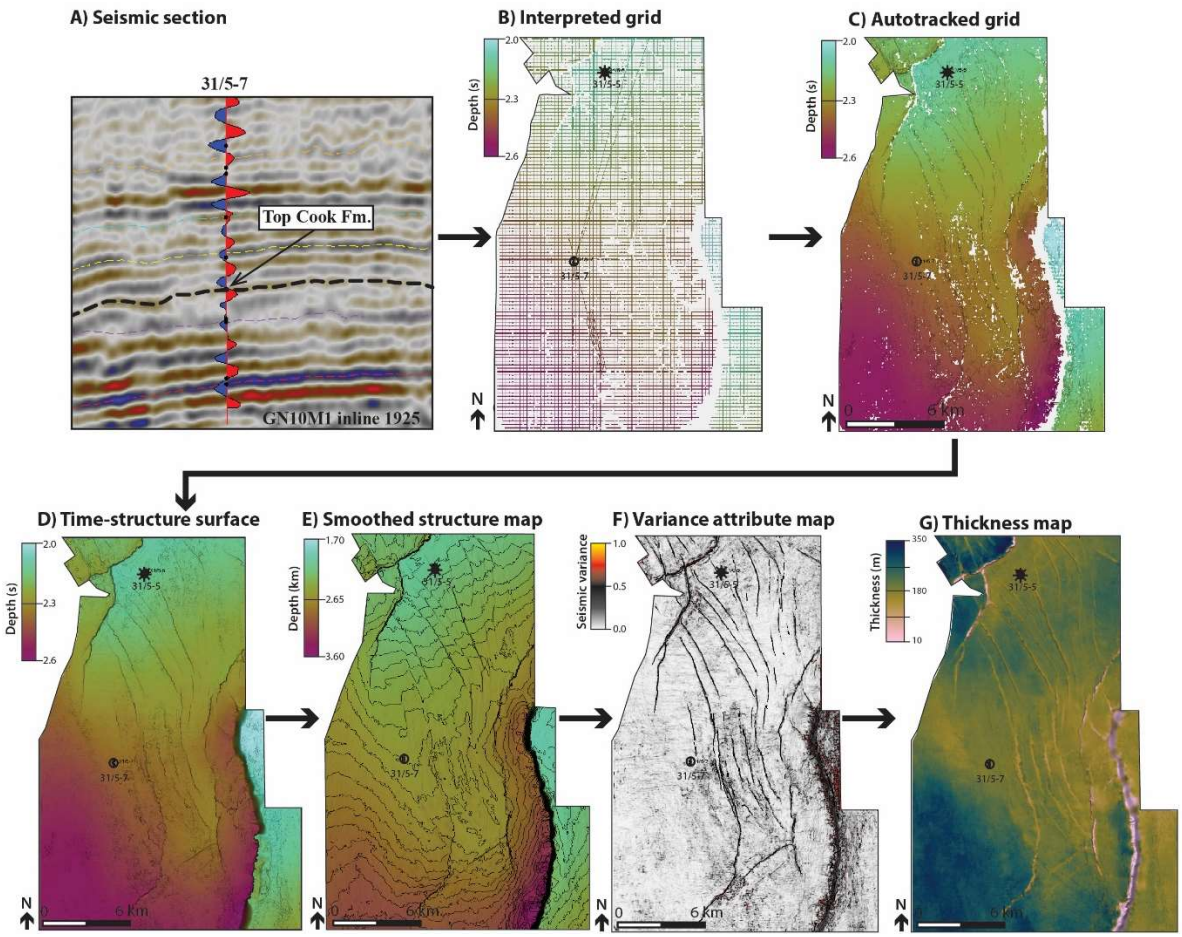

Figure 3.20 Diagram illustrating the seven stages in horizon interpretation using top Cook Formation as an example: A) interpretation in GN10M1 inline 1925, B) interpreted grid, C) autotracked grid, D) time-structure map, E) depth converted and smoothed structure map with contour lines (spacing 50 meters), F) variance attribute map with fault polygons, and G) thickness map of the bulk storage. Figure B-E is made using the 'hawaii' color scale, while figure G is made using the 'batlow' color scale from Crameri et al. (2020).

The time-structure surfaces were then depth converted to present the data on a more intuitively understandable scale (Figure 3.20E). Areas with poor seismic quality or complex reflectors can lead to irregularities in the surfaces and were reduced by using an operation called 'smoothing' (Figure 3.20E). Smoothing the surfaces can result in inaccuracies and should be applied with caution. Herein, the smoothing was not applied for more than three iterations with a filter width of three. The edited surfaces were revisited in seismic cross-section to assure that the smoothing did not remove important geological features and that the resulting surface still validated the geology of the subsurface.

To better visualize structural features, a seismic attribute map called variance was generated in Petrel (Figure 3.20F). A seismic attribute is a derivative of basic seismic measurements and can be related to time, amplitude, frequency, and attenuation measurements (Brown, 1996). The seismic attributes can be extracted along a horizon or summed over a window. In this study, variance attributes were generated for the entire 3D seismic volume, as well as along the interpreted surfaces. In Petrel the variance attribute measures the trace-to-trace variance in the seismic signal (Petrel E&P Software Platform, 2015). The variance attribute is useful in that it will highlight areas where there is little continuity of

the individual traces (i.e., faults and other boundaries; Bahorich and Farmer, 1995). Herein, variance maps were primarily used in fault interpretation (sub-section 3.3.3) and to assess the fault interaction styles.

The final step in the horizon interpretation workflow was to create thickness maps (Figure 3.20G). The thickness maps (i.e., isochron maps) are made by measuring the vertical thickness between two depth-structure surfaces and provide information that can be used to interpret variations in sediment accumulation, migration of depocenters because of tectonics, and depositional environments. Thickness maps are particularly important for assessing the presence of the CO_2 storage complex. As a final remark, horizon and fault interpretations are two mutually dependent processes and are, therefore, often organized in an iterative process.

3.3.3 Fault interpretation

As a reminder, this study aims to create a structural geomodel of the Aurora storage site, assess spatial and temporal evolution of faults, assess the presence of across-fault seals, and discuss gross rock volumes of potential structural closures. It has been shown that the fault interpretation strategy can influence the assessment of fault geometries (throw, strike, and dip) and the presence of across-fault seals (e.g., Manzocchi et al., 2010; Cunningham et al., 2020; Michie et al., preprint). Therefore, considerable effort was put forth into the fault interpretation by performing the following three steps.

The first step in the fault interpretation was to create a 3D variance volume using the GN10M1 survey. As previously mentioned, the variance attribute highlights areas where the seismic traces have large lateral and vertical variations (e.g., faults and lineaments; Petrel E&P Software Platform, 2015). The variance attribute volume was used to view time-slices and vertical-slices before performing fault interpretations. Moreover, time-slices of the variance attribute volume were used to estimate the vertical and lateral extent of the faults within the study area and to interpret their interaction style.

The second step was to interpret 2D fault sticks in seismic (Figure 3.21A). In seismic cross-sections, faults are visible because they represent areas where reflectors, and therefore successions, have been displaced. How accurately the fault geometry can be resolved in seismic data depends on the resolution (i.e., throw less than 7.5 m will not be visible within the GN10M1 volume; e.g., Manzocchi et al., 2010). To best visualize and interpret faults from seismic sections, lines (i.e., inlines, crosslines, or composite lines) oriented approximately perpendicular to the fault strike were prioritized. A total of 69 faults have been interpreted herein, with an inline/composite spacing between 2–5 (50–125 m), close to the optimum spacing of 100 m (Michie et al., preprint). Fault tips are interpreted with a smaller spacing (1–2) to map the complete resolvable lateral extent. A complete list of fault attributes is provided in Appendix 2.

The third step was to create 3D fault planes using the 2D fault sticks (Figure 3.21B). In Petrel, the 3D fault planes were generated automatically using the interpreted 2D fault sticks. While in Move, the software used in fault modelling, the 3D fault planes were generated manually (sub-section 3.3.3). Viewing the 2D fault sticks in a 3D visualization window was also used to quality check a fault interpretation. Any sharp spikes or jogs observed in the 3D fault plane could be erroneous, and the interpretation in a seismic cross-section window was revisited. Because all interpreted 2D fault sticks will be transferred into Move, two requirements must be met when mapping within Petrel. First, it is important to include sufficient interpretation points along a given 2D fault stick. This is because only the interpreted points will be transferred from Petrel to Move where a new 3D fault surface will be created. Second, hard-linked fault segments must be interpreted to cross each other in Petrel because intersection or linkage lines (branch lines) will be created in Move where fault segments are hard-linked.

3.3.4 Fault modelling

To assess vertical and lateral variations in throw and across-fault seals, fault modelling must first be performed and is the next step in the technical workflow (Figure 3.17). The fault modelling was performed using PETEX Move (v.2020.1), and as such all surfaces and fault interpretations were transferred from Petrel to Move, using the Move link for Petrel. Interpreted grids and autotracked horizons were transferred as points, and faults were transferred as 2D fault sticks. In total approximately 2200 2D fault sticks (69 faults), six interpretation grids, and six autotracked horizons were exported from Petrel to Move. Eight of the faults were used in fault throw- and juxtaposition analysis while five were used in membrane seal analysis (sub-section 3.3.5).

In Move, new 3D fault surfaces were created by Delaunay triangulation using the imported 2D fault sticks. The new 3D fault surface in Move was then compared to the 3D fault surface in Petrel to make sure the fault shapes were similar, and that they were structurally valid (Figure 3.21B and C). Intersection lines or branch lines were then created where fault segments were hard-linked with a larger fault. This was achieved by using the ‘split’ tool in Move.

To perform fault modelling, the lithology, age, and thickness of the stratigraphic units must be assigned between the interpreted horizons (Table 3.6). This information was obtained from injection well 31/5-7. It is important to note that the lithology has been oversimplified considerably for the purpose of fault modelling, and that information from the clay-rich Upper and Lower Amundsen Formation was not included in the model.

Table 3.6 Table of intervals, age, thickness, assigned rock type, and comments on lithology. Ages and lithology were obtained from NPD fact pages and Marjanac and Steel (1997). The age of the primary seal is estimated based on information from NPD fact pages. The thickness of the intervals was obtained from well 31/5-7 (data courtesy of Equinor ASA, Total, and Shell).

Intervals	**Age (Ma)**	**Thickness (31/5-7)**	**Assigned rock type**	**Comments on lithology**
Brent Group	168.3–166.1	86 m	Mixed sand	Sandstones, siltstones, and shales with subordinate coal beds.
Upper Drake Formation	~170–168.3	128 m	Mixed sand	Silty shales, coarsening upwards with increasing amount of siltstone and sandstone interbeds.
Primary seal unit	174.1–~170.0	53 m	Mudstone	Predominately clay-rich interval.
Secondary storage unit	182.7–174.1	57 m	Sandstone	More-or-less clean sandstones, with some heterolithic intervals. Predominately mudstones in the lower parts (Upper Amundsen Fm.).
Primary storage unit	190.8–182.7	116 m	Sandstone	Sandstones with thin calcite cemented streaks. Predominately mudstones in the lower parts (Lower Amundsen Fm.).
Statfjord Group	–190.8	-	Mixed sand	Mudstones interbedded with siltstones, sandstones, and limestones

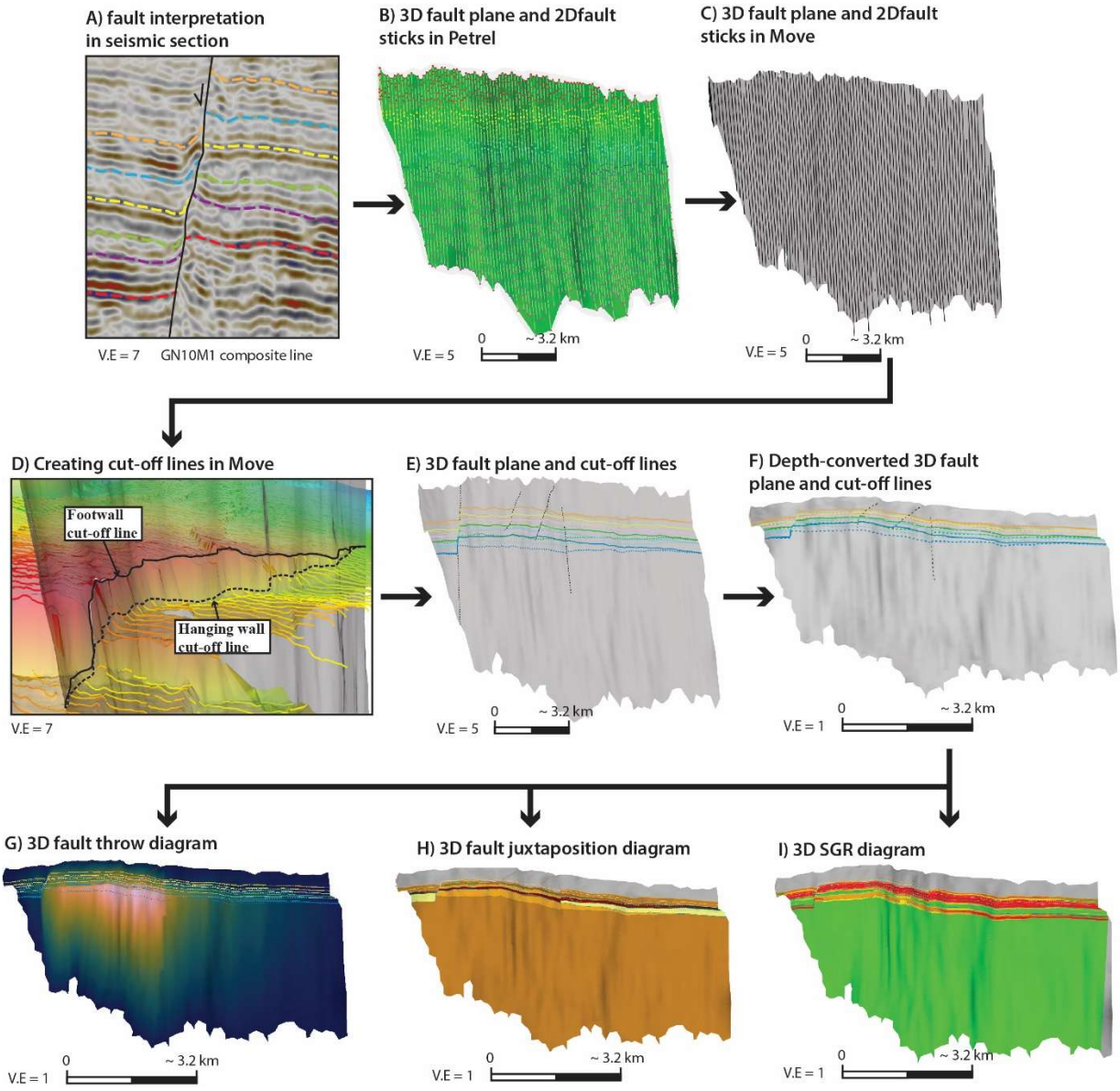

Figure 3.21 Illustration of the main stages in (A-C) fault interpretation, (D-F) fault modelling, and (G-I) fault analysis. A segment of the Svartalv Fault Zone is used as an example in the workflow. The cut-off lines and fault diagrams are presented and discussed in more detail in chapter 4. The 'batlow' color bar by Crameri et al. (2020) is used to display fault throw in figure G. Note the different vertical exaggerations used for the depth-converted fault.

To assess spatial and lateral variations in throw, the cut-off line method was applied. This method is commonly used when creating Allan diagrams to assess the presence of fault juxtaposition and membrane seals (e.g., Bretan et al., 2011; Deng et al., 2017; Mulrooney et al., 2020). Cut-off lines represent the intersection of a stratigraphic surface and a fault surface (Figure 3.21D). Normal faults have a hanging-wall cut-off line located below the footwall cut-off line, while the opposite is true for reverse faults.

Cut-off lines can however be challenging to create, and their quality depends on the detail and accuracy of the interpreted surface. In other words, higher certainty/quality of the interpreted surfaces created in Petrel, results in higher certainty/quality in the cut-off lines created in Move. In an attempt to ensure

high quality and predictable results, a similar method for creating cut-off lines proposed by Mulrooney et al. (2020) was favored over using automatic cut-off generation via the Move software. This method involves using the raw horizon interpretation grid alone, or in combination with the autotracked grid, and manually creating the cut-off lines by snapping the line to points at the intersection of the horizon interpretation and the fault plane (Figure 3.21D).

A smaller line spacing (25-100 m) is recommended when creating cut-off lines to avoid losing geological features close to the fault surface (Michie et al., preprint). By using the autotracked grid in combination with the horizon interpretation, a smaller line spacing (between 25–250 m) could be used when creating the cut-off lines. As opposed to that used in the horizon interpretation, which was every 10^{th} line, resulting in a line spacing of 250 m in inline direction and 125 m in crossline direction. Then, a horizontal plane was extended through this manually drawn cut-off line, and the final cut-off lines were generated where the horizontal plane intersects the targeted fault surface. This method prevents seismic artifacts (e.g., chaotic seismic reflectors) and extreme or erroneous structural orientations near the fault plane (e.g., transverse folding or drag geometries with dips >45°) from influencing the cut-off placement without dishonoring the raw seismic and horizon data (Mulrooney et al., 2020).

It is important to quality check the cut-off lines as they are made. To do this, corresponding seismic lines were simultaneously visualized in Petrel. This was especially important when the interpreted surface was difficult to trace due to areas with poor seismic quality. Cut-off lines that appeared erroneous, for example, if the hanging-wall cut-off line was located above the footwall line (indicating reverse movement), were reviewed using the seismic data and revised based on horizons of higher confidence. This often occurred near the fault tips where the fault throw is close to the vertical resolution. Manually editing the final cut-off lines should be performed with care and the seismic should be revisited to assure they are geological valid.

Finally, the in-house velocity model was used to depth-convert the fault interpretations and cut-off lines. Depth conversion of faults is important because it will reveal the true geometry and structure of the faults and, as a result, are better suited for across-fault seal assessment (e.g., Lyon et al., 2004). The modelled fault and cut-off lines, created using the time-migrated seismic data (before depth-conversion), were compared to the depth-converted fault and cut-off lines, to ensure that they were similar (Figure 3.21F and E).

3.3.5 Fault analysis

To assess the spatial and temporal evolution of faults and the presence of across-fault seals and their influence on CO_2 migration, fault analysis was performed (Figure 3.17). This includes creating throw profiles, fault throw diagrams, juxtaposition diagrams, SGR diagrams, and 1D SGR triangle diagrams

(Figure 3.21G-I). The presence of membrane seals due to disaggregation, cataclasis, and cementation has not been analyzed directly as assessment of well cores was beyond the scope of this study, however, their effect on fluid migration is briefly discussed in sub-section 5.2.2.

To assess the validity of the interpreted faults and fault growth trends, a maximum throw vs. length plot was created (sub-section 3.1.1). Maximum throw and fault length measurements were obtained from the Top Cook Formation cut-off lines in Move and quality checked with the depth-structure map and fault polygons in Petrel. The measurements were then compared with global measurements from over 20 contributions compiled in Kim and Sanderson (2005) and extracted measurements from Whipp et al. (2014).

To assess lateral propagation and interaction styles, fault throw diagrams (Figure 3.21G) and throw vs. length profiles were created. The software Move was used to create the fault throw diagrams by measuring the vertical distance between the modelled footwall and hanging-wall cut-off lines. The extrapolated fault throw was set to calculate the mean linear trend if the fault tips out in an erosional surface up-section (the Northern North Sea Unconformity Complex). Otherwise, the extrapolated fault throw was set to be zero at the fault tips. Corresponding throw vs. length profiles were automatically generated in Move using measurements of lateral throw variations from the modelled cut-off lines.

To assess fault evolution and nucleation, throw vs. depth profiles were created (sub-section 3.1.1). These profiles were created by measuring the throw at each interpreted horizon in section view in Petrel and plotting it against its corresponding depth. The expansion indices of the interpreted successions were calculated, by dividing the hanging-wall thickness with its corresponding footwall thickness and plotted together with the throw and depth measurements. Seismic sections and thickness maps were applied to measure the thicknesses. Due to relatively small thickness variations across second-order faults, the following methods were implemented to provide as accurate measurements as possible; i) thickness of the hanging-wall and footwall units was measured away from areas with drag (areas not related to syn-depositional sedimentation), ii) the average of multiple measurements was used to reduce errors in measuring the hanging-wall and footwall thicknesses, and iii) cut-off lines in fault throw diagrams were used to quality check the measured expansion indices.

To assess the presence of juxtaposition seals and their influence on CO_2 migration, Allan diagrams (i.e., 3D juxtaposition diagrams; Figure 4.21H) were created. These diagrams were made in Move by using the modelled cut-off lines and highlighting areas where permeable storage units on one side of the fault are juxtaposed against variably permeable units on the other side of the fault. Each interpreted unit was assigned a lithology (Table 3.6), and each juxtaposition scenario was assigned a color. For example, sandstone on sandstone juxtaposition was highlighted by a yellow color while sandstone on mudstone juxtaposition was highlighted with a dark red color (Figure 3.21H). The resulting 3D juxtaposition

diagrams provided a simple, yet informative way to analyze how stratigraphic thickness variations affected the across-fault sealing potential.

The shale gouge ratio method was used in this study to assess the presence of across-fault membrane seals and their influence on CO_2 migration. This method was favored, over other algorithms, because it uses data from well logs to determine the presence of clay smear in the fault and can therefore include clay contributions from thin intra-horizon clay-rich units that have not been interpreted in seismic (e.g., the Upper Amundsen Formation). Furthermore, this method provides for easy comparison with previous work using the same method (e.g., Bretan et al., 2011; Gassnova, 2012; Wu et al., 2021).

The volumetric clay fraction (V_{cl}) was derived using the gamma-ray log of four wells (31/5-7, 31/5-2, 31/2-1, and 31/2-5; Figure 3.22). For each targeted fault, two wells were used to include information from the hanging wall and footwall of the fault. To derive the V_{cl}, cut-off values were first assigned to the gamma-ray logs in the four wells to represent 100% shale (shale-line) and 0% shale (sand-line), similar to the method presented in Lyon et al. (2005). The shale-line was picked based on the gamma-ray values in formations that are known to have high clay content (i.e., the Draupne Formation and the Lower Drake Formation). And the sand-line was picked based on the low gamma-ray values in the storage formations (i.e., the Cook Formation and the Johansen Formation). Because the cut-off values are user-defined values, a precautionary principle was applied were higher sand- and shale-line cut-off value was favored so that the calculated SGR values show a higher risk scenario (i.e., less conservative values) rather than a lower risk scenario (Table 3.7).

Table 3.7 Wells and corresponding cut-off values used to create SGR diagrams and 1D SGR triangle diagrams.

Well	Company (year)	Shale-line cut-off value (API)	Sand-line cut-off value (API)
31/5-7	Equinor ASA (2019)	130	60
31/5-2	Saga Petroleum AS (1983)	106	60
31/2-1	Norske Shell AS (1979)	100	40
31/2-5	Norske Shell AS (1981)	115	50

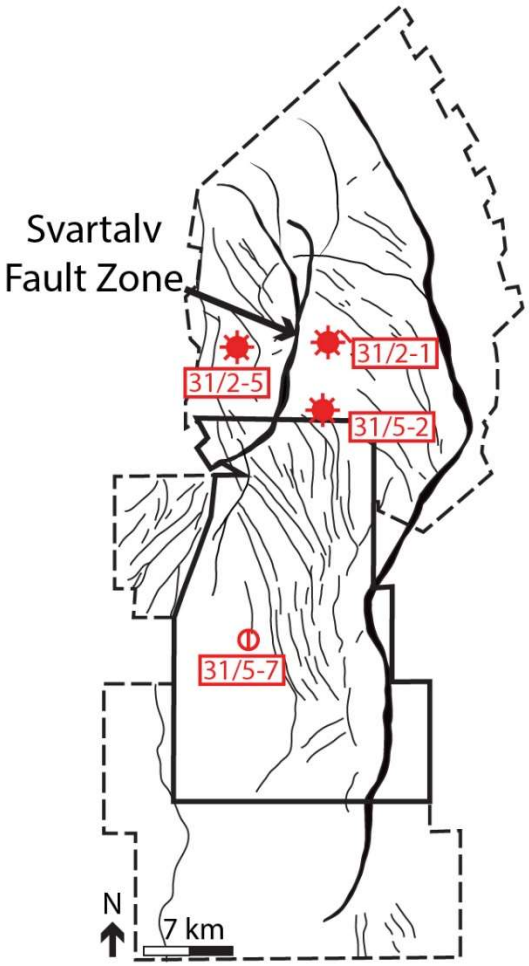

Figure 3.22 Fault heave map showing the location of wells used for SGR calculation. Well 31/5-7, 31/5-2, and 31/2-1 is in the footwall of the large scale Svartalv Fault Zone, while well 31/2-5 is in the hanging wall.

Once the cut-off values were assigned to each well, Move automatically calculates the SGR values and creates SGR diagrams (Figure 4.21I). The parameters were set so that it calculates the mean V_{cl} from both sides of a fault and by selecting the V_{cl} log alignment to be proportional to the thickness so that the log data is preserved when projecting it onto a fault plane. The calculated SGR values were also displayed using the 1D triangle diagram by Knipe (1997), which was used to assess how the gamma-ray logs from each of the four wells contributed to the presence of membrane seals. In both the 1D SGR triangle diagrams and the SGR diagrams, SGR values <15% are assumed to represent 'leaking' faults and colored green, SGR values between 15–20% represent the threshold between 'leaking' and 'sealing' faults and colored yellow, while SGR values >20% represent 'sealing' faults and colored orange to red (Figure 3.21I) based on the calibrated cut-off values in Yielding (2002).

Finally, the results from the across-fault seal assessment were used to discuss plausible CO_2 migration pathways and gross rock volumes of fault-bound traps in a fill-to-spill scenario. Plausible migration pathways were created perpendicular to the dip of the depth-structure maps in combination with information from the across-fault seal assessment. The volume of structural closures was calculated in

Petrel by using the ‘volume below surface (constant level)’ operation, assigning the depth of the seal, and applying a contour line polygon, at the same depth, as a border. Calculations of CO_2 column heights that can be supported by a fault (sub-section 3.1.2) was beyond the scope of the study, however, estimated of such column heights are provided from the Troll West field in Bretan et al. (2011). Limitations related to the methods applied are further discussed in section 5.3.

4 Results

The main objectives of this study are to establish a structural framework of the Aurora storage site, assess the spatial and temporal evolution of faults, assess the presence of across fault seals, and discuss plausible CO_2 migration pathways and gross rock volumes of relevant structural closures. In this chapter, presented results inform the structural and stratigraphic architecture (section 4.1) as well as the nature of across-fault juxtaposition and membrane seal potentials (section 4.2) within the study area. Figures showing seismic data in section 4.1.1 and 4.1.2 are presented in the time-domain (i.e., where elevation depth is given in ms TWT), all other figures (e.g., depth-structure maps, thickness maps, fault throw diagrams, juxtaposition diagrams, and SGR diagrams) show depth converted data (i.e., where elevation depth is given in meters).

4.1 Structural and stratigraphic characterization

Structural and stratigraphic architecture are presented and described to provide information about the structural evolution and how faults will influence migration of CO_2 within the study area (discussed in chapter 5). Interpreted seismic cross-sections, depth-structure maps, and thickness-maps are used to describe the architecture of the storage complex. Faults are presented in cross-sections and in fault heave polygons maps to show their vertical and lateral geometry, respectively. Based on measurements of throw, trace length, and depth, the mapped faults are categorized into two different fault populations. For the purpose of this study, faults located up-dip from the injection well will encounter the migrating CO_2. Therefore, detailed throw analysis for three faults located north of the well is presented.

4.1.1 The Aurora storage site

The study area is located in the northernmost part of the Aurora License (EL001) and is bordered by two large, N–S trending fault zones, the Tusse and the Svartalv fault zones (Figure 4.1). These fault zones have been extensively mapped and discussed in previous publications (e.g., Bretan et al., 2011; Bell et al., 2014; Whipp et al., 2014; Duffy et al., 2015; Sundal et al., 2016). Three seismic cross-sections are presented in Figure 4.2, Figure 4.3, and Figure 4.4 and provides an overview of the gross structural and stratigraphic architecture. The seismic sections show time migrated data which images down to -4000 ms TWT.

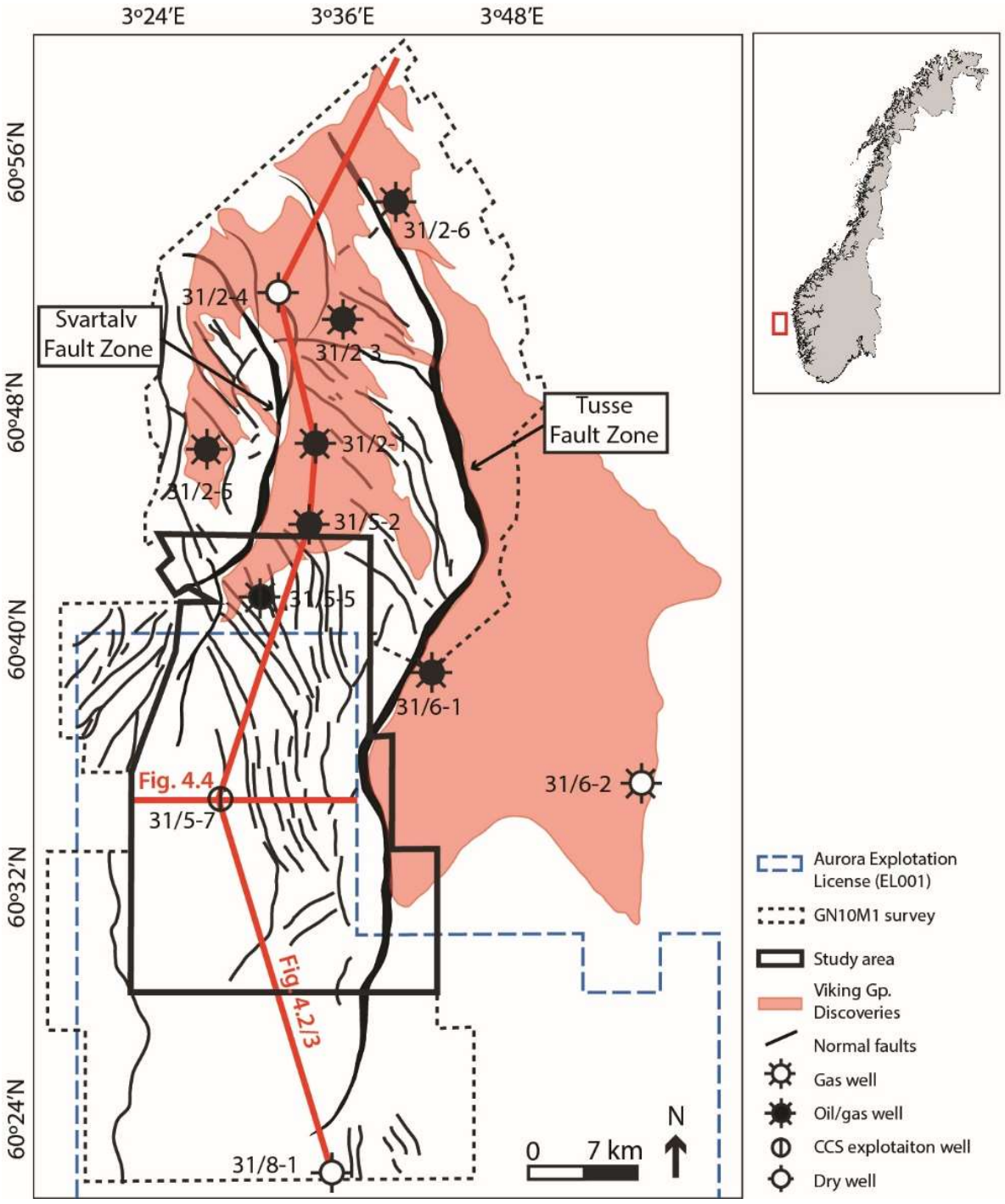

Figure 4.1 Map showing the main structural elements within the study area and location of seismic lines presented in Figure 4.2, 4.3, and 4.4. Normal faults are presented by heave polygons derived from the Top Cook Formation surface (i.e., top bulk storage). Note that only wells that are used in this chapter are included in the figure.

An approximately N–S trending composite line is displayed in Figure 4.2. This composite line intersects four wells (31/8-1, 31/5-7, 31/2-1, and 31/2-4) and extends through the entire GN10M1 seismic survey (Figure 4.1). The wells do not penetrate the crystalline basement, therefore an simplified interpretation

of the basement-cover contact is based on high amplitude reflectors that are observed in the deeper part of the GN10M1 seismic survey and 2D seismic lines (see Figure 3.14).

In the seismic section (Figure 4.2), the Jurassic Dunlin Group (i.e., the target group for CO_2 injection and storage), Brent Group, and Viking Group overly each other conformably, show relatively little thickness variations and dip towards the south. In the southern part of the composite line, the groups are located at 2700–2100 ms TWT (~3360 m TVDSS). Towards the north, between wells 31/2-1 and 31/2-4, the groups are shallower and are located at approximately 2250–1500 ms TWT (~2350 m TVDSS). Towards the north of the section, the Troll West field flatspot is observed within the Viking Group. The overlying Cretaceous the Cromer Knoll and Shetland groups unconformably onlaps the Jurassic successions. In contrast to the Jurassic successions, the Cretaceous successions show large thickness variations, with thickening towards the south and thinning towards the north. The Cenozoic Rogaland, Hordaland, and Nordland groups are present as thick units with some undulations in thickness.

Multiple faults are visible within the composite line in Figure 4.2. These faults intersect the Jurassic Dunlin, Brent, and Viking groups and form multiple horst and graben structures. The majority of the faults within the composite line are restricted to the Upper Triassic to Jurassic (or the Northern North Sea Unconformity Complex; NNSUC) successions and do not penetrate the basement (i.e., thin-skinned faults). The composite line also intersects a segment of the Tusse Fault zone in two places (Figure 4.1). The Tusse Fault Zone tips out up-section in Paleogene successions and displaces the basement down-section (i.e., thick-skinned fault).

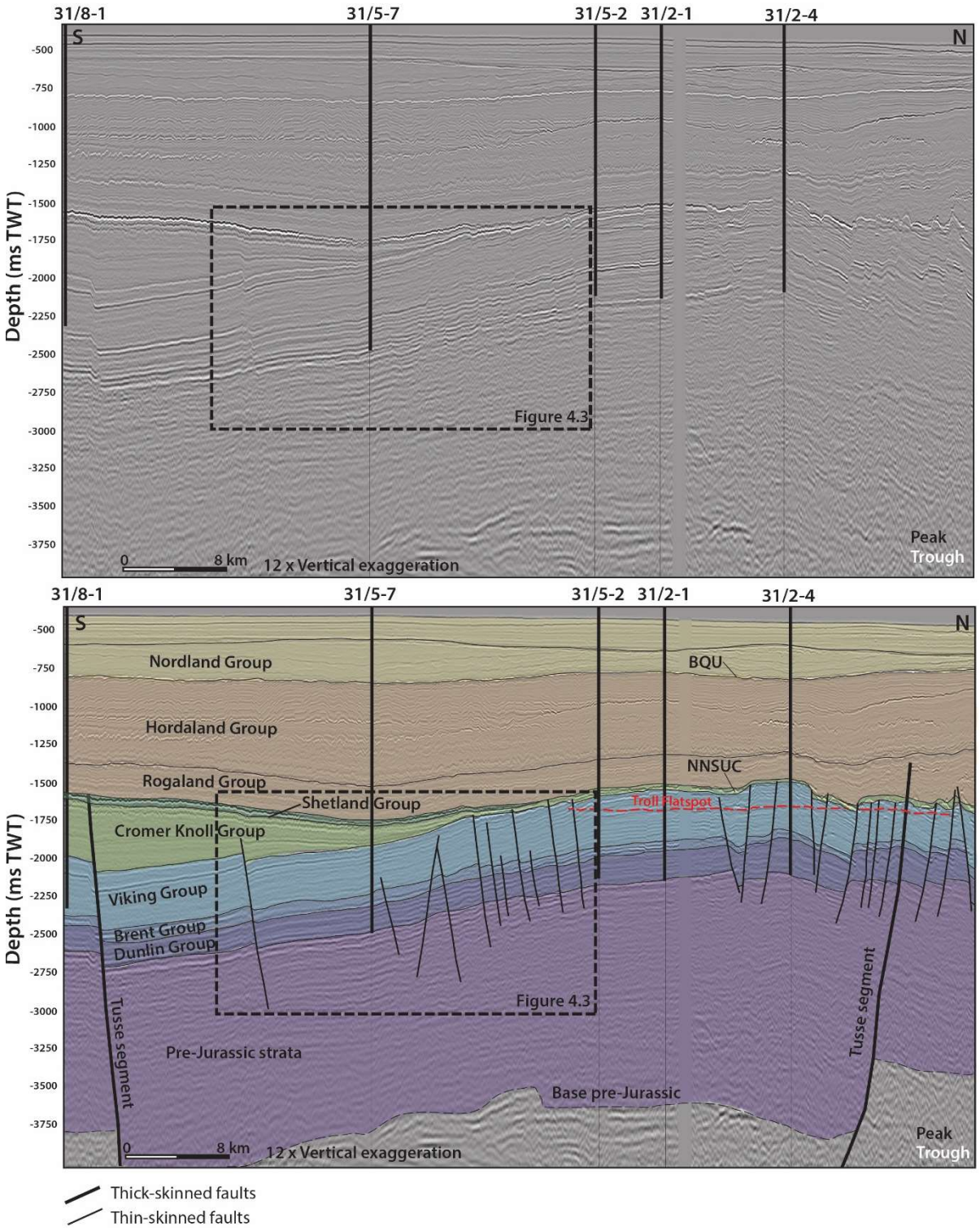

Figure 4.2 Composite seismic section trending approximately N–S through the GN10M1 survey. The composite section intersects four wells: 31/8-1, 31/5-7, 31/5-2, and 31/2-4. The location of the cross-section is illustrated in Figure 4.1. Abbreviations: BQU = Base Quaternary Unconformity, NNSUC = Northern North Sea Unconformity Complex.

An expanded view of the formations within the Dunlin Group is presented in Figure 4.3 where reflections are generally continuous and characterized by high amplitudes. The reflections become

slightly weaker and less continuous just north of well 31/5-7, where multiple thin-skinned faults intersect the units.

As previously stated in sub-section 3.3.2, five units have been interpreted in this study; the primary storage unit (i.e., Lower Amundsen Formation and Johansen Formation), the secondary storage unit (i.e., Cook Formation and Upper Amundsen Formation), the primary seal unit (i.e., the Lower Drake Formation), the Upper Drake Formation and the Brent Group (Figure 4.3). In the N–S composite seismic section, these units are buried between 2200–2600 ms TWT (2400–2800 m TVDSS) where they are intersected by well 31/5-7 and dip gently towards the south (~2°). Compared with the overlying Cretaceous successions, the formations within the Dunlin Group show little thickness variations, although some variations are apparent. The secondary storage unit, for example, shows some thinning towards the south and the north.

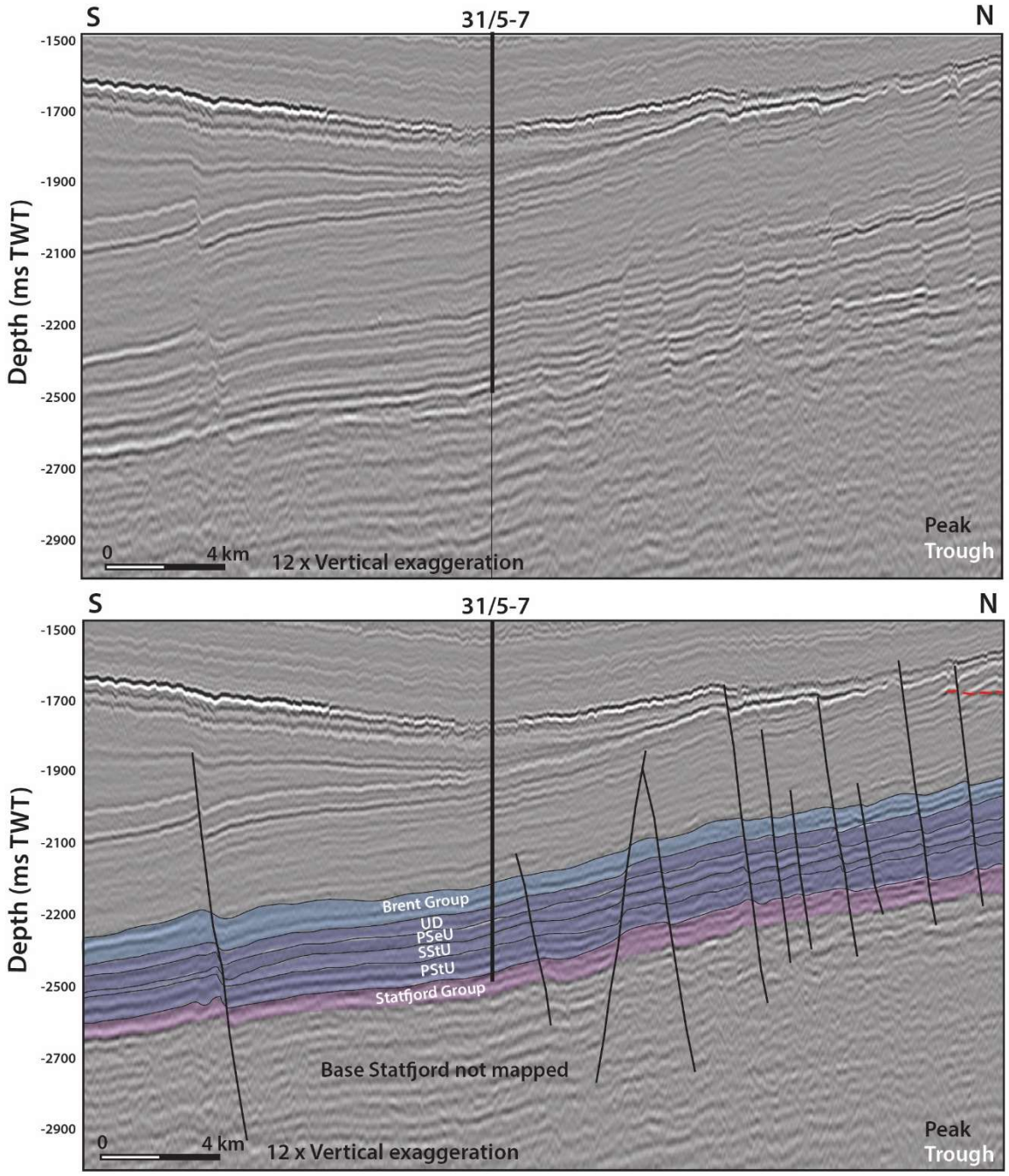

Figure 4.3 Close-up of the N–S trending composite line in Figure 4.2 showing the interpreted units within the study area. The base of the Triassic Statfjord Group has not been interpreted, therefore the thickness of the Statfjord Group is only indicative. Location of the cross-section is illustrated in Figure 4.1. Abbreviations: UD = Upper Drake Formation, PSeU = primary seal unit, SStU = secondary storage unit, PStU = primary storage unit.

A seismic inline is displayed in Figure 4.4 which trends E–W (perpendicular to Figure 4.3) and intersects injection well 31/5-7. Similar to observations in Figure 4.3, the secondary storage unit shows the largest thickness variations within the Dunlin Group, with thinning towards the west and the east. In Figure 4.4 the Triassic to Jurassic successions forms an anticline that is intersected by multiple thin-skinned faults which are concentrated at the crest. These thin-skinned faults extend into the Triassic successions down-section and do not intersect the successions above the NNSUC up-section. The

closest fault to well 31/5-7 is located approximately 1.9 km to the east and has a throw of 28 ms TWT (40 m) measured in the Top Cook Formation. Two thick-skinned west-dipping faults are present in the seismic inline. The thick-skinned Tusse Fault Zone is again present 9.2 km east of well 31/5-7 and has a throw of 420 ms TWT (820 m) measured in the Top Cook Formation in Figure 4.4.

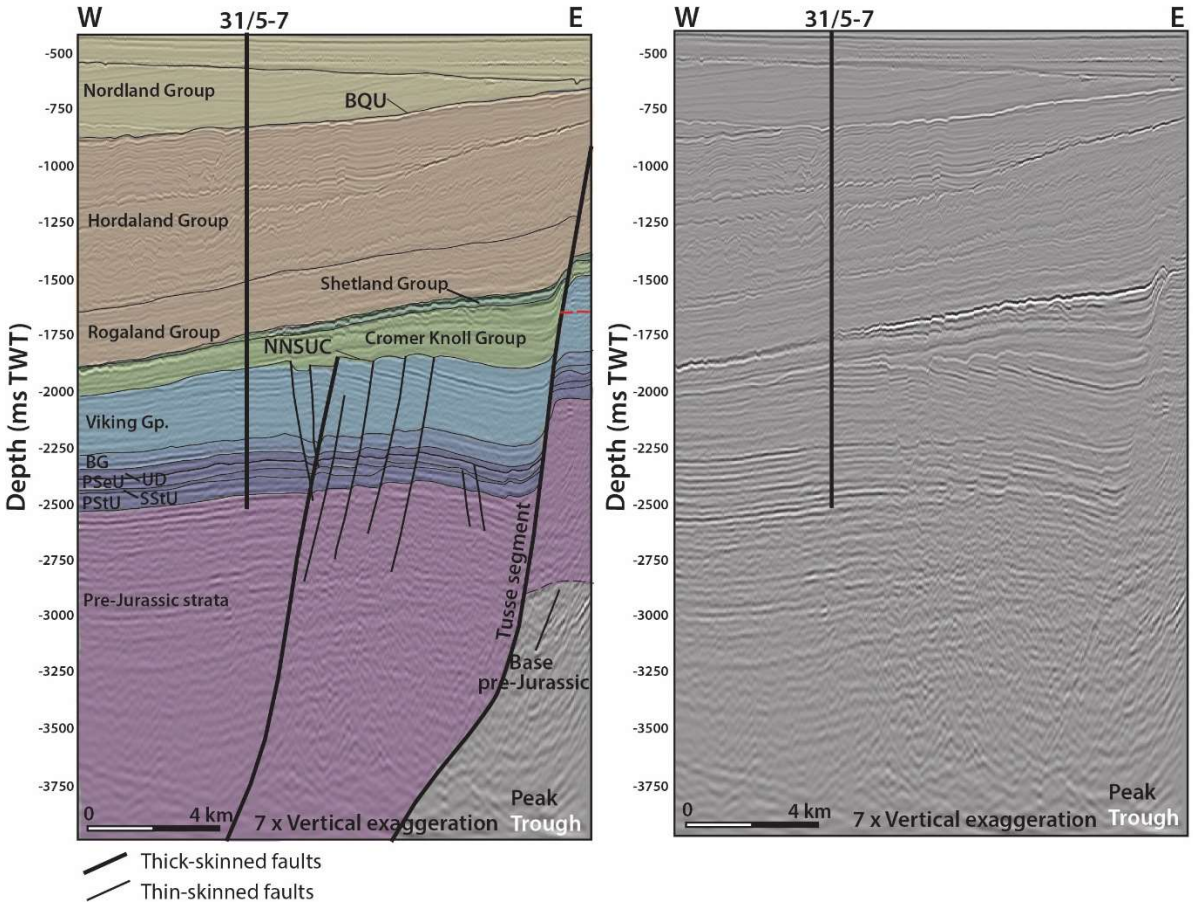

Figure 4.4 Seismic inline (1928 in GN10M1) trending E–W through the injection well (31/5-7). The location of the Troll flatspot (shown as a red dashed line) is visible within the Viking Group in the footwall of the Tusse segment. The location of the cross-section is illustrated in Figure 4.1. Abbreviations: BQU = Base Quaternary Unconformity, NNSUC = Northern North Sea Unconformity Complex, BG = Brent Group, UD = Upper Drake Formation, PSeU = primary seal unit, SStU = secondary storage unit, PStU = primary storage unit.

Below, the interpreted surfaces are presented in map-view in Figure 4.5 and Figure 4.6 and are used to describe the spatial distribution of faults and formations within the study area. These surfaces include the Top Statfjord Group, Top Johansen Formation, Top Cook Formation, Top Lower Drake Formation, Top Upper Drake Formation, and Top Brent Group. The surfaces have been depth converted and are therefore presented with meters as the vertical scale.

The interpreted surfaces are intersected and displaced by numerous faults which are concentrated in the northern and eastern parts of the study area (Figure 4.5). The Svartalv Fault Zone is present as three segments to the northwest while the Tusse Fault Zone is present in the southeastern part of the study area (Figure 4.5A). These faults have an N–S to NNE–SSW strike and are easy to identify in all the

extracted variance maps, however, the Svartalv Fault Zone appears to have a lower trace length up-section.

As seen in the variance maps, the injection well (31/5-7) was drilled in an area with a relatively low abundance of faulting. However, just 1.9 km east of the well, several predominately N–S striking faults intersect and displace the storage and seal units (highlighted in Figure 4.5B). These faults, located just east of the injection well, are generally curvilinear and isolated in map-view, but appear to form relay ramps with nearby faults (i.e., soft-linked faults; e.g., Larsen, 1988) and in cases form through-going faults (i.e., hard-linked faults). The extracted variance maps show that this area is more heavily faulted up-section (see variations in Figure 4.5A and Figure 4.5D).

Just 700 meters northeast of well 31/5-7, a single N–S striking fault with isolated fault tips is observed (Figure 4.5D). In the variance maps the fault is observed to intersect the Top Statfjord Group to Top Lower Drake Formation (Figure 4.5A to Figure 4.5D). Further north, multiple faults intersect the interpreted horizons. These faults have an approximately NW–SE strike and appear to interact, either by soft-linkage or hard-linkage, with two NNE–SSW to NE–SW striking segments of the Svartalv Fault Zone (highlighted in Figure 4.5C).

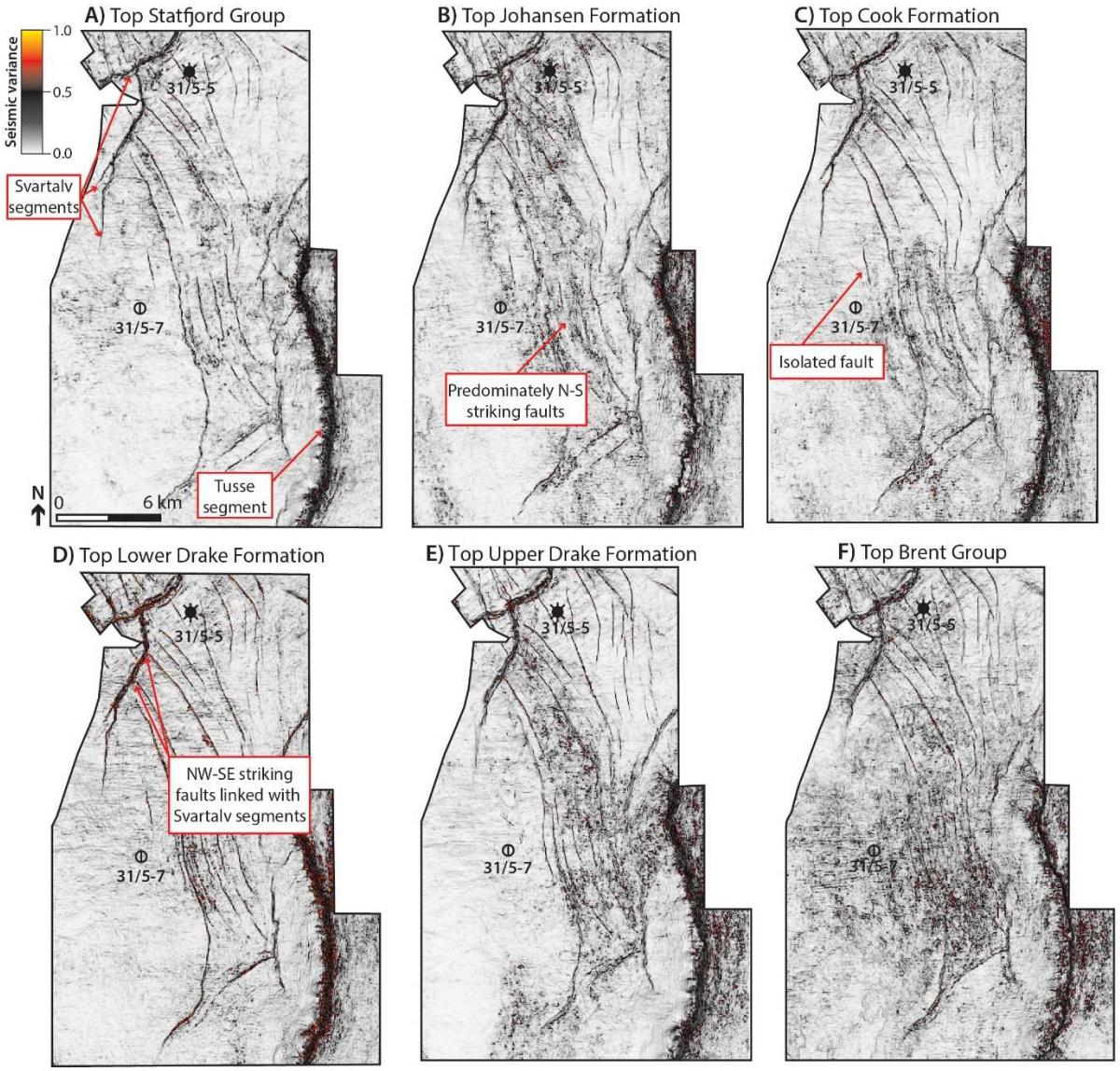

Figure 4.5 Variance seismic attribute maps showing structural features within the study area flattened on the six interpreted surfaces.

Depth-structure maps presented in Figure 4.6 show that all the interpreted surfaces have quite similar geometries, with the deepest areas located to the southwest and in the hanging wall of the Tusse fault. Along the hanging wall of the Tusse fault, multiple smaller-order transverse anticlines and synclines with wavelengths of 1–2 km and amplitudes of 50–80 ms TWT (150–200 m) are seen and exhibit E–W striking fold axis (highlighted in Figure 4.6A). East of the injection well (31/5-7), the surfaces become shallower creating a higher-order anticline with a wavelength of approximately 14 km and amplitude of 90 ms TWT (183 m). This anticline has an N–S striking fold axis and is intersected by multiple N–S striking faults. The shallowest areas are found in the northernmost part of the study area, in the footwall of two intersecting Svartalv segments.

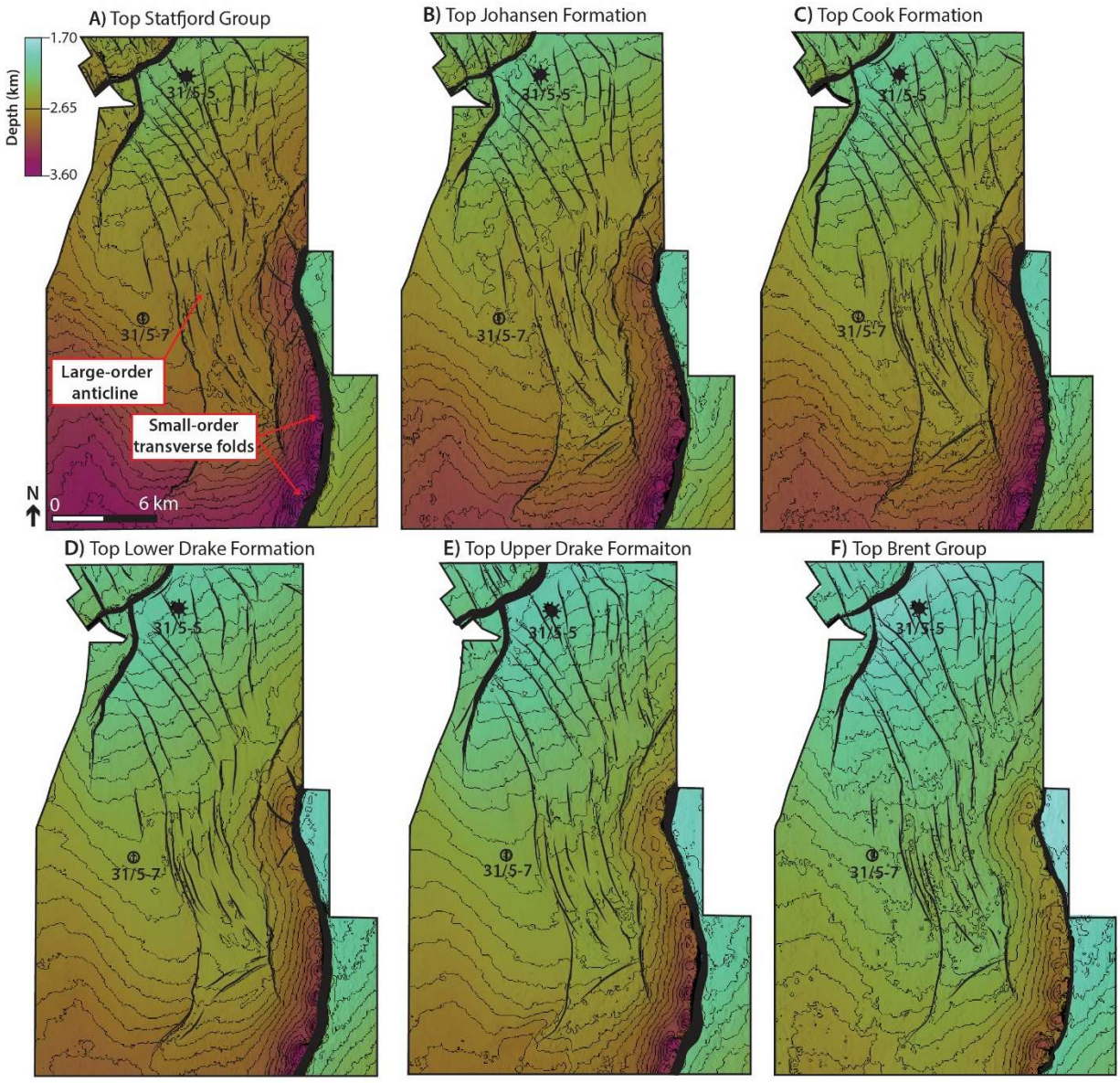

Figure 4.6 Depth-structure maps with contour line spacing of 50 meters. Location of higher- and smaller-order folds are shown in Figure 4.6A.

4.1.2 Target successions

Six thickness maps are shown in Figure 4.7 to Figure 4.12 and exhibit lateral thickness variations in the target successions. Thickness maps are presented accompanied by seismic cross-sections flattened on the respective horizons. The thickness maps, with exception of the Dunlin Group thickness map, are presented using the same color bar range (10–300 m). The maps are presented in depth-domain while seismic flattened and un-flattened sections are presented in time-domain. Measurements used to calculate the expansion index (E.I.) in the Dunlin and Brent groups are compiled in Appendix 1.

4.1.2.1 The primary storage unit

Herein, the primary storage unit primarily consists of the Johansen Formation and also contains the Lower Amundsen Formation (see sub-section 3.3.2). The primary storage unit thickness map shows that it is present throughout the study area (Figure 4.7A). The formation is thickest towards the southwest, where it reaches 300 meters. At the location of the injection well the thickness of the unit is approximately 130 meters, where the Lower Amundsen Formation measures 14 meters and the Johansen Formation measures 116 meters.

The primary storage unit becomes thinner and measures only 50 meters in thickness approximately 4 km northeast of the injection well. In the northern part of the study area, along the footwall of the Svartalv Fault Zone, the primary storage unit shows a relatively tabular thickness of approximately 130 meters. The unit is thickening in the hanging wall of the Svartalv fault segments (to 230–250 m), and towards the northeast within the study area (to 200–220 m). A flattened seismic NE–SW striking composite line is presented in Figure 4.7B to show the maximum thickness variations within the study area and the thinning that is present north of well 31/5-7.

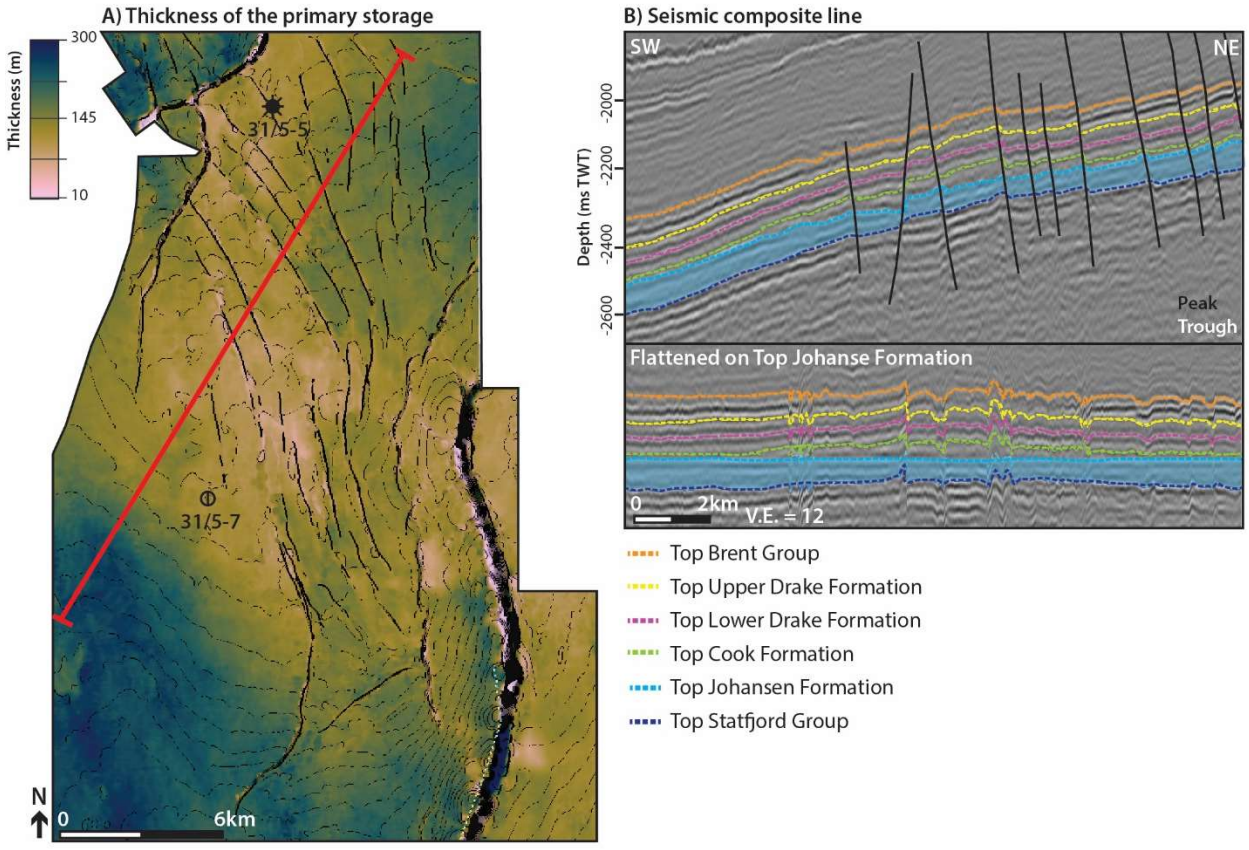

Figure 4.7 A) Thickness map of the primary storage unit with 50-meter contour line spacing. Faults are shown as heave polygons. B) Seismic composite line (top) and flattened on the Top Johansen Formation (bottom) illustrates the thickness variations from southwest to northeast. The location of the composite line is illustrated in the thickness map. Note that the thickness map is presented in depth-domain whereas the seismic composite section is presented in time-domain.

4.1.2.2 The secondary storage unit

Herein, the secondary storage unit is primarily comprised of the Cook Formation and also contains the Upper Amundsen Formation (sub-section 3.3.2; Figure 4.8). At the location of well 31/5-7 the secondary unit has a thickness of 64 meters, with the Cook Formation measuring 57 meters and the Upper Amundsen Formation measuring 7 meters. The secondary storage unit has an average thickness of 30 meters within the study area and reaches its maximum thickness (approximately 80–100 m) north of well 31/5-7. The aforementioned thickness variations are also observed in the flattened seismic composite line striking NE–SW through the study area (Figure 4.8B), with thinning towards the southwest and northeast, and thickening in the central part. This trend is the opposite of that observed in the underlying primary storage unit.

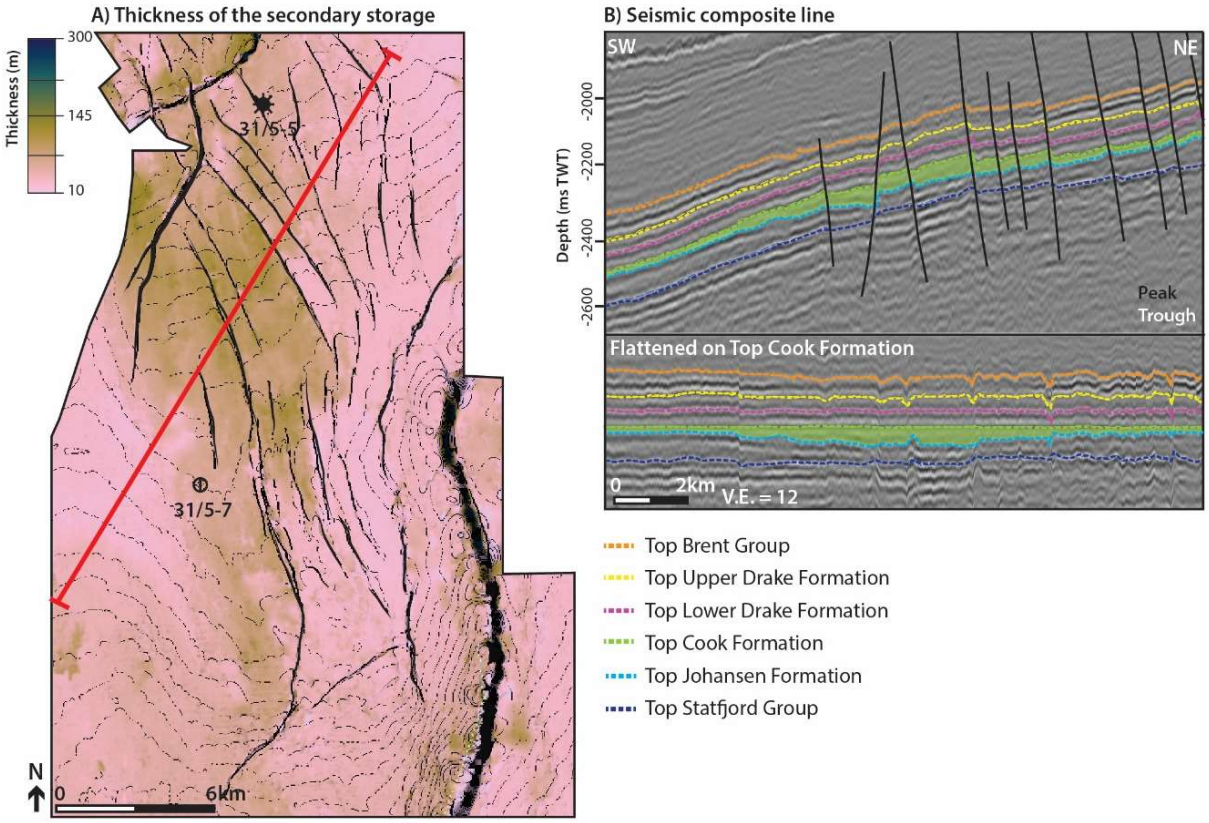

Figure 4.8 A) Thickness map of the secondary storage unit with 50-meter contour line spacing. Faults are shown as heave polygons. B) Seismic composite line (top) and flattened on the Top Cook Formation (bottom) illustrates the thickness variations from southwest to northeast. The location of the composite line is illustrated in the thickness map. Note that the thickness map is presented in depth-domain whereas the seismic composite section is presented in time-domain.

4.1.2.3 The primary seal unit

Herein, the primary seal unit comprises the lower part of the Drake Formation (i.e., the Lower Drake Formation) overlying the secondary storage unit, similar to Gassnova (2012). The thickness map in Figure 4.9A shows that the primary seal is present throughout the study area and has an average

thickness of 85 m. The unit is thickest to the southwest of the study area, where it measures 130–150 meters in thickness. The unit is thin towards the north and measures approximately 68 meters at the location of the injection well. Farther north, along the footwall of the Svartalv Fault Zone segments, the primary seal unit has a relatively constant thickness between 80–90 meters. The seismic inline presented in Figure 4.9 shows the variations in thickness east and west of injection well 31/5-7. On the horst east of well 31/5-7 the primary seal is observed to become thinner (to 60–70 m).

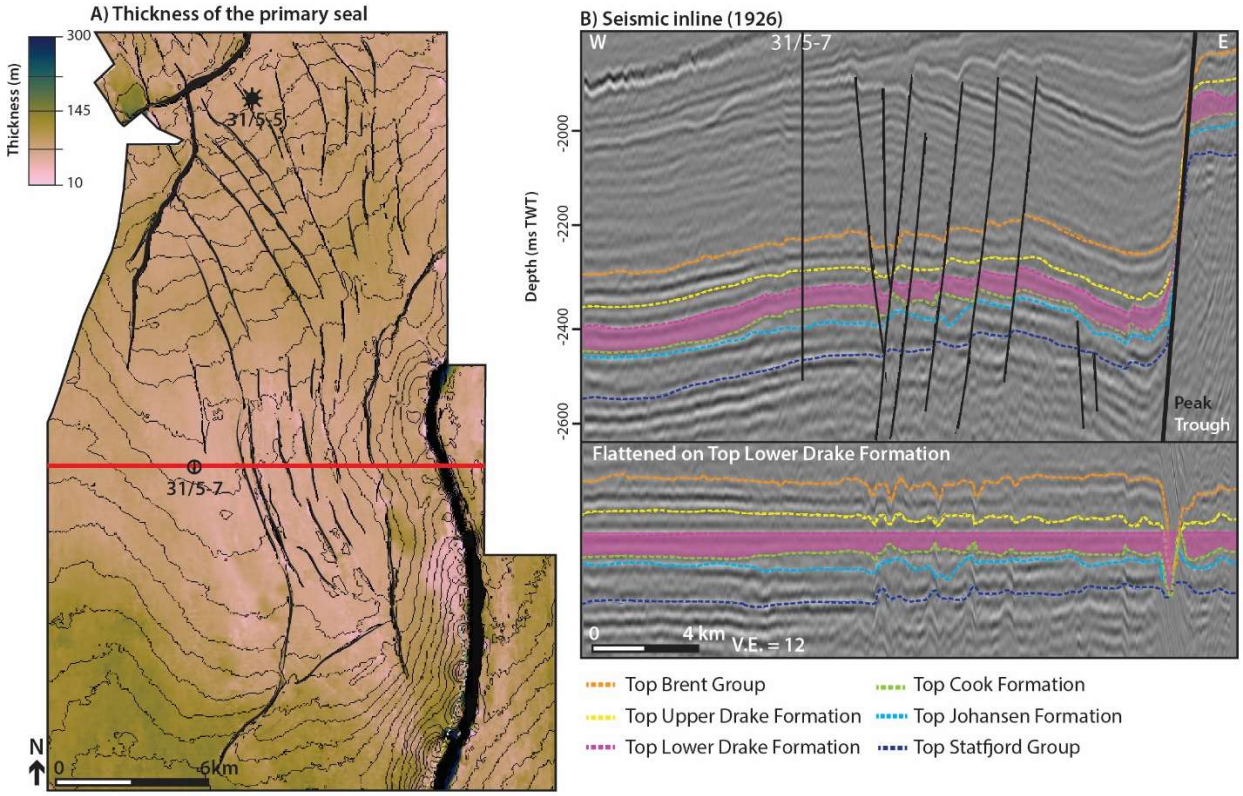

Figure 4.9 A) Thickness map of the primary seal unit with 50-meters contour line spacing. Faults are shown as heave polygons. B) Seismic composite line (top) and flattened on Top Lower Drake Formation (bottom) illustrates the thickness variations from east to west. The location of the composite line is illustrated in the thickness map. Note that the thickness map is presented in depth-domain whereas the seismic inline is presented in time-domain.

4.1.2.4 The Upper Drake Formation

The upper part of the Drake Formation is herein called the Upper Drake Formation, similar to Gassnova (2012). The Upper Drake Formation has an average thickness of 75 meters within the study area and at the location of the injection well (Figure 4.10A). The formation thickens towards the southwest, where it measures approximately 100 meters in thickness. An E–W striking seismic inline intersecting well 31/5-7 is selected to show that the Upper Drake Formation thins significantly, to between 30–40 meters, in the hanging wall of the Tusse Fault Zone segment (Figure 4.10B). This is partly due to the reflection selected for interpretation (see sub-section 3.3.2), and thus the thinning is slightly overestimated (~10–

15 m). Towards the north, in the footwall of the Svartalv Fault Zone segments, the Upper Drake Formation thickness is relatively tabular with thickness ranging between 70 and 80 meters.

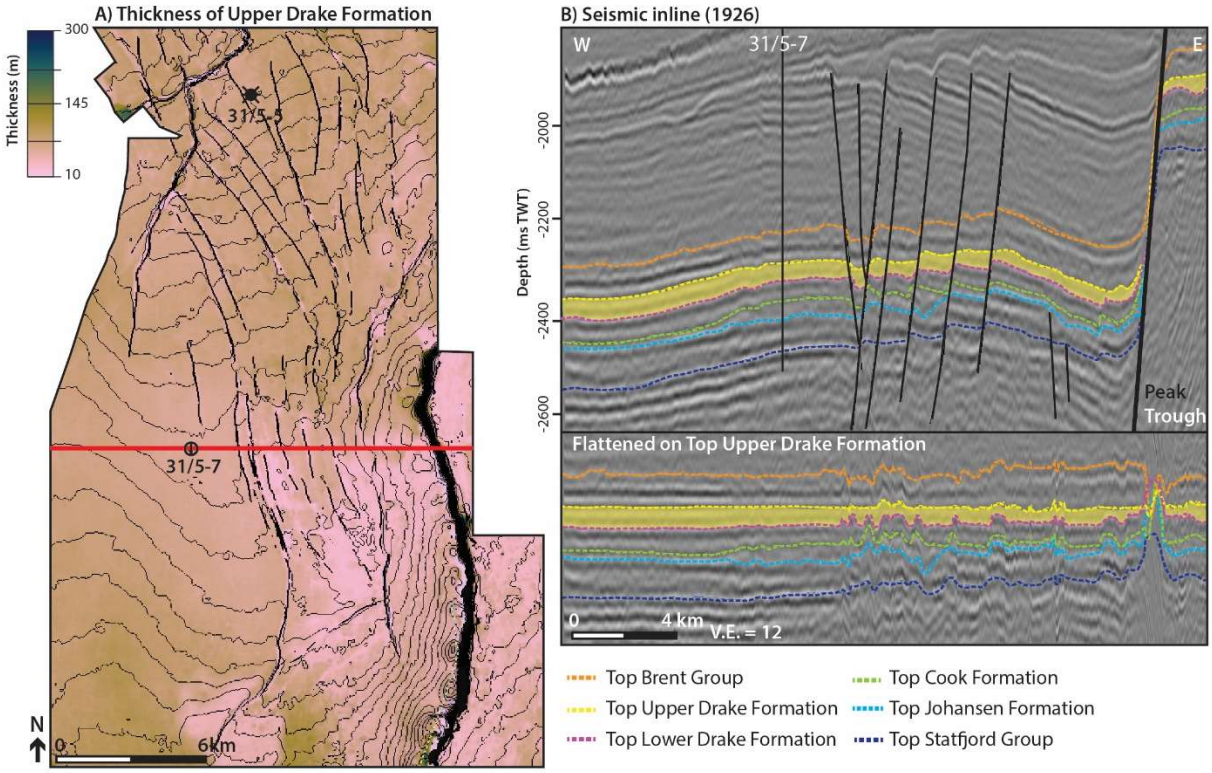

Figure 4.10 A) Thickness map of the Upper Drake Formation with 50-meters contour lines. Faults are shown as heave polygons. B) Seismic inline (top) and flattened on Top Upper Drake Formation line (bottom) illustrates the thickness variations from east to west. The location of the composite line is illustrated in the thickness map. Note that the thickness map is presented in depth-domain whereas the seismic is presented in time-domain.

4.1.2.5 The Dunlin Group

The thickness of the entire Dunlin Group is presented in Figure 4.11A. The group reaches a maximum thickness of approximately 600 meters to the southwest. In the hanging wall of the Tusse Fault Zone segment, the group is thickest to the south (440–450 m) and thins (to 290–300 m) northwards. In the southern part of the Tusse Fault Zone segment, the thickness of the Dunlin Group in the hanging wall is slightly thicker than the corresponding footwall (E.I. = 1.36). The Dunlin Group is thinnest (280–300 m) on the horst just east of the injection well. Further north, the group thickens (to 360–380) in the footwall of the Svartalv Fault Zone segments. Hanging-wall growth is also observed across the Svartalv Fault Zone segments (E.I. = 1.47), however little to no growth is observed across the thin-skinned faults.

A flattened composite line crossing the Svartalv Fault Zone, well 31/5-5, well 31/5-7, and the Tusse Fault Zone is created to show the thickness variations in seismic section (Figure 4.11B). While the growth in the hanging wall of Svartalv and Tusse is easy to distinguish in the thickness map, it is less obvious in the seismic composite line, in particular in the hanging wall of the Tusse Fault Zone.

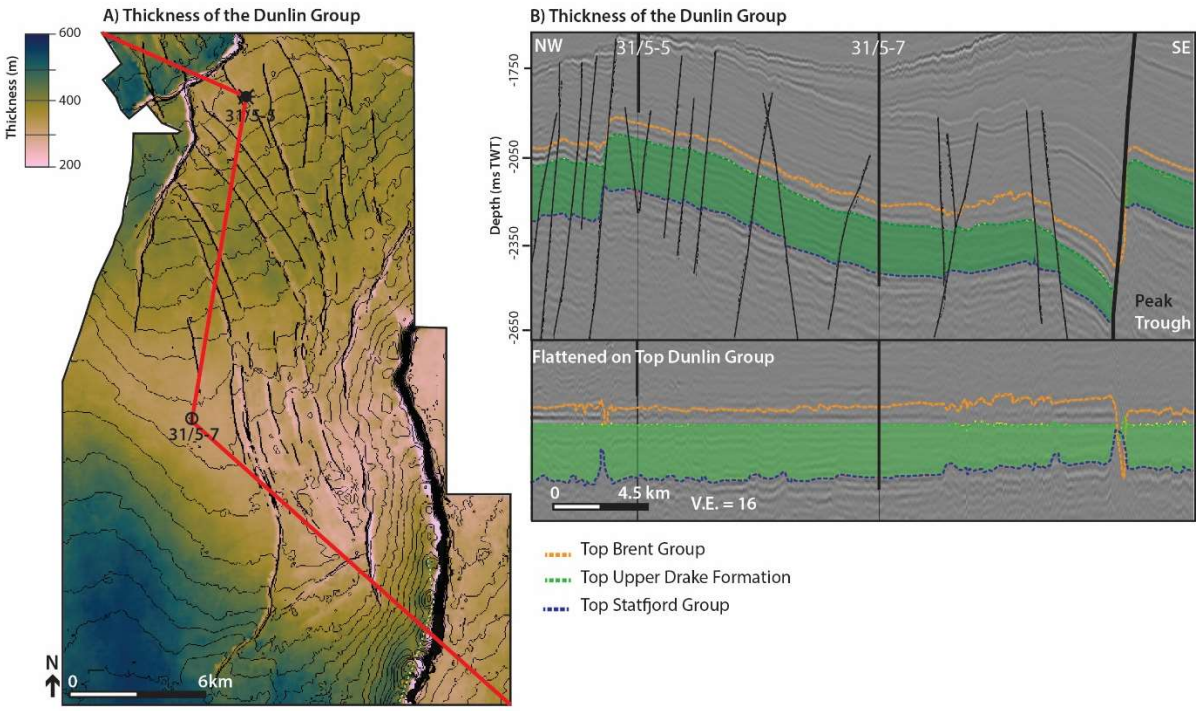

Figure 4.11 A) Thickness map of the Dunlin Group with 50-meters contour lines. Faults are shown as heave polygons. B) Seismic inline (top) and flattened on Top Dunlin Group (Top Upper Drake Formation; bottom) illustrates the thickness variations from northwest to southeast. The location of the composite line is illustrated in the thickness map. Note that the thickness map is presented in depth-domain whereas the seismic is presented in time-domain and that the thickness scale differs from the other thickness maps.

4.1.2.6 The Brent Group

The thickness of the Brent Group is presented in Figure 4.12A and is on average approximately 100 meters thick. Towards the north, the group thins to approximately 80 meters. Towards the southwest, in the hanging wall of the Tusse Fault Zone, the group becomes thicker and measures 250–260 meters. The Brent Group shows clear growth across the Tusse Fault Zone (E.I. = 3.00) and smaller growth across the Svartalv Fault Zone (E.I. = 1.14). In contrast, hanging-wall growth is difficult to distinguish across the thin-skinned faults. The same composite line presented for the Dunlin Group in Figure 4.11B is presented for the Brent Group (Figure 4.12B). The growth in the hanging wall of the Tusse Fault Zone is easy to distinguish in the flattened seismic composite line, while it is less obvious across the Svartalv Fault Zone.

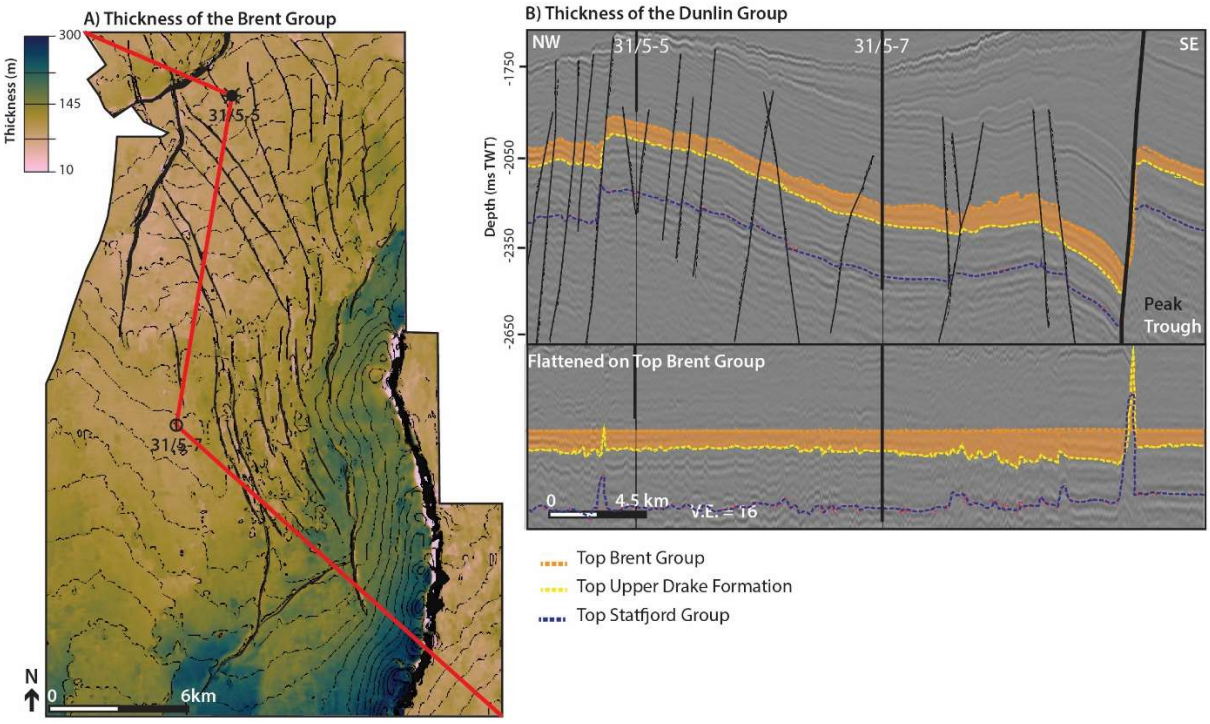

Figure 4.12 A) Thickness map of the Brent Group with 50-meter contour line spacing. Faults are presented as heave polygons. B) Seismic composite line (top) and flattened on Top Brent Group line (bottom) illustrates the thickness variations from northwest to southeast. The location of the composite line is illustrated in the thickness map. Note that the thickness map is presented in depth-domain whereas the seismic composite section is presented in time-domain.

4.1.3 Fault populations

In total 69 faults were mapped within the study area. The dip-direction, nature of linkage, and the vertical extent of faults that intersect the Top Cook Formation are illustrated in Figure 4.13. Based on basement-involvement, faults within the study area can be divided into two groups inspired by Gabrielsen (1984):

1) First-order faults that penetrate and displaces the basement-cover contact (i.e., thick-skinned faults).
2) Second-order faults that have no basement involvement (i.e., thin-skinned faults).

4.1.3.1 First-order faults

Six faults within the study area are considered first-order faults and displace the basement-cover contact by 1–3 km (measured in depth-converted 2D seismic lines). This includes three west-dipping segments of the Svartalv Fault Zone, here called Svartalv 1, Svartalv 2, and Svartalv 2.1 (Figure 4.13). In map-view, the Svartalv 1 extends out of the study area to the north and west and is a NE–SW striking fault with a concave-upwards geometry. The Svartalv 1 segment is cross-cut by Svartalv 2 which is N–S to NNE–SSW striking. Svartalv 2 has a trace length of 12.2 km (measured in the Top Cook Formation).

At the center of the fault, a 2.5 km long splay (Svartalv 2.1) with NNE-SSW strike is located in the hanging wall of Svartalv 2. Up-section, the Svartalv 1 and Svartalv 2 faults extend into Cenozoic successions, while Svartalv 2.1 is more limited and tips out within Jurassic successions (Figure 4.13B).

Two first-order hard-linked faults (F10 and F11) are located just 2 km east of injection well 31/5-7 (Figure 4.13). The two faults are west-dipping, predominately N–S striking, and have trace lengths of 7.7 and 5.6 km, respectively. The F10 fault has a concave-upwards geometry, while the F11 has a concave-downwards geometry. Up-section, these faults extend into Cretaceous successions. Towards the southeast of the study area, a segment of the Tusse Fault Zone is present (Figure 4.13). This section extends out of the study area to the north and south and dips towards the west. Up-section, the Tusse fault segment extends into Cenozoic successions.

The mean orientation of the first-order faults presented in Figure 4.14A is N–S (182°), however, a spread in strike orientations is present reflecting the undulating along-strike variations as seen in map view. The first-order faults are, on average, approximately 7 km long measured in the Top Cook Formation surface. The maximum throw of the first-order faults measured in the Top Cook Formation shows large variations from 43 to 940 meters, with the Tusse Fault Zone segment having the largest throw (see table in Appendix 2 for a complete list of measurements). The first-order faults also show changes in dip angle with depth, for example, the Tusse and Svartalv 2 faults have dips of 58-65° in the Jurassic successions which decreases to 28–30° in the crystalline basement (i.e., listric geometry established in depth-converted data).

4.1.3.2 Second-order faults

Sixty-three faults mapped within the study are classified as second-order faults as they show no basement-involvement. These faults are displayed in Figure 4.13 and are predominately located between the Svartalv Fault Zone and the Tusse Fault Zone segments. In contrast to the first-order faults, the second-order faults have no preferential dip-direction, with 39 faults dipping towards the NE, E, or SE and 24 dipping towards the NW, W, or SW (see Appendix 2; Figure 4.13). The mean orientation of the second-order faults is N–S (351°), which is slightly anti-clockwise to the first-order faults (Figure 4.14A). However, both the strike and fault trace shape changes within the study area. To the east of the injection well, the second-order faults are predominately N–S striking and concave towards the hanging wall of the Tusse fault segment. While further north and northwest, the strike changes and become predominately NW–SE striking, and the faults are concave towards the southwest and the Svartalv Fault Zone segments.

The vertical extent of the second-order faults is significantly shorter than the first-order faults. Down-section, the second-order faults tip-out in the Upper Triassic to Jurassic successions while up-section

the faults mainly terminate within the Jurassic or Cretaceous (or NNSUC) successions. On average the trace lengths of the second-order faults are approximately 3.6 km long and the majority of the faults have a maximum throw, measured within the Top Cook Formation, between 15–50 meters. In contrast to the first-order faults, the second-order faults are generally planar and steeply dipping (55–60°) in cross-section.

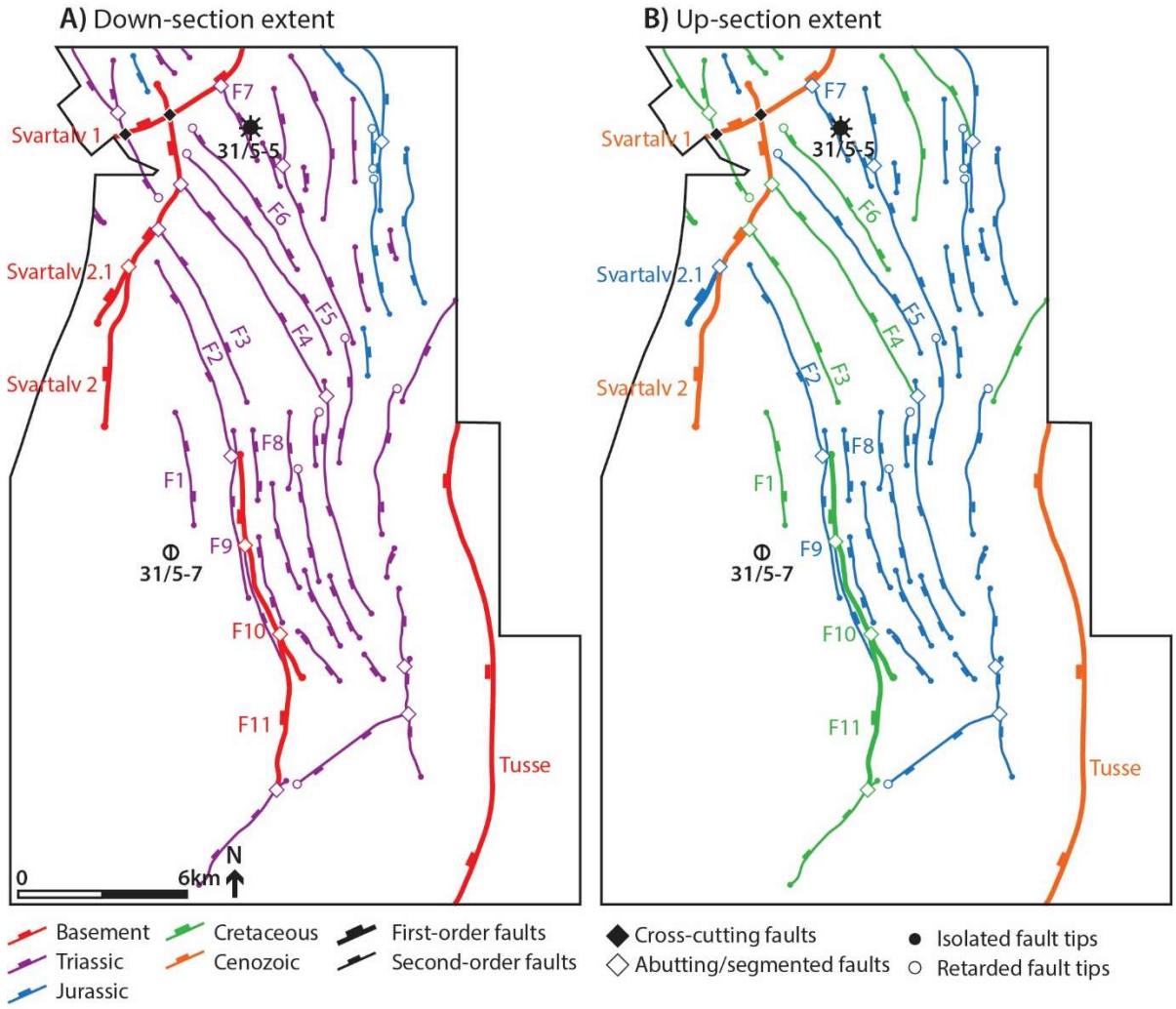

Figure 4.13 Maps showing faults intersecting the Top Cook Formation. Color codes show A) the down-section extent of faults, B) the up-section extent. The nature of fault interaction is indicated as cross-cutting, abutting, isolated, or retarded inspired by Duffy et al. (2015).

4.1.3.3 Fault interaction styles

Four types of fault tip interaction styles, similar to Duffy et al. (2015), are analyzed in this study; i) cross-cutting, ii) isolated or non-interacting fault tips, iii) abutting fault tips, and iv) retarded fault tips (Figure 4.13). The interaction styles are estimated based on extracted variance attribute maps, assessment of the Top Cook Formation depth-structure map, and throw vs. length profiles (presented in sub-section 4.1.4.2). Approximately 50% of the faults within the study area are isolated and show no

interaction with nearby faults. The most common fault tip interaction style (approximately 30%) is abutting. For example, north of injection well 31/5-7 several approximately NW–SE striking second-order faults are interpreted to abut against the first-order Svartalv 1 and Svartalv 2 faults. Approximately 20% show evidence that the propagation of the fault has been retarded by nearby faults and cross-cutting relationships are only observed in two locations, where Svartalv 1 and Svartalv 2 cross-cut each other, and where a southwest dipping second-order fault cross-cut the Svartalv 1 fault (Figure 4.13).

4.1.4 Fault throw

In the following sub-sections a maximum throw vs. length plot, fault throw diagrams, throw vs. length, and throw vs. depth profiles are presented for three faults and provide evidence for the spatial and temporal evolution of faults (section 5.1). These faults are selected due to their position relative to the injection well (i.e., they are positioned up-dip) and because they are representative of a number of faults within the study area. Fault throw diagrams and throw vs. length profiles for six additional faults in the proximity of the injection well are compiled in Appendix 3.

4.1.4.1 Maximum throw vs. length

Measurements of maximum throw values and trace lengths of the corresponding faults provide information that informs the spatio-temporal evolution of fault populations within the study area (further discussed in sub-section 5.1.2). The maximum throw and trace length measurements are plotted against global measurements of normal faults in Figure 4.14. The measurements were taken from the Top Cook Formation surface, which represents the upper extent of the bulk storage for CO_2 injection. Faults that extend beyond the study area have been excluded from plots (Figure 4.14). See table in Appendix 2 for a complete list of measurements used in the plot.

The maximum throw and trace length measurements for the two fault populations (i.e., first-order and second-order faults) are plotted together with their corresponding trendlines. A linear trendline is selected and they are set to intersect (0, 0), similar to Whipp et al. (2014). The slope of the trendlines corresponds to the ratio of maximum throw and trace length. Measurements of maximum throws and trace lengths obtained from the Top Brent Group in the Troll West and East fields (Whipp et al., 2014), are plotted together with the measurements from this study. The maximum throw vs. trace length measurements for the faults within this study area show a broadly linear trend when plotted in the log-log graph and conform to trends seen in the Troll West and East fields (Whipp et al., 2014), and global measurements from normal faults, from for example the Timor Sea in NW Australia (Walsh et al., 2002), the San Rafael Swell in Utah (Krantz, 1988), and the Krafla fissure in Iceland (Opheim and Gudmundsson, 1989; Figure 4.14B).

The first-order and second-order fault populations show slightly different trends in Figure 4.14B. The first-order faults have overall higher values of maximum throw and trace lengths and almost twice as high maximum throw vs. trace length ratio compared to the second-order faults. The faults from the Troll West and East field plot with a trendline between the first- and second-order faults populations within this study area (Figure 4.14B). Moreover, the faults plot with a generally large spread from the 1:10 to the 1:100 line, which conforms to the spread seen in the Troll East and West field and the global measurements.

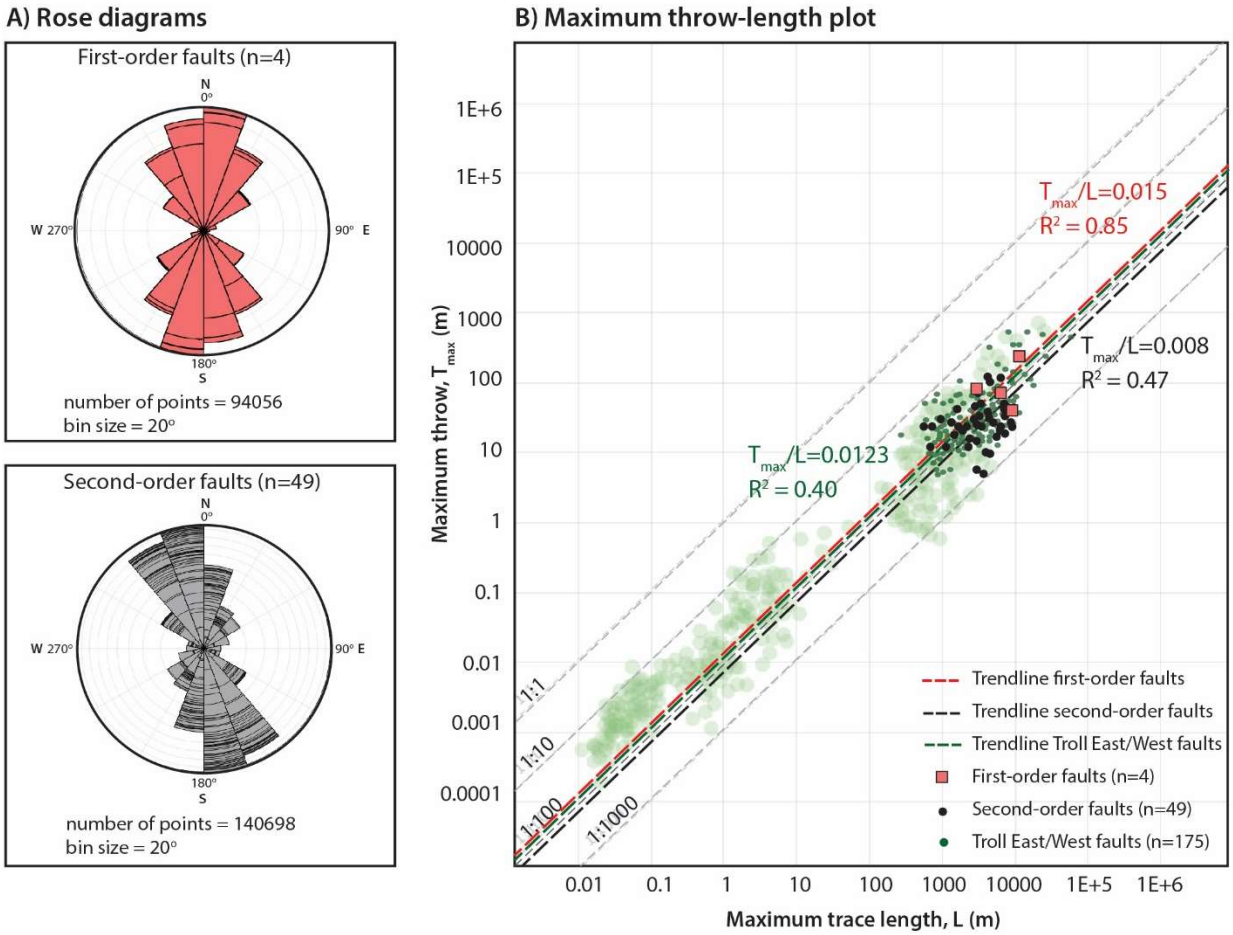

Figure 4.14 A) Rose diagrams showing the orientation of first-order and second-order faults. Fault orientations have been sorted into bins of 20° and plotted in terms of the frequency of a particular orientation. The number of points correlates to the number of individual mesh polygons. B) Maximum throw vs. trace length plot for first-order and second-order faults and associated trend lines and equations. Measurements from the Troll East and West fields (Whipp et al., 2014) and associated trendline and equation are highlighted in solid green. Global measurements of normal faults are obtained from PETETX Move (v.2020.1) likely compiled from Kim and Sanderson (2005). The global measurements are plotted as blurred green circles.

4.1.4.2 Lateral throw variations

Lateral variations in throw are analyzed to determine the spatial evolution of faults intersecting the study area and provide more firm interpretations on fault interaction styles (e.g., Duffy et al., 2015). The significance of the results is discussed in sub-section 5.1.2. As previously mentioned, three faults

were selected to perform a detailed throw analysis (Figure 4.15). This includes the first-order Svartalv 2, which potentially represents the western border of CO_2 migration. The F3 fault was selected because it is representative of multiple approximately NW–SE striking faults that interact with the Svartalv 1 and Svartalv 2 segments up-dip from the injection well 31/5-7. The F1 fault was selected due to its proximity to the injection well (31/5-7). Fault throw diagrams and throw vs. length profiles are presented in this section for these three faults, while six additional faults are included in Appendix 3.

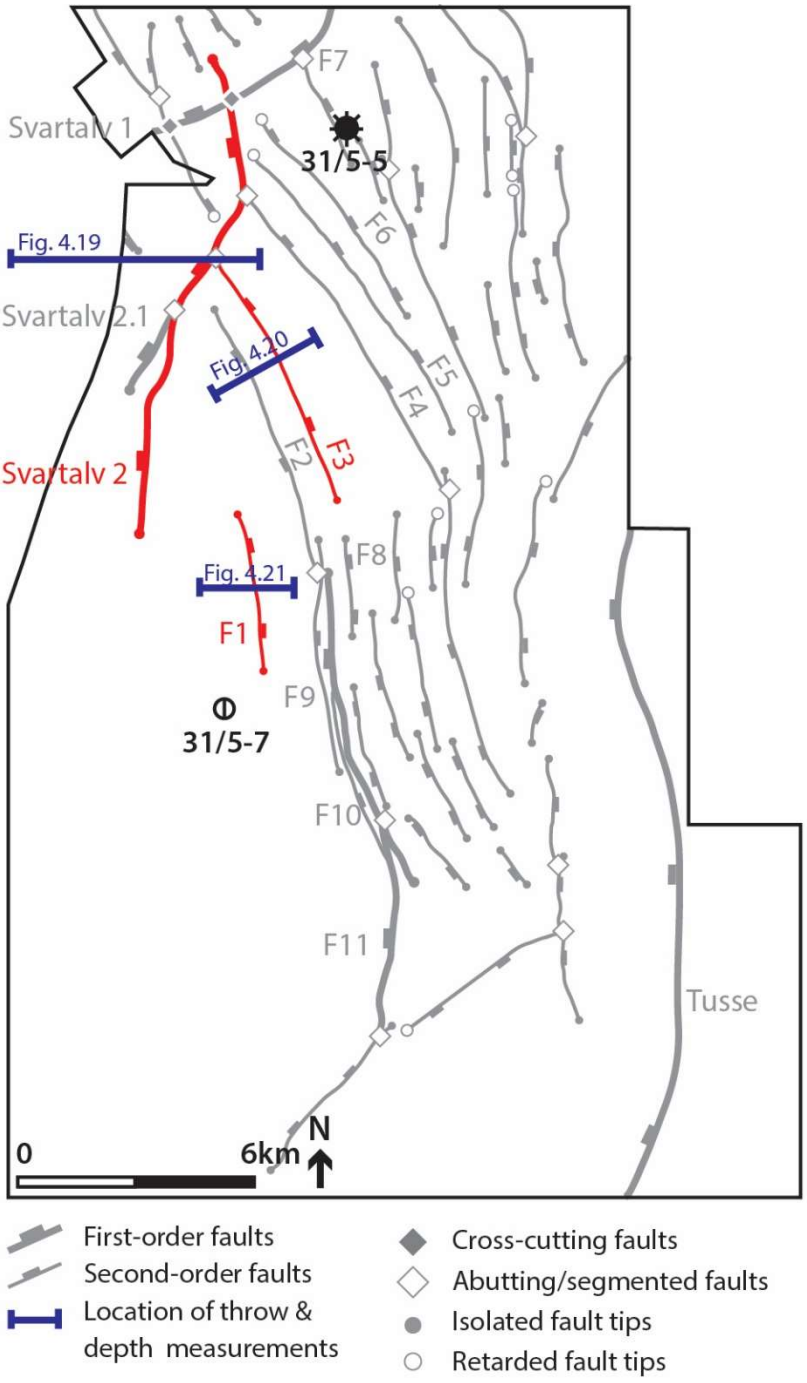

Figure 4.15 Fault trace map of the Top Cook Formation showing the location of three faults (red) presented in this sub-section. Six additional 3D throw diagrams and throw vs. length profiles are compiled in Appendix 3. The locations where throw and depth were measured (sub-section 4.1.4.3) are indicated with blue lines.

Fault throw diagram and throw vs. length profile are presented in Figure 4.16 for the first-order Svartalv 2 segment. The segment is approximately 12 km long and the projected fault throw contours show an asymmetrical shape, with a relatively flat upper tip-line in Figure 4.16A. In the fault throw diagram, two throw maximums (i.e., bulls-eyes) are observed within the Statfjord Group at the intersection with the second-order F3 and F4 faults. Svartalv 2 exhibits a general reduction in throw up-section. While, Svartalv 2 displays larger-scale along-strike undulations in strike, smaller-scale undulations (i.e., corrugations; e.g., Ferrill et al., 1999) are also observed in the fault throw diagram. These corrugations are observed to extend the entire vertical length of the fault plane, have wavelengths of approximately 400 m, and are sub-parallel to the dip direction of the fault. Simple mapping of ten corrugation axes on the fault plane shows a principal orientation of 270/63 (Figure 4.16A).

The throw vs. length profile in Figure 4.16C exhibits a step-like shape, where the 'steps' coincide with sites where four faults interact with the Svartalv 2 segment. To the south, Svartalv 2.1 abuts against the Svartalv 2 in the hanging wall. This is seen in the Svartalv 2 throw vs. length profile (Figure 4.16C) as an abrupt change in throw (approximately 60 m). Further north, the Svartalv 2 segment interacts with two NW–SE striking second-order faults (F3 and F4) in the footwall, which are seen as locations of smaller throw changes (20–30 m) in the throw vs. length profile. The throw maximum (approximately 300 m) corresponds to the Top Statfjord Group and is positioned at the site where the Svartalv 2 segment is intersected by the F3 fault. At the northernmost part of Svartalv 2, it is cross-cut by the first-order Svartalv 1 segment in the footwall and displaces both the footwall and the hanging-wall cut-off lines. This is seen in the throw vs. length diagram in Figure 4.15 as an abrupt change in throw (86–145 meters).

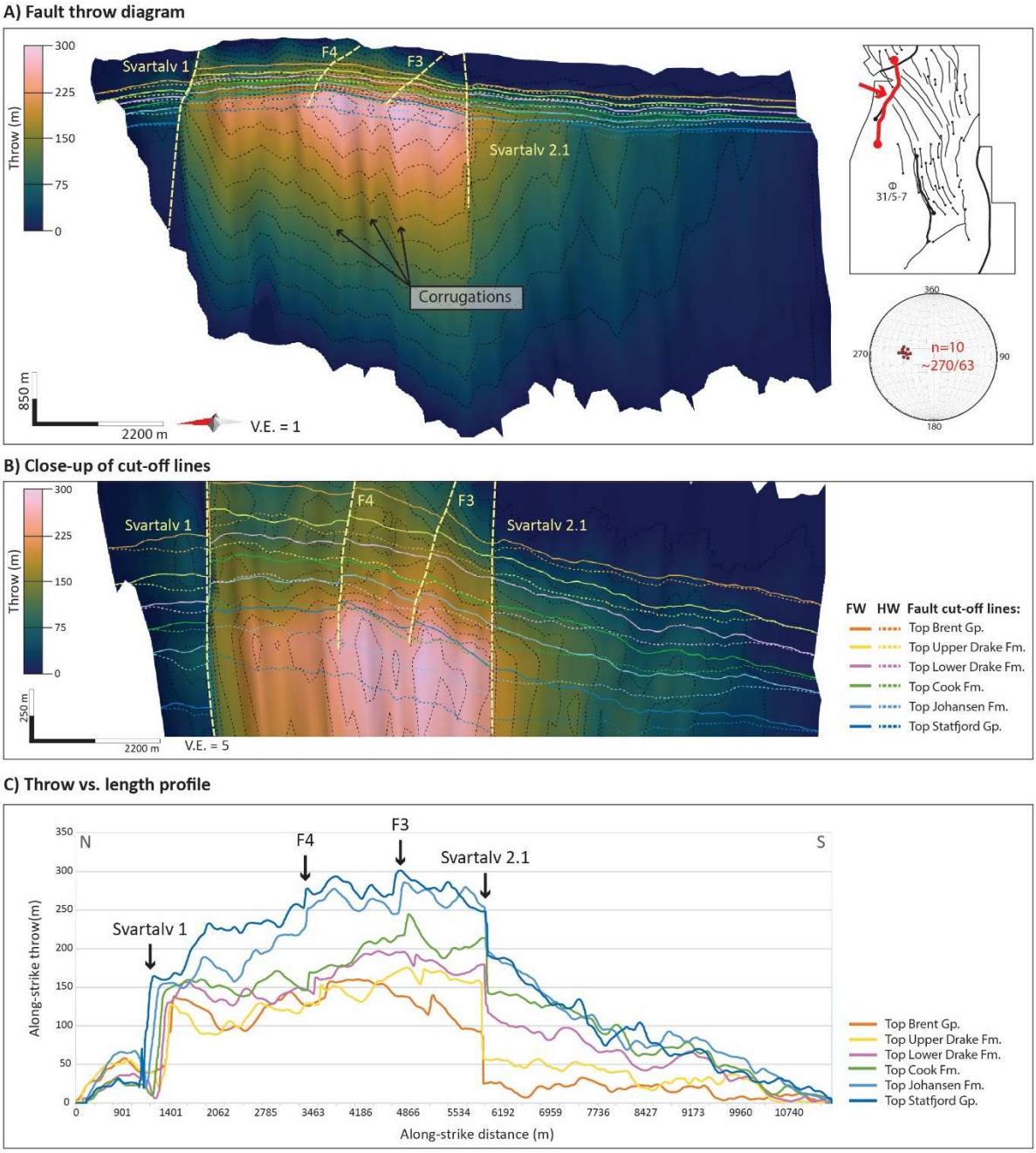

Figure 4.16 A) Svartalv 2 fault throw diagram showing horizon-fault intersection (cut-off) lines and a 25-meter throw contour spacing. Inset shows locations of fault and viewing direction and the stereonet shows strike and plunge of ten corrugation axes. B) Expanded view of the fault with a vertical exaggeration of 5. C) Throw vs. length profile of the Svartalv 2 segment. Note that throw below the Statfjord Group hanging-wall cut-off line have been extrapolated and are likely not representative of vertical throw variations.

The fault throw diagram and throw vs. length profile for the second-order F3 fault are presented in Figure 4.17. The fault is approximately 6.8 km long and is hard-linked with the Svartalv 2 segment to the northwest. The fault throw contours shown in Figure 4.17A have an overall elliptical shape with a slightly flatter upper tip-line compared to the base tip-line. The maximum throw, of approximately 75 meters, is spread out over a wider area and corresponds to the Top Statfjord Group and the Top Johansen Formation. In contrast to Svartalv 2, F3 does not exhibit obvious corrugations in the fault plane.

The fault throw diagram in Figure 4.17A shows that the largest throw measurements are spread out over a wide area that is located slightly northwest off-center, that is, towards the intersection with the Svartalv 1 fault. This asymmetric throw distribution can also be observed in the throw vs. length diagram (Figure 4.17B). Towards the southeastern tip, the throw decreases gradually to zero (or below the threshold of vertical resolution), while the throw gradient is steeper at the northwestern tip where it has 10–30 meters of throw. F3 exhibits a general reduction in throw up-section, similar to Svartalv 2.

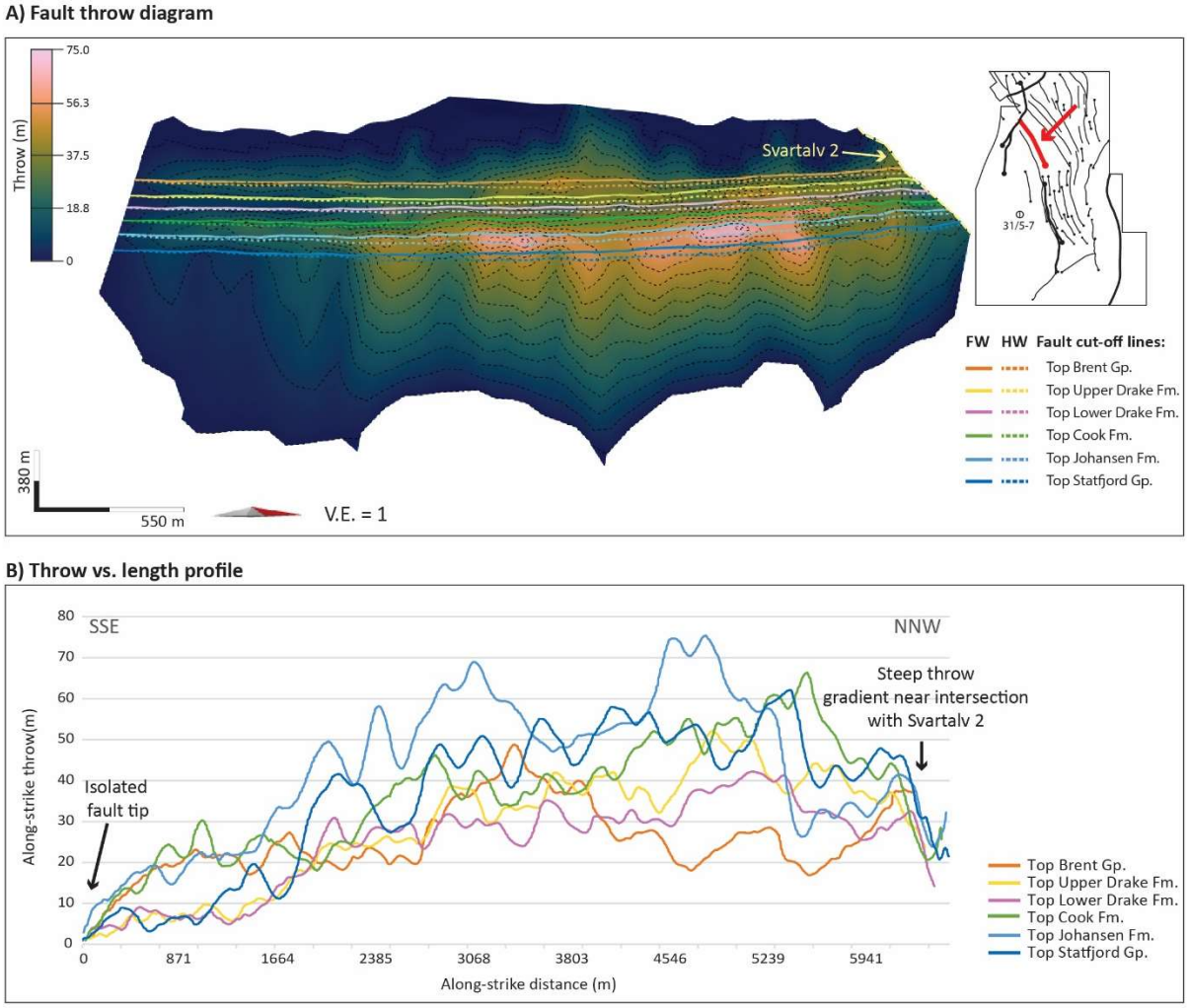

Figure 4.17 A) F3 fault throw diagram showing horizon-fault intersection (cut-off) lines and a 5-meter throw contour spacing. Inset shows the location of the fault and viewing direction. B) Throw vs. length profile of the F3 fault.

Fault throw diagram and throw vs. length profile for the F1 fault are presented in Figure 4.18. The fault is approximately 4 km long and is located just 700 meters northeast of the injection well (31/5-7). In comparison with the Svartalv 1 and F3 fault, the F1 does not exhibit a flat upper tip-line. The fault throw diagram in Figure 4.18A shows that a single throw maximum, of approximately 40 meters, is located within the Top Statfjord Group. Similar to F3, F1 does not exhibit obvious corrugations in the fault plane.

The throw vs. length profile in Figure 4.18B shows that throw distribution is again asymmetric where the maximum throw is located north of center. The throw profile shows that the throw decreases to zero (or below the vertical resolution) towards both lateral fault tips. However, a slightly steeper throw gradient is observed at the northern fault tip compared to the southern. F1 exhibits a general reduction in throw up-section, similar to Svartalv 2 and F2.

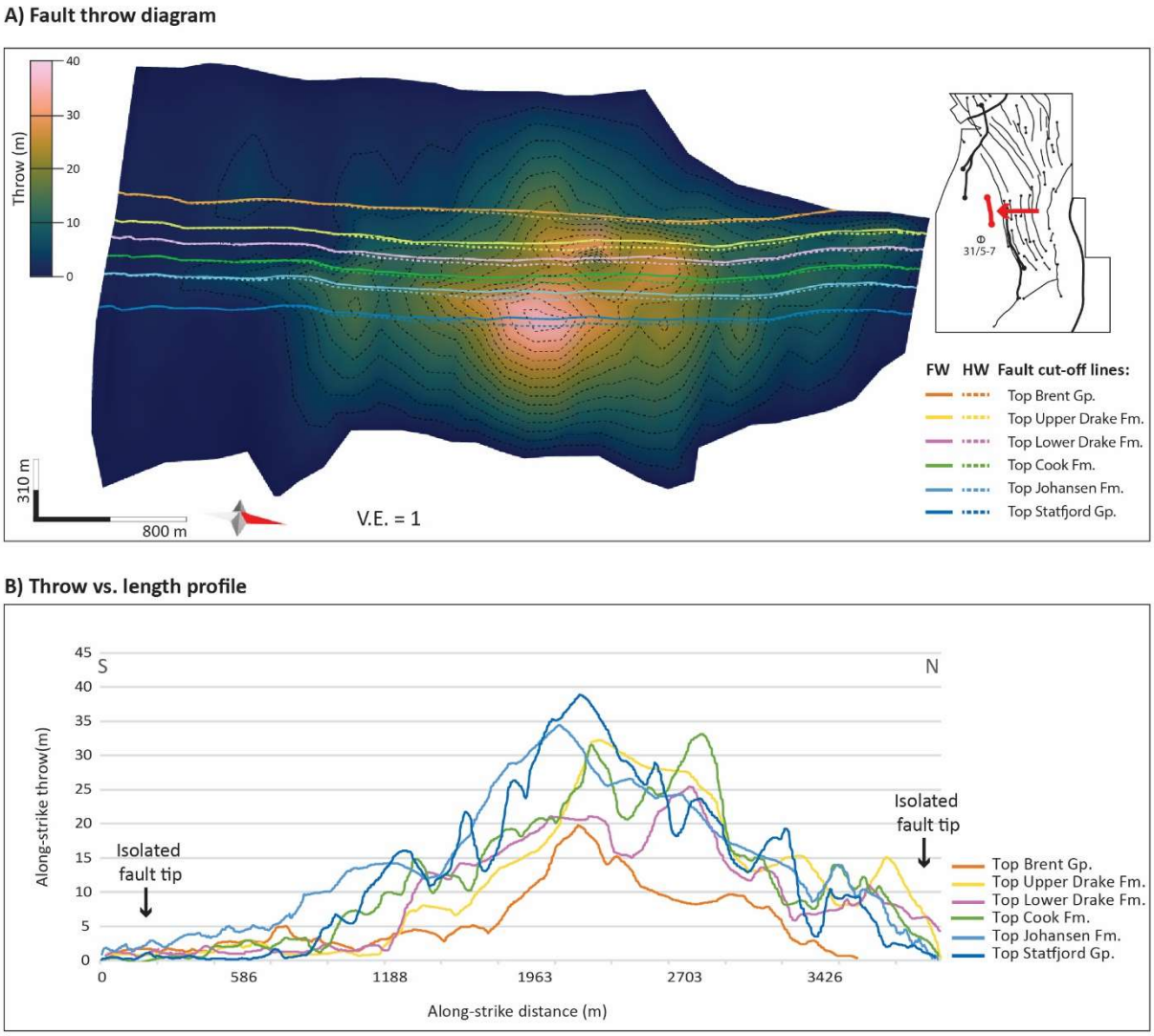

Figure 4.18 A) F1 fault throw diagram showing horizon-fault intersection (cut-off) lines and a 5-meter throw contour spacing. Inset shows the location of the fault and viewing direction. B) Throw vs. length profile of the F1 fault.

4.1.4.3 Vertical throw variations

Vertical variations in throw are analyzed for the Svartalv 2, F3, and F1 faults and presented in throw vs. depth profiles to determine the temporal evolution of faults intersecting the study area (discussed in sub-section 5.1.1). Measurement of throw, depth and expansion indices are compiled in Appendix 4.

The throw vs. depth profile in Figure 4.19 shows an increasing throw with depth. Up-section the fault tips out in the Northern North Sea Unconformity Complex (NNSUC) where a throw of 59 meters is measured. Down-section, the fault displaces the basement cover contact by 961 meters. The expansion index (E.I.) is greater than 1 (i.e., the hanging-wall thickness is greater than the footwall thickness) for all the interpreted successions except the Upper Drake Formation. The expansion index profile shows that the highest contrast in hanging-wall and footwall thickness is found in the Brent Group (E.I. = 1.27) and the primary storage unit (E.I. = 1.44).

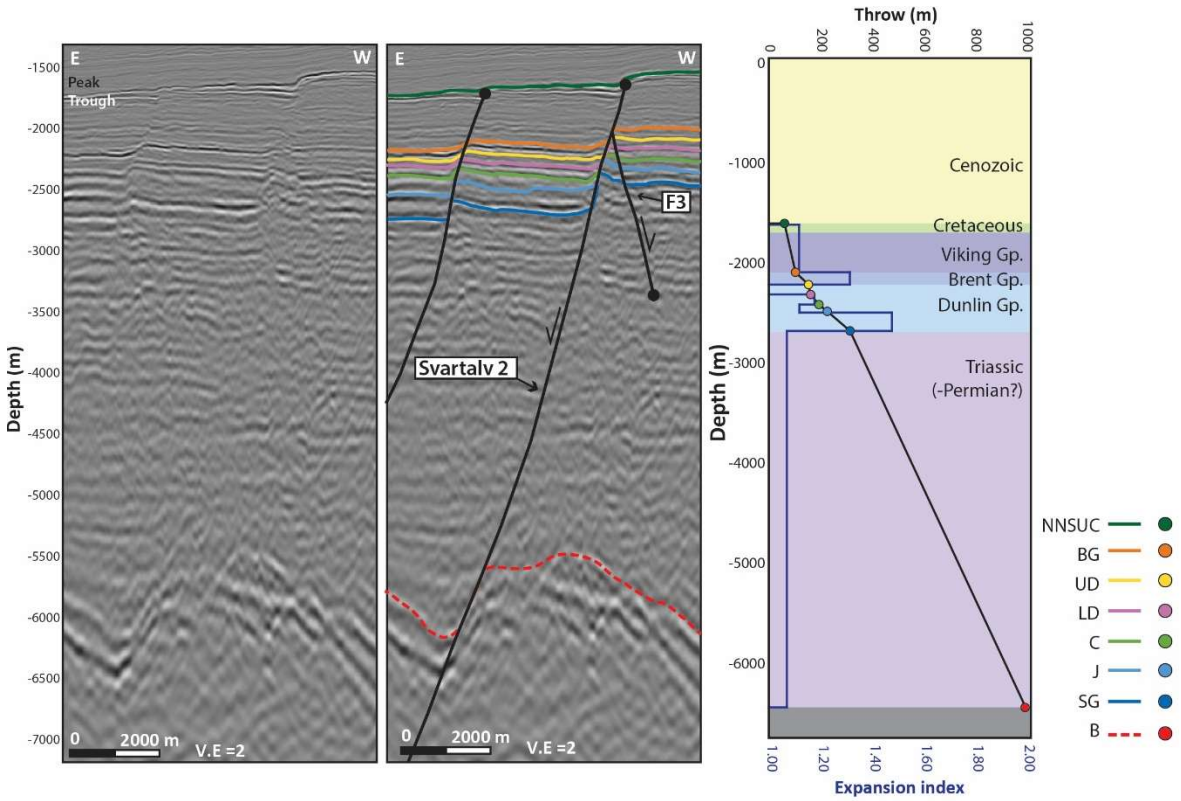

Figure 4.19 Left) E–W oriented seismic inline (2317; un-interpreted) Centre) with interpreted horizons and faults and Right) throw vs. depth profile and E.I. for the first-order Svartalv 2 segment. See Figure 4.15 for the location of the seismic line. Abbreviations: NNSUC = Northern North Sea Unconformity Complex, BG = Top Brent Group, UD = Top Upper Drake Formation, LD = Top Lower Drake Formation, C = Top Cook Formation, J = Top Johansen Formation, SG = Top Statfjord Group, B = Basement-cover contact.

The throw vs. depth profile and E.I. for F3 are presented in Figure 4.20. Up-section, the fault tips out in the Northern North Sea Unconformity Complex (NNSUC) where 32 meters of throw is measured. The throw increases down-section and reaches a maximum of 66 meters within the Top Statfjord Group (Early Jurassic). Further down-section, the throw decreases, and the fault tips out within the Upper Triassic successions. Hanging-wall growth is less obvious in the seismic cross-sections, however, the expansion index profile show that expansion indices are greater than 1 for the interpreted Dunlin, Brent, and Viking groups, with the highest value measured within the primary (E.I. = 1.14) and secondary storage unit (E.I. = 1.16). These measurements are relatively small to those observed in Svartalv 2.

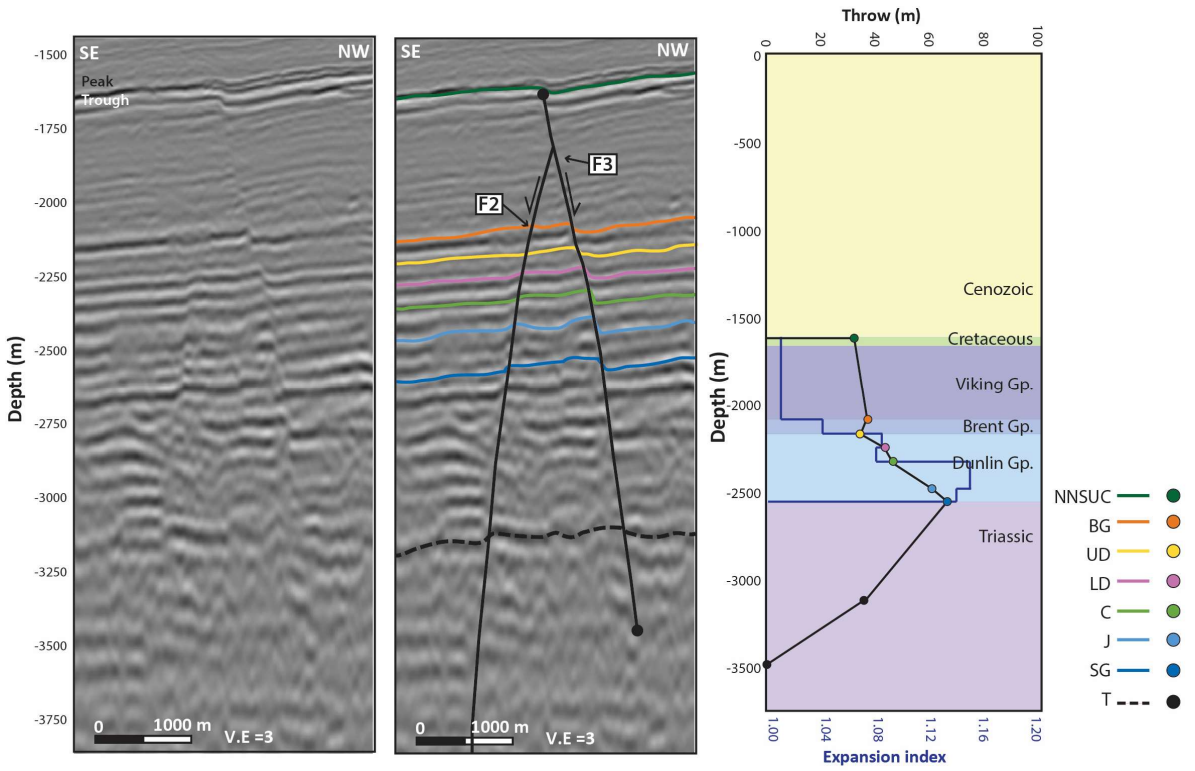

Figure 4.20 Left) E–W oriented seismic composite line (un-interpreted) Centre) with interpreted horizons and faults and Right) throw vs. depth profile and E.I. for the second-order F3 fault. See Figure 4.15 for the location of the seismic line. Abbreviations: NNSUC = Northern North Sea Unconformity Complex, BG = Top Brent Group, UD = Top Upper Drake Formation, LD = Top Lower Drake Formation, C = Top Cook Formation, J = Top Johansen Formation, SG = Top Statfjord Group, T = Intra Triassic marker.

The throw vs. depth profile and E.I. for F1 (second-order) is presented in Figure 4.21. In contrast to Svartalv 2 and F3, the F1 fault has zero throw at the upper fault-tip. The throw increases down-section and reaches a maximum of 38 meters in the Top Statfjord Group and the Intra Triassic Marker (Late Triassic to Early Jurassic). Down-section the fault tips out in the Upper Triassic successions. Again, hanging-wall expansion is not easily observed in the seismic section. Calculated E.I. is below 1 for the Viking Group, Upper Drake Formation, and below the Intra Triassic marker (Figure 4.21). The calculated E.I. are low compared to those for Svartalv 2 and F3, with the highest value in the primary storage unit (E.I. = 1.02) and above the Intra Triassic marker (E.I. = 1.03).

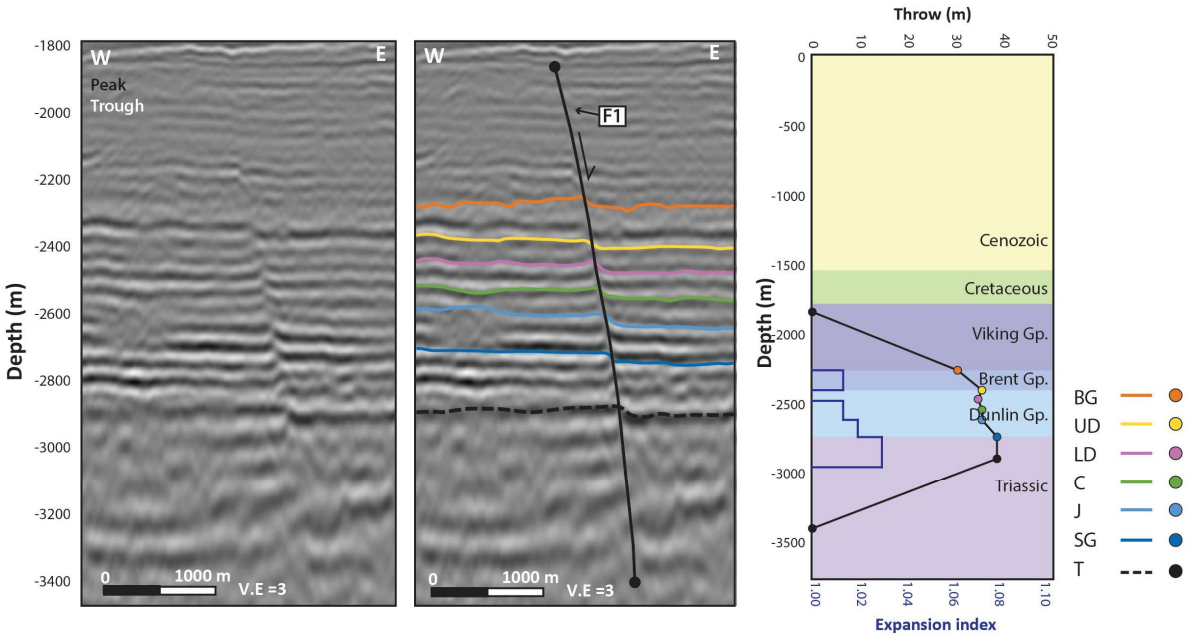

Figure 4.21 Left) E–W oriented seismic composite line (un-interpreted) Centre) with interpreted horizons and faults and Right) throw vs. depth profile and E.I. for the second-order F1 fault. See Figure 4.15 for the location of the seismic line. Abbreviations: BG = Top Brent Group, UD = Top Upper Drake Formation, LD = Top Lower Drake Formation, C = Top Cook Formation, J = Top Johansen Formation, SG = Top Statfjord Group, T = Intra Triassic marker.

In addition to faults presented in detail in this sub-section (i.e., Svartalv 1, F1, and F3), cut-off lines for six additional faults were created. The overall vertical throw trends and simple estimation of expansion using the modelled cut-off lines (Early Jurassic to Middle Jurassic) are summarized in Table 4.1. Fault throw diagrams, throw vs. length profiles, and measurements used to calculate expansion indices are shown in Appendix 3. It is important to note that these observations are restricted to the modelled cut-off lines, and as a result, provide less reliable observations of vertical throw variation and hanging-wall growth compared to the detailed throw vs. depth profiles presented above.

Table 4.1 Summarized overall vertical throw trends and simple estimation of expansion within the Dunlin and Brent groups using modelled cut-off lines for six additional faults. Expansion indices less than 1 are listed as n/a. The location of faults is shown in Figure 4.15. Fault-strike, fault-dip, and fault population classification are listed.

Fault name	**Fault-strike**	**Fault-dip**	**Up-section throw trend**	**Dunlin Gp. E.I.**	**Brent Gp. E.I.**	**Fault population**
Svartalv 1	NE–SW	NW	Decreasing	1.4	1.12	First-order
F2	NW–SE	NE	Decreasing	1.11	n/a	Second-order
F4	NW–SE	NE	Decreasing	1.07	1.05	Second-order
F8	N–S	E	Increasing	n/a	n/a	Second-order
F9	N–S	E	Increasing	n/a	n/a	Second-order
F10	N–S	W	Increasing	n/a	1.1	First-order

The summary in Table 4.1 shows that the modelled faults have an overall throw trend of either increasing or decreasing up-section. Three faults show an overall decrease in throw up-section and largest growth measured in the Dunlin Group. This throw trend is observed within Svartalv 1 or faults that are located in proximity to or interact with it. Three faults show the opposite overall vertical throw trend, with increasing throw up-section and show no expansion in the Dunlin Group. These faults are located east of the injection well 31/5-7 and are predominately N–S striking.

4.2 Across-fault seal assessment

To select faults of particular interest for across-fault seal assessment, assumptions are made that CO_2 will be injected into well 31/5-7, will migrate up-dip, and will be injected into both storage units. As presented in sub-section 4.1.1, the storage complex dip towards the south, and, therefore, buoyant CO_2 is likely to migrate northwards. Furthermore, the strike of the faults are observed to vary northwards within the study area, from predominately N–S striking east of the injection well, to NW–SE or NE–SW striking north of the injection well (e.g., Figure 4.5). Based on these assumptions and observations, this section is divided into across-fault seal assessments of faults that are parallel to migration direction (sub-section 4.2.1) and faults that are oblique to migration direction (sub-section 4.2.2). Fault juxtaposition diagrams are presented for eight faults and membrane seal diagrams using the SGR method (i.e., SGR diagrams) are presented for five faults. In addition, 1D triangle diagrams (Knipe, 1997) populated with SGR values are presented in sub-section 4.2.3 to provide background for the SGR diagrams. The assigned lithologies used in the fault juxtaposition diagram are listed in Table 3.6 and cut-off values selected to create the SGR diagrams and SGR triangle diagrams are listed in Table 3.7. Finally, a generalized overview of juxtaposition and membrane seals within the storage units is presented, which provide background for the discussion of plausible CO_2 migration paths in section 5.2.

4.2.1 Faults parallel to migration direction

Faults F1, F9, and F10 are located 700–2100 m northeast of the injection well and may, therefore, be the first faults that come in contact with the CO_2 plume. These faults are NNW–SSE to N–S striking and thus parallel to the CO_2 migration direction. In the fault juxtaposition diagrams, emphasis is placed on storage unit juxtapositions, where the Top Johansen Formation and Top Cook Formation cut-off lines represent the upper extent of the primary storage unit and the secondary storage unit, respectively.

Fault juxtaposition diagram for the second-order F1 is presented in Figure 4.22. F1 is located 700 meters northeast of 31/5-7 and dip towards the east. As such, the injection well is located in the footwall of the fault. The fault juxtaposition diagram in Figure 4.22 shows that the primary storage unit (i.e., Lower Amundsen and Johansen formations) in the footwall (FW) of F1 are juxtaposed against the secondary

storage unit (i.e., Cook and Upper Amundsen formations) in the hanging wall (HW) creating sandstone on sandstone juxtaposition. F1 also juxtaposes the secondary storage unit (FW) against the primary seal unit (HW). This relationship potentially creates a juxtaposition seal.

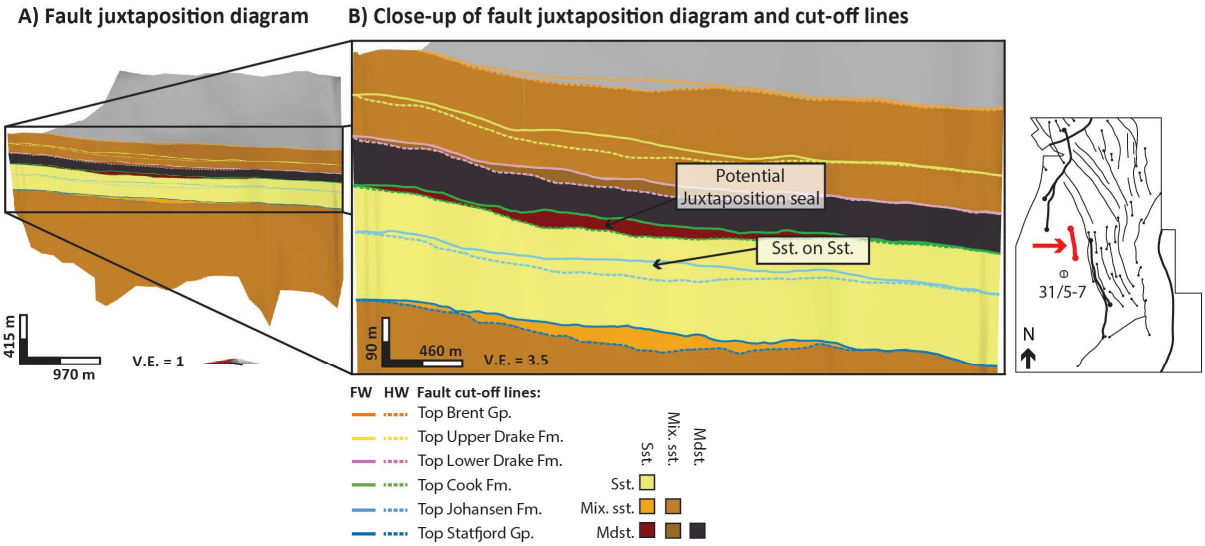

Figure 4.22 Fault juxtaposition (Allan) diagram and cut-off lines for F1. A) the fault with no vertical exaggeration and B) a close-up of the fault with 3.5 times the vertical exaggeration. Inset map shows the location of the fault and viewing direction. Abbreviations: Sst. = sandstone, Mix.Sst = mixed sandstone, and Mdst. = mudstone.

Fault juxtaposition diagram for the second-order F9 is presented in Figure 4.23. F9 is located approximately 1.5 km east of well 31/5-7 and dips towards the east. As such, the injection well is located in the footwall of the fault. The fault juxtaposition diagram in Figure 4.23 shows similar juxtaposition scenarios to F1. That is, the primary storage unit (FW) is juxtaposed against the secondary storage unit (HW) and the secondary storage unit (FW) is juxtaposed against the primary seal (HW).

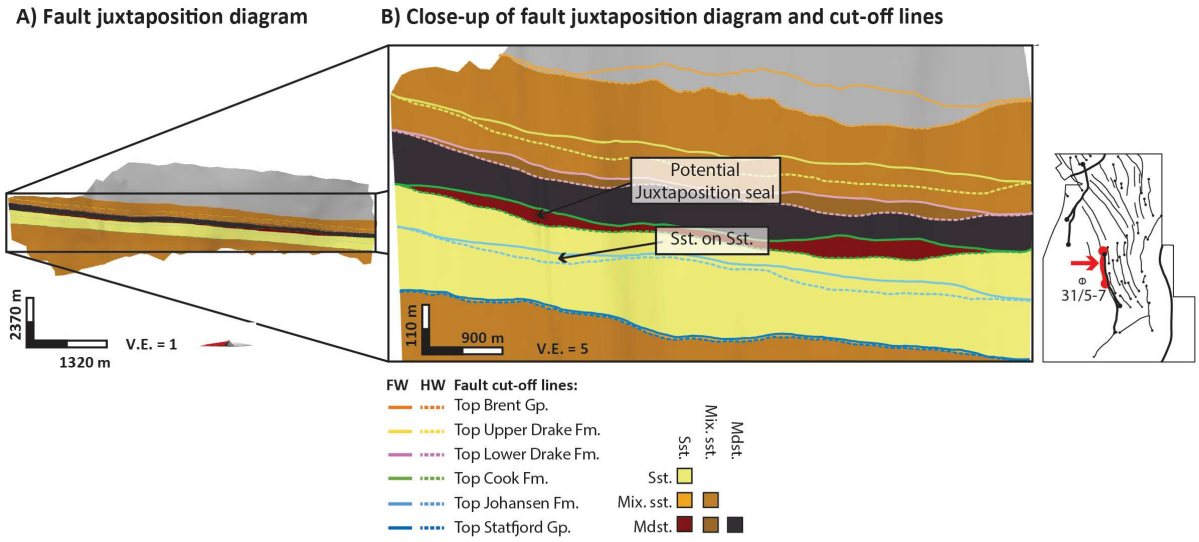

Figure 4.23 Fault juxtaposition (Allan) diagram and cut-off lines for F9. A) the fault with no vertical exaggeration and B) a close-up of the fault with 5 times the vertical exaggeration. Inset map shows the location of the fault and viewing direction. Abbreviations: Sst. = sandstone, Mix.Sst = mixed sandstone, and Mdst. = mudstone.

Fault juxtaposition diagram for the first-order F10 fault is presented in Figure 4.24. F10 is located approximately 2.1 km east of the injection well and 600 meters east of F9. In contrast to F1 and F9, F10 dips towards the west and as such, the injection well is located in the hanging wall of the fault. The fault juxtaposition diagram in Figure 4.24 shows that the lower parts of the primary seal unit (HW) are juxtaposed against the Statfjord Group (FW; i.e., sandstone on 'mixed sand' juxtaposition). Moreover, the secondary storage unit (HW) is juxtaposed against the primary storage unit (FW).

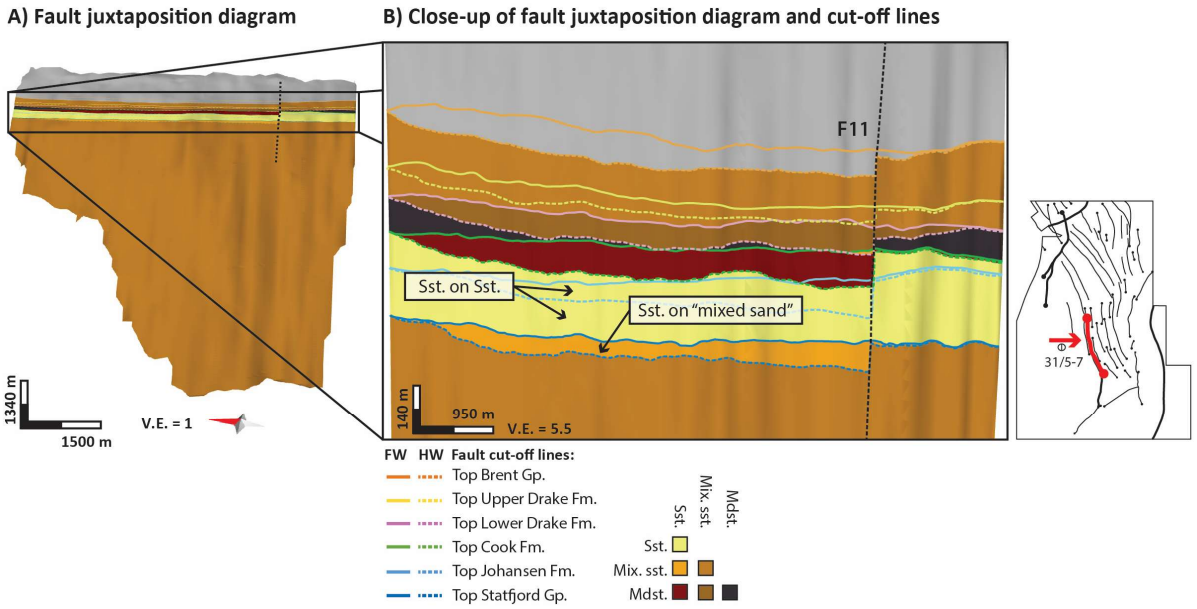

Figure 4.24 Fault juxtaposition (Allan) diagram and cut-off lines for F10. A) the fault with no vertical exaggeration and B) a close-up of the fault with 5.5 times the vertical exaggeration. Inset map shows the location of the fault and viewing direction. Abbreviations: Sst. = sandstone, Mix.Sst = mixed sandstone, and Mdst. = mudstone.

4.2.2 Faults oblique to the migration direction

North of injection well 31/5-7 the strike of the fault changes to approximately NW–SE, and as such, the faults are oriented oblique to the dip of the storage units and migration direction for CO_2. This includes three NW–SE striking second-order faults (F2, F3, and F4) and two NNE–SSW to NE–SW striking first-order segments (Svartalv 1 and Svartalv 2). Due to the strike of these faults, they may have a larger influence on the migration of CO_2 and potentially redirect or create structural closures (further discussed in section 5.2). These faults are, therefore, of particular interest, and both juxtaposition diagrams and SGR diagrams are presented below.

Fault juxtaposition diagram for the second-order F2 fault is presented in Figure 4.25. F2 is located from 2.8 km north of well 31/5-7 and extends 6.2 km north-westwards. The fault dips towards the southwest, therefore, the injection well is located in the hanging wall of the fault. The fault juxtaposition diagram in Figure 4.25 shows similar juxtaposition scenarios to F10. Where the primary storage unit (HW) is

juxtaposed against ‘mixed sands’ (i.e., the Statfjord Group; FW) or self-juxtaposed, and the secondary storage unit (HW) is self-juxtaposed or juxtaposed against the primary storage unit (FW).

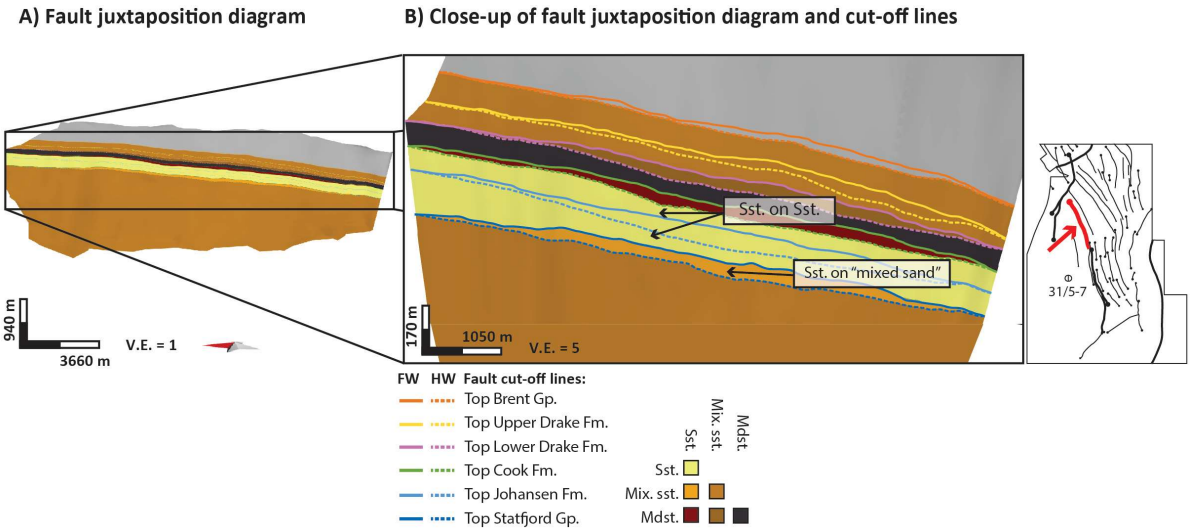

Figure 4.25 Fault juxtaposition (Allan) diagram and cut-off lines for F2. A) the fault with no vertical exaggeration and B) a close-up of the fault with 5 times the vertical exaggeration. Inset map shows the location of the fault and viewing direction. Abbreviations: Sst. = sandstone, Mix.Sst = mixed sandstone, and Mdst. = mudstone.

An SGR diagram for the F2 fault is presented in Figure 4.26. The diagram shows that for areas where the lower parts of the primary seal (HW) are juxtaposed against ‘mixed sands’ (FW), the calculated SGR is increasing downward from <15% to >40%. In areas where the primary storage unit (HW) is juxtaposed against the secondary storage unit (FW), the SGR is generally below 15%. Some higher SGR values (>20%) are present in the secondary storage unit towards the north, however, these areas are thin and discontinuous. Overall, the SGR diagram show SGR values <15% where the primary storage unit is self-juxtaposed.

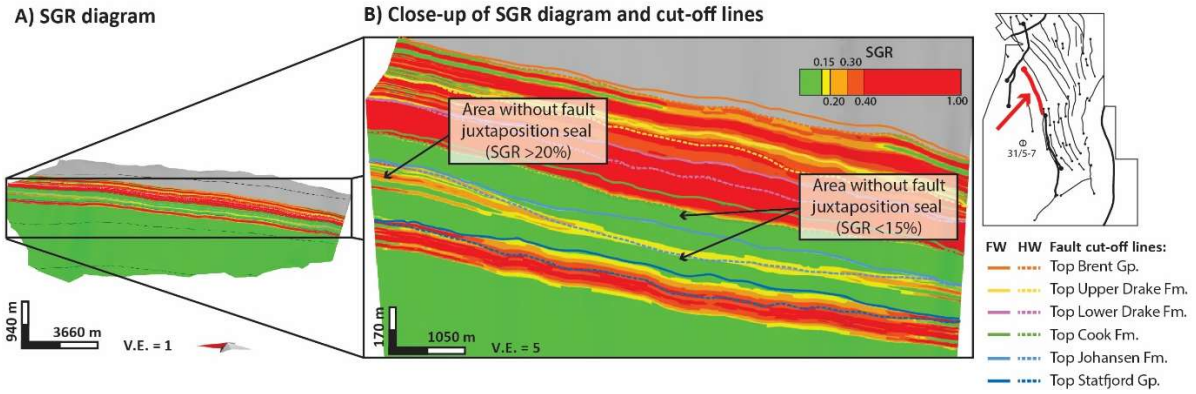

Figure 4.26 SGR (Allan) diagram and cut-off lines for F2 A) the fault with no vertical exaggeration and B) a close-up with 5 times the vertical exaggeration. Inset map shows the location of the fault and viewing direction.

Fault juxtaposition diagram for the second-order F3 fault is presented in Figure 4.27. F3 is located approximately 600 meters northeast of F2 and interpreted to hard-link with the first-order Svartalv 2 to the northwest (Figure 4.17). The fault dips towards the northeast and as such, the injection well is

located in the footwall of the fault. The fault juxtaposition diagram in Figure 4.27 shows that the primary storage unit (FW) is juxtaposed against the secondary storage unit (HW). While the secondary storage unit (FW) are juxtaposed against the primary seal unit (HW), potentially creating a juxtaposition seal.

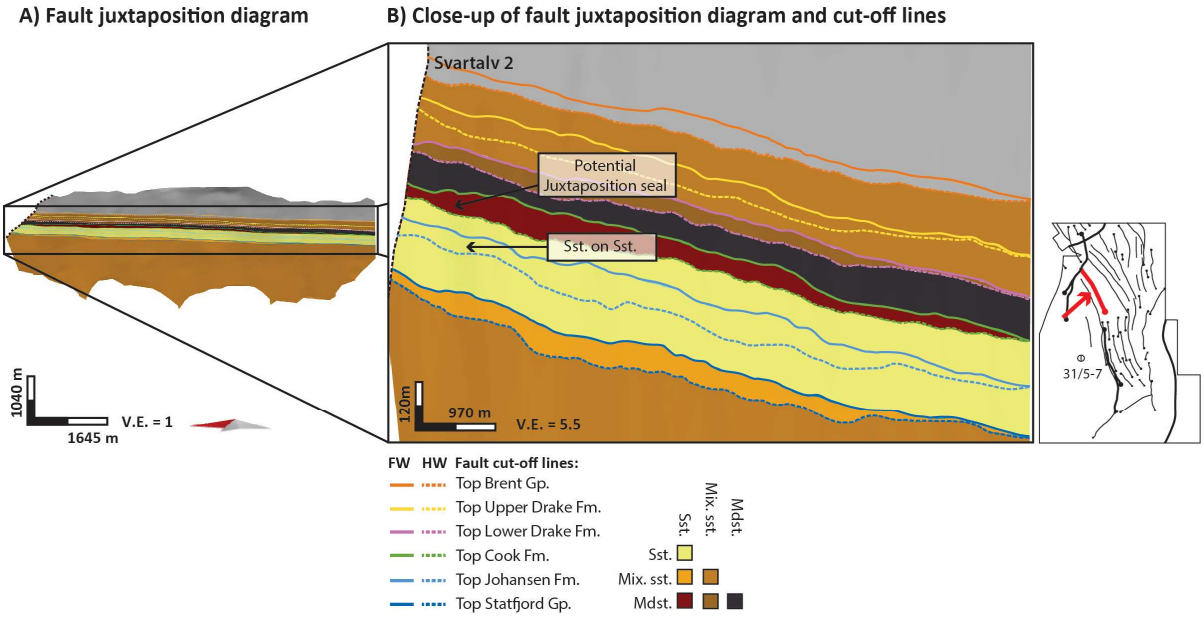

Figure 4.27 Fault juxtaposition (Allan) diagram and cut-off lines for F3. A) the fault with no vertical exaggeration and B) a close-up of the fault with 5.5 times the vertical exaggeration. Inset map shows the location of the fault and viewing direction. Abbreviations: Sst. = sandstone, Mix.Sst = mixed sandstone, and Mdst. = mudstone.

An SGR diagram for the F3 fault is presented in Figure 4.28. The diagram shows that in areas where the primary storage unit (FW) is juxtaposed against the secondary storage unit (HW), the calculated SGR is generally between 15–20%. Furthermore, in areas where the secondary storage (FW) is juxtaposed against the primary seal (HW), the calculated SGR is >40%.

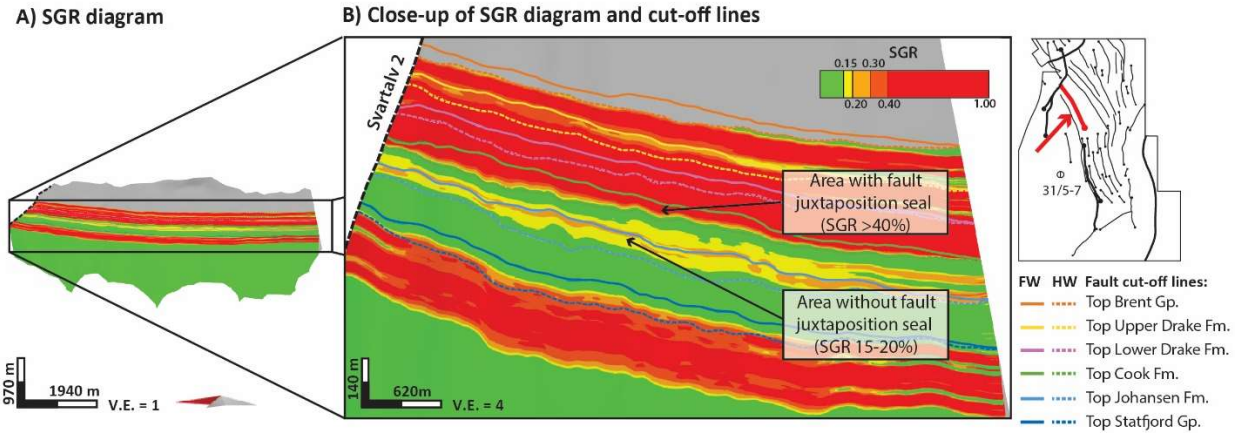

Figure 4.28 SGR (Allan) diagram and cut-off lines for F3. A) the fault with no vertical exaggeration and B) a close-up with 4 times the vertical exaggeration. Inset map shows the location of the fault and viewing direction.

Fault juxtaposition diagram for the second-order F4 fault is presented in Figure 4.29. F4 is located approximately 1600 meters northeast of F3 and is, similar to F3, interpreted to hard-link with Svartalv

2 to the northwest. The fault shows similar juxtaposition scenarios to the F3 fault. Where the primary storage unit (FW) is juxtaposed against the secondary storage unit (HW). While the secondary storage unit (FW) is juxtaposed against the primary seal unit (HW), potentially creating a juxtaposition seal.

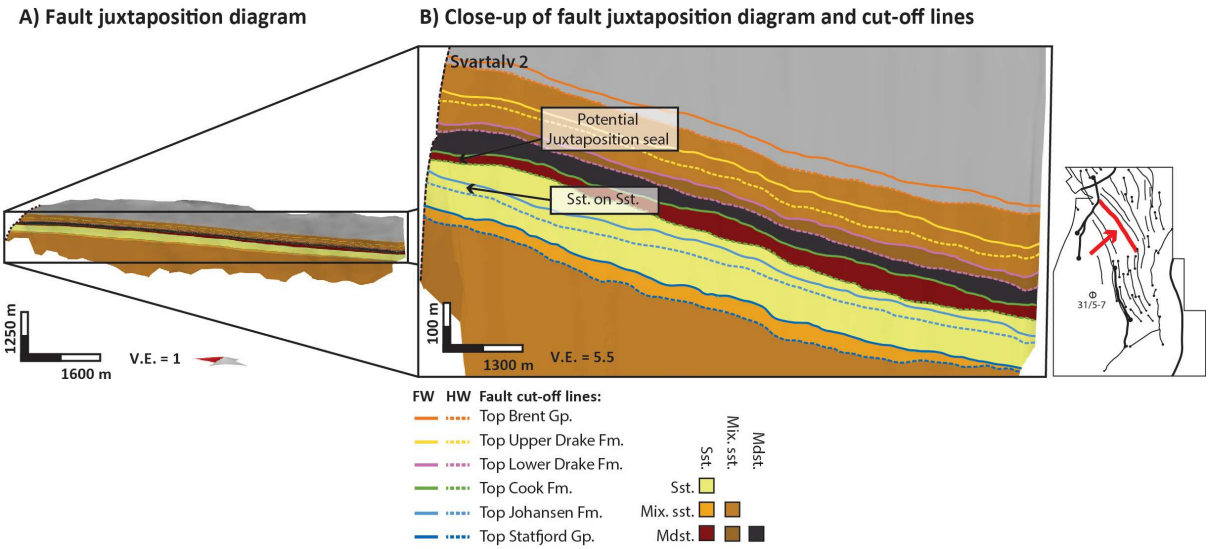

Figure 4.29 Fault juxtaposition (Allan) diagram and cut-off lines for F4. A) the fault with no vertical exaggeration and B) a close-up of the fault with 5.5 times the vertical exaggeration. Inset map shows the location of the fault and viewing direction. Abbreviations: Sst. = sandstone, Mix. Sst = mixed sandstone, and Mdst. = mudstone.

An SGR diagram for the F4 fault is presented in Figure 4.30. Similar to F3, the diagram shows that for areas where the primary seal unit (FW) is juxtaposed against the secondary seal unit (HW), the calculated SGR is between 15–20%. Furthermore, in areas where the secondary storage (FW) is juxtaposed against the primary seal (HW), the calculated SGR is >40%.

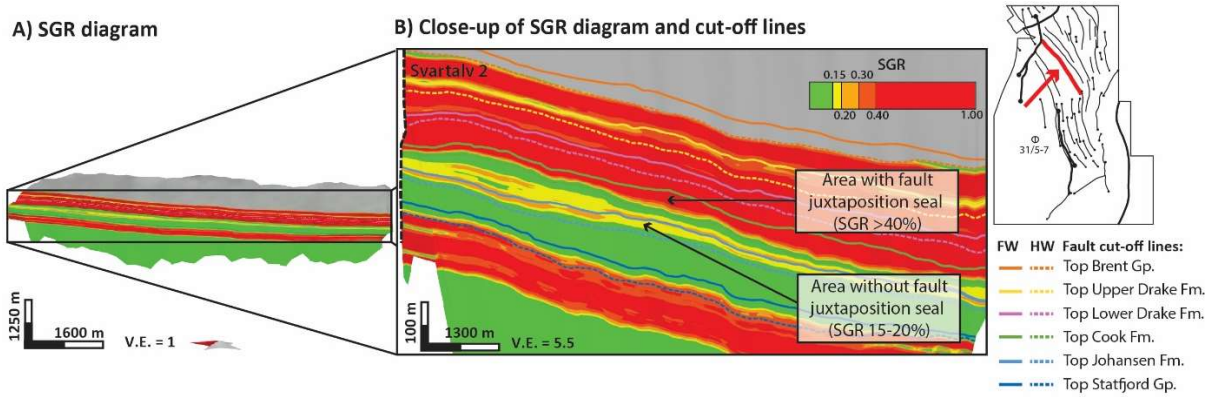

Figure 4.30 SGR (Allan) diagram and cut-off lines for F4. A) the fault with no vertical exaggeration and B) a close-up with 5.5 times the vertical exaggeration. Inset map shows the location of the fault and viewing direction.

Fault juxtaposition diagram for the first-order Svartalv 2 fault is presented in Figure 4.31. The Svartalv 2 fault extends from 5.7 km north of well 31/5-7 to the northernmost part of the study area. The fault dips towards the west which means that the injection well is located in the footwall. The fault

juxtaposition diagram in Figure 4.31 shows a complex pattern of multiple juxtaposition scenarios influenced by four intersecting faults (F3, F4, Svartalv 2.1, and Svartalv 1).

South of the intersection with Svartalv 2.1, the primary storage unit (FW) is juxtaposed against the primary seal (HW), creating a potential juxtaposition seal. Moreover, the secondary storage unit (FW) is juxtaposed against the Upper Drake Formation (HW) which is modelled as a 'mixed sand' lithology. At the intersection with F3, the primary storage unit (FW) is juxtaposed against the Upper Drake Formation (HW), while a small part of the secondary storage unit (FW) is juxtaposed against the Brent Group (HW), which is modelled as a 'mixed sand' lithology. At the intersection with F4, both storage units (FW) are juxtaposed against the Upper Drake Formation (HW).

In the northernmost parts of the study area, the first-order Svartalv 2 fault is cross-cut by the first-order Svartalv 1 fault (Figure 4.31). Just south of this intersection, the primary storage unit (FW) is juxtaposed against the primary seal unit (HW), while the secondary storage unit (FW) is primarily juxtaposed against the Upper Drake Formation (HW). The lowermost parts of the primary seal (FW) is juxtaposed against the secondary seal (FW), creating a thin sandstone on sandstone juxtaposition.

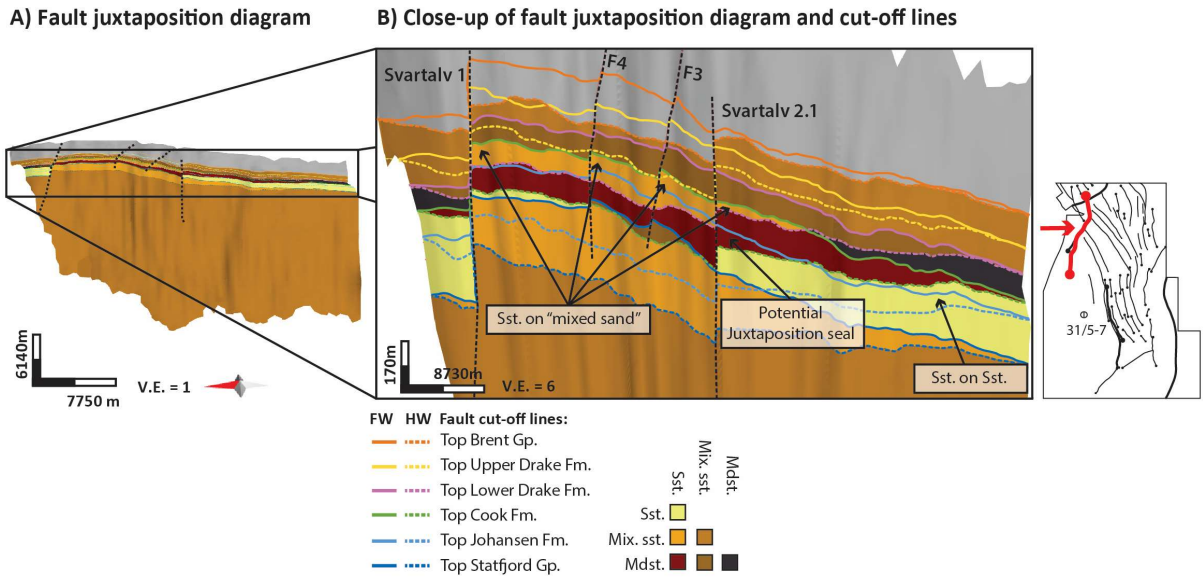

Figure 4.31 Fault juxtaposition (Allan) diagram and cut-off lines for Svartalv 2. A) the fault with no vertical exaggeration and B) a close-up with 6 times the vertical exaggeration. Inset map shows the location of the fault and viewing direction. Abbreviations: Sst. = sandstone, Mix. Sst = mixed sandstone, and Mdst. = mudstone.

SGR diagram for the Svartalv 2 is presented in Figure 4.32. The diagram shows that in areas where the storage formations (FW) are juxtaposed against the mixed sand of the Upper Drake Formation (HW), the calculated SGR is >30–40%. The lowermost parts of the primary storage unit (FW) show SGR <15% where it is juxtaposed against the secondary storage unit (HW).

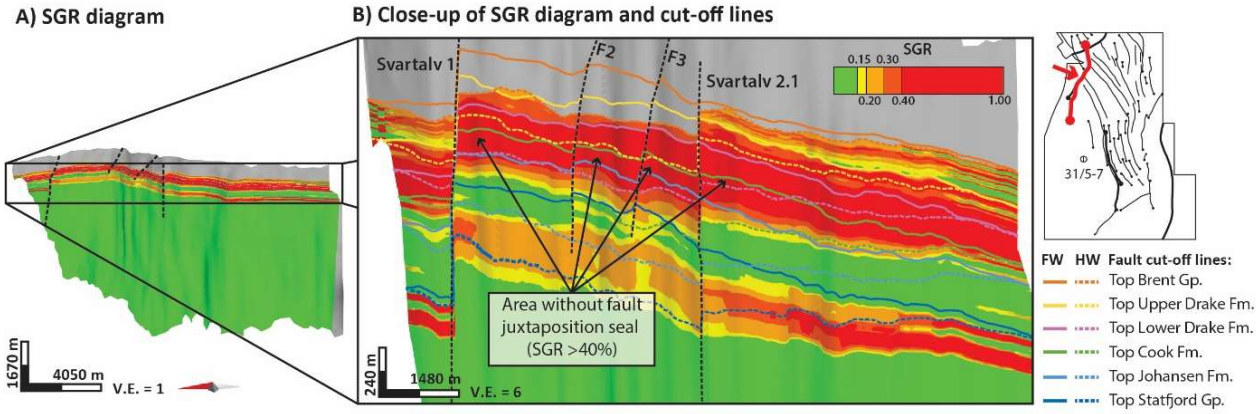

Figure 4.32 SGR (Allan) diagram and cut-off lines for Svartalv 2. A) the fault with no vertical exaggeration and B) a close-up with 6 times the vertical exaggeration. Inset map shows the location of the fault and viewing direction.

Fault juxtaposition diagram for the first-order Svartalv 1 segment is presented in Figure 4.33. Svartalv 1 is located approximately 13.7 km north of injection well 31/5-7 and dips towards the northwest. As such, the injection well is located in the footwall of the fault. It extends outside of the study area to the west and to the north and is intersected by two faults, the first-order Svartalv 2 fault, and a second-order NW–SE striking fault. These two intersecting faults influence the juxtaposition scenarios in Figure 4.33.

Southwest of the intersection with the Svartalv 2 fault, the primary storage unit (FW) is juxtaposed against the primary seal (HW) and the secondary storage unit (FW) is juxtaposed against the Upper Drake Formation (HW). Northeast of the intersection with Svartalv 2, the primary storage unit (FW) is first juxtaposed against the Upper Drake Formation and then the Brent Group (HW; 'mixed sand units') towards the northern border of the study area. The secondary storage unit (FW) is predominately juxtaposed against the Brent Group (HW).

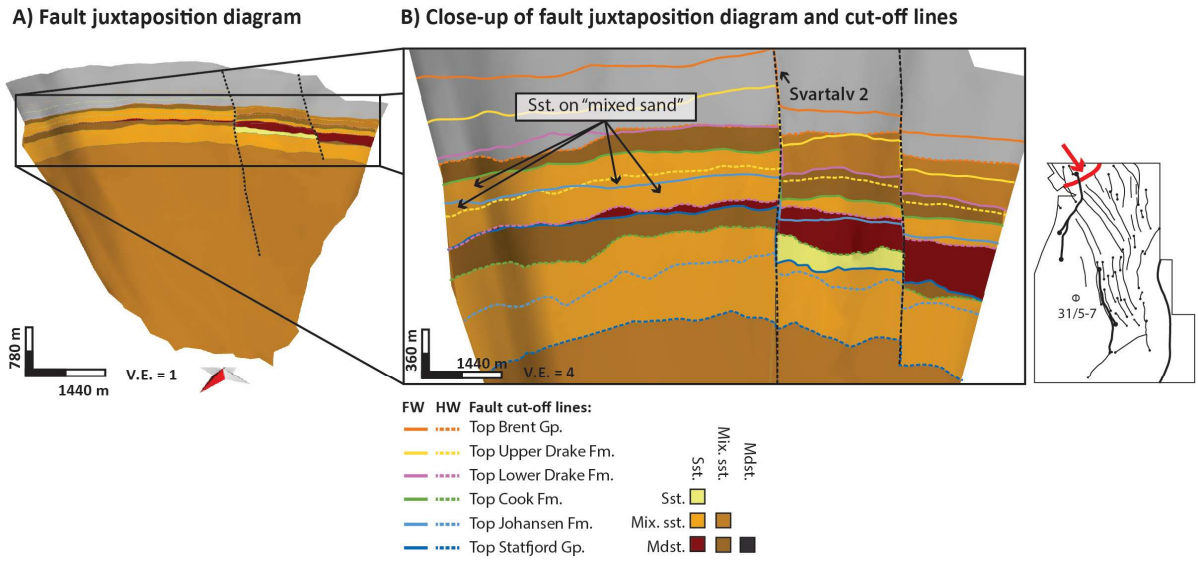

Figure 4.33 Fault juxtaposition (Allan) diagram and cut-off lines for Svartalv 1. A) the fault with no vertical exaggeration and B) a close-up of the fault with 4 times the vertical exaggeration. Inset map shows the location

of the fault and viewing direction. Note that the fault extends outside of the study area and that the entire extent of the fault is not mapped. Abbreviations: Sst. = sandstone, Mix. Sst = mixed sandstone, and Mdst. = mudstone.

SGR diagram for the Svartalv 1 segment is presented in Figure 4.34. In areas north of the intersection with Svartalv 2, where the storage units (FW) are juxtaposed against the Upper Drake Formation and the Brent Group (HW), the SGR is generally over 30% within the primary storage unit and 40% within the secondary storage unit.

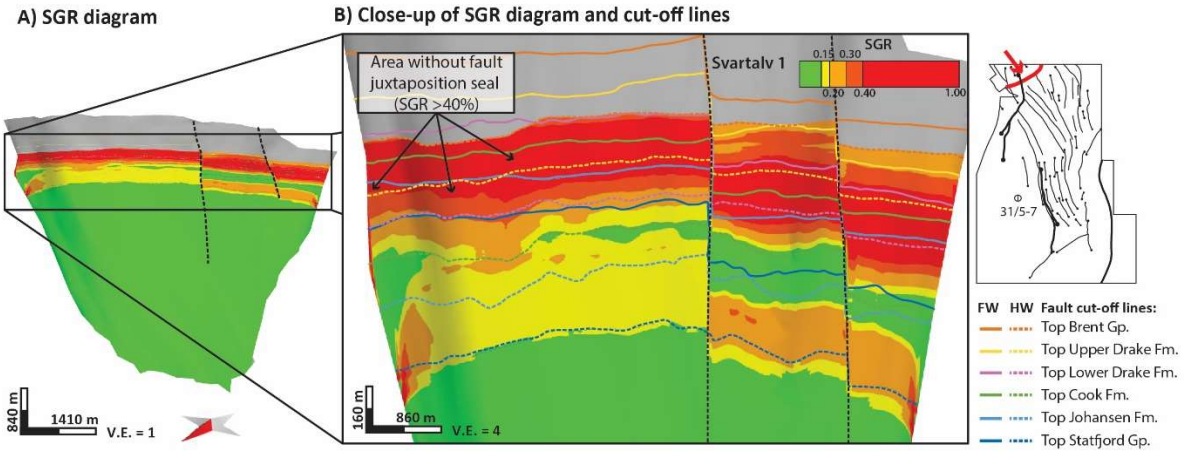

Figure 4.34 SGR (Allan) diagram and cut-off lines for Svartalv 1. A) the fault with no vertical exaggeration and B) a close-up with 4 times the vertical exaggeration. Inset map shows the location of the fault and viewing direction.

4.2.3 Triangle diagrams

To provide background for the SGR diagrams presented in the previous sub-section, 1D triangle diagrams (Knipe, 1997) are created using gamma-ray logs from four wells (31/5-7, 31/5-2, 31/2-1, and 31/2-5). As a reminder, the primary storage unit mapped herein comprises the Johansen and Lower Amundsen formation, while the secondary storage unit comprises the Cook and Upper Amundsen formation. To include information from both the hanging wall and the footwall side, well 31/5-7 and 31/2-5 were used to create SGR diagrams for Svartalv 1 and Svartalv 2, while well 31/5-7 and 31/5-2 were used for F1, F2, and F3. The selected API cut-off values for each well are listed in Table 3.7.

Figure 4.35 shows a 1D triangle diagram populated with SGR values calculated using data from the injection well (31/5-7). Well 31/5-7 is approximately 8.3–13.7 km southeast of the Svartalv 2 and Svartalv 1 faults. The diagram shows that in areas where the storage units are self-juxtaposed, the calculated SGR is generally below 15%. An exception is present within the upper parts of the Johansen Formation, where higher gamma-ray values contribute to higher calculated SGR values (15–40%) for throws less than 75 m. The presence of a thin Upper Amundsen Formation contributes to higher SGR values (15–20%) for low throws (<50 m) where the primary storage unit (FW) is juxtaposed against the secondary storage unit (HW) as seen in Figure 4.28 and Figure 4.30. For larger throws (>50 m), SGR

is generally exceeding 30% where storage units (FW) become juxtaposed against the Upper Drake Formation and the Brent Group (HW).

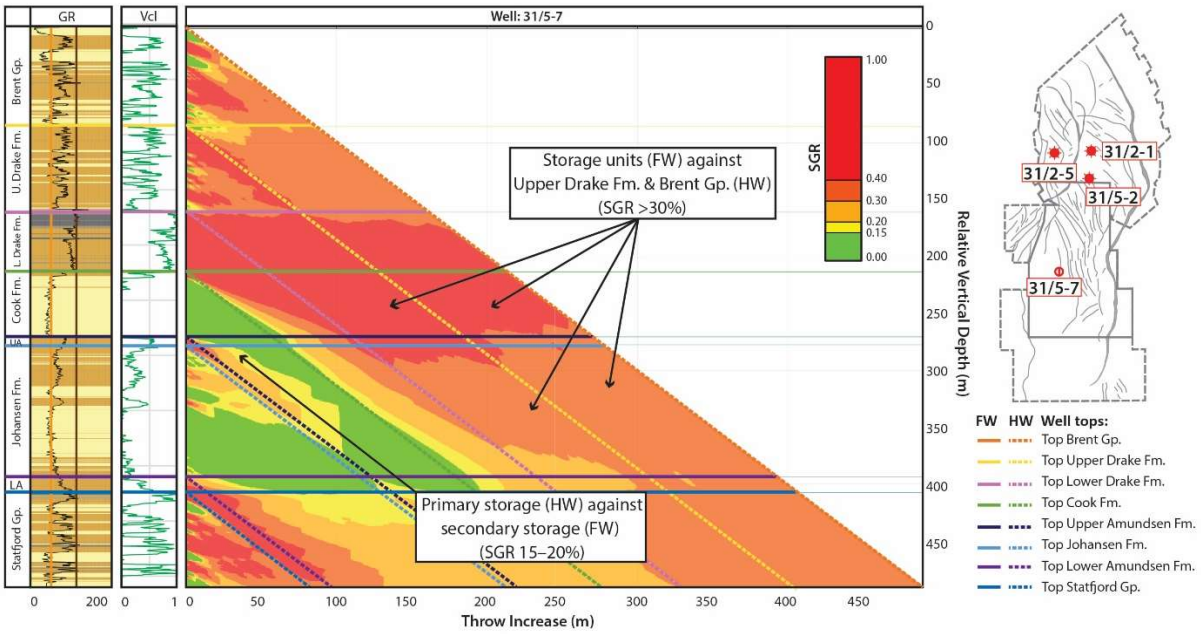

Figure 4.35 1D triangle diagram showing SGR for well 31/5-7. Gamma-ray log and normalized V_{cl} are presented to the left. For well 31/5-7 a sand-line at 60 API° and shale-line at 130 API° is chosen. Abbreviations: LA = Lower Amundsen Formation, UA = Upper Amundsen Formation.

Figure 4.36 shows a 1D triangle diagram with SGR values calculated using data from well 31/5-2. The well is located in the footwall of the Svartalv Fault Zone approximately 5.3–8.2 km northeast of the Svartalv 1 and Svartalv 2 faults. The well shows overall higher SGR values for the different juxtaposition scenarios, compared to well 31/5-7, partly due to a thicker Upper Amundsen Formation and thinner Cook Formation. Similar to well 31/5-7, areas where the storage formations are self-juxtaposed show low SGR (>15%), and areas where the storage units (FW) are juxtaposed against the Upper Drake Formation or the Brent Group (HW), the SGR value is high (>40%).

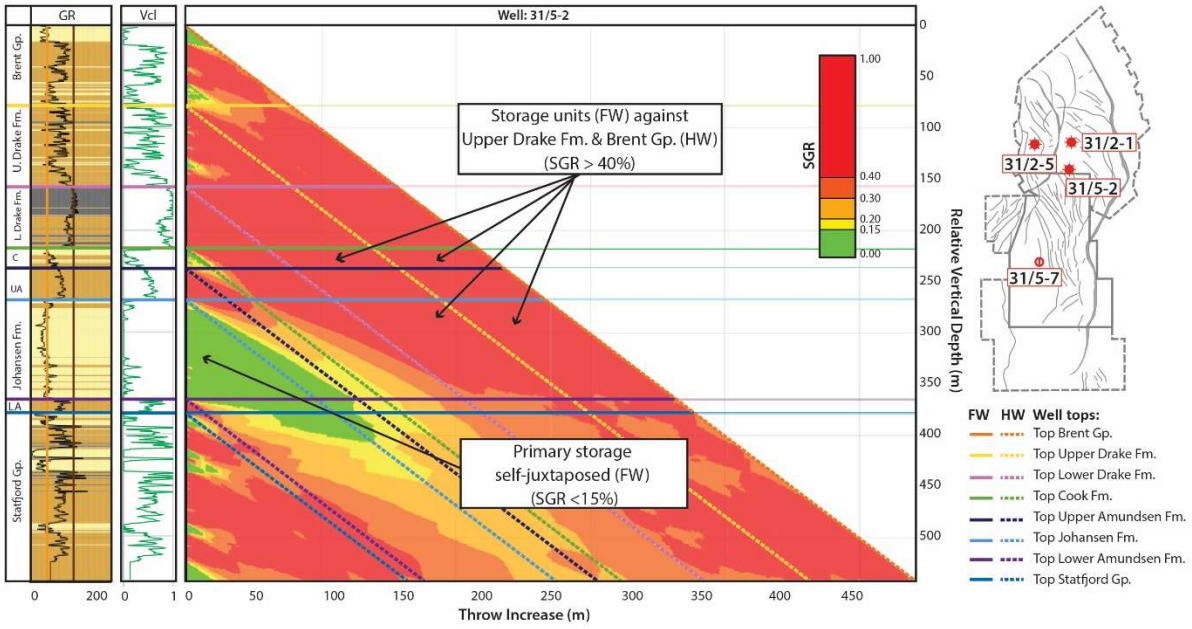

Figure 4.36 1D triangle diagram with SGR calculated for well 31/5-2. Gamma-ray log and normalized V_{cl} are presented to the left. For well 31/5-2 a sand-line at 60 API° and shale-line at 106 API° is chosen. Abbreviations: LA = Lower Amundsen Formation, UA = Upper Amundsen Formation, C = Cook Formation.

Figure 4.37 shows a 1D triangle diagram with calculated SGR values using data from well 31/2-1. The well is located in the footwall of the Svartalv Fault Zone, approximately 9–12.4 km northeast of Svartalv 1 and Svartalv 2. The gamma-ray log shows lower values for the primary seal (i.e., the Lower Drake Formation), the Upper Drake Formation, and the Brent Group, compared to well 31/5-7 and 31/2-5, which results in overall lower calculated SGR values in the 1D triangle diagram. Similar to well 31/5-2 and 31/5-7, areas where the Johansen Formation is self-juxtaposed show low SGR (<15%), while some areas where the Cook Formation is self-juxtaposed show higher SGR (>30%). At locations where the storage formations (FW) are juxtaposed onto the Upper Drake Formation or the Brent Group (HW), SGR values are lower than in wells 31/5-7 and 31/5-2 (20–40%).

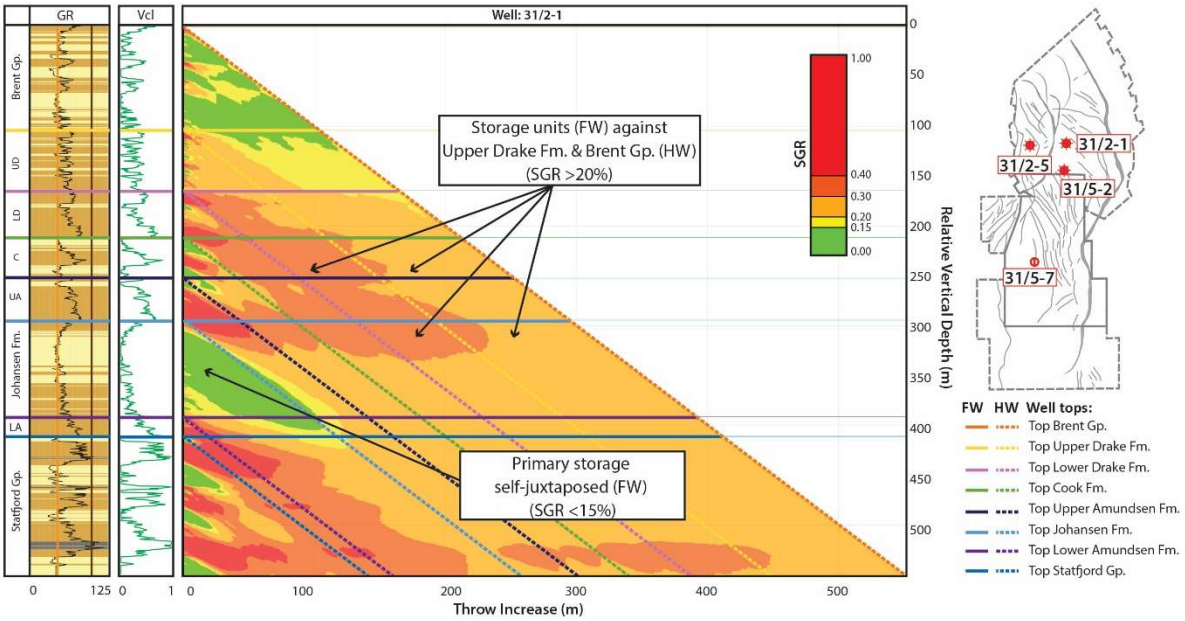

Figure 4.37 1D triangle diagram with SGR calculated for well 31/2-1. Gamma-ray log and normalized V_{cl} are presented to the left. For well 31/2-1 a sand-line at 40 API° and shale-line at 100 API° is chosen. Abbreviations: LA = Lower Amundsen Formation, UA = Upper Amundsen Formation, LD = Lower Drake Formation, UD = Upper Drake Formation.

Figure 4.38 shows a 1D triangle diagram with SGR values calculated using data from well 31/2-5. Well 31/2-5 is located in the hanging wall of the Svartalv Fault Zone, approximately 7.8–13.4 km northwest of Svartalv 1 and Svartalv 2. Similar to the aforementioned wells, the 1D triangle diagram in Figure 4.38 shows that when the storage units are self-juxtaposed, SGR values are generally low (<15%). At higher throws (>80 m), where the storage formations are juxtaposed against the Upper Drake Formation or the Brent Group, the SGR is generally high (>30%).

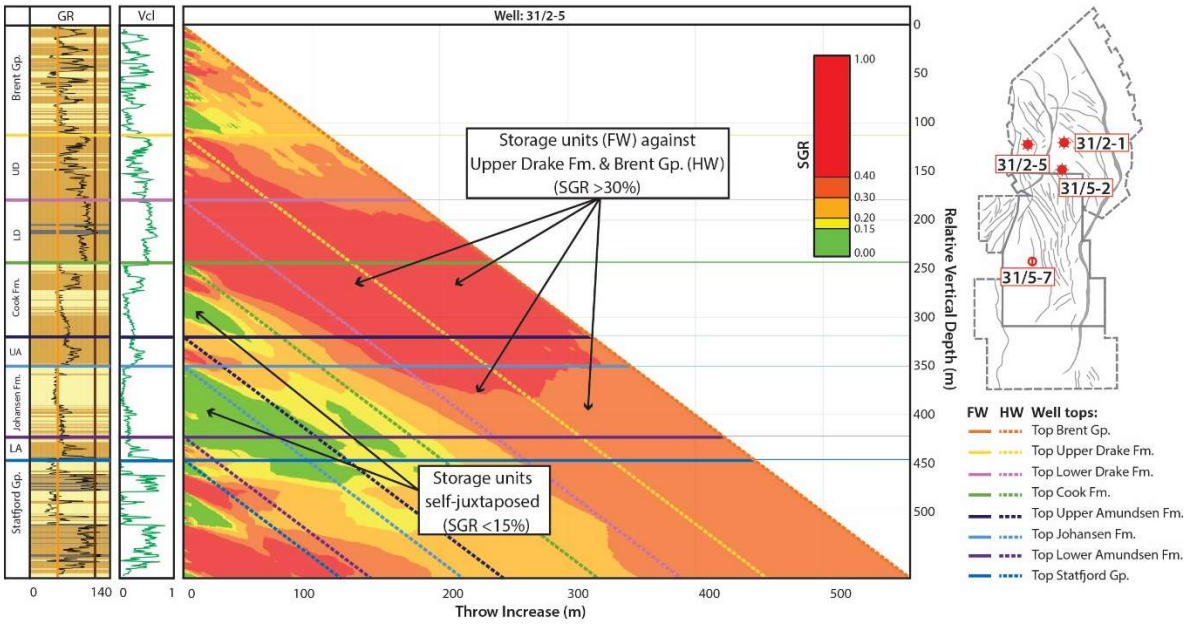

Figure 4.38 1D triangle diagram with calculated SGR for well 31/2-5. Gamma-ray log and normalized V_{cl} are presented to the left. For well 31/2-1 a sand-line at 40 API° and shale-line at 100 API° is chosen. Abbreviations: LA = Lower Amundsen Formation, UA = Upper Amundsen Formation, LD = Lower Drake Formation, UD = Upper Drake Formation.

The four wells show slightly different calculated SGR values, with well 31/2-1 showing the overall lowest SGR values and well 31/5-2 showing the highest. Some similarities are however present. For example, all wells show that in areas where the storage formations are self-juxtaposed the SGR is <15%. The clay-rich Upper Amundsen Formation becomes thicker northwards, from 7 m in well 31/5-7 to 31 m in well 31/5-2 and 31/2-5. Therefore, it contributes to higher SGR values (15–20%) in areas where the primary storage unit (FW) is juxtaposed against the secondary storage unit (HW). Furthermore, in areas where the storage formations (FW) are juxtaposed against the 'mixed sand' units of the Upper Drake Formation or the Brent Group (HW) the SGR generally >30%.

Synthesis of results presented in section 4.2 (i.e., thickness maps, throw measurements, juxtaposition diagrams, SGR diagrams, and 1D SGR triangle diagrams) provide background for a generalized overview of juxtaposition scenarios and membrane seal scenarios within the study area. First, faults can be categorized into one of the following generalized juxtaposition scenarios:

1) Second-order, W and SW-dipping faults where the storage units are primarily self-juxtaposed.
2) Second-order, E and NE-dipping faults where the primary storage unit (FW) is juxtaposed against the secondary storage unit (HW), and the secondary storage unit (FW) is juxtaposed against the primary seal (HW), creating potential juxtaposition seals.
3) First-order, W-dipping faults show more complex juxtaposition scenarios where parts of the storage formations (FW) are juxtaposed against 'mixed sand' (i.e., the Upper Drake Formation and the Brent Group; HW).

An overview of these juxtaposition scenarios within the upper parts of the storage units is presented in Figure 4.39. Within the primary storage unit, the most common juxtaposition scenario is sandstone on sandstone juxtaposition (Figure 4.39A). Some exceptions are present where E-dipping second-order faults with throws exceeding the thickness of the primary seal unit (>80 m) juxtapose the primary storage unit (FW) against the primary seal unit (HW). Along the Svartalv Fault Zone segments, multiple juxtaposition scenarios are present, including areas with potential juxtaposition seals. Within the secondary storage unit, E and NE dipping second-order faults exhibit potential juxtaposition seals, while W and SW dipping second-order fault exhibits sandstone on sandstone juxtapositions (Figure 4.39B). Along the Svartalv Fault Zone, the most common juxtaposition scenario is sandstone on 'mixed sand'.

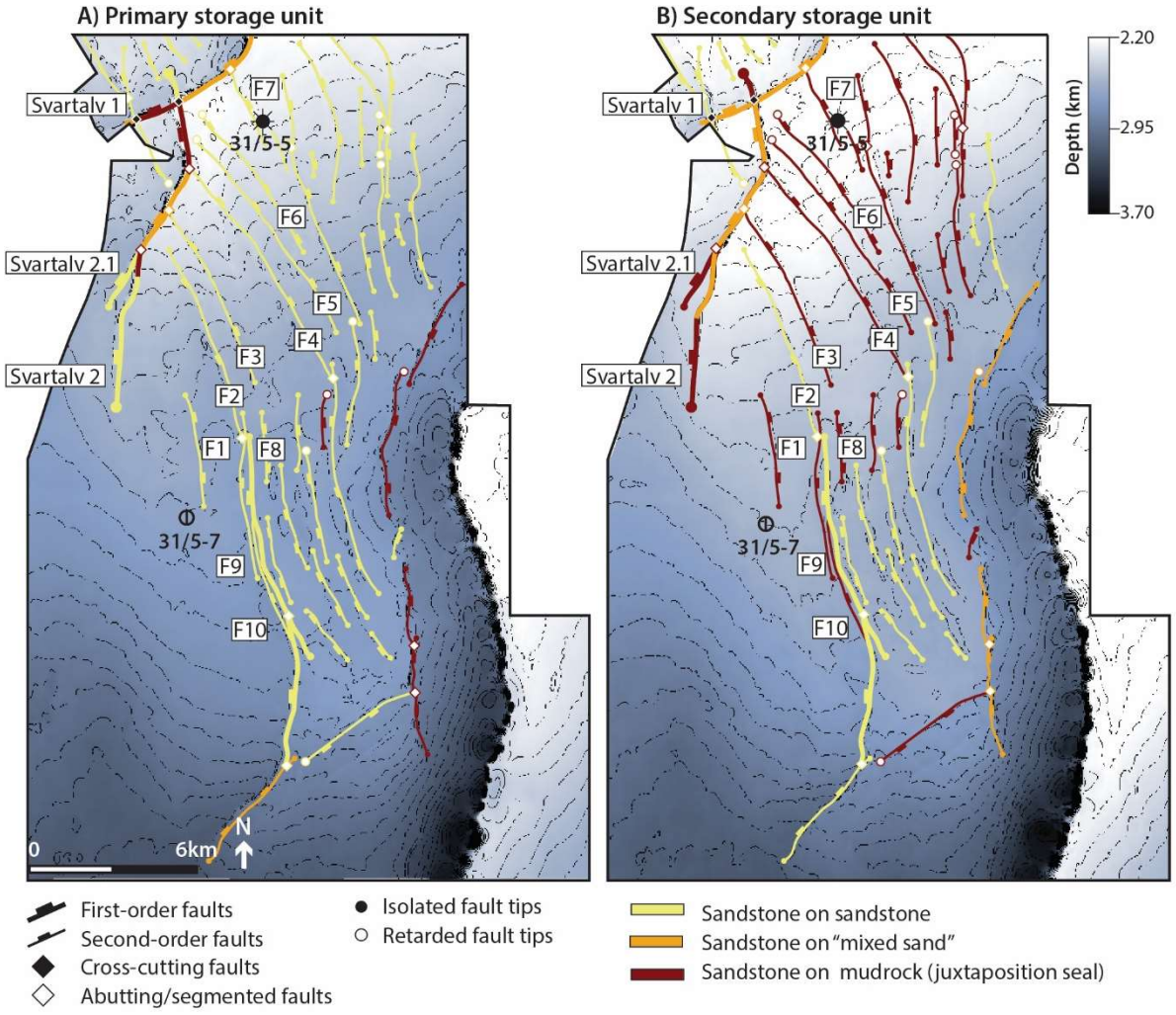

Figure 4.39 Maps showing the likely juxtaposition scenarios for the faults within the A) primary storage unit and the B) secondary storage unit. The depth maps are illustrated with 50-meter contour spacing.

A similar categorization can be made using information from the SGR diagrams and 1D SGR triangle diagrams. These results suggest that faults can be classified into one of the following generalized classifications:

1) Second-order, W and SW-dipping faults generally have SGR values <15% in both storage units.

2) Second-order, E and NE dipping faults have SGR values between 15–20% where the primary storage unit (FW) is juxtaposed against the secondary storage unit (HW), and SGR values >40% where the secondary storage (FW) unit is juxtaposed against the primary seal (HW).
3) First-order, W and NW dipping faults have SGR values >30–40% for juxtaposition scenarios involving both storage units.

An overview of these categorizations is illustrated in Figure 4.40. Cut-off values for SGR are set to follow the calibration by Yielding (2002) (Figure 3.12). In the primary storage unit, the majority of second-order faults north of well 31/5-7 have SGR values between 15–20%, while west-dipping faults located east of the well have SGR <15%. An exception from this generalization is F2, that have slightly higher SGR values (15–20%) at the fault tips (Figure 4.40A). Within the secondary storage unit, the majority of faults north of well 31/5-7 have SGR values exceeding 20%, while west-dipping faults east of the well have SGR <15% (Figure 4.40B). In both storage units, the calculated SGR along the Svartalv Fault Zone segments are >20%.

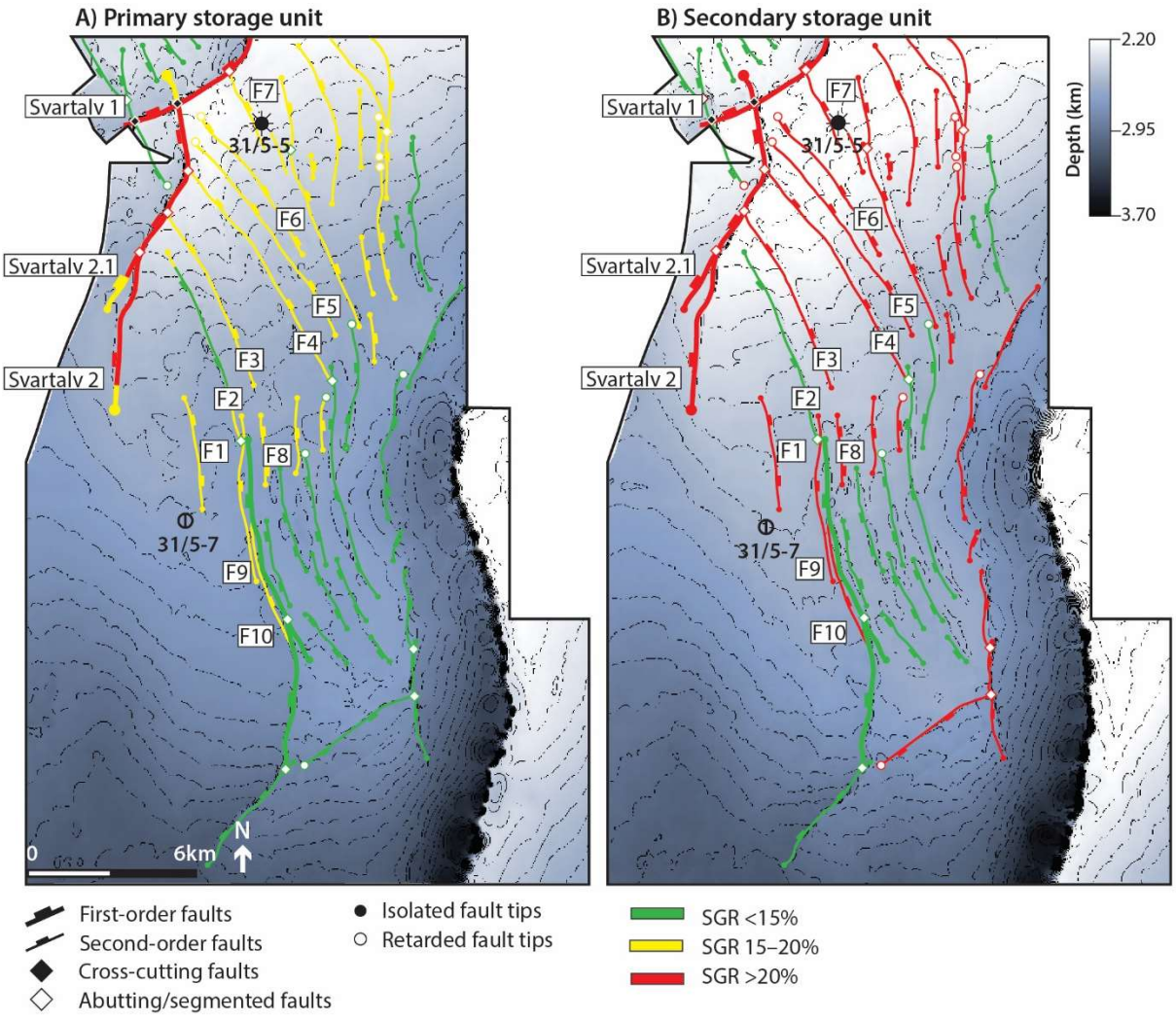

Figure 4.40 Maps showing the likely calculated SGR valued for the faults within the A) primary storage unit and the B) secondary storage unit. The depth maps are illustrated with 50-meter contour spacing.

5 Discussion

In the previous chapter, the structural and stratigraphic architecture, fault juxtaposition, and membrane seal diagrams of target faults are presented. In this chapter, these results are used to discuss the structural evolution (section 5.1), across fault seal assessment, plausible migration routes for injected CO_2, and gross rock volumes of structural closures (section 5.2). Furthermore, limitations and uncertainties in this study are discussed in section 5.3, and suggestions for further research in section 5.4.

5.1 Structural evolution

As presented in section 2.2, numerous studies have described the structural evolution of the northern North Sea and the Horda Platform (e.g., Ziegler, 1990; Færseth et al., 1995; Færseth, 1996; Christiansson et al., 2000). Due to their proximity to the Aurora storage site, five recent studies within the Smeaheia fault block (Mulrooney et al., 2020; Wu et al., 2021), the Troll West and East fields (Whipp et al., 2014; Duffy et al., 2015), and the Oseberg fields (Deng et al., 2017), are of particular interest. These studies serve as a basis for comparison against which the results in section 4.1 are discussed. In this discussion, special emphasis will be given to the timing and nucleation, lateral propagation, interaction, and extension directions.

5.1.1 Timing and nucleation

Synthesis of thickness maps (sub-section 4.1.2) and throw vs. depth profiles (sub-section 4.1.4) provide insight into the fault evolution and timing of the first- and second-order fault populations within the Aurora storage site. Furthermore, comparison with previous work (e.g., Bell et al., 2014; Whipp et al., 2014; Duffy et al., 2015; Mulrooney et al., 2020) corroborates the diachronous nature of Middle Jurassic to Early Cretaceous rifting (i.e., Rift Phase 2) in the Horda Platform area. The fault activity within the study area is discussed below and summarized in Figure 5.1.

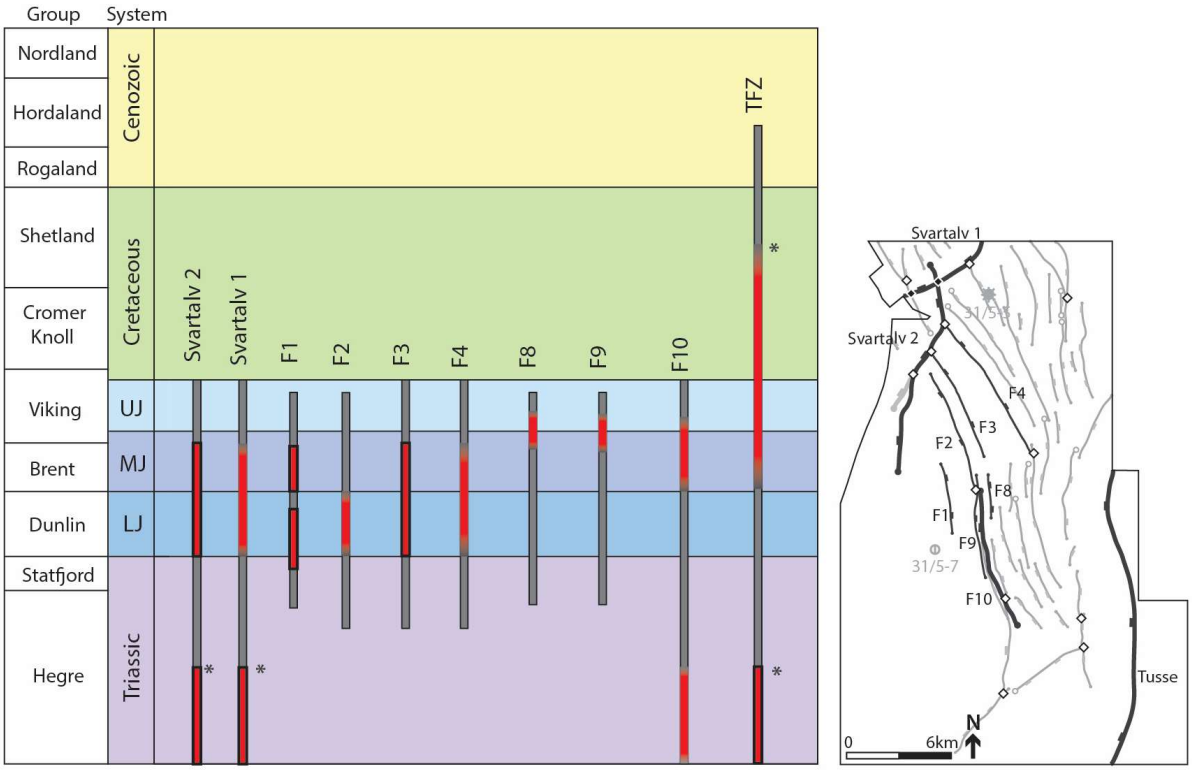

Figure 5.1 Fault activity diagram showing stratigraphic successions intersected by faults modelled in GN10M1. Grey bars represent simple displacement of successions, while red bars indicate fault activity. Fault activity for Svartalv 2, F1, and F3 are discerned from detailed measurements of E.I. indices, while additional information from modelled Jurassic cut-off lines and thickness-maps are used to suggest fault activity for the remaining faults. *Fault activity during the Cretaceous and Triassic for the Tusse Fault Zone (TFZ) farther north are from Bell et al. (2014) and activity in the Triassic for the Svartalv Fault Zone are from Whipp et al. (2014). Blurred red boxes indicate higher uncertainty regarding initiation and cessation of activity compared to solid boxes. Inset map shows the location of the faults. Abbreviations: LJ = Lower Jurassic, MJ = Middle Jurassic, UJ = Upper Jurassic.

5.1.1.1 Evolution of first-order faults

As presented in section 2.2, strain was focused in the northern Horda Platform during the Permian to Triassic (Rift Phase 1; Færseth, 1996). This led to the formation of large (>100 km long and up to 4 km throw) predominately N–S striking faults with basement-involvement (i.e., first-order faults), such as the Tusse and Svartalv fault zones (e.g., Færseth, 1996; Bell et al., 2014; Whipp et al., 2014).

The Svartalv 2 fault modelled in this study represents a segment of the Svartalv Fault Zone. The throw vs. depth profile for the first-order Svartalv 2 fault in Figure 4.19 shows a continuous increase in throw down-section from the Northern North Sea Unconformity Complex (NNSUC; Gabrielsen et al., 2001) to the basement-cover contact, with the maximum throw (approximately 650 meters) accumulated in the Triassic succession. This trend indicates that the fault nucleated in the Triassic successions, likely during Rift Phase 1 (Figure 5.1). This trend is also observed in the Tusse Fault Zone, the Vette Fault Zone, and the Øygarden Fault Complex which are all interpreted to have nucleated during Rift Phase 1 (e.g., Bell et al., 2014; Whipp et al., 2014; Duffy et al., 2015; Mulrooney et al., 2020).

In addition, hanging-wall growth can be used to evaluate fault activity of the Svartalv 2 segment by measuring expansion indices (E.I.; Thorsen, 1963). In Figure 4.19, E.I. over 1 (i.e., hanging-wall growth) is observed in all successions, except for the Upper Drake Formation, indicating syn-depositional fault activity. The largest E.I. value (1.44) is present within the Lower Jurassic primary storage unit, while a second lower-order E.I. peak (1.27) is observed in the Middle Jurassic Brent Group indicating periods of reactivation. Hanging-wall growth observed within the uppermost successions coincides with the NNSUC. Consequently, these E.I. measurements are less reliable indicators of fault activity as erosion of the footwall can lead to abnormally high E.I., (e.g., Thorsen, 1963; Jackson et al., 2017).

Furthermore, information on hanging-wall growth can be derived from thickness maps in sub-section 4.1.2. The thickness map of the Lower Jurassic Dunlin Group exhibits an overall increase in thickness towards the southwest (Figure 4.11). However, some growth is observed in the hanging wall of the Svartalv Fault Zone (E.I. = 1.47), and in the hanging wall of the southern part of the Tusse Fault Zone (E.I. = 1.36). The overlying Middle Jurassic Brent Group shows a more prominent hanging-wall growth across the Tusse Fault Zone segment (E.I. = 3.00; Figure 4.12). In contrast to the Dunlin Group, the growth in the hanging wall of the Svartalv Fault Zone segments is significantly smaller (E.I. between 1.05 and 1.14) in the Brent Group. Decreasing fault activity of the Svartalv Fault Zone up-section is also supported by the observation of decreasing throw up-section in the throw vs. length profiles for Svartalv 2 and Svartalv 1 (Figure 4.16 and Appendix 3). These observations indicate that the Svartalv Fault Zone became less active during the Middle Jurassic as faulting localized on the Tusse Fault Zone segment (Figure 5.1). Local growth (50 ms TWT) within the Brent Group in the hanging wall of the Svartalv and the Tusse fault zones is also reported in the Troll West and East fields (Whipp et al., 2014), and some authors suggest that the initiation of Rift Phase 2 coincided, in places, with the deposition of the uppermost Brent Group (Helland-Hansen et al., 1992).

However, the expansion indices observed herein for the Brent Group along the Tusse Fault Zone are small compared to those observed in the Troll Fault System further west (Whipp et al., 2014) and in the Lower to mid-Upper Jurassic successions in the Troll West field (Bell et al., 2014; Duffy et al., 2015). Furthermore, the hanging-wall growth observed within the study area could also be influenced by differential compaction (e.g., coals in the Ness Formation) which may have modified the depositional geometry of the succession (Whipp et al., 2014). In light of these observations, there are some uncertainties related to the reactivation of the Tusse Fault Zone during Middle Jurassic observed locally within the study area (Figure 5.1).

5.1.1.2 Evolution of second-order faults

As presented in section 2.2, NW–SE striking second-order faults formed in the Oseberg fields during Early to Middle Jurassic, while both N–S and NW–SE striking second-order faults formed in the Oseberg fields, the Troll fields, and the Smeaheia fault block during Middle Jurassic to Early Cretaceous (Whipp et al., 2014; Duffy et al., 2015; Deng et al., 2017; Mulrooney et al., 2020). In the Aurora storage site, there is no obvious hanging-wall growth observed across the second-order faults in the modelled thickness maps (sub-section 4.1.2). Therefore, detailed throw vs. depth profiles of the F3 and F1 faults are used to discuss the fault evolution and timing of the second-order faults within the study area.

The second-order F3 fault is representative of multiple NW–SE striking faults within the Aurora storage site. The throw vs. depth profile for F3 in Figure 4.20 shows a distinctively different geometry compared to the first-order Svartalv 2 segment, with throw maximum located in the Top Statfjord Group and decreasing throw up- and down-section. Hanging-wall growth is observed in the interpreted Jurassic successions, with the maximum expansion index (E.I. = 1.16) located in the Lower Jurassic secondary storage unit indicating the time of fault nucleation and maximum fault movement. Similar expansion indices (E.I. between 1.1 and 1.4) are observed across NW–SE striking second-order faults in the Oseberg fields, which nucleated during Early to Middle Jurassic (Deng et al., 2017). Similar to Svartalv 2, F3 has a flat upper tip-line coinciding with the NNSUC which indicates that the fault tip was eroded during the development of the NNSUC, and as a result, leads to unreliable E.I. measurements.

The second-order F1 fault, on the other hand, shows no flat upper tip-line indicating that the upper fault tip was not eroded (and/or did not breach the free surface; Figure 4.21). F1 shows a maximum throw and expansion index (E.I. = 1.03) located in the Late Triassic to Early Jurassic successions indicating the depth of fault nucleation and activity (Figure 5.1). However, F1 has a second (lower order) throw maximum and E.I. measurement located within the Middle Jurassic successions. This secondary throw maximum can be seen as reactivation of the fault during Early to Middle Jurassic (Figure 5.1), or vertical linkage of two separate faults (i.e., dip-linkage).

While detailed throw vs. depth profiles and expansion indices were created for three faults, the vertical throw trend and expansion indices of Early to Middle Jurassic successions was estimated using modeled cut-off lines of six additional faults (Table 4.1 and Appendix 3). The results show that, while some variations occur, the general trend is that second-order, predominately NW–SE striking faults, located in the northwestern half of the study area exhibit decreasing throw and expansion indices up-section. On the contrary, N–S striking faults located in the eastern half of the study area generally exhibit the opposite trend, with increasing throw up-section and no growth in the Lower Jurassic Dunlin Group. Combining these observations with information from the detailed throw vs. depth profiles and expansion indices, a generalized trend can be suggested where NW–SE striking second-order faults

formed during the Early to Middle Jurassic, while the N–S striking second-order faults formed later, potentially during the Middle Jurassic to Early Cretaceous (Rift Phase 2; Figure 5.1).

Previous studies evaluating the evolution of second-order faults located in the Smeaheia Fault Block (Mulrooney et al., 2020) and the Troll West and East fields (Bell et al., 2014; Whipp et al., 2014; Duffy et al., 2015) found that they formed during the Late Jurassic to Early Cretaceous. In contrast, a study evaluating the evolution of second-order faults in the Oseberg fields found that NW–SE striking second-order faults formed earlier, during Early Jurassic to Middle Jurassic times while N–S striking second-order faults formed during Middle Jurassic to Early Cretaceous (Deng et al., 2017). In addition, due to the relatively high expansion indices (E.I. >1.1) measured across the NW–SE striking second-order faults, Deng et al. (2017) suggest that the late stages of the inter-rift phase experienced relatively strong tectonic rifting. The observations within the Aurora storage site made herein, show strikingly similar observations to Deng et al. (2017) in terms of nucleation and hanging-wall growth. Furthermore, a comparison of fault evolution and timing made herein with previous work supports the diachronous nature of Rift Phase 2 with the youngest faults located towards the east (Bell et al., 2014).

5.1.2 Lateral propagation and interaction

Synthesis of the maximum throw vs. length plot (Figure 4.14B), the Top Cook Formation depth-structure map (Figure 4.13), fault throw diagrams, and throw vs. length profiles (Figure 4.16, Figure 4.17, Figure 4.18, and Appendix 3) provide evidence for fault growth, lateral propagation, nucleation sites, and interaction styles.

The maximum throw vs. length plots in Figure 4.14B can be used to validate the analysis of modelled faults and assess fault growth trends (e.g., Kim and Sanderson, 2005). All faults mapped within the study area plot adjacent to the 1:100 line, with a spread from the 1:10 to the 1:1000 line, which is a typical trend for normal faults (e.g., Kim and Sanderson, 2005). Moreover, this trend aligns with measurements from the Troll West and East fields (Whipp et al., 2014) and the Smeaheia fault block (Wu et al., 2021), further corroborating the analysis herein.

As introduced in sub-section 3.1.1, there are currently two fault growth models, here called the ‘propagation’ (Walsh and Watterson, 1988; Trudgill and Cartwright, 1994; Cartwright et al., 1995) and the ‘constant length’ fault growth models (Walsh et al., 2002; Walsh et al., 2003). On the one hand, Figure 4.14B shows that when plotting a linear trendline through the measurements of maximum throw and length, similar T_{max}/L ratios and coefficient of explanation (R^2) to those in Whipp et al. (2014) are obtained. Assuming that faults within the Aurora storage site represent slightly different stages throughout the fault life, the observation that the two fault populations have a constant relation between the maximum throw and length are in accordance with the propagation fault growth model by Walsh et

al. (2002) and Walsh et al. (2003). On the other hand, different T_{max}/L ratios are observed when plotting individual trendlines through the two fault populations (Figure 4.14B). The first-order faults have approximately twice as high maximum throw vs. length ratios ($T_{max}/L = 0.015$) compared to the second-order faults ($T_{max}/L = 0.008$). As discussed in the previous sub-section, first-order faults are interpreted to be older and more mature than second-order faults. Therefore, the difference in T_{max}/L ratios between the two fault populations is in accordance with the theories behind the constant length growth model by Walsh et al. (2002) and Walsh et al. (2003), which argue that progressive increase in T_{max}/L ratio could reflect fault system maturity.

However, a more detailed investigation is needed to explain fault growth trends and to draw more firm conclusions. For instance, some second-order faults in Figure 4.14B have higher T_{max}/L ratios compared to the first-order faults. Furthermore, the measurements in Figure 4.14B are obtained from the Lower Jurassic Top Cook Formation. As discussed in sub-section 5.1.1, the first-order faults likely nucleated in Triassic successions while the second-order faults nucleated during Early to Middle Jurassic and Middle Jurassic to Cretaceous (potentially). Therefore, these measurements are unlikely to represent the absolute maximum throw for all faults within the study area. In addition, the measurements are plotted on a logarithmic scale which may unintentionally mask variability and statistical spread (Rotevatn et al., 2019). Finally, other factors such as i) material properties (Cowie and Scholz, 1992), ii) errors in measurements (further discussed in sub-section 5.3.2; Gillespie et al., 1992), iii) segmentation and linkage (e.g., Peacock and Sanderson, 1991), and iv) reactivation of pre-existing structures (Kim et al., 2001) can affect the ratios.

In addition to understanding how faults within the Aurora storage site evolved over time, it is important to understand how these faults propagated and interacted. This is particularly important in CO_2 storage sites as hard-linked faults could create structural closures for CO_2 to accumulate in while soft-linked faults may serve as lateral conduits for CO_2 migration (Rotevatn et al., 2007). Four types of fault tip interaction was assessed herein; isolated, retarded, abutting, and cross-cutting, similar to the approach presented in Duffy et al. (2015). Focus is placed on describing the different interaction styles for the Svartalv 2, F3, and F1 fault using throw vs. length profiles (Figure 4.16C, Figure 4.17B, and Figure 4.18B), while additional information from six throw vs. length profiles are provided in Appendix 3.

The Svartalv 2 segment in Figure 4.16 shows a step-like throw vs. length profile indicating hard-linkage with nearby faults (e.g., Duffy et al., 2015). The steps in throw, which are in the footwall of Svartalv 2 at the intersection with the F3 and F4 faults, suggest that the lateral propagation of the second-order faults was impeded during Early to Middle Jurassic when they encountered the Svartalv 2 segment. A larger step in throw, displacing both the hanging wall and footwall cut-off lines, occurs where Svartalv 1 crosscuts the Svartalv 2 (throw vs. length profile for Svartalv 1 is shown in Appendix 3). This may indicate that the two first-order faults were hard-linked prior to the deposition of the Lower to Middle

Jurassic successions, potentially during the Permian to Triassic rift phase (Rift Phase 1). As the faults became reactivated during the Early Jurassic to Middle Jurassic, they accumulated throw as a thoroughgoing fault.

The F3 fault in Figure 4.17 is representative of an NW–SE striking second-order fault north of well 31/5-7 that nucleated during Early to Middle Jurassic (Figure 5.1). The 3D fault throw diagram and the throw vs. length profile in Figure 4.17 show that the maximum throw is located approximately 500 m southeast of the intersection with Svartalv 2 and that the throw gradient is steeper towards this intersection. This suggests that the fault nucleated away from Svartalv 2. As the fault grew it abutted against and became hard-linked with Svartalv 2 after which further extension led to mutual throw at the intersection point. A similar trend is observed for F4, which indicate hard-linkage with Svartalv 2 (Appendix 3). In contrast, F1 in Figure 4.18 shows a near symmetrical throw vs. length profile indicating that the fault grew with isolated fault tips and little interaction with nearby faults.

The fault trace map in Figure 4.13, summarizing the various interaction styles within the study area, shows that approximately 50% of second-order fault tips are isolated from the first-order faults, 30% abut against them, and 20% show evidence that the propagation has been retarded by them. A similar pattern is found in the Troll West field, where approximately 60% of the second-order faults are isolated, ca. 30% abut, and ca. 10% are retarded by the first-order faults (Duffy et al., 2015). Herein, cross-cutting interactions are only observed in two places where the Svartalv 1 cross-cuts the Svartalv 2 fault, and where a second-order fault cross-cut the Svartalv 1 fault (e.g., Figure 4.13). These observations likely reflect that the first-order fault population is more developed and mature compared to the second-order, a suggestion supported by the observations in the Troll West and East fields (Duffy et al., 2015). Moreover, the observation that the second-order faults abut against and become retarded by the first-order faults, suggests that the first-order faults have acted as barriers and perturbed the stress field, thus restricting the lateral propagation of the second-order faults in accordance with the findings of Henza et al. (2010) and Duffy et al. (2015).

5.1.3 Extension directions

While most authors agree that the extension direction during Rift Phase 1 was approximately E–W oriented (e.g., Færseth, 1996; Bell et al., 2014), there is no consensus on the direction of extension during Rift Phase 2. As mentioned in sub-section 2.2.4, some authors suggest that the extension direction remained E–W oriented throughout both rift phases (Badley et al., 1988; Brun and Tron, 1993), while others suggest that it changed. For example, from E–W oriented during Rift Phase 2, to NE–SW oriented during the late inter-rift period and then back to E–W during Rift Phase 1 (Deng et al., 2017).

The interpretations herein on fault nucleation in the Aurora storage site, suggest that the N–S striking first-order faults nucleated during Rift Phase 1 (i.e., Permian to Triassic), second-order predominately NW–SE striking faults nucleated during the late inter-rift period (i.e., Early Jurassic to Middle Jurassic), and N–S striking second-order faults nucleated during Rift Phase 2 (i.e., Middle Jurassic to Early Cretaceous; Figure 5.1). Rose diagrams are presented in Figure 5.2 to show the variations in strike for faults that nucleated during Rift Phase 1, late inter-rift phase, and Rift Phase 2.

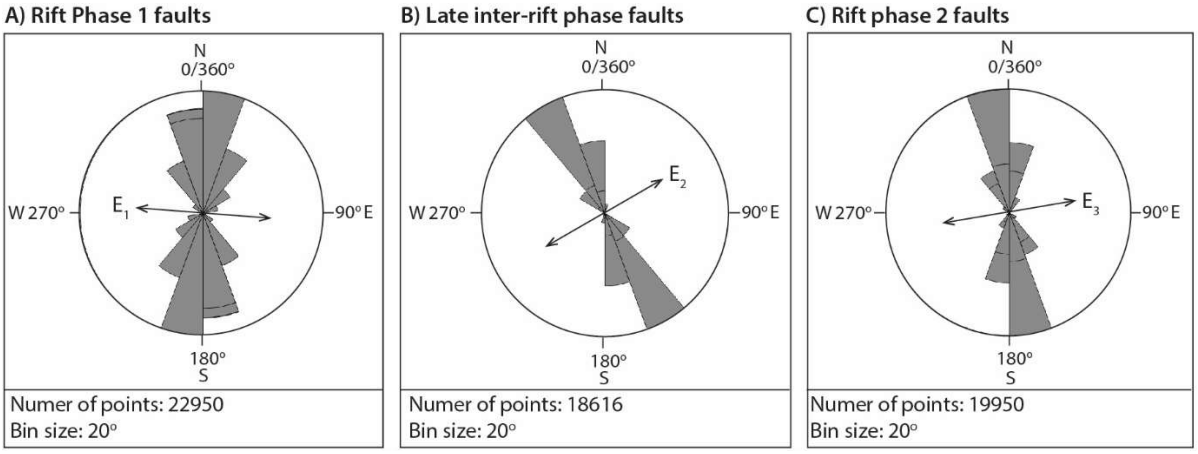

Figure 5.2 Rose diagrams showing the variations in strike for A) faults nucleated during Rift Phase 1, B) faults developed during late inter-rift phase, and C) faults developed during Rift Phase 2. Proposed extension directions are illustrated in the rose diagrams (E_1, E_2, and E_3) perpendicular to the main strike orientation. The location of the faults within the study area is illustrated in Figure 5.3.

An estimation of extension direction based on local observations within the Aurora storage site is presented in Figure 5.2. These extension directions are based on a simplified assumption, that newly formed faults develop perpendicular to the extension direction and are close to dip-slip (Anderson, 1951). Similar assumptions are made in the assessment of extension directions within the Oseberg field (Deng et al., 2017) and in the generic model presented by Whipp et al. (2014).

Figure 5.2A shows that the faults nucleating during Rift Phase 1 (i.e., first-order faults) are approximately N–S oriented with the largest frequency of strike orientation being 187°. This indicates that the faults developed in approximately E–W (277°) extension direction. E–W extension during Rift Phase 1 is further supported by the observation of corrugations with approximately the same orientations (~270°) in the Svartalv 2 fault plane (Figure 4.16A), which are generally assumed to indicate movement direction (Needham et al., 1996; Lohr et al., 2008).

Figure 5.2B shows that faults nucleating during the late inter-rift period (i.e., second-order faults) have an approximately NW–SE orientation with the largest frequency of strike being 333°, indicating approximately NE–SW (243°) extension direction. This represents a 34° anticlockwise rotation in extension direction between the rift phases. The proposed NE–SW extension direction is also supported by the presence of an approximately NW–SE striking second-order fault cross-cutting a NE–SW segment of the Svartalv Fault Zone (Figure 5.3). Faults that cross-cut pre-existing faults are good

indicators of extension direction as they do not appear to be influenced by the pre-existing faults (e.g., Tomasso et al., 2008; Bell et al., 2014).

Figure 5.2C shows that second-order faults, which are interpreted to have formed during Rift Phase 2, are predominately N–S striking with the largest frequency of strike being 350° which suggests an extension direction that is approximately E–W (260°) oriented. This represents a 17° clockwise rotation in extension direction from the late inter-rift period. The proposed E–W oriented extension during Rift Phase 2 (Figure 5.3B) is supported by the nucleation of both predominately N–S striking second-order faults and reactivation of the approximately N–S striking Tusse Fault Zone segment. Again, the proposed variations in extension directions show similarities to those proposed by Deng et al. (2017) in the Oseberg fields corroborating the interpretations herein.

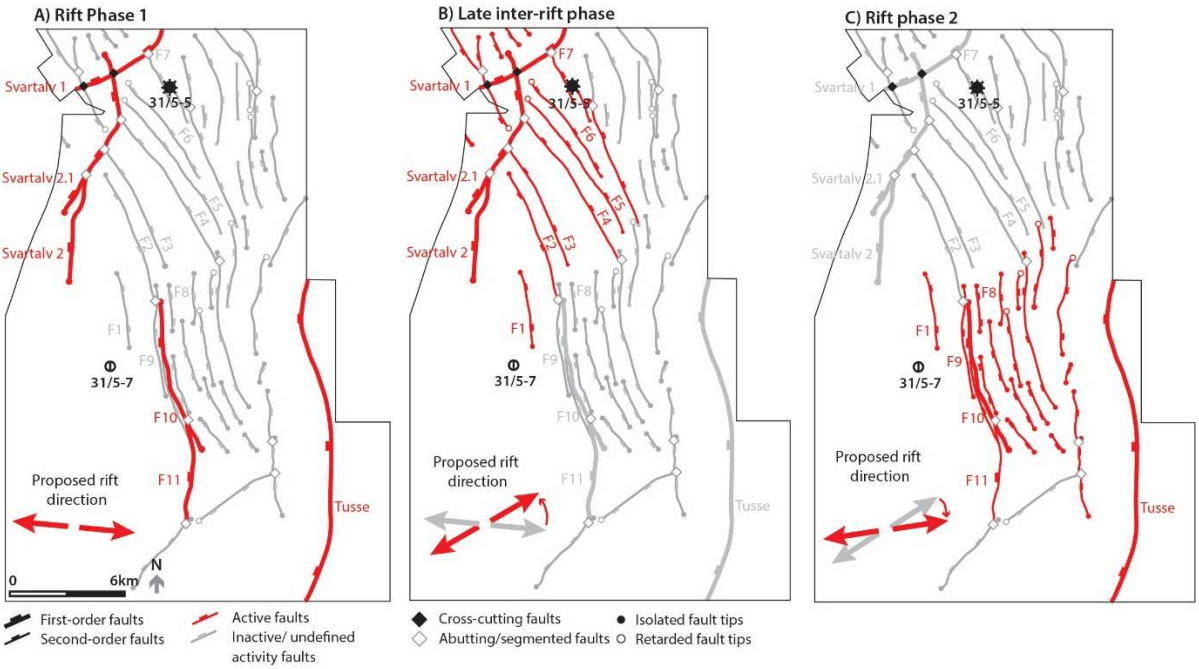

Figure 5.3 Fault trace map showing the location of faults that were active during A) Rift Phase 1 (Permian to Triassic), B) late inter-rift phase (Early Jurassic to Middle Jurassic), and C) Rift Phase 2 (Middle Jurassic to Early Cretaceous). Active faults are highlighted in red while inactive faults or faults with undefined fault activity are highlighted in grey. The proposed extension direction from Figure 5.2 is illustrated with red arrows with grey arrows representing the previous rift orientation.

As mentioned, the above analysis is derived from an assumption that faults develop perpendicular to the extension direction, which implies that newly formed second-order faults develop relatively independently of pre-existing structures. This assumption is however disputed. Maerten et al. (2002) used geomechanical modelling to demonstrate that stress perturbations surrounding large segmented structures with varying fault strike, such as the firs-order faults modelled herein, can cause reorientation of the stress field and nucleation of faults oblique to the extension direction. Furthermore, Henza et al. (2010) demonstrated, using scaled experimental models, that pre-existing structures have direct control on the size and strike of faults that form during subsequent phases of extension.

It is, therefore, possible that the reactivation of the Svartalv Fault Zone, which displays variation in fault strike (Figure 5.2), during the late inter-rift phase was caused by approximately E–W extension, and that stress perturbations surrounding these faults resulted in local NE–SW oriented extension and nucleation of approximately NW–SE oriented faults within the study area (Whipp et al., 2014; Duffy et al., 2015; Phillips et al., 2019). This interpretation is in support of the suggestion that regional extension remained E–W oriented throughout the rift phases (Badley et al., 1988; Brun and Tron, 1993). Furthermore, faults within the study area display along-strike variations, and some faults (e.g., Svartalv 1) are approximately NE–SW oriented, which indicates that they are oriented unfavorably for nucleation or reactivation with regards to the proposed extension directions. It is therefore likely that the structural evolution of the Aurora storage site is more complex than the overview presented herein (Figure 5.3).

Bearing these observations in mind, the discussion in section 5.1 regarding fault nucleation, propagation, interaction, and extension directions within the Aurora storage site can be summarized as follows:

1) E–W oriented extension during Permian to Triassic (Rift Phase 1) led to the development of basement involved N–S striking faults, such as the Svartalv and Tusse fault zones (Figure 5.3A).
2) Extension rotated anticlockwise (34°) during Early to Middle Jurassic (late inter-rift phase) to approximately NE–SW orientation which led to formation of approximately NW–SE oriented second-order faults and reactivation along the Svartalv Fault Zone (Figure 5.3B).
3) During the late inter-rift phase, the first order Svartalv Fault Zone acted as a barrier for lateral propagation of the NW–SE striking second-order faults as observed by abutting or retarded fault tips.
4) Clockwise rotation (17°) from the late inter-rift phase to approximately E–W rift orientation during Middle Jurassic to Early Cretaceous (Rift Phase 2) likely localized strain along the Tusse Fault Zone segment and led to formation of N–S striking second-order faults (Figure 5.3B).

These interpretations are consistent with the finding that the initiation of Rift Phase 2 was diachronous and that faults towards the east are younger (e.g., Bell et al., 2014). Moreover, they suggest that the late inter-rift period was more active than previously assumed, as advocated by Deng et al. (2017).

5.2 Across-fault seal assessment and CO_2 migration pathways

The structural and stratigraphic architecture of the study area, presented in section 4.1 and across-fault seal analysis presented in 4.2, provides a framework in which plausible CO_2 migration pathways can be discussed. In the following sub-sections, CO_2 migration pathways are discussed solely based on the presence of fault juxtaposition seals (sub-section 5.2.1) or membrane seals (sub-section 5.2.2) for the

primary and the secondary storage units. Plausible migration paths near injection well 31/5-7 and gross rock volumes of three triangular two-way closures are discussed in sub-section 5.2.3.

5.2.1 Fault juxtaposition seals

As mentioned in sub-section 3.1.2, fault juxtaposition assessment is a widely used method to predict fault seals (e.g., Lyon et al., 2005; Bretan et al., 2011; Mulrooney et al., 2020) and Færseth et al. (2007) suggest that they have a higher probability of sealing compared to, for example, membrane seals. This sub-section describes a scenario solely based on the presence of juxtaposition seals and their effect on fault transmissivity and CO_2 migration paths. As introduced in sub-section 3.1.2, in a juxtaposition scenario two assumptions are made; i) juxtaposition of the storage unit against a low-permeability lithology creates a barrier to migrating fluids, and ii) juxtaposition of the storage unit against the same, or another high-permeability units is likely to allow across-fault migration of fluids (Allan, 1989).

As suggested in sub-section 4.2.2, the modelled faults within the study area can be categorized into one of three juxtaposition scenarios based on the throw, dip-direction, and relative position of faults with respect to the injection well (31/5-7). Assumptions are made that; i) well 31/5-7 will be used as an injection well, ii) CO_2 will be injected into both storage units, iii) CO_2 will rise to the top of the porous and permeable storage units and migrate up-dip due to buoyancy and density contrasts, and iv) the Upper Amundsen Formation, located between the two storage units, provide a more or less efficient flow baffle. Combining the juxtaposition scenarios with the assumptions mentioned above, faults within the Aurora storage site are likely to affect migration of CO_2 in one of the following ways (Figure 5.4):

1) Second-order, W and SW dipping faults allow across-fault migration within both storage units (Figure 5.4A).
2) Second-order, E and NE dipping faults allow CO_2 to migrate from the primary storage (FW) to the secondary storage unit (HW) and potentially baffle CO_2 in the secondary storage unit (Figure 5.4A).
3) First-order, W and NW dipping faults potentially allow CO_2 to migrate from the storage units (FW) and into the Upper Drake Formation or the Brent Group (HW; Figure 5.4B).

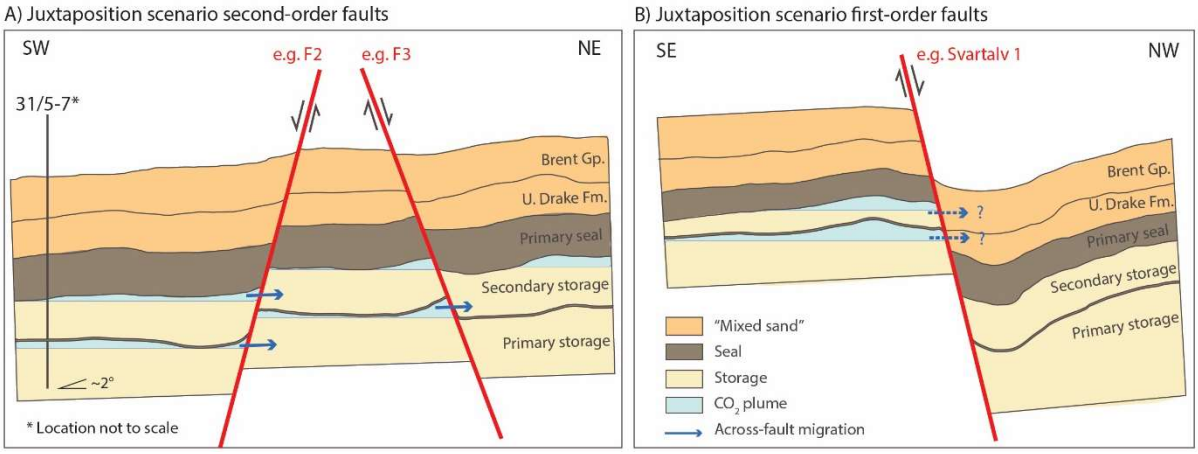

Figure 5.4 Conceptual cross-sections showing CO_2 migration within the storage units. Three scenarios are shown only considering juxtaposition seals: A) migration through two second-order faults with opposite dip-direction (SW and NE) and B) migration through a first-order NW dipping fault. The F2, F3, and Svartalv 1 faults are used as examples as they are representative of one of the three juxtaposition scenarios mentioned above. The CO_2 plume is illustrated in a fill-to-spill scenario and the thickness of the Upper Amundsen Formation is inferred.

Plausible CO_2 migration routes within the two storage units where fault juxtaposition seals are the only sealing mechanism are presented in Figure 5.5. In Figure 5.5A most of the second-order faults will cause sandstone on sandstone juxtaposition and are less likely to create baffles or barriers to migrating CO_2, in a juxtaposition scenario. However, CO_2 can migrate from the primary storage unit and into the secondary storage unit as it encounters multiple northeast dipping second-order faults to the north (Figure 5.4A).

Buoyant CO_2 will likely migrate northwards and encounter Svartalv 2 approximately 9.9 km north of injection well 31/5-7 where the primary storage unit is juxtaposed against a 'mixed sand' unit (i.e., the Upper Drake Formation). Depending on how sand-rich these units are, the CO_2 could potentially migrate across the fault or continue northeastward within the footwall. At the northern part of the study area, the Svartalv 1 fault juxtaposes the primary storage unit against 'mixed sand' units (i.e., the Upper Drake Formation and the Brent Group). Again, the sealing potential of these successions will decide if the CO_2 migrates across the fault or becomes trapped in the footwall until a certain CO_2 column height is reached (i.e., a spill point), and migration northeastwards out of the study area. The final structural closure is estimated to be located approximately 20 km north of well 31/5-7 and 400 m below the flatspot of the Troll West field (Bretan et al., 2011; Furre et al., 2020).

In Figure 5.5B, most of the northeast dipping faults juxtapose the upper parts of the secondary storage (FW) against the primary seal (HW) and are, therefore, more likely to influence the migration of CO_2 by channeling it northwestward towards the Svartalv Fault Zone segments. Again, the Svartalv 2 and Svartalv 1 faults offset the entire primary seal unit and, therefore, juxtapose the storage unit against 'mixed sand' units (i.e., Upper Drake Formation and Brent Group) potentially allowing CO_2 to migrate across the fault (Figure 5.4B). The presence of potential juxtaposition seals along the NE dipping second-order faults could temporarily delimit or prevent CO_2 from migrating northeastward and rather

accumulate in the footwall, thereby increasing the pressure of CO_2 against the Svartalv Fault Zone segments.

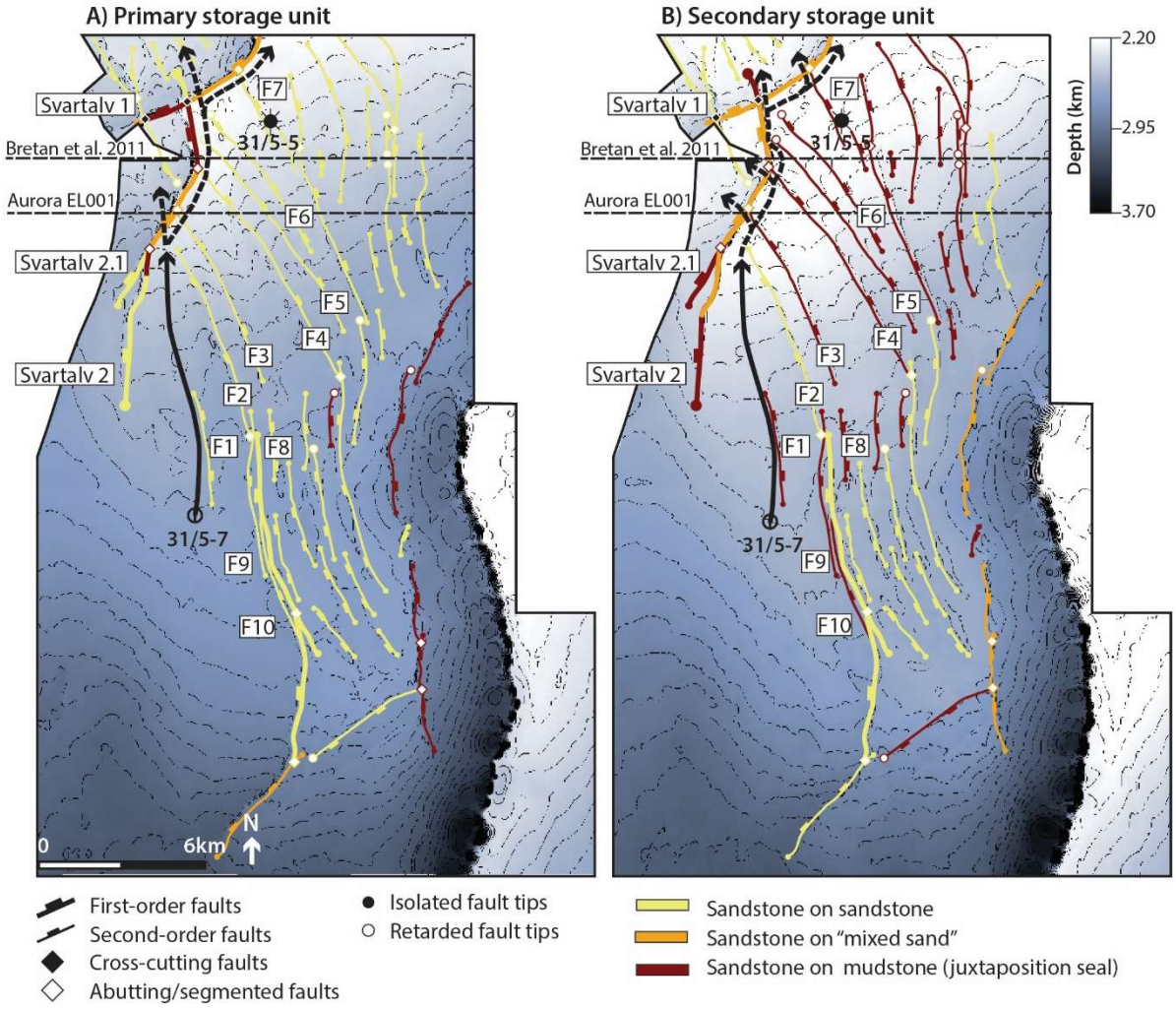

Figure 5.5 Depth-structure maps showing the juxtaposition scenarios for faults within A) the primary storage unit and B) the secondary storage unit. Arrows indicate potential migration routes, drawn perpendicular to the contour lines. Solid lines indicate more plausible migration routes than the dashed lines. Contour spacing is 50 meters. The southern extent of the study area in Bretan et al. (2011) and the northern extent of the Aurora Exploitation License (EL001) is shown on the map.

As seen in Figure 5.5, in a juxtaposition seal scenario, northwards migrating CO_2 within both storage units could potentially migrate across the Svartalv Fault Zone segments and out of the storage units into the 'mixed sand' lithologies of the Upper Drake Formation and the Brent Group. Previous studies performing fault juxtaposition analysis have been conducted within the Troll West field (Bretan et al., 2011) and overlap the northern part of the study area herein (Figure 5.5). When comparing the work herein with previous studies it is important remember that the primary and secondary storage units interpreted herein which include the Johansen and Cook formations also include the Upper and Lower Amundsen formations (sub-section 3.3.2). Furthermore, it is important to note that Bretan et al. (2011) only considered the Johansen Formation as a storage unit and that it was conducted prior to drilling well 31/5-7. Regardless, Bretan et al. (2011) found similar results, in that the Johansen Formation becomes

juxtaposed against the Upper Drake Formation and the Brent Group along the Svartalv 1 fault. They also show that within the Troll West field (just north of the Aurora storage site) the throw of Svartalv 1 increases and the Johansen Formation becomes juxtaposed against the Fensfjord and Krossfjord formations, which are hydrocarbon-bearing in the Troll West field. Migration of injected CO_2 into these formations is undesirable, if it occurs prior to the end of the field life, as it could conflict with production (e.g., Gassnova, 2012).

In addition, the report by Gassnova (2012), covering the majority of the Aurora Exploitation License (EL001), the study area, and the Troll fields, is worth mentioning. The report evaluated the across-fault juxtapositions along both the Svartalv 1 and Svartalv 2 faults (albeit at a lower resolution) and included the Cook Formation as a storage unit. Overall, the report shows similar results to this study, observing juxtaposition of the storage units against the Upper Drake Formation and the Brent Group along the Svartalv 1 and Svartalv 2 faults. The report by Gassnova was, similar to Bretan et al. (2011), conducted prior to the drilling of well 31/5-7 and as a result, the well control is less precise within the study area compared to this thesis (see Table 3.5 in sub-section 3.3.2). Based on the across-fault juxtaposition analysis, Gassnova (2012) stated that there is a risk of migration across the Svartalv Fault Zone and therefore proposed that the injection well should be drilled approximately 12 km further south of well 31/5-7. However, the current assessment of the Svartalv Fault Zone by Equinor (2019), using recently acquired 3D seismic data (CGG17M01), is that the fault is sealing despite the juxtaposition of storage units against the Brent and lower Viking groups and that the well needed to be drilled further north to encounter more suitable reservoir sandstones for CO_2 injection.

5.2.2 Membrane seals

While membrane seals have been observed to occur in hydrocarbon fields (e.g., Yielding et al.; Fristad et al., 1997; Lyon et al., 2005; Færseth et al., 2007), there are still considerable limitations related to the methods used to predict them, such as the SGR method applied herein (further discussed in sub-section 5.3.3). In this sub-section, the effect of membrane seals on migration of CO_2 is assessed. As previously mentioned, the calculated SGR values herein are compared to calibrated values from Yielding (2002) which assumes that areas with; i) SGR less than 15% are 'leaking', ii) SGR between 15–20% represents a threshold between 'leaking' and 'sealing', and iii) SGR >20% are 'sealing' (sub-section 3.1.2; Yielding, 2002; Yielding et al., 2010).

An advantage of using the SGR method is that it includes information from thin, clay-rich units that have not been mapped in this study, for example, the Upper Amundsen Formation. The clay-rich Upper Amundsen Formation is only 7 meters thick in the injection well (31/5-7) but becomes thicker (up to 31 m) towards the north in wells 31/5-2 and 31/2-5. Moreover, the primary seal (i.e., the Lower Drake Formation) which is 53 meters thick in well 31/5-7 becomes slightly thicker towards the north (~60 m

in wells 31/5-2 and 31/2-5). Well logs from 31/5-2 and 31/2-5 also show relatively high gamma-ray contents for the Upper Amundsen Formation (~80 API) and the Lower Drake Formation (~100 API). The calculated SGR increases with increasing thickness of clay-rich units and, as a result, it is expected that the SGR values increase towards the north. This trend is also observed in the 1D triangle diagrams, where the Upper Amundsen Formation and the primary seal contribute to higher SGR values in wells 31/5-2 and 31/2-5 (Figure 4.36, Figure 4.38).

Based on the categorizations of membrane seal scenarios in sub-section 4.2.2, and the calibrations by Yielding (2002), generalized interferences on how membrane seals will affect the migrating CO_2 can be made (Figure 5.6):

1) Second-order, W and SW dipping faults are likely to allow across-fault migration of CO_2 for both storage units (SGR <15%; Figure 5.6A).
2) Second-order, E and NE dipping faults are likely to create flow and pressure baffles within the secondary storage unit (SGR >20%), while there is more uncertainty related to the presence of baffles where the primary storage (FW) is juxtaposed against the secondary-storage unit (SGR between 15–20%; Figure 5.6A).
3) First-order, W and NW dipping faults are likely to prevent across-fault migration in both storage units (SGR >20%; Figure 5.6B).

An exception from these generalized inferences is found in the W and SW dipping second-order F2 fault near well 31/5-7. In well 31/5-7, the upper parts of the Johansen Formation are heterogeneous with thin layers that exhibit high gamma-ray values (80–90 API; Figure 4.35). These layers will therefore contribute to higher SGR values (15–20%) for low throws (<50 m). This is seen in the fault tips of the F2 fault (Figure 4.26) where the primary storage unit is self-juxtaposed. Northwards, in well 31/5-2, 31/2-5, and 31/2-1, the Johansen Formation is observed to be more homogeneous (Figure 4.36, Figure 4.37, and Figure 4.38). As such, it is expected that W and SW dipping faults have lower SGR values (<15%) for low throws further north potentially allowing across-fault migration of CO_2.

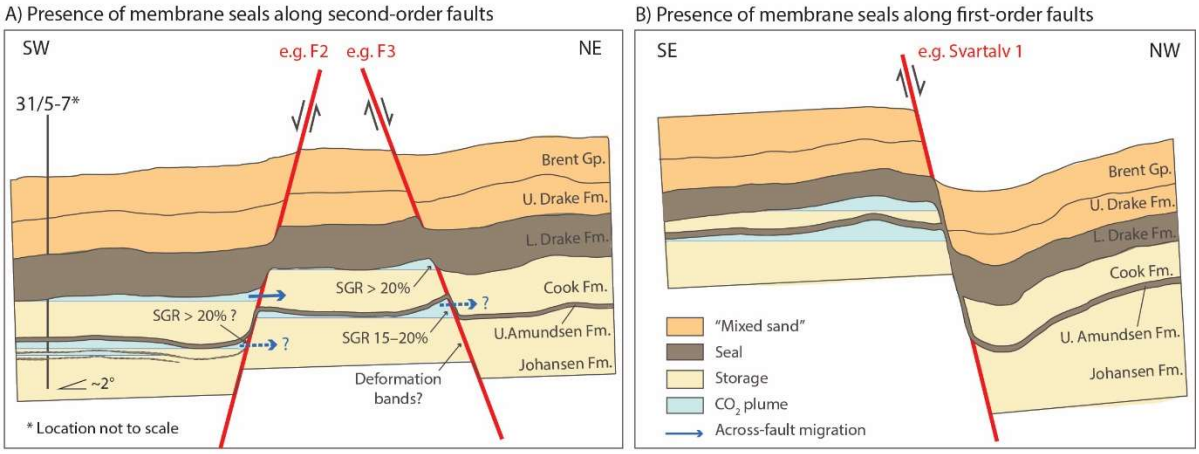

Figure 5.6 Conceptual cross-sections showing CO_2 migration within the storage units. Three scenarios are shown where only membrane seals, using the SGR method, are assessed: A) migration through two second-order faults with the opposite dip-direction (SW and NE) and B) migration through a first-order NW dipping fault. The F2, F3, and Svartalv 1 faults are used as examples as they are representative of one of the three membrane seal scenarios mentioned above. The presence of the Upper Amundsen Formation is estimated as well as thin clay-rich layers within the Johansen Formation. The CO_2 plume is illustrated in a fill-to-spill scenario.

As presented in the 1D triangle diagrams, SGR diagrams, and illustrated in Figure 5.6A, some areas along the modelled faults have SGR values <15% indicating that the clay smears are discontinuous and associated with across-fault communication (e.g., Yielding, 2002; Yielding et al., 2010). Since the second-order faults are interpreted to have nucleated in Lower Jurassic to Cretaceous successions during the late inter-rift period of Rift Phase 2, the burial depth of the sand-rich storage units is assumed to have been shallow (<1 km) at the time of faulting. Therefore, faults that juxtapose the storage units against each other and have low SGR values (<15%), such as the W and SW dipping second-order faults, are likely to be dominated by disaggregation and potentially minor cataclastic deformation bands (Fossen et al., 2007).

The influence of deformation bands on fluid flow is, however, not clear. On the one hand, Fisher and Knipe (2001) suggested that disaggregation bands in phyllosilicate-bearing sandstones reduce the permeability of up to one order of magnitude compared to the host rock, while cataclastic bands on average reduce the permeability between one and two orders of magnitudes. Cementation and dissolution of the deformation bands due to quartz cementation (>90° and >3 km burial depth; Walderhaug, 1996) leads to a significant increase in reduction of the porosity and permeability (e.g., Ngwenya et al., 2000).

On the other hand, disaggregation and mildly cataclastic deformation bands in the damage and process zone of faults in the Ferron Sandstone (Utah) have been observed to increase the porosity compared to the host rock (Braathen et al., 2018). Furthermore, field studies of highly porous sandstones such as the Entrada and Navajo Sandstones in Utah have demonstrated that deformation bands occur in extensive (up to 100 m wide) damage and process zones (Shipton and Cowie, 2001; Rotevatn et al., 2007). Due to limitations related to resolution in seismic data, these zones may not be resolvable but could influence

fluid flow in the region ahead of the seismically mapped faults (Fossen et al., 2007). The presence of deformation bands could, therefore, act as both baffles or conduits to the migration of CO_2 in areas with sandstone on sandstone juxtapositions or in areas not resolved in the seismic section.

However, Fisher and Knipe (2001) suggested, compiling data from the Middle Jurassic Brent Group in the North Sea, that faults in clean sandstones are not likely to affect fluid flow and that the presence of clay smear is the dominant factor that leads to across-fault membrane seals. This is further supported by Yielding (2002), who suggests that in areas where Brent Group juxtapositions have SGR values <15%, and the fault rock is dominated by disaggregation and cataclastic deformation bands, faults are generally unable to provide a seal. Detailed analysis of well cores from the Aurora storage site, preferably from areas near faults, is needed to determine the presence of deformation bands and their effect on migration of CO_2. This is, however, beyond the scope of this study. Therefore, an assumption is made that the presence of deformation bands within the Aurora storage site have a negligible effect on fluid migration.

Based on the considerations above, information from the SGR diagrams, and 1D triangle diagrams presented in section 4.2, plausible CO_2 migration routes within the upper parts of the storage units are presented in Figure 5.7. In the primary storage unit, E and NE dipping faults are assumed to have SGR values between 15–20% (Figure 5.7A), which represents threshold values between faults that baffle or allow across-fault migration (Yielding, 2002). It is, therefore, uncertain whether these faults will affect the migration route. Within the upper parts of the secondary storage unit, E and NE dipping faults have SGR values exceeding 20% and are, therefore, more likely to baffle migration of CO_2 (Figure 5.7B). Within both storage units, W and SW dipping second-order faults will have a negligible effect on across-fault migration (SGR <15%), while the Svartalv Fault Zone are likely to be sealing (SGR >30%) and rather favor migration north to northeastward in the footwall (Figure 5.7A and B).

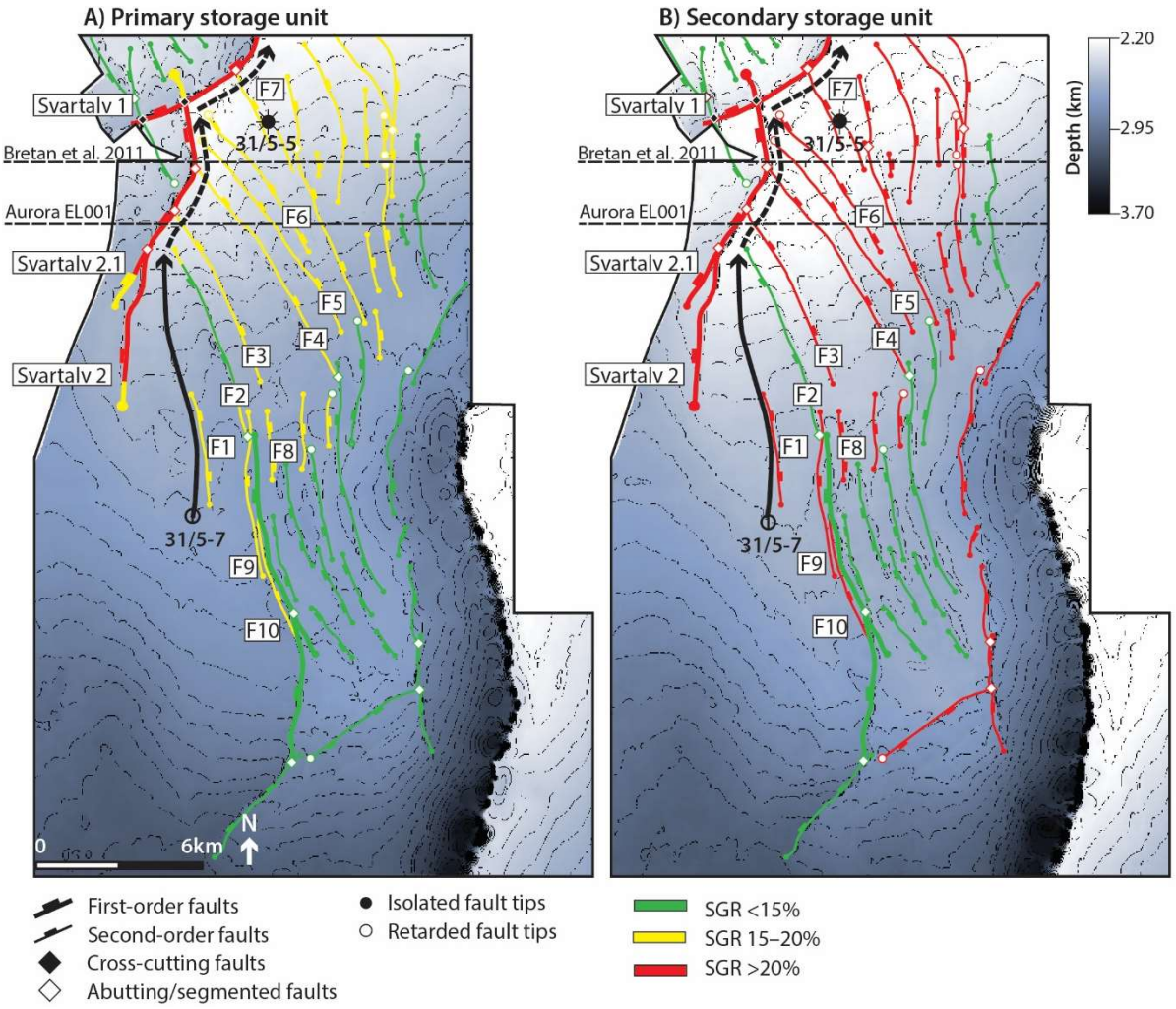

Figure 5.7 Depth-structure maps showing SGR values for faults within the A) primary storage unit and the B) secondary storage unit. Arrows indicate potential migration routes based on the membrane seal scenarios and drawn perpendicular to the contour lines. A solid line indicates more plausible migration routes than the dashed lines. Contour spacing is 50 meters. The southern extent of the study area in Bretan et al. (2011) and the northern extent of the Aurora Exploitation License (EL001) is shown on the map.

Previous studies have mapped the entire length of the Svartalv 1 fault and used the SGR method to assess the presence of across-fault seals (Bretan et al., 2011; Gassnova, 2012). Bretan et al. (2011) found that SGR values were >25% across the Svartalv 1 fault for the Johansen Formation (primary storage unit), and >35% in the southern segment mapped herein. In contrast, Gassnova (2012) concluded that for throws exceeding 300 meters along the Svartalv 1 segment the, SGR values are <25% and are, therefore, less likely to prevent across-fault migration. It is, however, important to note that Gassnova (2012) only included clay contributions from the Drake Formation which could result in lower calculated SGR values.

The work herein suggests that the Svartalv 1 fault has SGR >30% for the majority of primary storage unit and SGR >40% for the secondary storage unit (Figure 4.34), corroborating the interpretation by Bretan et al. (2011). It is important to note that only the southern segment of the Svartalv Fault Zone is mapped herein, and that maximum throw for the fault is expected to occur further north within the Troll

West field (e.g., Bretan et al., 2011). As calculated SGR values decrease with increasing throw values, it is expected that there are more uncertainties related to the presence of a membrane seal further north, as shown in Bretan et al. (2011). While it is beyond the scope of this study, renewed assessment of SGR values along the entire Svartalv Fault Zone is necessary to assess the possibility of across-fault migration within both storage units.

5.2.3 CO_2 migration near the injection well and potential structural traps

Based on the results from fault juxtaposition and membrane seal assessments, it is possible to assess plausible CO_2 migration pathways near the injection well and the gross rock volume of potential fault-bound traps. As previously interpreted, the migration pathways will differ depending on whether the plume is located within the primary or the secondary storage unit. Due to uncertainties related to across-fault migration, if calculated SGR values are less than 20% (Yielding, 2002), a precautionary principle is applied for the following interpretations where only SGR values exceeding 20% are considered to have a baffling effect.

The injected CO_2 is likely to first encounter the east-dipping F1 fault located just 700 m northeast of well 31/5-7 (Figure 5.8). In a fill-to-spill scenario, buoyant CO_2 migrating within the uppermost parts of the secondary storage unit is likely to be channeled northwestward due to a small (~30m) juxtaposition seal. In contrast, F1 is more likely to allow across-fault migration for CO_2 within the primary storage unit. If the plume becomes more than 1800 meters wide, it will encounter the east-dipping F9 fault (Figure 5.8). Again, due to the dip of the fault, CO_2 migrating within the upper parts of the secondary storage unit is likely to become channeled northwestward due to the presence of a small (~40m) juxtaposition seal, while CO_2 within the primary storage unit likely migrates across the fault. Despite the different sealing potential of the faults within the primary and secondary storage unit, injected CO_2 is likely to overall migrate perpendicular to the contour lines and parallel to the strike of faults near the injection well. It is, therefore, unlikely that faults near the injection well will cause significant pressure buildup due to the accumulation of CO_2. Instead, they may channel migration of CO_2 within the uppermost parts of the secondary storage unit, increasing the plume front advancement as suggested by Andersen and Sundal (2021). Migration near the injection well is, however, influenced by other factors than across-fault seals. As highlighted in Sundal et al. (2016), factors such as discrete layers of carbonate cemented zones and mudstone, tight calcite cemented layers, injection scheme, and anisotropy in relative permeabilities are important to consider in the Aurora storage site. However, the influence of these factors was beyond the scope of this study.

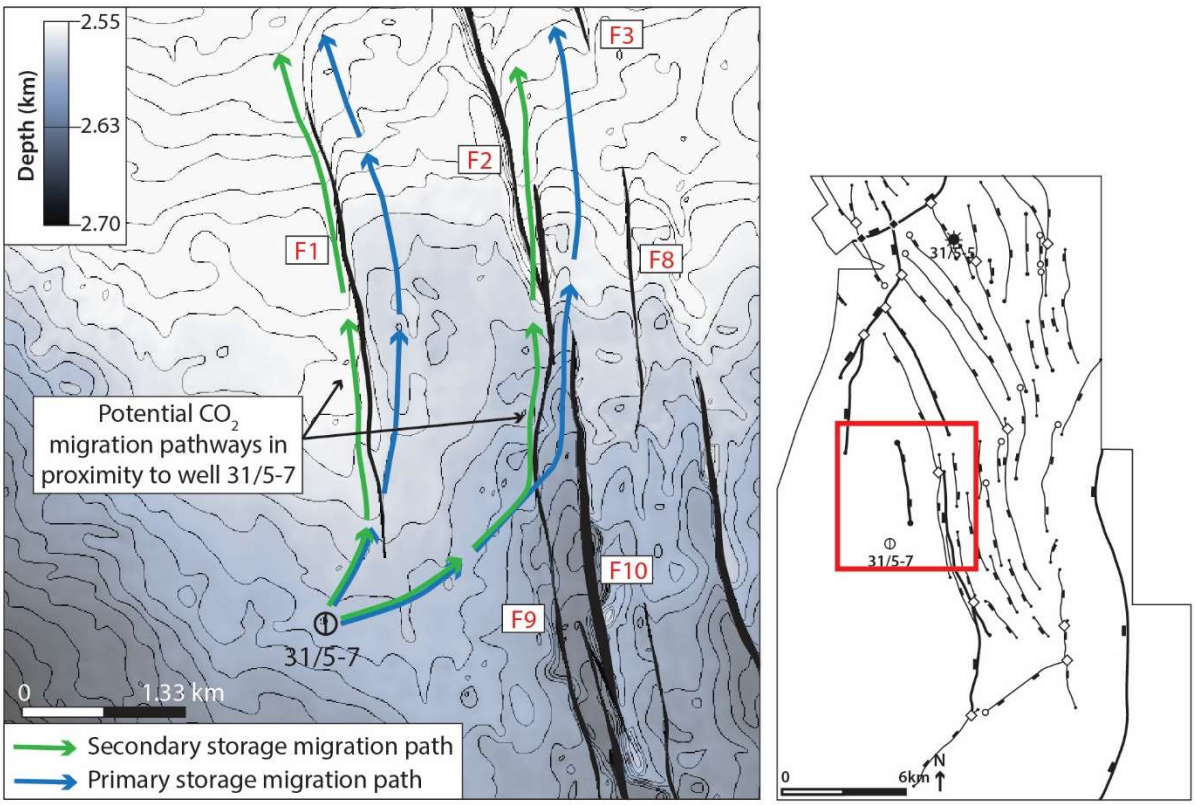

Figure 5.8 Potential migration pathways within the storage units near the injection well. Inset map shows the location of the close-up. A depth structure map of the Top Cook Formation is displayed with a contour spacing of 10 meters and fault heave polygons.

Synthesis of variance attribute maps and throw vs. length profiles show that fault-bound traps are present north of the injection well. The abutting interactions between Svartalv 2 and the second-order F3 and F4 faults create triangular two-way closures located 9.9 and 11.4 km north of well 31/5-7, respectively (Figure 5.9). Assuming a fill-to-spill scenario where equal amounts of CO_2 are injected into the storage units, information about across-fault seals and depth-structure maps can be combined to assess the gross rock volume of potential traps within the study area. As shown in Figure 5.5 and Figure 5.7, closures along the Svartalv 1 and Svartalv 2 faults depend on the presence of a membrane seal, and the assumption that SGR >20% are likely to prevent across-fault migration (Yielding, 2002).

The first triangular two-way closure is located where F3 abuts against Svartalv 1 (Figure 5.9). The Svartalv 2 fault has SGR values exceeding 30% in both storage formations and is therefore likely to prevent across-fault migration. In contrast, the F3 fault only forms a juxtaposition seal within the uppermost part (28 m) of the secondary storage unit. Based on the height of the juxtaposition seal and the dip of the depth-structure map, the gross rock volume of the closure equates to $1.5 \times 10^6\,m^3$. The F3 fault shows SGR values <20% within the primary storage unit, and it is, therefore, more likely that CO_2 would migrate across this fault. The second triangular two-way closure is located where F4 abuts against Svartalv 2 (Figure 5.9) and shows a similar juxtaposition scenario within the secondary storage unit. Here the height of the juxtaposition seal is 24 meters which equates to a gross rock volume of

approximately 4.1 × 10^6 m^3. Within the primary storage unit, the calculated SGR <20%, and it is, therefore, more likely that CO_2 migrates across this fault.

The final triangular two-way closure is located where Svartalv 1 and Svartalv 2 cross-cut each other 13.7 km north of well 31/5-7 (Figure 5.9). Due to the strike of the Svartalv 1 fault (~NE–SW) relative to the overall dip of the storage units (SSW), CO_2 is expected to migrate northeastward after a CO_2 column height (i.e., spill point) is reached. Based on the presence of a membrane seal, the dip of the surfaces, and the assumption that the Upper Amundsen Formation provides a flow baffle, the height of the closure within the primary and secondary storage units are approximately 70 and 76 meters, respectively. These heights equate to a gross rock volume of 68 × 10^6 m^3 in the primary storage unit and 96.3 × 10^6 m^3 in the secondary storage unit. The sandstone on sandstone juxtaposition observed in Figure 4.32 in the lower parts of the primary storage unit is located approximately 30 m below the height of the closure. Accumulated CO_2 is therefore likely to spill northeastward and into the Troll West fields before it reaches the sandstone on sandstone juxtaposition.

Bretan et al. (2011) observed similar structural closures within the Troll West field and estimated that each closure had a gross rock volume of approximately 75 × 10^6 m^3. The final closure for CO_2 is interpreted to be located more than 20 km north of well 31/5-7 beneath the Troll West field (Furre et al., 2020). Sundal et al. (2015) simulated the CO_2 plume within the primary and secondary storage unit in the Aurora storage site. They predicted that the total migration distance was 9.8–12.8 km after 150 years. Applying this estimate, and given a similar structural dip, it would take the plume 116–152 years to reach the first triangular structure, 134–175 years to reach the second, and 161–210 years to reach the third. These estimations suggest that CO_2 injected into well 31/5-7 will migrate out of the Aurora Exploitation License and into the Troll License long after the anticipated end of field life for the Troll fields in the year 2054 (Equinor, 2019).

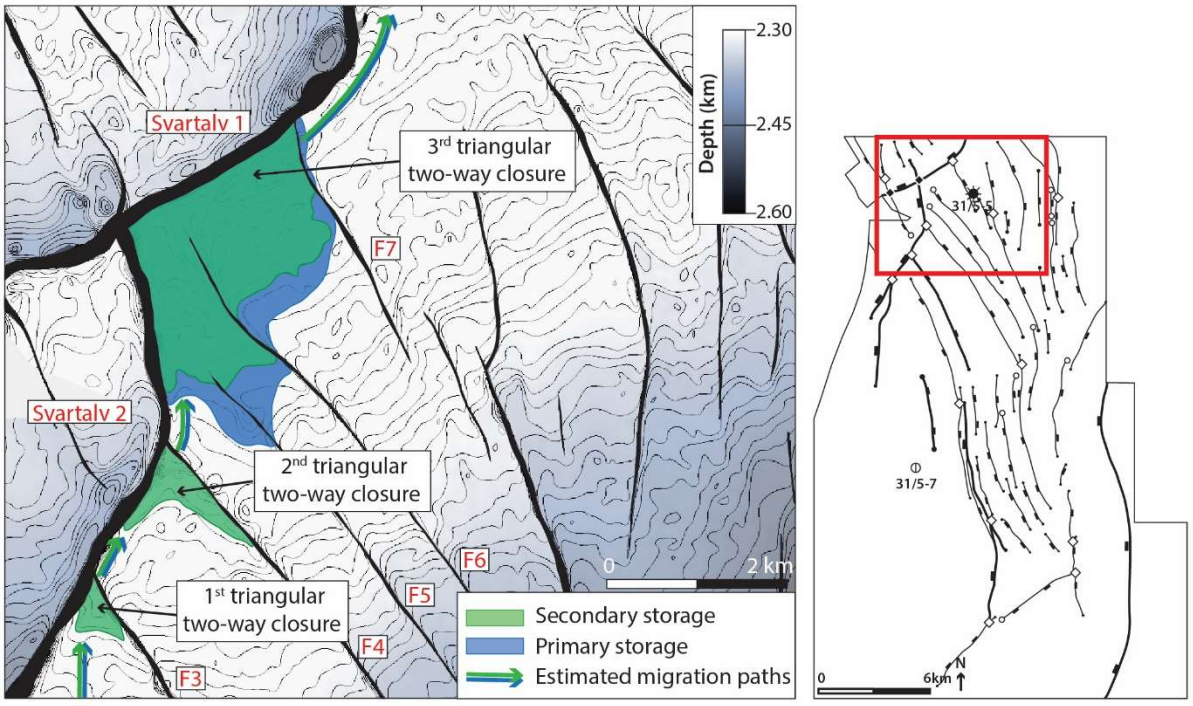

Figure 5.9 Expanded map view of potential trapped/baffled CO_2 accumulations and migration pathways within the primary and secondary storage units. The inset map shows the location of the map. A depth structure map of the Top Cook Formation is displayed with a 10-meter contour spacing.

As mentioned in subsection 3.1.2.2, leakage of CO_2 across a fault occurs when the buoyancy pressure of CO_2 exceeds the capillary entry pressure of the fault, and is, therefore, not necessarily confined to the structural closures presented herein (e.g., Bretan et al., 2003; Manzocchi et al., 2010). Calculations of CO_2 column heights that can be supported by the Svartalv Fault Zone are beyond the scope of this study, but estimates of such column heights within the Troll Field (Bretan et al., 2011) found that SGR values of 25% correspond to trapped CO_2 column heights over 100 m. Furthermore, they suggested that a column height over 300 m would be required for up-fault migration to occur. Applying these estimates, migration from the storage units across the Svartalv Fault Zone and into the Upper Drake Formation and Brent Group is unlikely to occur until at least 100 m of CO_2 accumulates in the footwall, which exceeds the height of the estimated closures (maximum 76 m).

To provide a rough estimate of the storage capacity of the closures herein, the methodology in NPD CO2 Atlas (2011) is applied using values of porosities from Gassnova (2012), net-to-gross ratios from Fawad and Mondol (2018), density of CO_2 at 2.6 km depth, and storage efficiency from NPD CO2 Atlas (2011) (Table 5.1). It is important to note that these values are representative for the Johansen and Cook formations, and, therefore, only provides a rough estimate of the primary and secondary storage units interpreted herein.

Table 5.1 List of values used to provide a rough estimate of the mass of CO_2 that can be stored within the interpreted structural closures.

Unit	GRV (10^6 m^3)	Porosity (%)	Net-to-gross ratio	CO_2 density (kg/m^3)	Storage efficiency	Mass CO_2 (Mt)
Secondary storage unit	93.6	14	0.45*	700	3%	0.135
Primary storage unit	68	21	0.45*	700	3%	0.124

*Net-to-gross ratios are from the Johansen Formation and is used herein as an approximation for the storage units.

As mentioned in section 1.1, 1.5 Mt CO_2 per year over 25 years will be injected in the first phase of the Northern Lights project (Equinor, 2019). The estimated capacity of the closures in Table 5.1, therefore, represents 0.3–0.4% of the total CO_2 injected into the Aurora storage site (37.5 Mt). The interpretation of storage capacity made herein suggest that the presence of structural closures, influenced by second-order NW-SE striking and NE-dipping faults, may contribute positively to the overall storage capacity of the Aurora storage site without presenting a risk of up-fault migration due to pressure build-up and reactivation, following the suggestions in Bretan et al. (2011), and migrate into the Troll West field likely after the end of the field life, applying the estimates in Sundal et al. (2015). This interpretation is in agreement with Furre et al. (2020), who suggested that due to the relatively small throws of the NW–SE striking faults, they are not likely to cause significant, additional pressure build-up and reservoir compartmentalization.

It is important to note that the estimated closure volumes presented herein are solely based on structural trapping and that CO_2 is mobile (i.e., a fill-to-spill scenario). However, other trapping mechanisms such as capillary or residual trapping, solubility trapping, and mineralization will increase the volume of CO_2 that can be stored within the Aurora storage site (Benson and Cole, 2008). The simulation of CO_2 plume distribution by Sundal et al. (2015) suggested that the immobilized fraction of CO_2 within the Aurora storage site after 150 years varied in the range of 50–80%, which is 18.75–30 Mt CO_2 of the total injected CO_2 in the first phase of the Northern Lights project.

Bearing in mind the assumptions and objections discussed in section 5.2, across-fault seal assessment and CO_2 migration pathways can be summarized as follows:

1) The overall CO_2 migration direction is towards the north within the study area.
2) W and SW dipping second-order faults are less likely to baffle CO_2 within both storage units.
3) E and NE dipping second-order faults exhibit a juxtaposition seal within the upper parts of the secondary storage unit potentially baffling migration of CO_2.
4) The Svartalv Fault Zone is less likely to prevent across-fault migration due to juxtaposition seals as the storage units are juxtaposed against ‘mixed sand’ units (i.e., the Upper Drake Formation and the Brent Group). However, relatively high SGR values (>30%) are estimated across the Svartalv Fault Zone, which is associated with the presence of a membrane seal potentially preventing across-fault migration (Yielding, 2002).

5) Triangular two-way closures created by intersections of NW–SE striking, and NE dipping second-order faults and the Svartalv Fault Zone likely baffle migrating CO_2 thus contribute to the storage capacity of the Aurora storage site.

5.3 Limitations

Analysis of the sub-surface is related to uncertainties and limitations. Limitations related to seismic resolution have been discussed in sub-section 3.2.5. In this section, limitations, and uncertainties related to the interpreted geomodel, fault throw analysis, and across-fault seal assessment are presented.

5.3.1 The interpreted geomodel

Limitations related to the interpreted geomodel include the size of the study area, the reflector picked for interpretation, and modelling of faults with throws close to the vertical resolution.

The study area applied herein covers approximately 420 km^2 (e.g., Figure 1.2) within the Horda Platform (~15 000 km^2). It is, therefore, challenging to interpret the structural evolution based solely on observations within the study area. Comparison with previous work on structural evolution within the Horda Platform (Whipp et al., 2014; Duffy et al., 2015; Deng et al., 2017; Mulrooney et al., 2020; Wu et al., 2021) was, therefore, necessary to support the interpretations made herein.

While the confidence for the reflections picked within the Dunlin Group is high due to information from the recently drilled 31/5-7 well, some uncertainty is related to the Top Brent Group reflector pick (Table 3.4). In this study, the Top Brent Group reflector is picked on the trough located approximately 8 m above the formation top in 31/5-7. This trough was selected, over the underlying peak, to achieve a better correlation with the Top Brent Group picks within the Troll West field (e.g., 31/2-5 and 31/5-2) and because the reflector has a higher amplitude and is more continuous throughout the study area. This interpretation could potentially result in the top of the Brent Group being located within the lowermost parts of the overlying Heather Formation. If so, some of the hanging-wall growth observed within the Brent Group in the hanging wall of faults within the study area, in particular, across the Svartalv and the Tusse fault zones (Figure 4.12), could be related to fault activity during the deposition of the lowermost Heather Formation. However, this has relatively little influence on the interpretation of fault evolution within the study area as both the upper parts of the Brent Group and the lower parts of the Heather Formation were deposited during Middle Jurassic (Deegan and Scull, 1977). In addition, it is unlikely to influence juxtaposition scenarios. This is because the hanging-wall cut-off line for the Top Brent Group reflector is located more than 8 m (i.e., 35 m) above the footwall cut-off line for the Top Cook Formation along the fault with the largest throw (i.e., Svartalv 1; Figure 4.33 and Figure 4.34).

Some uncertainty is also related to the thickness of the target successions. The reflector picked for Top Upper Drake Formation and Top Johansen Formation disappears, in places, because the thickness is below the vertical resolution (7.5–15m; sub-section 3.2.5). This occurs in a small area on the horst southeast of injection well 31/5-7 in the Top Johansen Formation (Figure 4.7), and the hanging wall of the Tusse Fault Zone segment in the Upper Drake Formation (Figure 4.10). In these areas, the underlying reflector with the same polarity is chosen to create a continuous surface. As such, the thickness of these successions is, in places, somewhat underestimated (~10–15 m), and the thickness of the overlying successions is correspondingly somewhat overestimated. The underestimated thickness of the Upper Drake Formation in the hanging wall of the Tusse Fault Zone segment could contribute to the growth observed in the overlying Brent Group. However, reducing the hanging-wall thickness of the Brent Group by 15 meters only reduces the expansion index to 2.45–2.80 (from 2.60–3.00), which is still the largest expansion indices observed for the interpreted successions. Moreover, the uncertainty in thickness for these two successions is largest in the area southeast of injection well 31/5-7 (i.e., away from the migration direction of CO_2). As such, it does not influence the modelled fault juxtaposition and SGR diagrams.

In addition, fault interpretations strategies can influence the assessment of across-fault seals (e.g., Michie et al., preprint). To provide a robust fault interpretation, the faults herein are interpreted with a spacing of 50–125 m, close to the optimum spacing of 100 m suggested by Cunningham et al. (2020) and Michie et al. (preprint), while cut-off lines have been picked with smaller spacing, compared to the horizon interpretation. However, due to limitations in vertical resolution (7.5–15m), there are still higher uncertainties related to the measured throw for second-order faults, which have throws closer to the vertical resolution (5–50 m), compared to first-order faults, which generally have larger throws (43–940m). Consequently, higher uncertainty is related to the across-fault seal assessment of the second-order faults compared to the first-order faults. Considering that second-order faults may have an influence on migrating CO_2 within the Aurora storage site (section 5.2), it is necessary to improve methods used to interpret faults with throw close to the vertical resolution of the seismic data, thus reducing the uncertainties related to across-fault migration.

As a final remark, while the same 3D seismic survey (GN10M1) is applied herein and in Gassnova (2012), different velocity models have been applied to perform the depth conversion. This could explain the difference in throw observed in the Svartalv Fault Zone. For example, Gassnova (2012) observes that the storage units are offset by 300 m across the Svartalv Fault Zone, while the storage units are offset by 380 m herein in the approximately same region. Regardless, the juxtaposition scenarios observed herein and in Gassnova (2012) show relatively similar results.

5.3.2 Fault throw analysis

Limitations related to the fault throw analysis performed herein include challenges in measuring the exact fault throw and trace length, which could have implications for the interpretation of fault growth, evolution, and across-fault seal assessment.

As previously mentioned, the large scatter in measurements observed in the maximum throw vs. length plot in Figure 4.14 could be attributed to material properties (Cowie and Scholz, 1992), mechanical stratigraphy (Schultz and Fossen, 2002), kinematic interaction in linked faults (e.g., Peacock and Sanderson, 1991) or reactivation of pre-existing structures (Kim et al., 2001). However, the scatter could also be a result of measurement errors (e.g., Kim and Sanderson, 2005). This includes failure to resolve low-displacement fault tips and damage zones due to limitations in seismic resolution, which will lead to an underestimated fault trace length and exclusion of fault drag which leads to underestimated displacement (or throw).

In this study, the throw has been used as a proxy for displacement. While this is relatively common practice due to the challenge in identifying kinematic indicators in seismic (e.g., Walsh and Watterson, 1988; Peacock and Sanderson, 1991; Whipp et al., 2014), it will result in slight under-representation of true displacement (Lohr et al., 2008). With steeper faults being better represented than more gently dipping or listric faults. Studies have also shown that faults with trace lengths less than a few kilometers long, can have fault traces that are underestimated by 250–1000 meters (Pickering et al., 1997). The smaller-scale second-order faults mapped in this study, may therefore appear less under-thrown in Figure 4.14 than what they are. This further supports the interpretation that less mature faults (second-order faults) have lower T_{max}/L ratios compared to more mature faults (first-order faults; Walsh et al., 2002; Walsh et al., 2003).

As previously presented, expansion indices (E.I.) was used herein to constrain fault activity (Thorsen, 1963). However, despite the observation that calculated E.I. values are exceeding 1 for interpreted units within the Dunlin and Brent groups, it is important to note that the difference in hanging wall and footwall thicknesses is relatively small, in particular across second-order faults (see values used for E.I. calculations in Appendix 4). As a result, they are more sensitive to small errors in measurements. Furthermore, thickness variations near the fault can be a result of drag, burial-related compaction, and erosion of the footwall (e.g., the NNSUC), which are not related to syn-rift sedimentation Jackson et al. (2017). While measures were implemented to reduce these uncertainties (sub-section 3.3.5), there are still higher uncertainties related to measured E.I. values of second-order faults compared to first-order faults.

Finally, it is important to note that vertical and lateral variations in throw were assessed using three and nine faults, respectively, in combination with information from thickness maps, depth-structure maps,

and extracted variance maps. Assessment of vertical and lateral variations of throw for a larger sample size of faults will provide higher confidence in determining the structural evolution of the study area. This was however beyond the scope of this study.

5.3.3 Across-fault seal assessment

Limitations and uncertainties related to across-fault seal assessment include challenges in resolving structural complexities, predicting fault rock composition, estimating the volumetric clay fraction using well data, and applying methods developed for hydrocarbon reservoirs to proposed CO_2 storage sites.

In seismic, faults are interpreted where the reflections are offset, as discrete fault surfaces, and interpreted horizons are extrapolated onto this fault surface to create 3D juxtaposition and SGR diagrams (Allan diagrams; Allan, 1989). However, outcrop studies show that faults are often represented by complex geometries, usually consisting of multiple slip surfaces (e.g., Childs et al., 1997; Shipton and Cowie, 2001), which may be too small to be resolved in seismic data. Therefore, Childs et al. (1997) question whether it is possible to use juxtaposition diagrams to predict the sealing potential of fault zones in the sub-surface. Furthermore, Færseth et al. (2007) suggest that if multiple slip surfaces are present in the fault zone, the probability that a juxtaposition seal or membrane seal prevents across-fault migration is reduced by 30–40%. Herein, juxtaposition seals within the uppermost parts of the secondary storage units across E and NE dipping second-order fault are assumed to be present. If these faults contain multiple slip surfaces, not resolvable in seismic, their baffling effect within the storage site could be reduced.

The presence of membrane seals is proven to occur in hydrocarbon reservoirs within the North Sea, for example, in the Brage Field (Færseth et al., 2007), Visund, and Oseberg fields (Fristad et al., 1997), and the Gullfaks Field (Yielding et al.). Moreover, the methods used to estimate the presence of membrane seals (e.g., the SGR algorithm applied herein) have been successfully applied to estimate the sealing potential of faults in hydrocarbon fields (e.g., Fristad et al., 1997; Lyon et al., 2005). However, predicting the presence of membrane seals, using the SGR method is associated with significant uncertainties arising from limited subsurface data and challenges in predicting fault zone structure and composition. As previously mentioned, the SGR method uses information from well logs as a proxy for fault rock composition (Yielding et al., 1997; Freeman et al., 1998). In this study, volumetric clay fraction was obtained from wells located between 5.3–13.7 km away from the target faults. These estimates were then used as a proxy for fault rock composition. Any lithological variations between the wells and the targeted fault are therefore ignored, which leads to uncertainties in estimating the fault rock composition using well data. Furthermore, Childs et al. (1997) questioned whether well data can be used, at all, to predict the complex distribution of fault rocks within a fault zone.

As previously mentioned, the presence of membrane seals in Figure 5.7 is based on the calibrated SGR cut-off values in Yielding (2002), which are compiled from sealing and leaking faults in hydrocarbon fields in the North Sea (Figure 3.12). However, some deviation from this trend is observed in the Oseberg fields located approximately 20 km west of the Aurora storage site. For example, Fristad et al. (1997) observed a cut-off value of 18% for sealing and leaking faults, while a renewed assessment of the Oseberg field by Helland (2016) found that SGR values less than 24% could allow across-fault fluid migration. Applying an SGR cut-off value of 24% instead of 20% will, however, have little influence on the interpretation of membrane seals herein as the Svartalv Fault Zone has SGR values exceeding 30%. Nonetheless, these observations show that using regional SGR cut-off values to assess the presence of membrane seals locally within a storage site is associated with some uncertainties.

Furthermore, the robustness of the SGR approach relies on accurate determinations of the clay volume using well data. Herein, the gamma-ray log was used to calculate the V_{cl}, similar to Bretan et al. (2011), due to the extensive knowledge of clay-rich and sand-rich successions within the North Sea. However, high gamma-ray values might be caused by high quantities of organic matter instead of high clay content (e.g., Bretan et al., 2003). Therefore, thorium and neutron-density logs can be used to better estimate clay-rich successions (Rider, 2000). These methods were not applied herein, and as such, there could be some uncertainty in the selected cut-off values for 100% sand (sand-line) and 100% shale (shale-line). In addition, uncertainties arise from the estimation of the sand- and shale-line as they are user-defined values. To reduce these uncertainties, a precautionary principle was applied, where higher sand and shale cut-off values were favored (i.e., less conservative values). Figure 5.10 shows that even if higher API (10 API) values are selected, the calculated SGR is still higher than 20% where the storage units are juxtaposed against the Upper Drake Formation or the Brent Group. This observation further supports the sealing potential of the Svartalv Fault Zone, assuming that SGR >20% is related to the presence of a membrane seal (Yielding, 2002). In contrast, these values will result in SGR <15% in areas where the secondary storage unit (FW) is juxtaposed against the primary storage unit (HW) across NE dipping second-order faults (Figure 5.10) indicating a larger uncertainty related to these membrane seals.

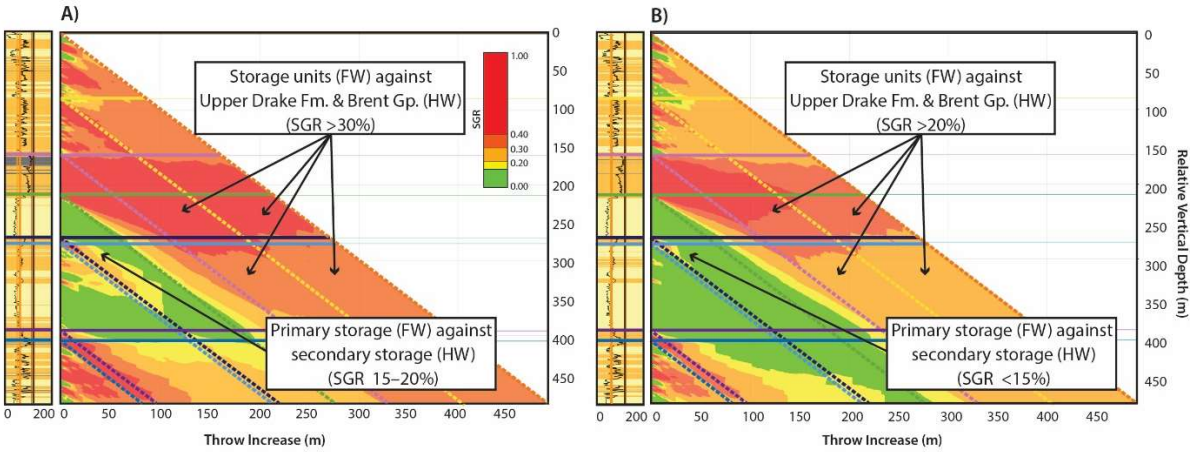

Figure 5.10 1D triangle diagrams created using gamma-ray log from well 31/5-7 using different cut-off values for sand and shale, A) using 60 API (sand-line) and 130 API (shale-line) and B) using 70 API (sand-line) and 140 API (shale-line).

As a final remark, recent studies question whether applying approaches to estimate the presence of membrane seals, developed for hydrocarbon reservoirs, directly to CO_2 storage sites will be successful (e.g., Miocic et al., 2019; Karolytė et al., 2020). Miocic et al. (2019) assessed uncertainties in fault seal parameters (i.e., wettability properties, fault rock composition, and reservoir depth on retention potential) and implications for CO_2 column heights. They found that a higher phyllosilicate content within the fault rock, which is assumed to increase the capillary threshold pressure, may have the opposite effect due to increased CO_2-wetting behavior with phyllosilicates. Moreover, they found that deep storage units (>1800 m) and high pressures could lead to accumulations of smaller CO_2 column heights compared to hydrocarbon heights at the same depth and pressure. The estimated CO_2 column heights in Bretan et al. (2011) indicating that SGR values of 25% can hold a CO_2 column height of 100 m, is calculated based on methods used to predict hydrocarbon column heights. Taking into consideration the work by Miocic et al. (2019), the estimated column heights by Bretan et al. (2011) supported by the Svartalv Fault Zone may, therefore, be an overestimation. Consequently, it is uncertain whether the fault zone can hold CO_2 column heights of 70 and 76 m (i.e., heights of closures) before leaking into the hanging wall. Further research on methods developed to predict CO_2 column heights is therefore necessary.

It is clear from the objections presented in section 5.3 that there are significant uncertainties related to assessing across-fault seals. In particular, assessment of membrane seals in CO_2 storage sites. Reflecting these objections, it is therefore higher uncertainties related to the sealing potential of faults that offset the primary seal (i.e., the Svartalv Fault Zone), compared to faults that have throws less than the thickness of the primary seal (i.e., second-order faults). These observations can be used as a general suggestion for future fault-controlled CO_2 storage sites and stress the importance of developing methods to predict the presence of membrane seals more accurately in CO_2 storage sites.

5.4 Suggestions for further research

This study provides an improved understanding of the structural characterization and evolution of the Aurora storage site, and across-fault seal assessment. However, additional research is necessary to mature the Aurora storage site as a CO_2 prospect and further reduce uncertainties related to CO_2 storage. This includes:

- Applying the 3D geomodel created in this study as a framework for dynamic pressure and fluid simulations. In this study, the migration routes are estimated by assuming that CO_2 will migrate perpendicular to the contour lines in a fill-to-spill scenario. However, a numerical simulation of the plume distribution and pressure evolution would provide a more accurate estimate of CO_2 migration, similar to the numerical simulations in Eigestad et al. (2009) and Sundal et al. (2015).

- Calculating the storage capacity of the Aurora storage site. In this study, a rough estimate of the storage capacity of structural closures has been provided assuming a fill-to-spill scenario. However, to provide a more accurate estimate of the storage capacity within the Aurora storage site, additional information on capillary or residual trapping, solubility trapping, and mineralization (Benson and Cole, 2008) is needed.

- Performing structural characterization and across-fault seal assessment of a larger area. The study area in this thesis was made assuming that well 31/5-7 will be used as an injector. In future expansions of the storage site, or the northern North Sea in general, additional injectors are likely to be drilled (Equinor, 2019). Therefore, structural characterization and across-fault seal assessment of a larger area are necessary. Furthermore, CO_2 injected into well 31/5-7 will likely migrate into the Troll West field (supported herein; Gassnova, 2012; Equinor, 2019). Across-fault seal assessment within the Troll West field has previously been conducted by Bretan et al. (2011). However, their study was performed prior to the drilling of injection well 31/5-7 and only included the Johansen Formation as a storage unit. Renewed assessment, using information from 31/5-7 and including both storage units, is necessary to evaluate the presence of across-fault seals, in particular, across the entire Svartalv Fault Zone.

- Perform detailed stratigraphic assessment within the study area. Herein, the clay-rich Upper Amundsen formations have not been interpreted as it is too thin to provide as a primary seal (Sundal et al., 2015). However, the Upper Amundsen could potentially have a baffling effect on buoyant CO_2 rising to the top of the Johansen Formation. Furthermore, the Upper Amundsen Formation becomes slightly thicker towards the north and is therefore likely to have a larger influence on membrane seals across the Svartalv Fault Zone. It is therefore desirable to assess the presence and lateral continuity of Upper Amundsen Formation. In addition, when creating juxtaposition diagrams herein, the Upper Drake Formation and the Brent Group are assigned a simplified lithology (i.e.,

mixed sand). Detailed assessment of lithological variations within the Upper Drake Formation and the Brent Group is necessary and will strengthen the across-fault seal assessment of the Svartalv Fault Zone.

- Improving methods to predict across-fault seals. As discussed in this study, there are uncertainties related to the present-day methods used to predict across-fault seals in a CO_2 storage site. As suggested by Miocic et al. (2019), across-fault seal predictions could be improved during operations within the Aurora storage site by monitoring and developing a database similar to those used to predict hydrocarbon column heights (e.g., Yielding et al., 2010).

- Assessing the risk of CO_2 leakage due to fault reactivation. In this study, across-fault migration has been assessed. However, leakage can still occur if pressure build-up due to CO_2 injection reactivates the fault providing up-fault fluid pathways to shallower successions (Raleigh et al., 1976). The risk of up-fault migration is considered to be low within the Aurora storage site (Gassnova, 2012). However, a renewed assessment considering that the injection well (31/5-7) is drilled relatively close to multiple second-order faults, could be desirable. Such assessment requires knowledge on *in-situ* stress states, pore-pressure, mechanical strength of the fault rock, and orientations of the fault with respect to the principal stress axis (e.g., Streit and Hillis, 2004). Furthermore, a detailed assessment of strike attributes could reveal orientations of corrugations observed on the fault plane, such as those on the Svartalv 2 fault plane (Figure 4.16), which could be useful for assessing slip tendencies. While this was beyond the scope of this study, the structural geomodel presented herein can serve as a basis for such assessments.

6 Conclusions

Injection of CO_2 within the Aurora storage site is scheduled to commence in 2024 using the 31/5-7 well as an injector. Faults within the Aurora storage site can act as lateral barriers, potentially trapping or baffling migration of CO_2, or conduits, allowing across-fault migration. In light of this, the main objectives of this study were to i) establish a structural geomodel of the Aurora storage site, ii) assess the spatial and temporal evolution of faults, iii) assess the presence of across-fault seals, and iv) discuss plausible CO_2 migration pathways and gross rock volumes of relevant structural closures.

Objective i) was met by creating a detailed 3D geomodel of the Aurora storage site, using the GN10M1 3D seismic survey, 2D seismic lines, and well data. Furthermore, objective ii) was achieved by assessing depth-structure maps, thickness maps, and fault geometries (e.g., strike, dip, and throw). The key observations and results from objective i) and ii) are:

- The Lower Jurassic storage complex is located at approximately 2.6 km TVDSS at the location of the injection well (31/5-7), dipping gently (~2°) towards the south, and thus migration of CO_2 towards the north is expected.
- Thickness maps of the storage complex show that they are present throughout the study area with little signs of thinning. More precisely, the primary storage unit represents 81% of the bulk storage unit and is on average 130 m thick. The secondary storage unit is thinner, averaging 30 m thick, and contributes to the bulk storage volume. The primary seal shows little thickness variation and is 80 m thick, on average.
- The Aurora storage site comprises two fault populations. First-order faults displace the basement-cover contact, are predominately N–S (182°) striking, and listric in section view. Measured at the Top Cook Formation surface, the faults have an average trace length of 7 km, and maximum throws in the range of 43–940 m. Second-order faults exhibit a variation in strike from approximately NW–SE to N–S striking, with the mean strike orientation being approximately N–S (351°). Furthermore, they show no preferred dip direction and are largely restricted to the upper Triassic to Cretaceous successions. Measured at the Top Cook Formation, they have an average trace length of 3.6 km and the majority of the faults have throws between 15–50 m.
- The first-order Svartalv and Tusse fault zones nucleated within the Triassic succession, during Rift Phase 1. Hanging-wall growth is observed across both fault zones in the Lower Jurassic Dunlin Group and the Middle Jurassic Brent Group. However, thicker hanging-wall growth in the Dunlin Group is observed across the Svartalv Fault zone compared to the Tusse Fault Zone, while the

opposite trend is observed in the Brent Group. This observation indicates that reactivation of the Svartalv Fault Zone during the Jurassic likely occurred prior to reactivation of the Tusse Fault Zone.

- Second-order approximately NW–SE striking faults within the Aurora storage site likely formed during the Early to Middle Jurassic (late inter-rift phase), while approximately N–S striking faults formed later, likely during the Middle Jurassic to Cretaceous (Rift Phase 2).

- Within the Aurora storage site, the most common fault tip interaction style of the second-order faults is abutting or isolated fault tips. Towards the north in the study area, multiple NW–SE striking second-order faults show abutting interactions with the NNE–SSW to NE–SW striking Svartalv Fault Zone indicating hard-linkage.

- A model of extension directions within the Aurora storage site suggests that first-order faults likely formed due to E–W oriented extension during Rift Phase 1, before anticlockwise rotation (34°) of the extension direction to approximately NE–SW during the late inter-rift phase led to the formation of approximately NW–SE striking second-order faults and reactivation of the Svartalv Fault Zone. Clockwise rotation (17°) to approximately E–W oriented extension during Rift Phase 2 (potentially) led to formation of N–S striking faults and reactivation of the Tusse Fault Zone.

Objectives iii) and iv) were met by assessing the presence of across-fault juxtaposition seals and membrane seals using the SGR method. Data from the injection well 31/5-7 (completed March 2020) provides increased well control within the Aurora storage site, which strengthens the juxtaposition and membrane seal assessment compared to previous work. The key observations and results from objectives iii) and iv) are:

- Interpretation and detailed juxtaposition analysis show that second-order faults generally have throws less than the thickness of the primary seal (<80 m) and will therefore not offset the primary seal. However, E and NE dipping faults are likely to create juxtaposition seals within the upper parts of the secondary storage unit potentially baffle migrating CO_2. Furthermore, the faults juxtapose the primary storage unit in the footwall against the secondary storage unit in the hanging wall potentially allowing CO_2 to migrate across. In contrast, both storage units are self-juxtaposed across W and SW dipping faults and are more likely to allow across-fault migration.

- Membrane seal assessment, using the SGR method, shows that E and NE dipping second-order faults have SGR values between 15–20% where the upper parts of the primary storage unit in the footwall are juxtaposed against the secondary storage unit in the hanging wall, potentially exhibiting a minor influence on migration of CO_2. In contrast, W and SW dipping faults generally exhibit SGR <15% where the storage units are self-juxtaposed, and are, therefore, likely to allow across-fault migration.

- The Svartalv Fault Zone is characterized by throws exceeding 80 m, therefore, offsetting the primary seal and juxtaposing the storage units against shallower successions (i.e., the Upper Drake Formation and the Brent Group). Migration of CO_2 across these faults is, therefore, more likely to occur depending on how sand-rich the shallower successions are. However, membrane seal assessment of the Svartalv Fault Zone shows that the calculated SGR values are over 30% within both storage units, potentially creating baffles preventing this across-fault migration.

- Three two-way closures are present north of the injection well. Assuming that both juxtaposition seals and membrane seals are present, the combined gross rock volumes of these structural closures are 68×10^6 m^3 within the primary storage unit and 93.6×10^6 m^3 within the secondary storage unit. In a fill-to-spill scenario, buoyant CO_2 is likely to accumulate within these closures, thus improving the storage capacity of the Aurora storage site.

- Applying present-day methods to assess across-fault seals within the Aurora storage site show that injected CO_2 is unlikely to migrate out of the storage units and rather accumulate within small baffles, and migrate northwards into the Troll West field, likely after the end of the field life. These interpretations indicate that faults within the storage site have a mostly positive impact on CO_2 storage and present a low risk of unwanted across-fault migration.

- Drawing on the results observed within the Aurora storage site, the following suggestions are made with respect to future fault-controlled CO_2 storage prospects, particularly within the Horda Platform area of the northern North Sea. Firstly, prospects intersected by faults with throws less than the thickness of the primary seal can contribute positively to the storage of CO_2 due to the presence of small juxtaposition seals or membrane seals baffling fluid flow, thus increasing the overall storage capacity. Secondly, prospects intersected by faults that have throws larger than the thickness of the primary seal increase uncertainty related to across-fault migration due to limitations in present-day methods used to predict the presence of membrane seals.

Reference list

Allan, U. S. (1989) Model for hydrocarbon migration and entrapment within faulted structures. *AAPG Bulletin* 73 (7)**,** pp 803-811.

Andersen, O. and Sundal, A. (2021) Estimating caprock impact on CO2 migration in the Gassum Formation using 2D seismic line data. *Transport in Porous Media,* pp 1-29.

Andersen, T. B. and Jamtveit, B. (1990) Uplift of deep crust during orogenic extensional collapse: A model based on field studies in the Sogn ‐ Sunnfjord Region of western Norway. *Tectonics,* 9 (5)**,** pp 1097-1111.

Anderson, E. M. (1951) *The dynamics of faulting and dyke formation with applications to Britain.* 2 ed. Edinburgh and London: Oliver and Boyd.

Arts, R., Chadwick, A., Eiken, O., Thibeau, S. and Nooner, S. (2008) Ten years' experience of monitoring CO2 injection in the Utsira Sand at Sleipner, offshore Norway. *First break,* 26 (1)**,** pp 65-72.

Asquith, G. B., Krygowski, D. and Gibson, C. R. (2004) *Basic well log analysis.* 2 ed. Tulsa: AAPG Methods in Exploration Series.

Aydin, A. (1978) Small faults formed as deformation bands in sandstone, *In* Byerlee, J. and Wyss, M. (ed.) *Rock Friction and Earthquake Prediction. Contribution to Current Research in Geophysics (CCRG).* Basel: Birkhauser, pp 913-930.

Badley, M., Price, J., Dahl, C. R. and Agdestein, T. (1988) The structural evolution of the northern Viking Graben and its bearing upon extensional modes of basin formation. *Journal of the Geological Society,* 145 (3)**,** pp 455-472.

Bahorich, M. and Farmer, S. (1995) 3-D seismic discontinuity for faults and stratigraphic features: The coherence cube. *The leading edge,* 14 (10)**,** pp 1053-1058.

Bartholomew, I., Peters, J. and Powell, C. (1993) Regional structural evolution of the North Sea: oblique slip and the reactivation of basement lineaments. *Geological Society, London, Petroleum Geology Conference series.* Geological Society of London*,* 4 (1), pp 1109-1122.

Bell, R. E., Jackson, C. A. L., Whipp, P. S. and Clements, B. (2014) Strain migration during multiphase extension: Observations from the northern North Sea. *Tectonics,* 33 (10)**,** pp 1936-1963.

Benson, S. M. and Cole, D. R. (2008) CO2 sequestration in deep sedimentary formations. *Elements,* 4 (5)**,** pp 325-331.

Berkhout, A. J. (1982) *Seismic migration: imaging of acoustic energy by wave field extrapolation.* 2 ed. Amsterdam: Elsevier Science Publication. Co.

Biddle, K. T. and Wielchowsky, C. C. (1994) Hydrocarbon Traps, *In* Magoon, L. and Dow, W. (ed.) *M 60: The Petroleum System–From Source to Trap.* AAPG Memoire, pp 3-24.

Bjørlykke, K. (1993) Fluid flow in sedimentary basins. *Sedimentary Geology,* 86 (1-2)**,** pp 137-158.

Bolle, L. (1992) Troll Field: Norway's Giant Offshore Gas Field: Chapter 28, *In* Halibouty, M. (ed.) *Giant Oil and Gas Fields of the Decade 1978-1988.* AAPG Memoir, pp 5479-5490.

Bouvier, J., Kaars-Sijpesteijn, C., Kluesner, D., Onyejekwe, C. and Van der Pal, R. (1989) Three-dimensional seismic interpretation and fault sealing investigations, Nun River Field, Nigeria. *AAPG bulletin,* 73 (11)**,** pp 1397-1414.

Braathen, A., Midtkandal, I., Mulrooney, M. J., Appleyard, T. R., Haile, B. G. and van Yperen, A. E. (2018) Growth‐faults from delta collapse‐structural and sedimentological investigation of the Last Chance delta, Ferron Sandstone, Utah. *Basin Research,* 30 (4)**,** pp 688-707.

Braathen, A., Nordgulen, Ø., Osmundsen, P.-T., Andersen, T. B., Solli, A. and Roberts, D. (2000) Devonian, orogen-parallel, opposed extension in the Central Norwegian Caledonides. *Geology,* 28 (7)**,** pp 615-618.

Braathen, A., Osmundsen, P. T., Nordgulen, Ø., Roberts, D. and Meyer, G. B. (2002) Orogen-parallel extension of the Caledonides in northern Central Norway: an overview. *Norwegian Journal of Geology,* 82 (4)**,** pp 225-241.

Brekke, H., Sjulstad, H., Magnus, C. and Williams, R. (2001) Sedimentary Environments Offshore Norway–Palaeozoic to Recent. *Norwegian Petroleum Society Special Publications,* 10 pp 7-37.

Bretan, P. and Yielding, G. (2005) Using buoyancy pressure profiles to assess uncertainty in fault seal calibration, *In* Boult, P. and Kaldi, J. (ed.) *AAPG Hedberg Series.* Tulsa, pp 151-162.

Bretan, P., Yielding, G. and Jones, H. (2003) Using calibrated shale gouge ratio to estimate hydrocarbon column heights. *American Association of Petroleum Geologists Bulletin,* 87 (3)**,** pp 397-413.

Bretan, P., Yielding, G., Mathiassen, O. M. and Thorsnes, T. (2011) Fault-seal analysis for CO2 storage: an example from the Troll area, Norwegian Continental Shelf. *Petroleum Geoscience,* 17 (2)**,** pp 181-192.

Brown, A. R. (1996) *Interpretation of three-dimentional seismic data.* 3 ed. Tulsa: AAPG Memoir 42.

Brown, A. R. (2011) *Interpretation of three-dimensional seismic data.* 7 ed. Tulsa: The AAPG and the Society of Exploration Geophysicists.

Brun, J.-P. and Tron, V. (1993) Development of the North Viking Graben: inferences from laboratory modelling. *Sedimentary Geology,* 86 (1-2)**,** pp 31-51.

Caine, J. S., Evans, J. P. and Forster, C. B. (1996) Fault zone architecture and permeability structure. *Geology,* 24 (11)**,** pp 1025-1028.

Cameron, T., Bulat, J. and Mesdag, C. (1993) High resolution seismic profile through a Late Cenozoic delta complex in the southern North Sea. *Marine and Petroleum Geology,* 10 (6)**,** pp 591-599.

Cameron, T., Stoker, M. and Long, D. (1987) The history of Quaternary sedimentation in the UK sector of the North Sea Basin. *Journal of the Geological Society,* 144 (1)**,** pp 43-58.

Cartwright, J., Bouroullec, R., James, D. and Johnson, H. (1998) Polycyclic motion history of some Gulf Coast growth faults from high-resolution displacement analysis. *Geology,* 26 (9)**,** pp 819-822.

Cartwright, J. and Huuse, M. (2005) 3D seismic technology: the geological 'Hubble'. *Basin Research,* 17 (1)**,** pp 1-20.

Cartwright, J. A., Trudgill, B. D. and Mansfield, C. S. (1995) Fault growth by segment linkage: an explanation for scatter in maximum displacement and trace length data from the Canyonlands Grabens of SE Utah. *Journal of Structural Geology,* 17 (9)**,** pp 1319-1326.

Cartwringt, J. and Mansfield, C. (1998) Lateral displacement variation and lateral tip geometry of normal fault in the Canyonlands National Park. *Journal of Structural Geology,* 20 (1)**,** pp 3-19.

Childs, C., Walsh, J. J. and Watterson, J. (1997) Complexity in fault zone structure and implications for fault seal prediction, *In* Møller-Pedersen, P. and Koestler, A. G. (ed.) *Hydrocarbon Seals: Importance for Exploration and Production.* Singapore: Norwegian Petroleum Society Special Publications, pp 61-72.

Christiansson, P., Faleide, J. and Berge, A. (2000) Crustal structure in the northern North Sea: an integrated geophysical study. *Geological Society, London, Special Publications,* 167 (1)**,** pp 15-40.

Coward, M. (1990) The Precambrian, Caledonian and Variscan framework to NW Europe. *Geological Society, London, Special Publications,* 55 (1)**,** pp 1-34.

Cowie, P. A. and Scholz, C. H. (1992) Displacement-length scaling relationship for faults: data synthesis and discussion. *Journal of Structural Geology,* 14 (10)**,** pp 1149-1156.

Cowie, P. A. and Shipton, Z. K. (1998) Fault tip displacement gradients and process zone dimensions. *Journal of Structural Geology,* 20 (8)**,** pp 983-997.

Cowie, P. A., Underhill, J. R., Behn, M. D., Lin, J. and Gill, C. E. (2005) Spatio-temporal evolution of strain accumulation derived from multi-scale observations of Late Jurassic rifting in the northern North Sea: A critical test of models for lithospheric extension. *Earth and Planetary Science Letters,* 234 (3-4)**,** pp 401-419.

Crameri, F., Shephard, G. E. and Heron, P. J. (2020) The misuse of colour in science communication. *Nature communications,* 11 (1)**,** pp 1-10.

Cunningham, J., Cardozo, N., Townsend, C. and Callow, R. (2020) The Impact of Seismic Interpretation Methods on the Analysis of Faults: A Case Study from the Snøhvit Field, Barents Sea. *Solid Earth Discussions,* 12 (3)**,** pp 1-48.

Davies, R. J., Turner, J. and Underhill, J. R. (2001) Sequential dip-slip fault movement during rifting: a new model for the evolution of the Jurassic trilete North Sea rift system. *Petroleum Geoscience,* 7 (4)**,** pp 371-388.

Deegan, C. and Scull, B. (1977) *A standard lithostratigraphic nomenclature for the central and the northern north sea*. Norwegian Petroleum Directorate Bulletin 1. Available: https://www.npd.no/globalassets/1-npd/publikasjoner/npd-bulletins/npd-bulletin-1-1977.pdf [Accessed 08.06.2021].

Deng, C., Fossen, H., Gawthorpe, R. L., Rotevatn, A., Jackson, C. A. and FazliKhani, H. (2017) Influence of fault reactivation during multiphase rifting: The Oseberg area, northern North Sea rift. *Marine and petroleum geology,* 86 pp 1252-1272.

Denham, L. and Sheriff, R. (1981) What is horizontal resolution? *Expanded Abstract of 50th Annual Int. SEG Meeting. Session G17.* pp 119-134.

Dennis, J. G. (1967) *International tectonic dictionary: English terminology.* 1 ed. Tulsa: American Association of Petroleum Geologists.

Doré, A., Lundin, E., Fichler, C. and Olesen, O. (1997) Patterns of basement structure and reactivation along the NE Atlantic margin. *Journal of the Geological Society,* 154 (1)**,** pp 85-92.

Duffy, O. B., Bell, R. E., Jackson, C. A.-L., Gawthorpe, R. L. and Whipp, P. S. (2015) Fault growth and interactions in a multiphase rift fault network: Horda Platform, Norwegian North Sea. *Journal of Structural Geology,* 80 pp 99-119.

Eidvin, T., Riis, F. and Rasmussen, E. S. (2014) Oligocene to Lower Pliocene deposits of the Norwegian continental shelf, Norwegian Sea, Svalbard, Denmark and their relation to the uplift of Fennoscandia: A synthesis. *Marine and Petroleum Geology,* 56 pp 184-221.

Eidvin, T., Riis, F. and Rundberg, Y. (1999) Upper Cainozoic stratigraphy in the central North Sea (Ekofisk and Sleipner fields). *Norwegian Journal of Geology,* 79 (2)**,** pp 97-128.

Eigestad, G. T., Dahle, H. K., Hellevang, B., Riis, F., Johansen, W. T. and Øian, E. (2009) Geological modeling and simulation of CO 2 injection in the Johansen formation. *Computational Geosciences,* 13 (4)**,** pp 435.

Eiken, O., Ringrose, P., Hermanrud, C., Nazarian, B., Torp, T. and Høier, L. (2011) Lessons learned from 14 years of CCS operations: Sleipner, In Salah and Snøhvit. *Energy Procedia,* 4 pp 5541-5548.

Equinor (2019) *Northern Lights Project Concept report*. Equinor. Available: https://northernlightsccs.com/wp-content/uploads/2021/03/Northern-Lights-Project-Concept-report.pdf [Accessed 08.06.2021].

Færseth, R. (1996) Interaction of Permo-Triassic and Jurassic extensional fault-blocks during the development of the northern North Sea. *Journal of Geological Society,* 153 pp 931-944.

Færseth, R., Macintyre, R. and Naterstad, J. (1976) Mesozoic alkaline dykes in the Sunnhordland region, western Norway: ages, geochemistry and regional significance. *Lithos,* 9 (4)**,** pp 331-345.

Færseth, R. B., Gabrielsen, R. H. and Hurich, C. A. (1995) Influence of basement in structuring of the North Sea basin, offshore southwest Norway. *Norwegian Journal of Geology,* 75 (2-3)**,** pp 105-119.

Færseth, R. B., Johnsen, E. and Sperrevik, S. (2007) Methodology for risking fault seal capacity: Implications of fault zone architecture. *AAPG bulletin,* 91 (9)**,** pp 1231-1246.

Faleide, J. I., Bjørlykke, K. and Gabrielsen, R. H. (2010) Geology of the Norwegian continental shelf, *In* Bjørlykke, K. (ed.) *Petroleum Geoscience.* Heidelberg: Springer, pp 467-499.

Faleide, J. I., Kyrkjebo, R., Kjennerud, T., Gabrielsen, R. H., Jordt, H., Fanavoll, S. and Bjerke, M. D. (2002) Tectonic impact on sedimentary processes during Cenozoic evolution of the northern North Sea and surrounding areas. *Special Publication-Geological Society of London,* 196 pp 235-270.

Fawad, M. and Mondol, N. (2018) Reservoir Characterisation of Johansen Formation as Potential CO2 Storage Reservoir in the Northern North Sea. *Fifth CO2 Geological Storage Workshop.* European Association of Geoscientists & Engineers*,* 2018 (1), pp 1-5.

Ferrill, D. A., Stamatakos, J. A. and Sims, D. (1999) Normal fault corrugation: Implications for growth and seismicity of active normal faults. *Journal of Structural Geology,* 21 (8-9)**,** pp 1027-1038.

Fisher, Q. and Knipe, R. (2001) The permeability of faults within siliciclastic petroleum reservoirs of the North Sea and Norwegian Continental Shelf. *Marine and Petroleum Geology,* 18 (10)**,** pp 1063-1081.

Fisher, Q., Knipe, R. and Worden, R. (2000) Microstructures of deformed and non-deformed sandstones from the North Sea: implications for the origins of quartz cement in sandstones, *In* Worden, R. and Morad, S. (ed.) *Quartz Cementation in Sandstones.* Oxford: Blackwell Science, pp 129-146.

Fisher, Q. and Knipe, R. J. (1998) Fault sealing processes in siliciclastic sediments. *Geological Society, London, Special Publications,* 147 (1)**,** pp 117-134.

Fossen, H. (1992) The role of extensional tectonics in the Caledonides of south Norway. *Journal of structural geology,* 14 (8-9)**,** pp 1033-1046.

Fossen, H. (2016) *Structural geology.* 2 ed. Cambridge: Cambridge University Press.

Fossen, H. and Dunlap, W. J. (1998) Timing and kinematics of Caledonian thrusting and extensional collapse, southern Norway: evidence from 40Ar/39Ar thermochronology. *Journal of structural geology,* 20 (6)**,** pp 765-781.

Fossen, H., Schultz, R. A., Shipton, Z. K. and Mair, K. (2007) Deformation bands in sandstone: a review. *Journal of the Geological Society,* 164 (4)**,** pp 755-769.

Freeman, B., Yielding, G., Needham, D. T. and Badley, M. E. (1998) Fault seal prediction: the gouge ratio method, *In* Coward, M. P., Daltaban, T. S. and Johnson, H. (ed.) *Structural Geology in Reservoir Characterization.* London: Geological Society Special Publication, pp 19-25.

Fristad, T., Groth, A., Yielding, G. and Freeman, B. (1997) Quantitative fault seal prediction: a case study from Oseberg Syd, *In* Møller-Pedersen, P. and Koestler, A. G. (ed.) *Hydrocarbon Seals: Importance for Exploration and Production.* Singapore: Norwegian Petroleum Society Special Publications, Elsevier, pp 107-124.

Fulljames, J., Zijerveld, L., Franssen, C., Ingram, G. and Richard, P. (1996) Fault seal processes: systematic analyses of fault seals over geological and production timescales, *In* Møller-Pedersen, P. and Koestler, A. G. (ed.) *Hydrocarbons Seals: Importance for Exploration and Production.* Singapore: Norwegian Petroleum Society Special Publication, Elsevier, pp 51-59.

Furre, A.-K., Meneguolo, R., Pinturier, L. and Bakke, K. (2020) Planning deep subsurface CO2 storage monitoring for the Norwegian full-scale CCS project. *First Break,* 38 (10)**,** pp 55-60.

Gabrielsen, R. (1984) Long-lived fault zones and their influence on the tectonic development of the southwestern Barents Sea. *Journal of the Geological Society,* 141 (4)**,** pp 651-662.

Gabrielsen, R. H., Faerseth, R. B., Steel, R. J., Idil, S. and Kløvjan, O. S. (1990) Architectural style of basin fill in the northern Viking Graben, (ed.) *Tectonic Evolution of the North Sea Rifts.* 1 Oxford: International Lithosphere Program, pp 158-179.

Gabrielsen, R. H., Kyrkjebø, R., Faleide, J. I., Fjeldskaar, W. and Kjennerud, T. (2001) The Cretaceous post-rift basin configuration of the northern North Sea. *Petroleum Geoscience,* 7 (2)**,** pp 137-154.

Gassnova (2012) *Geological storage of CO2 from Mongstad. Interim report Johansen Formation*. Report TL02-GTL-Z-RA-0001. Gassnova and Ross Offshore. Available: https://ccsnorway.com/earlier-norwegian-ccs-projects/ [Accessed 08.06.2021].

Gee, D. G., Fossen, H., Henriksen, N. and Higgins, A. K. (2008) From the early Paleozoic platforms of Baltica and Laurentia to the Caledonide Orogen of Scandinavia and Greenland. *Episodes,* 31 (1)**,** pp 44-51.

Gee, D. G. and Sturt, B. A. (1985) *The Caledonide orogen – Scandinavia and related areas.* 1 ed. Chichester: John Wiley and Sons.

Gillespie, P., Walsh, J. t. and Watterson, J. (1992) Limitations of dimension and displacement data from single faults and the consequences for data analysis and interpretation. *Journal of Structural Geology,* 14 (10)**,** pp 1157-1172.

Graue, E., Helland-Hansen, W., Johnsen, J., Lomo, L. and Nottvedt, A. (1987) Advance and retreat of Brent delta system, Norwegian North Sea, *In* Brooks, J. and Glennie, K. W. (ed.) *Geology of North West Europe.* London: Graham & Trotman, pp 915-937.

Harris, D., Yielding, G., Levine, P., Maxwell, G. and Rose, P. (2000) Quantifying the effect of faults on flow of hydrocarbon through reservoirs: a fault seal analysis case study from the Strathspey field. North Sea. *Field Rehabilitation II abstracts.* Geological Society, London*,* pp

Helland-Hansen, W., Ashton, M., Lømo, L. and Steel, R. (1992) Advance and retreat of the Brent delta: recent contributions to the depositional model. *Geological Society, London, Special Publications,* 61 (1)**,** pp 109-127.

Helland, E. J. (2016) *Middle Jurassic Brent Group fault seal prediction for the Oseberg area.* Master thesis, University of Stavanger.

Henza, A. A., Withjack, M. O. and Schlische, R. W. (2010) Normal-fault development during two phases of non-coaxial extension: An experimental study. *Journal of Structural Geology,* 32 (11)**,** pp 1656-1667.

Herron, D. A. (2011) *First steps in seismic interpretation.* 1 ed. Tulsa: Society of Exploration Geophysicists.

Hongxing, G. and Anderson, J. K. (2007) Fault throw profile and kinematics of Normal fault: conceptual models and geologic examples. *Geol. J. China Univ.,* 13 (1)**,** pp 75-88.

Hossack, J. and Cooper, M. (1986) Collision tectonics in the Scandinavian Caledonides. *Geological Society, London, Special Publications,* 19 (1)**,** pp 285-304.

IEA (2021) *Net Zero by 2050.* International Energy Agency. Available: https://www.iea.org/reports/net-zero-by-2050 [Accessed 27.05.2021].

IPCC (2018) *Global warming of 1.5 C. An IPCC Special Report.* Intergovernmental Panel on Climate Change Special Report. Available: https://www.ipcc.ch/sr15/ [Accessed 08.06.2021].

Isaksen, D. and Tonstad, K. (1989) *A revised Cretaceous and Tertiary lithostratigraphic nomenclature for the Norwegian North Sea*. Norwegian Petroleum Directorate Bulletin No 5. Available: https://www.npd.no/globalassets/1-npd/publikasjoner/npd-bulletins/npd-bulletin-5-1989.pdf [Accessed 08.06.2021].

Jackson, C. A.-L., Bell, R. E., Rotevatn, A. and Tvedt, A. B. (2017) Techniques to determine the kinematics of synsedimentary normal faults and implications for fault growth models. *Geological Society, London, Special Publications,* 439 (1)**,** pp 187-217.

Jev, B., Kaars-Sijpesteijn, C., Peters, M., Watts, N. and Wilkie, J. (1993) Akaso field, Nigeria: Use of integrated 3-D seismic, fault slicing, clay smearing, and RFT pressure data on fault trapping and dynamic leakage. *AAPG bulletin,* 77 (8)**,** pp 1389-1404.

Jordt, H., Faleide, J. I., Bjørlykke, K. and Ibrahim, M. T. (1995) Cenozoic sequence stratigraphy of the central and northern North Sea Basin: tectonic development, sediment distribution and provenance areas. *Marine and Petroleum Geology,* 12 (8)**,** pp 845-879.

Karolytė, R., Johnson, G., Yielding, G. and Gilfillan, S. M. (2020) Fault seal modelling–the influence of fluid properties on fault sealing capacity in hydrocarbon and CO2 systems. *Petroleum Geoscience,* 26 (3)**,** pp 481-497.

Kearey, P., Brooks, M. and Hill, I. (2002) *An introduction to geophysical exploration.* 1 ed. Oxford: Blackwell Publishing Ltd.

Khani, H. F., Fossen, H., Gawthorpe, R., Faleide, J. I. and Bell, R. E. (2017) Basement structure and its influence on the structural configuration of the northern North Sea rift. *Tectonics,* 36 (6)**,** pp 1151-1177.

Kim, Y.-S., Andrews, J. R. and Sanderson, D. J. (2001) Reactivated strike–slip faults: examples from north Cornwall, UK. *Tectonophysics,* 340 (3-4)**,** pp 173-194.

Kim, Y.-S. and Sanderson, D. J. (2005) The relationship between displacement and length of faults: a review. *Earth-Science Reviews,* 68 (3-4)**,** pp 317-334.

Knipe, R. (1992) Faulting processes and fault seal, *In* Larsen, R., Brekke, B., Larsen, B. and Talleraas, E. (ed.) *Structural and tectonic modelling and its application to petroleum geology.* Norwegian Petroleum Society Special Publications, pp 325-342.

Knipe, R. J. (1997) Juxtaposition and seal diagrams to help analyze fault seals in hydrocarbon reservoirs. *AAPG Bulletin,* 81 (2)**,** pp 187-195.

Knox, R. O. B. and Harland, R. (1979) Stratigraphical relationships of the early Palaeogene ash-series of NW Europe. *Journal of the Geological Society,* 136 (4)**,** pp 463-470.

Krantz, R. W. (1988) Multiple fault sets and three-dimensional strain: theory and application. *Journal of Structural Geology,* 10 (3)**,** pp 225-237.

Kyrkjebø, R., Gabrielsen, R. and Faleide, J. (2004) Unconformities related to the Jurassic–Cretaceous synrift–post-rift transition of the northern North Sea. *Journal of the Geological Society,* 161 (1)**,** pp 1-17.

Larsen, P.-H. (1988) Relay structures in a Lower Permian basement-involved extension system, East Greenland. *Journal of Structural Geology,* 10 (1)**,** pp 3-8.

Leith, C. K. (1923) *Structural geology.* 1 ed. New York: H. Holt and Co.

Lervik, K., Spencer, A. and Warrington, G. (1989) Outline of Triassic stratigraphy and structure in the central and northern North Sea, *In* Collenson, J. (ed.) *Correlation in hydrocarbon exploration.* London: Graham & Trotman, pp 173-189.

Lindsay, N., Murphy, F., Walsh, J. and Watterson, J. (1993) Outcrop studies of shale smears on fault surfaces, *In* Flint, S. and Bryant, I. (ed.) *The geological modelling of hydrocarbon reservoirs and outcrop analogues.* Blackwell Scientific Publications, pp 113-123.

Loewenthal, D., Lu, L., Roberson, R. and Sherwood, J. (1976) The wave equation applied to migration. *Geophysical Prospecting,* 24 (2)**,** pp 380-399.

Lohr, T., Krawczyk, C. M., Oncken, O. and Tanner, D. C. (2008) Evolution of a fault surface from 3D attribute analysis and displacement measurements. *Journal of Structural Geology,* 30 (6)**,** pp 690-700.

Lothe, A., Gabrielsen, R., Hagen, N. B. and Larsen, B. (2002) An experimental study of the texture of deformation bands: effects on the porosity and permeability of sandstones. *Petroleum Geoscience,* 8 (3)**,** pp 195-207.

Lundmark, A., Sæther, T. and Sørlie, R. (2013) Ordovician to Silurian magmatism on the Utsira High, North Sea: implications for correlations between the onshore and offshore Caledonides. *Geological Society, London, Special Publications,* 390 (1)**,** pp 513-523.

Lyon, P., Boult, P., Mitchell, A. and Hillis, R. (2004) Improving fault geometry interpretation through'pseudo-depth'conversion of seismic data in the Penola Trough, Otway Basin, *In* Boult, P., Johns, D. and Lang, S. (ed.) *Eastern Australian Basin Symposium II.* Adelaide: Petroleum Exploration Society of Australia, Special Publication, pp 395-706.

Lyon, P. J., Boult, P. J., Hillis, R. R. and Mildren, S. D. (2005) Sealing by shale gouge and subsequent seal breach by reactivation: A case study of the Zema Prospect, Otway Basin. *AAPG Special Volumes,* 2 pp 179-197.

Maerten, L., Gillespie, P. and Pollard, D. D. (2002) Effects of local stress perturbation on secondary fault development. *Journal of Structural Geology,* 24 (1)**,** pp 145-153.

Mandl, G., De Jong, L. and Maltha, A. (1977) Shear zones in granular material. *Rock mechanics,* 9 (2-3)**,** pp 95-144.

Manzocchi, T., Childs, C. and Walsh, J. (2010) Faults and fault properties in hydrocarbon flow models. *Geofluids,* 10 (1‐2)**,** pp 94-113.

Marjanac, T. and Steel, R. J. (1997) Dunlin Group sequence stratigraphy in the northern North sea: a model for Cook Sandstone deposition. *AAPG bulletin,* 81 (2)**,** pp 276-292.

Marshall, J. and Hewett, A. (2003) Devonian, *In* Evans, D., Graham, C., Armour, A. and Bathurst, P. (ed.) *The Millenium Atlas: petroleum geology of the central and northern North Sea.* Geological Society of London, pp 65-81.

McGrath, A. G. and Davison, I. (1995) Damage zone geometry around fault tips. *Journal of Structural Geology,* 17 (7)**,** pp 1011-1024.

Michie, E. A. H., Mulrooney, M. J. and Braathen, A. (preprint) Fault Interpretation Uncertainties using Seismic Data, and the Effects on Fault Seal Analysis: A Case Study from the Horda Platform, with Implications for CO2 storage. *Solid Earth Discussions,* https://doi.org/10.5194/se-2021-23, in review, 2021 pp 1-68.

Milnes, A., Wennberg, O., Skår, Ø. and Koestler, A. (1997) Contraction, extension and timing in the South Norwegian Caledonides: the Sognefjord transect. *Geological Society, London, Special Publications,* 121 (1)**,** pp 123-148.

Miocic, J., Johnson, G. and Bond, C. E. (2019) Uncertainty in fault seal parameters: implications for CO2 column height retention and storage capacity in geological CO2 storage projects. *Solid earth,* 10 pp 951-967.

Mulrooney, M. J., Osmond, J. L., Skurtveit, E., Faleide, J. I. and Braathen, A. (2020) Structural analysis of the Smeaheia fault block, a potential CO2 storage site, northern Horda Platform, North Sea. *Marine and Petroleum Geology,* pp 104598.

NCCS (2019) *Norwegian CCS Research Centre (NCCS)-Annual Report 2019*. Sintef Report. Available: https://www.sintef.no/globalassets/project/nccs/annual-2019/nccs_annual_report_2019_rev_lr.pdf [Accessed 17.02.2021].

Needham, D., Yielding, G. and Freeman, B. (1996) Analysis of fault geometry and displacement patterns. *Geological Society, London, Special Publications,* 99 (1)**,** pp 189-199.

Ngwenya, B., Elphick, S., Main, I. and Shimmield, G. (2000) Experimental constraints on the diagenetic self-sealing capacity of faults in high porosity rocks. *Earth and Planetary Science Letters,* 183 (1-2)**,** pp 187-199.

Nicol, A., Childs, C., Walsh, J., Manzocchi, T. and Schöpfer, M. (2017) Interactions and growth of faults in an outcrop-scale system. *Geological Society, London, Special Publications,* 439 (1)**,** pp 23-39.

Norton, M., Coney, P. and Davis, G. (1986) Collapse of the Caledonian orogen and the Old Red Sandstone. *Nature,* 323 (6084)**,** pp 147-149.

Norton, M. G. (1987) The Nordfjord-Sogn Detachment, W. Norway. *Norwegian Journal of Geology,* 67 (2)**,** pp 93-106.

Norwegian Ministry of Petroleum and Energy *Longship – Carbon capture and storage*. (2019) Meld. St. 33 Report to the Stortinget (white paper)

Nottvedt, A., Gabrielsen, R. and Steel, R. (1995) Tectonostratigraphy and sedimentary architecture of rift basins, with reference to the northern North Sea. *Marine and Petroleum Geology,* 12 (8)**,** pp 881-901.

NPD (2014) *Norwegian Petroleum Directorate - Geology of the North Sea*. Available: https://www.npd.no/en/facts/publications/co2-atlases/co2-atlas-for-the-norwegian-continental-shelf/4-the-norwegian-north-sea/4.1-geology-of-the-north-sea/ [Accessed 08.06.2021].

NPD CO2 Atlas (2011) *CO2 Storage Atlas Norwegian North Sea*. Norwegian Petroleum Directorate. Available: https://www.npd.no/globalassets/1-npd/publikasjoner/atlas-eng/co2-atlas-north-sea.pdf [Accessed 08.06.2021].

NPD Factmaps 2020. *Norwegian Petroleum Directorate Factmaps* [Online]. Available: https://factmaps.npd.no/factmaps/3_0/?run=FieldByNPDID&NPDID=46437 [Accessed 23.04 2020].

NPD Factpages 2020. *Norwegian Petroleum Directorate Factpages* [Online]. Available: https://factpages.npd.no/ [Accessed 08.08 2020].

Ocamb, R. D. (1961) Growth faults of south Louisiana. *Gulf Coast Association of Geological Societies Transactions,* 11 pp 139-175.

Odinsen, T., Christiansson, P., Gabrielsen, R. H., Faleide, J. I. and Berge, A. M. (2000a) The geometries and deep structure of the northern North Sea rift. *Geological Society of London,* 167 pp 41-57.

Odinsen, T., Reemst, P., Van Der Beek, P., Faleide, J. I. and Gabrielsen, R. H. (2000b) Permo-Triassic and Jurassic extension in the northern North Sea: results from tectonostratigraphic forward modelling. *Geological Society, London, Special Publications,* 167 (1)**,** pp 83-103.

Opheim, J. A. and Gudmundsson, A. (1989) Formation and geometry of fractures, and related volcanism, of the Krafla fissure swarm, northeast Iceland. *Geological Society of America Bulletin,* 101 (12)**,** pp 1608-1622.

Osmundsen, P. and Andersen, T. (2001) The middle Devonian basins of western Norway: sedimentary response to large-scale transtensional tectonics? *Tectonophysics,* 332 (1-2)**,** pp 51-68.

Ottesen, D., Dowdeswell, J. A. and Bugge, T. (2014) Morphology, sedimentary infill and depositional environments of the Early Quaternary North Sea Basin (56–62 N). *Marine and Petroleum Geology,* 56 pp 123-146.

Peacock, D., Knipe, R. and Sanderson, D. (2000) Glossary of normal faults. *Journal of Structural Geology,* 22 (3)**,** pp 291-305.

Peacock, D. and Sanderson, D. (1991) Displacements, segment linkage and relay ramps in normal fault zones. *Journal of Structural Geology,* 13 (6)**,** pp 721-733.

Pei, Y., Paton, D., Knipe, R. and Wu, K. (2015) A Review Of Fault Sealing Behaviour And Its Evaluation In Siliciclastic Rocks. *Earth-Science Reviews,* 150 pp 121-138.

Petrel E&P Software Platform 2015. *Recommended Seismic Volume Attributes* [Online]. Schlumberger Available: file:///C:/Users/Nora/Downloads/Petrel_Recommended_Seismic_Volume_Attributes_2015_Poster%20(2).pdf [Accessed 08.06.21].

Phillips, T. B., Fazlikhani, H., Gawthorpe, R. L., Fossen, H., Jackson, C. A.-L., Bell, R. E., Faleide, J. I. and Rotevatn, A. (2019) The Influence of Structural Inheritance and Multiphase Extension on Rift Development, the NorthernNorth Sea. *Tectonics,* 38 (12)**,** pp 4099-4126.

Pickering, G., Peacock, D. C. and Lee, J. (1997) Modeling tip zones to predict the throw and length characteristics of faults. *AAPG bulletin,* 81 (1)**,** pp 82-99.

Purcell, W. (1949) Capillary pressures-their measurement using mercury and the calculation of permeability therefrom. *Journal of Petroleum Technology,* 1 (02)**,** pp 39-48.

Raleigh, C., Healy, J. and Bredehoeft, J. (1976) An experiment in earthquake control at Rangely, Colorado. *Science,* 191 (4233)**,** pp 1230-1237.

Ravnås, R. and Steel, R. (1997) Contrasting styles of Late Jurassic syn-rift turbidite sedimentation: a comparative study of the Magnus and Oseberg areas, northern North Sea. *Marine and Petroleum Geology,* 14 (4)**,** pp 417-449.

Rider, M. (2000) The geological interpretation of well logs second edition. *Rider–French Consulting Ltd, Sutherland, The United Kingdom,* pp 126-128.

Roberts, A., Yielding, G., Kusznir, N., Walker, I. and Dorn-Lopez, D. (1993) Mesozoic extension in the North Sea: constraints from flexural backstripping, forward modelling and fault populations. *Geological Society, London, Petroleum Geology Conference series.* Geological Society of London*,* 4 (1), pp 1123-1136.

Roberts, D. and Gee, D. G. (1985) An introduction to the structure of the Scandinavian Caledonides. *The Caledonide orogen–Scandinavia and related areas,* 1 pp 55-68.

Rotevatn, A., Fossen, H., Hesthammer, J., Aas, T. E. and Howell, J. A. (2007) Are relay ramps conduits for fluid flow? Structural analysis of a relay ramp in Arches National Park, Utah. *Geological Society, London, Special Publications,* 270 (1)**,** pp 55-71.

Rotevatn, A., Jackson, C. A.-L., Tvedt, A. B., Bell, R. E. and Blækkan, I. (2019) How do normal faults grow? *Journal of Structural Geology,* 125 (2019)**,** pp 174-184.

Schlische, R. W. (1995) Geometry and origin of fault-related folds in extensional settings. *AAPG bulletin,* 79 (11)**,** pp 1661-1678.

Schowalter, T. T. (1979) Mechanics of secondary hydrocarbon migration and entrapment. *AAPG bulletin,* 63 (5)**,** pp 723-760.

Schultz, R. A. and Fossen, H. (2002) Displacement–length scaling in three dimensions: the importance of aspect ratio and application to deformation bands. *Journal of Structural Geology,* 24 (9)**,** pp 1389-1411.

Sejrup, H. P., Aarseth, I., Haflidason, H. and Løvlie, R. (1996) Quaternary of the Norwegian Channel: glaciation history and palaeoceanography. *Norwegian Journal of Geology,* pp 65-86.

Serck, C. S. and Braathen, A. (2019) Extensional fault and fold growth: Impact on accommodation evolution and sedimentary infill. *Basin Research,* 31 (5)**,** pp 967-990.

Sheriff, R. E. (1977) Limitations on resolution of seismic reflections and geologic detail derivable from them: Section 1. Fundamentals of Stratigraphic Interpretation of Seismic Data, *In* Payton, C. (ed.) *Seismic Stratigraphy – Applications to Hydrocarbon Exploration.* AAPG Memoir, pp 3-14.

Shipton, Z. and Cowie, P. (2001) Damage zone and slip-surface evolution over μm to km scales in high-porosity Navajo sandstone, Utah. *Journal of Structural Geology,* 23 (12)**,** pp 1825-1844.

Sperrevik, S., Gillespie, P. A., Fisher, Q. J., Halvorsen, T. and Knipe, R. J. (2002) Empirical estimation of fault rock properties. *Norwegian Petroleum Society Special Publications,* 11 pp 109-125.

Steel, R. (1993) Triassic–Jurassic megasequence stratigraphy in the Northern North Sea: rift to post-rift evolution. *Geological Society, London, Petroleum Geology Conference series.* Geological Society of London*,* 4 (1), pp 299-315.

Steel, R., Næhle, S., Nilsen, H., Røe, S. and Spinnangr, A. (1977) Coarsening-upward cycles in the alluvium of Hornelen Basin (Devonian) Norway: Sedimentary response to tectonic events. *Geological Society of America Bulletin,* 88 (8)**,** pp 1124-1134.

Streit, J. E. and Hillis, R. R. (2004) Estimating fault stability and sustainable fluid pressures for underground storage of CO2 in porous rock. *Energy,* 29 (9-10)**,** pp 1445-1456.

Sundal, A., Miri, R., Ravn, T. and Aagaard, P. (2015) Modelling CO2 migration in aquifers; considering 3D seismic property data and the effect of site-typical depositional heterogeneities. *International Journal of Greenhouse Gas Control,* 39 pp 349-365.

Sundal, A., Nystuen, J. P., Rørvik, K.-L., Dypvik, H. and Aagaard, P. (2016) The Lower Jurassic Johansen Formation, northern North Sea–Depositional model and reservoir characterization for CO2 storage. *Marine and Petroleum Geology,* 77 pp 1376-1401.

Thorsen, C. E. (1963) Age of growth faulting in southeast Louisiana. *Gulf Coast Association of Geological Societies Transactions,* 13 pp 103-110.

Tomasso, M., Underhill, J. R., Hodgkinson, R. A. and Young, M. J. (2008) Structural styles and depositional architecture in the Triassic of the Ninian and Alwyn North fields: Implications for basin development and prospectivity in the Northern North Sea. *Marine and Petroleum Geology,* 25 (7)**,** pp 588-605.

Torp, T. A. and Gale, J. (2004) Demonstrating storage of CO2 in geological reservoirs: The Sleipner and SACS projects. *Energy,* 29 (9-10)**,** pp 1361-1369.

Torsvik, T. H., Andersen, T. B., Eide, E. A. and Walderhaug, H. J. (1997) The age and tectonic significance of dolerite dykes in western Norway. *Journal of the Geological Society,* 154 (6)**,** pp 961-973.

Torsvik, T. H., Carlos, D., Mosar, J., Cocks, L. R. M. and Malme, T. (2002) Global reconstructions and North Atlantic paleogeography 440 Ma to recent, *In* Eide, E. (ed.) *BATLAS–Mid Norway plate reconstruction atlas with global and Atlantic perspectives.* . Trondheim: Geological Survey of Norway, pp 18-39.

Trudgill, B. D. and Cartwright, J. (1994) Relay-ramp forms and normal-fault linkages, Canyonlands National Park, Utah. *Geological Society of America Bulletin,* 106 (9)**,** pp 1143-1157.

Underhill, J. R. and Partington, M. (1993) Jurassic thermal doming and deflation in the North Sea: implications of the sequence stratigraphic evidence. *Geological Society, London, Petroleum Geology Conference Series.* Geological Society of London*,* 4 (1), pp 337-345.

Vollset, J. and Doré, A. (1984) *A revised Triassic and Jurassic lithostratigraphic nomenclature for the Norwegian North Sea*. Norwegian Petroleum Directorate Bulletin 3. Available: https://www.npd.no/globalassets/1-npd/publikasjoner/npd-bulletins/npd-bulletin-3-1984.pdf [Accessed 08.06.21].

Walderhaug, O. (1996) Kinetic modeling of quartz cementation and porosity loss in deeply buried sandstone reservoirs. *AAPG bulletin,* 80 (5)**,** pp 731-745.

Walsh, J., Bailey, W., Childs, C., Nicol, A. and Bonson, C. (2003) Formation of segmented normal faults: a 3-D perspective. *Journal of Structural Geology,* 25 (8)**,** pp 1251-1262.

Walsh, J., Nicol, A. and Childs, C. (2002) An alternative model for the growth of faults. *Journal of Structural Geology,* 24 (11)**,** pp 1669-1675.

Walsh, J. and Watterson, J. (1987) Distributions of cumulative displacement and seismic slip on a single normal fault surface. *Journal of Structural Geology,* 9 (8)**,** pp 1039-1046.

Walsh, J. J. and Watterson, J. (1988) Analysis of the relationship between displacements and dimensions of faults. *Journal of Structural geology,* 10 (3)**,** pp 239-247.

Watterson, J. (1986) Fault dimensions, displacements and growth. *Pure and Applied Geophysics,* 124 (1-2)**,** pp 365-373.

Watts, N. (1987) Theoretical aspects of cap-rock and fault seals for single-and two-phase hydrocarbon columns. *Marine and Petroleum Geology,* 4 (4)**,** pp 274-307.

Weber, K., Mandl, G., Pilaar, W., Lehner, B. and Precious, R. The role of faults in hydrocarbon migration and trapping in Nigerian growth fault structures. *Offshore Technology Conference*, Texas, 7th May 1978.

Whipp, P., Jackson, C. L., Gawthorpe, R., Dreyer, T. and Quinn, D. (2014) Normal fault array evolution above a reactivated rift fabric; a subsurface example from the northern Horda Platform, Norwegian North Sea. *Basin Research,* 26 (4)**,** pp 523-549.

Wu, L., Thorsen, R., Ringrose, P., Ottesen, S. and Hartvedt, K. (2021) Significance of fault seal in assessing CO2 storage capacity and leakage risks-An example from offshore Norway. *Petroleum Geoscience,* 27 (1)**,** pp 1-20.

Yielding, G. (2002) Shale gouge ratio—Calibration by geohistory, *In* Koestler, A. G. and Hundsdale, R. (ed.) *Norwegian Petroleum Society Special Publications.* Amsterdam: Elsevier, pp 1-15.

Yielding, G., Bretan, P. and Freeman, B. (2010) Fault seal calibration: a brief review. *Geological Society, London, Special Publications,* 347 (1)**,** pp 243-255.

Yielding, G., Freeman, B. and Needham, D. T. (1997) Quantitative fault seal prediction. *AAPG Bulletin,* 81 (6)**,** pp 897-917.

Yielding, G., Øverland, J. and Byberg, G. Characterization of fault zones in the Gullfaks Field for reservoir modelling, *In* Fleet, A. and Boldy, S. (ed.) *Geological Society, London, Petroleum Geology Conference series.* Geological Society of London, pp 1177-1185.

Ziegler, P. (1975a) Geologic evolution of North Sea and its tectonic framework. *AAPG bulletin,* 59 (7)**,** pp 1073-1097.

Ziegler, P. (1975b) North Sea Basin history in the tectonic framework of North-Western Europe, *In* Woodland, A. (ed.) *Petroleum and the Continental Shelf og North-West Europe.* Essex: Geology, pp 131-49.

Ziegler, P. (1982) Triassic rifts and facies patterns in Western and Central Europe. *Geologische Rundschau,* 71 (3)**,** pp 747-772.

Ziegler, P. (1990) Tectonic and palaeogeographic development of the North Sea rift system, *In* Blundell, D. J. and Gibbs, A. D. (ed.) *Tectonic evolution of the North Sea rifts.* Oxford: Clarendon Press, pp 1-36.

Appendices

Appendix 1

Table Appendix 1. Estimates of hanging-wall thickness (HW) and footwall thickness (FW) of the Svartalv fault segments and the Tusse fault segment using the thickness maps. Calculates expansion index (E.I.) is presented as a range due to variations in thickness along the faults.

Succession	Svartalv fault segment			Tusse fault segment		
	HW (m)	FW (m)	E.I.	HW (m)	FW (m)	E.I.
BRENT GP.	100–120	95–105	1.05–1.14	240–260	80–100	2.60–3.00
DUNLIN GP.	470–500	320–340	1.47	330–450	280–330	1.18–1.36

Appendix 2

Table Appendix 2. Complete list of faults modelled in this study with max throw and trace length measured in the Top Cook Formation surface. Location of faults are shown in Figure Appendix 2. Comments on whether the entire trace length is measured is included. In addition, up-section, down-section, strike, and dip attributes are added. Abbreviations: LC = Lower Cretaceous, P = Paleogene, MJ = Middle Jurassic, N = Neogene, UJ = Upper Jurassic, B = Brent Group, UT = Upper Triassic, PT = Permian to Triassic, SW = Southwest, S = South, SE = Southeast, NW = Northwest, N = North, NE = Northeast.

Fault	Max throw (m)	Trace length (m)	Entire trace length imaged?	Up-section extent	Down-section extent	Strike	Dip
Svartalv 1	370	6350	No	LC	B	SW	NW
Svartalv 2	300	12000	Yes	P	B	S/SW	W/NW
Svartalv 2.1	92	2500	Yes	MJ	B	SW	NW
Tusse	940	165000	No	N	B	S	W
F1	33	4083	Yes	LC	UT	N	E
F2	54	6641	Yes	UJ	PT	SE	SW
F3	47	6700	Yes	LC	PT	NW	NE
F4	48	8800	Yes	LC	PT	NW	NE
F5	29	8000	Yes	UJ	UT	NW	NE
F6	25	6000	Yes	LC	UT	NW	NE
F7	26	3100	Yes	UJ	UT	NW	NE
F8	13	2096	Yes	UJ	UT	N	E
F9*	17	5739	Yes	UJ	UT	N	E
F10*	43	7743	Yes	UJ	B	S	W

F11	76	5619	Yes	UJ	B	S	W
F12	115	4257	Yes	UJ	PT	SW	NW
F13	27	2600	Yes	UJ	UT	N	E
F14	44	6850	Yes	UJ	UT	NW	NE
F15	50	2635	Yes	LC	UT	N	E
F16	13	1064	Yes	MJ	UT	N	E
F17	37	5893	No	LC	UT	NW	NE
F18	30	3800	No	LC	UT	NW	NE
F19	21	1593	Yes	UJ	UT	N	E
F20	10	1496	Yes	UJ	LJ	N	E
F21	23	4808	No	UJ	LJ	NW	NE
F22	26	2878	Yes	UJ	LJ	N	E
F23	46	4220	Yes	UJ	UT	N	E
F24	29	2559	Yes	UJ	LJ	N	E
F25	16	2153	Yes	UJ	UT	N	E
F26	10	1868	Yes	UJ	UT	N	E
F27	32	2310	Yes	UJ	LJ	N	E
F28	13	2146	Yes	UJ	UT	NW	SE
F29	22	9	Yes	UJ	PT	N	E
F30	25	3299	Yes	UJ	UT	NW	SE
F31	30	4110	Yes	UJ	UT	NE	SE
F32	288	4300	Yes	LC	UT	NE	SE
F33	130	5249	Yes	UJ	UT	N	E
F34	25	1422	Yes	MJ	UT	N	E
F35	196	3008	Yes	UJ	UT	N	E
F36	18	632	Yes	UJ	UT	N	E
F37	19	4160	Yes	UJ	MJ	NW	E
F38	0*	0*	Yes	UJ	LJ	NW	NE
F39	80	1000	Yes	UJ	LJ	NW	NE
F40	13	596	Yes	UJ	LJ	NW	NE
F41	136	4416	Yes	UJ	PT	N	E
F42	20	6930	Yes	MJ	LJ	N	E
F43	26	8577	Yes	MJ	UT	S	W
F44	6	2758	Yes	MJ	LJ	S	W
F45	25	8083	Yes	MJ	UT	S	W
F46	35	6810	Yes	UJ	UT	SE	SW
F47	36	2975	Yes	UJ	UT	S	W
F48	33	2975	Yes	UJ	UT	SE	SW
F49	41	3846	Yes	UJ	UT	S	W

F50	31	2842	Yes	UJ	UT	SE	SW
F51	5	3408	Yes	UJ	UT	SE	SW
F52	31	2747	Yes	UJ	UT	SE	SW
F53	48	7757	Yes	UJ	UT	SE	SW
F54	26	515	Yes	UJ	UT	S	W
F55	20	4080	No	UJ	UT	SE	SW
F56	7	890	No	UJ	UT	SE	SW
F57	50	370	Yes	MJ	UT	SE	SW
F58	50	1560	No	UJ	UT	SE	SW
F59	13	540	No	UJ	UT	SE	SW
F60	40	1450	No	UJ	UT	SE	SW
F61	39	935	No	UJ	UT	SE	SW
F62	26	656	Yes	MJ	UT	W	E
F63	55	3124	Yes	UJ	PT	N	E

*Does not displace Top Cook Formation

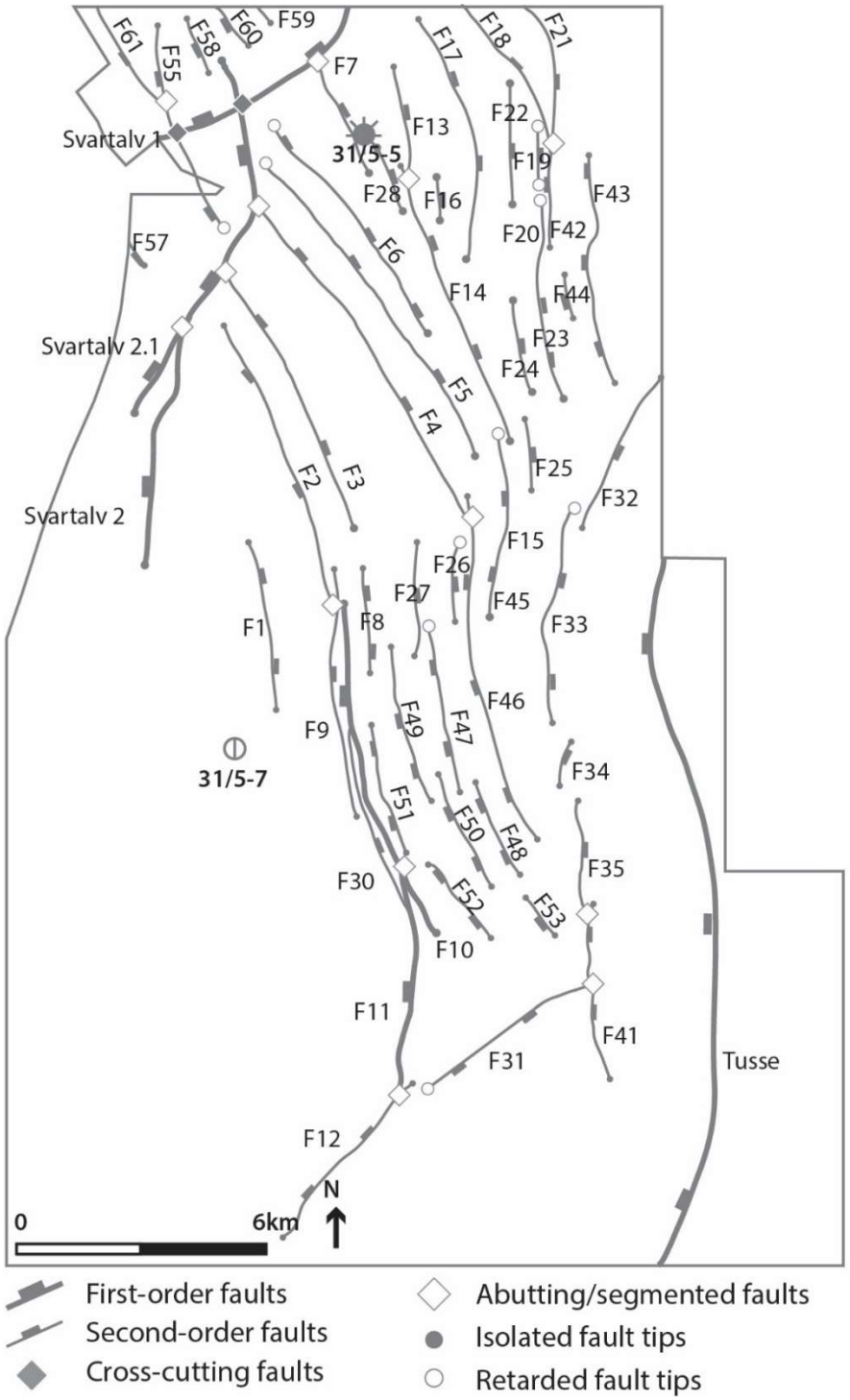

Figure Appendix 2 Overview of the majority of interpreted faults within this study intersecting the Top Cook Formation surface. Note that some of the faults in Table Appendix 2 have not been included in the fault trace map due to very low throws and/or trace lengths.

Appendix 3

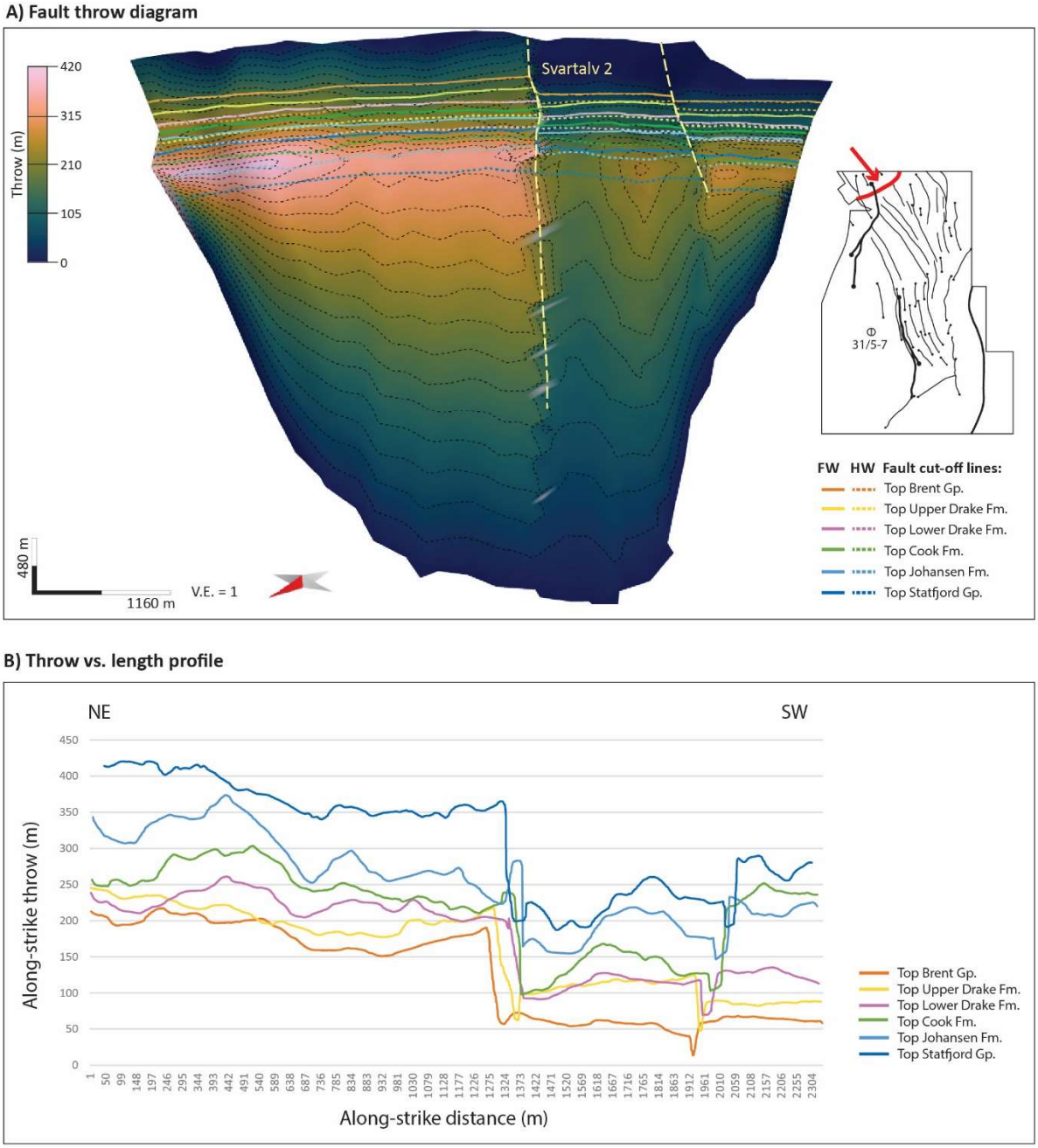

Figure Appendix 3. 1. A) Svartalv 1 fault throw diagram showing horizon-fault intersection (cut-off) lines and a 25-meter throw contour spacing. Inset shows location of fault and viewing direction. B) Throw vs. length profile of the Svartalv 2 segment. Note that throw below the Statfjord Group hanging-wall cut-off line have been extrapolated and is likely not representative for the vertical throw variation.

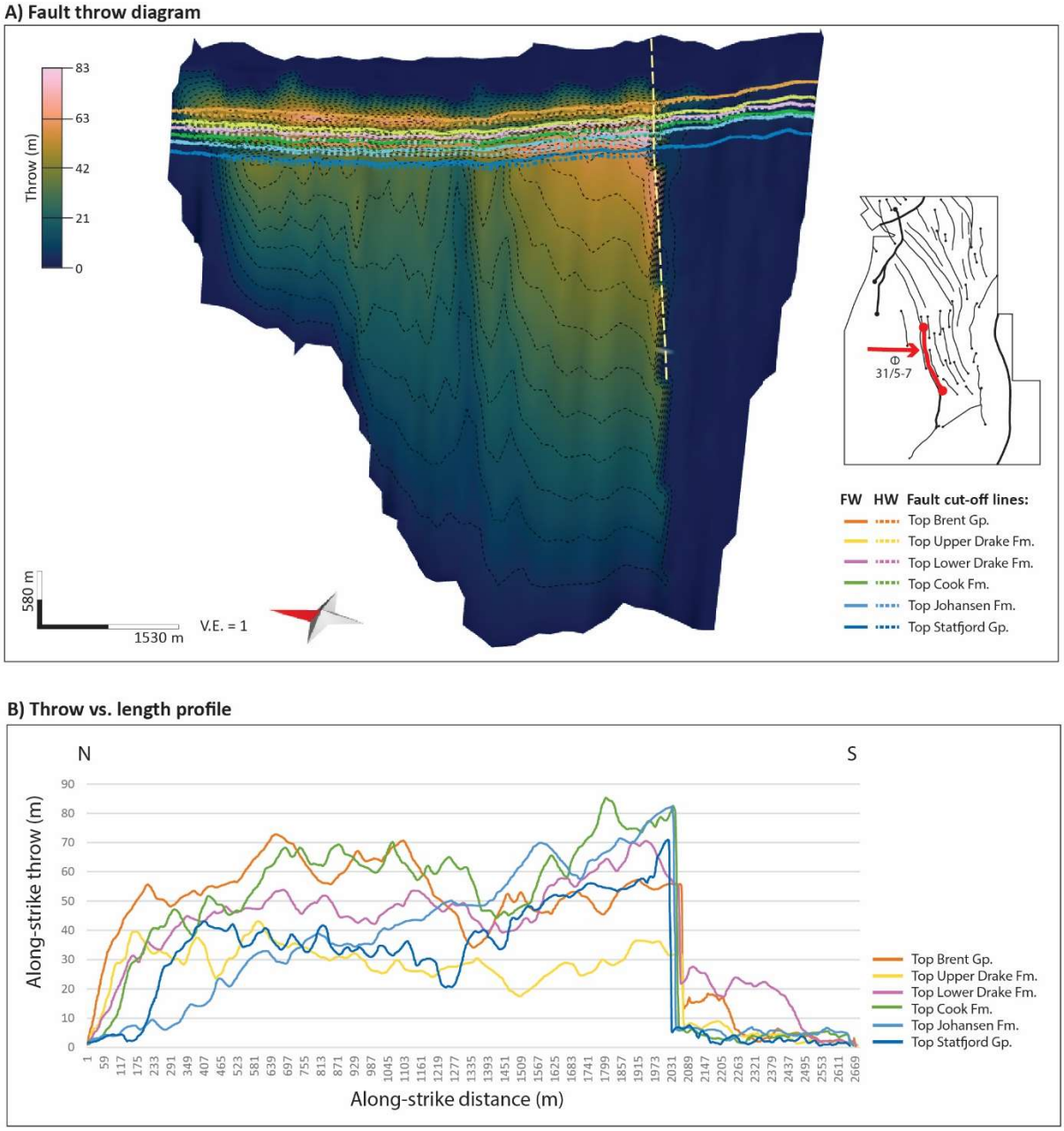

Figure Appendix 3. 2. A) F10 fault throw diagram showing horizon-fault intersection (cut-off) lines and a 5-meter throw contour spacing. Inset shows location of fault and viewing direction. B) Throw vs. length profile of the Svartalv 2 segment. Note that throw below the Statfjord Group hanging-wall cut-off line have been extrapolated and is likely not representative for the vertical throw variation.

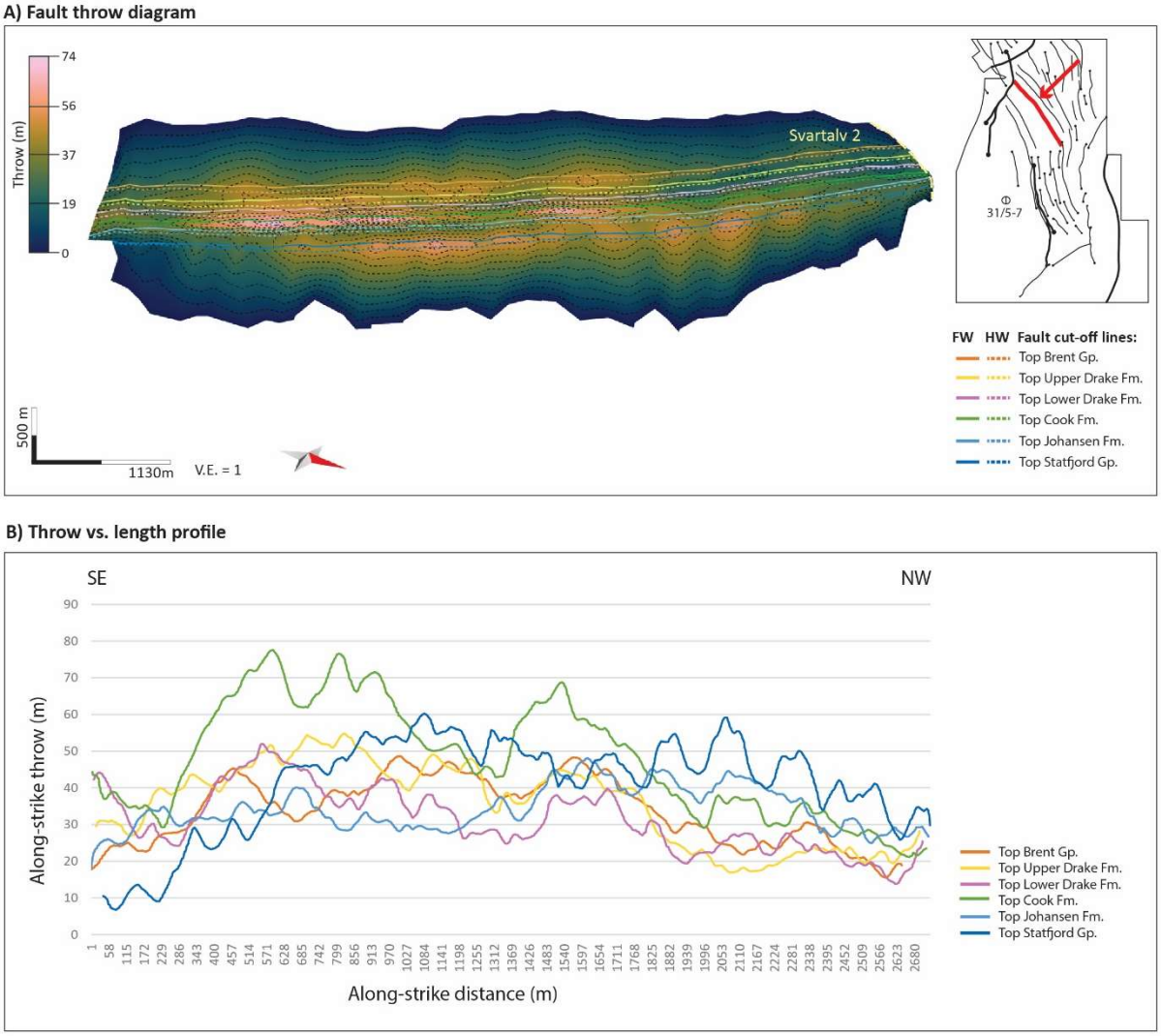

Figure Appendix 3. 3. A) F4 fault throw diagram showing horizon-fault intersection (cut-off) lines and a 5-meter throw contour spacing. Inset shows location of fault and viewing direction. B) Throw vs. length profile of the Svartalv 2 segment. Note that throw below the Statfjord Group hanging-wall cut-off line have been extrapolated and is likely not representative for the vertical throw variation.

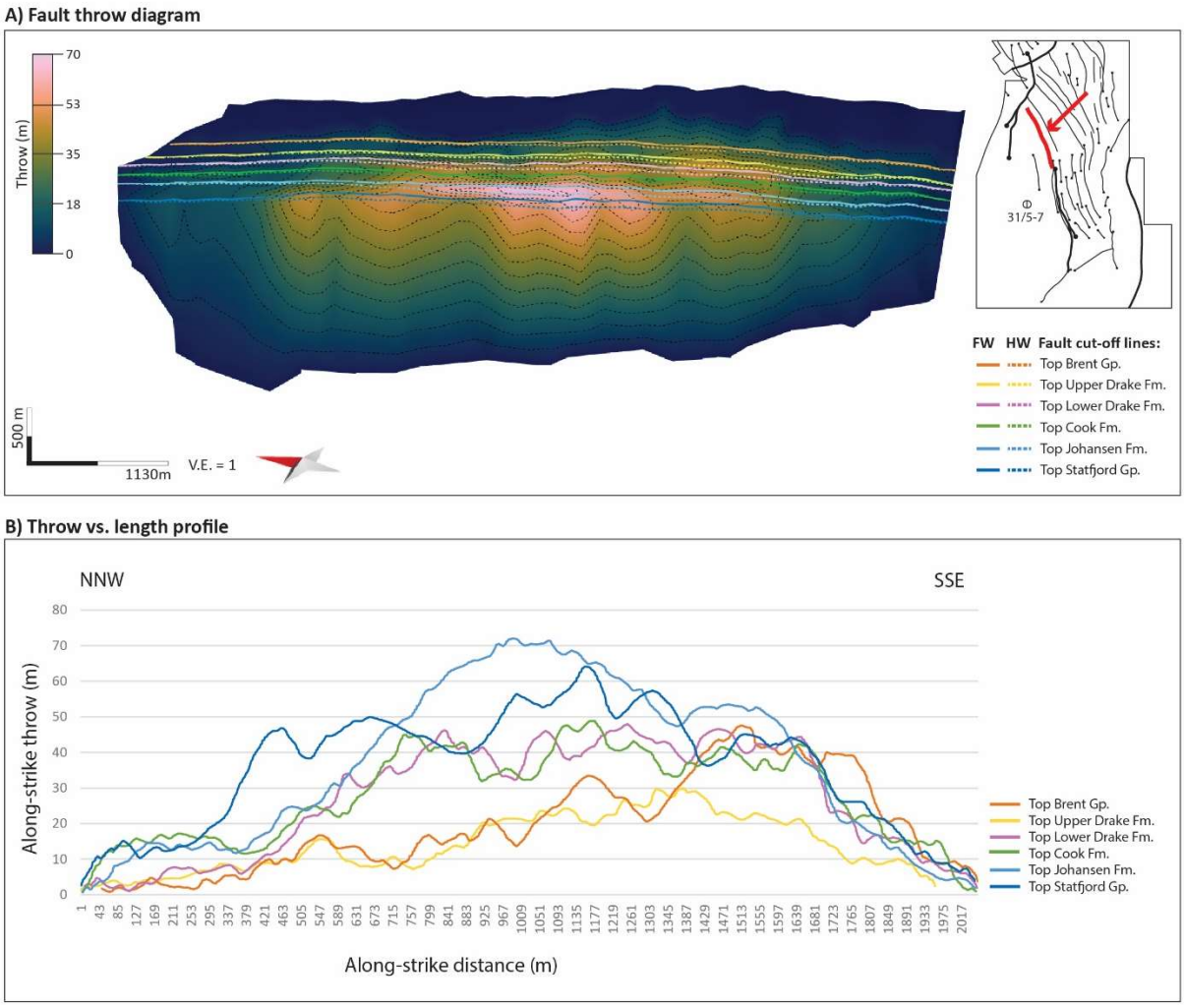

Figure Appendix 3. 4. A) F2 fault throw diagram showing horizon-fault intersection (cut-off) lines and a 5-meter throw contour spacing. Inset shows location of fault and viewing direction. B) Throw vs. length profile of the Svartalv 2 segment. Note that throw below the Statfjord Group hanging-wall cut-off line have been extrapolated and is likely not representative for the vertical throw variation.

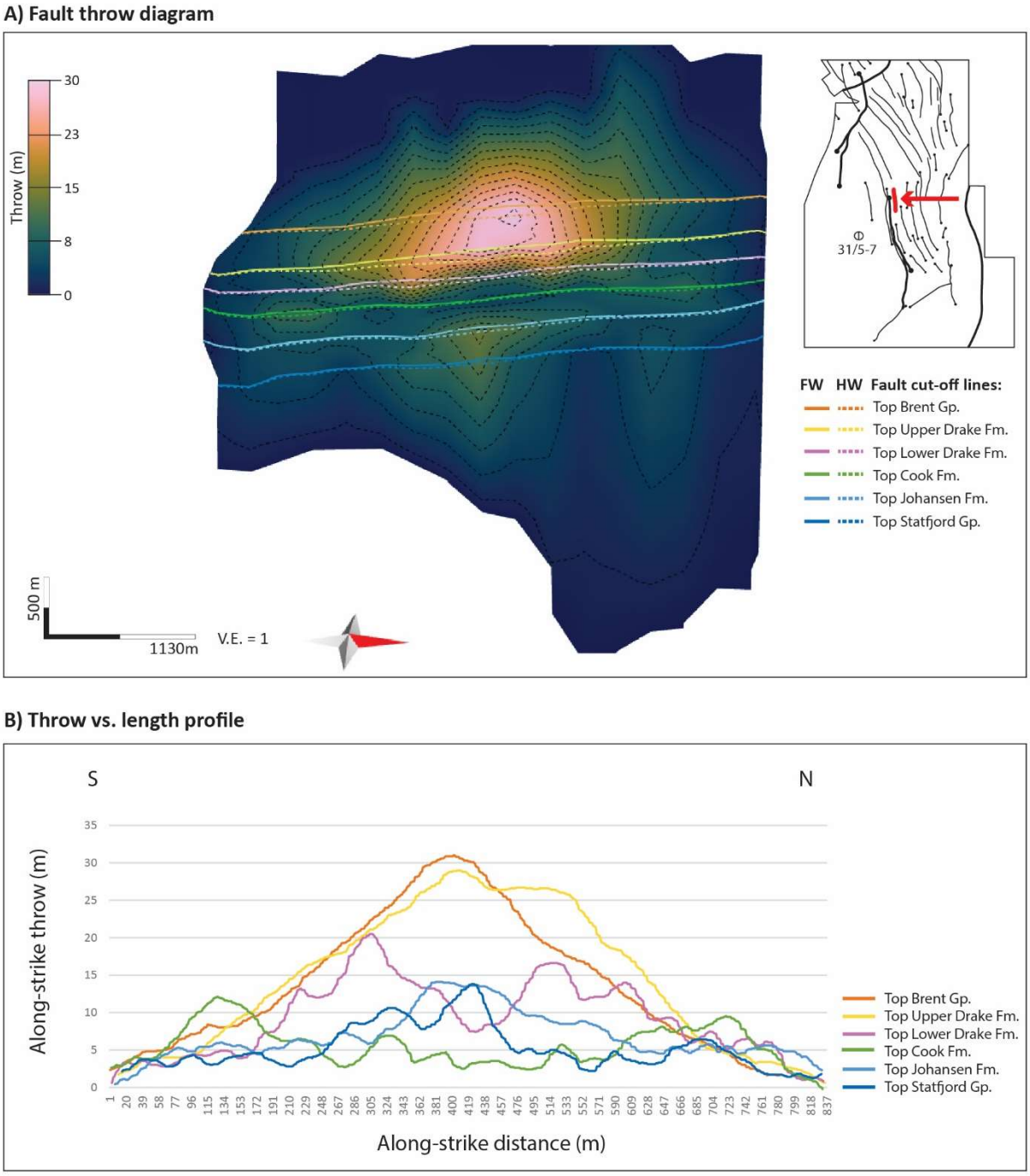

Figure Appendix 3. 5. A) F8 fault throw diagram showing horizon-fault intersection (cut-off) lines and a 2-meter throw contour spacing. Inset shows location of fault and viewing direction. B) Throw vs. length profile of the Svartalv 2 segment. Note that throw below the Statfjord Group hanging-wall cut-off line have been extrapolated and is likely not representative for the vertical throw variation.

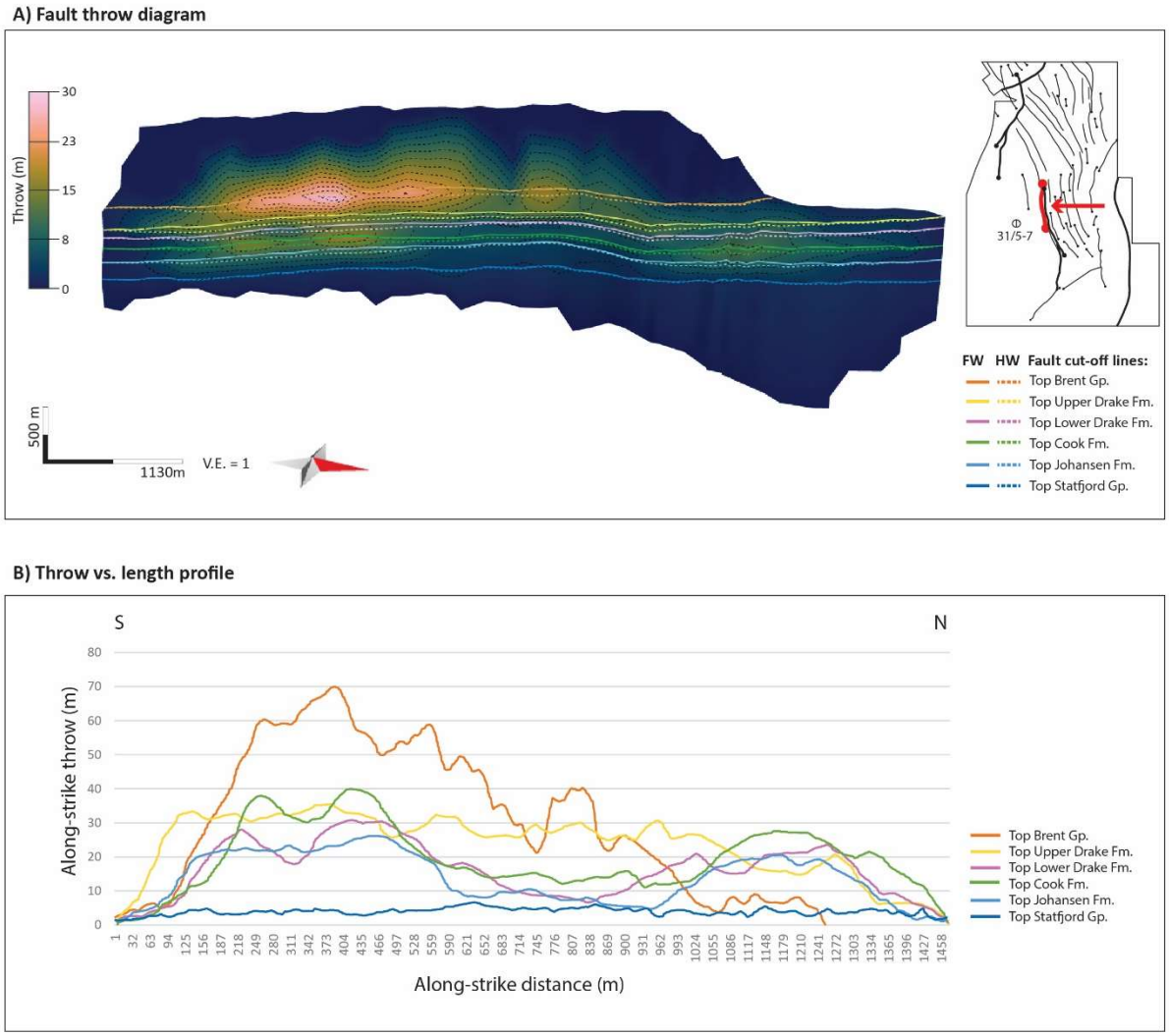

Figure Appendix 3. 6. A) F9 fault throw diagram showing horizon-fault intersection (cut-off) lines and a 2-meter throw contour spacing. Inset shows location of fault and viewing direction. B) Throw vs. length profile of the Svartalv 2 segment. Note that throw below the Statfjord Group hanging-wall cut-off line have been extrapolated and is likely not representative for the vertical throw variation.

Table Appendix 3. 1. Measurements of hanging wall (HW) and footwall (FW) thicknesses for the Dunlin and Brent groups, using the modelled cut-off lines in fault throw diagrams presented above, and corresponding expansion indices (E.I.).

Fault name	Dunlin Gp. (HW; m)	Dunlin Gp. (FW; m)	Dunlin Gp. E.I.	Brent Gp. (HW; m)	Brent Gp. (FW; m)	Brent Gp. E.I.
F2	392	353	1.11	96	96	1.00
F4	401	375	1.07	99	94	1.05
F10	337	338	0.99	131	119	1.01
F8	308	325	0.94	115	120	0.95
F9	291	318	0.91	129	136	0.95
Svartalv 1	459	321	1.43	112	100	1.12

Appendix 4

Table Appendix 4. 1. Left) maximum throw values measured at corresponding target succession intervals for the Svartalv 2 segment. Right) target succession thickness in the hanging wall (HW) and the footwall (FW) of the Svartalv 2 segment and the corresponding E.I. Abbreviations: E.I. = Expansion Index, NNSUC = Northern North Sea Unconformity Complex.

Horizon	Throw (m)	Depth (m)
NNSUC	59	1692
Top Brent Gp.	98	2098
Top upper Drake Fm.	150	2212
Top lower Drake Fm.	156	2295
Top Cook Fm.	193	2408
Top Johansen Fm.	218	2462
Top Statfjord Fm.	308	2659
Top Basement	961	6452

Unit	HW thickness (m)	FW thickness (m)	E.I.
Viking Gp.	424	383	1.10
Brent Gp.	98	77	1.27
Upper Drake Fm.	82	87	0.94
Primary seal unit	98	84	1.17
Secondary seal unit	98	88	1.11
Primary storage unit	188	130	1.44
Permian-Triassic	3508	3337	1.05

Table Appendix 4. 2. Left) maximum throw values measured at corresponding target succession intervals for the F3 fault. Right) target succession thickness in the hanging wall (HW) and the footwall (FW) of the F3 fault and the corresponding E.I. Abbreviations: E.I. = Expansion Index, NNSUC = Northern North Sea Unconformity Complex.

Horizon	Throw (m)	Depth (m)
NNSUC	32	1623
Top Brent Gp.	37	2087
Top upper Drake Fm.	34	2162
Top lower Drake Fm.	43	2240
Top Cook Fm.	46	2323
Top Johansen Fm.	60	2471
Top Statfjord Fm.	66	2548

Unit	HW thickness (m)	FW thickness (m)	E.I.
Viking Gp.	478	480	1.01
Brent Gp.	85	82	1.04
Upper Drake Fm.	83	77	1.07
Primary seal unit	85	80	1.06
Secondary storage unit	103	89	1.16
Primary storage unit	128	112	1.14
Upper Triassic	566	572	0.98

Intra Triassic Marker	35	3105
Lower fault-tip	0	3468

Table Appendix 4. 3. Left) maximum throw values measured at corresponding target succession intervals for the F1 fault. Right) target succession thickness in the hanging wall (HW) and the footwall (FW) of the F1 fault and the corresponding E.I. Abbreviations: E.I. = Expansion Index, NNSUC = Northern North Sea Unconformity Complex.

Horizon	**Throw (m)**	**Depth (m)**
Upper fault-tip	0	1840
Top Brent Gp.	30	2272
Top upper Drake Fm.	35	2414
Top lower Drake Fm.	34	2481
Top Cook Fm.	35	2559
Top Johansen Fm.	35	2635
Top Statfjord Fm.	38	2757
Intra Triassic Marker	38	2918
Lower fault-tip	0	3434

Unit	**HW thickness (m)**	**FW thickness (m)**	**E.I.**
Viking Gp.	441	446	0.95
Brent Gp.	113	112	1.01
Upper Drake Fm.	76	71	0.07
Primary seal unit	75	74	1.01
Secondary storage unit	77	76	1.01
Primary storage unit	120	118	1.02
Above Intra Triassic marker	160	156	1.03
Below Intra Triassic marker	523	547	0.96